Theoretical and Experimental Investigation on Nanostructures

PAN HUI

(*B. Sc.* Xidian University)

A THESIS SUBMITTED

FOR THE DEGREE OF DOCTOR OF PHILOSOPHY

DEPARTMENT OF PHYSICS

NATIONAL UNIVERSITY OF SINGAPORE

2006

ACKNOWLEDGEMENTS

First and foremost, I would like to express my sincerest gratitude to my supervisors, Assoc. Prof. Feng Yuan Ping and principal scientist Lin Jianyi, for their invaluable inspiration, guidance and encouragement throughout the course of my work.

I also would like to express my sincerest gratitude to Assoc. Prof. Ji Wei (Physics), Asst. Prof. Sow Chorng Haur (Physics), Asst. Prof. Wang Xue Sen (Physics), Assoc. Prof. Ding Jun (Material Science, especially for magnetic measurements and studies in Chapter 6), Prof. Huan Cheng Hon (NTU), Assoc. Prof. Shen Zexiang (NTU) and Prof You Jinkua (Xiamen University), for their constant support, guidance and cooperation.

I also thank all my friends and group members, Chen Weizhe, Dong Yufeng, Gao Han (IMRE), Gao Xinyu, Huang Min, Wang Yihua (Charter Semiconductor), Lim Sanhua, Liu Binghai, Luo Jizhong (ICES), Ni Zhenghua, Peng Guowen, Poh Cheekok, Sun Han, Sun Yiyang, Wang Yanhua, Wu Rongqing, Wu Xiaobing, Zhang Jie, Zhang Xinhuai (computer center), Zhu Yanwu, Zheng Yuebing (IMRE), and Yi Jiabao (Material Science, specially for magnetic measurement), for their cooperation, valuable discussion and help.

Particularly, I should thank my wife, Huang Jiayi, for her everlasting support and love.

Last but not least, I thank my parents and grandparents for their support, tolerance, and love.

Table of Contents

SUMMARY

Nanostructures have attracted increasing interests in theoretical physics, solid state science and practical technological applications, such as nanodevices, optical devices, and high-density storage. Among these nanostructures, carbon nanotubes, metal nanowires, and semiconductor nanowires (Si and ZnO) are very important to future information technology.

The overall objective of this thesis was to study the physical properties, i.e. structural, electronic and optical properties, and to investigate the potential applications of these nanostructures. In achieving this overall objective, both theoretical calculation and experimental study had been successfully conducted. Theoretically, first-principles method was used to calculate the electronic and optical properties of these nanostructures. Experimentally, template-based synthesis and thermal evaporation were employed to fabricate the nanostructures to investigate their electronic and optical properties and to identify their potential applications.

Calculations based on first-principles were carried out to study carbon and carbon-related nanotubes. More specifically, the calculations have shown that carbon nanoscroll has semi-metal property and shares the optical property of single-wall and multi-wall carbon nanotubes. The calculations have also revealed that the functonalization of carbon nanotubes can greatly change their electronic and optical properties, resulting in charge transfer and reduction of band gap etc. The first-principles calculations have further been extended to the study of boron carbonitride nanotubes and it has been found that their

electronic and optical properties are dependent on the diameter and chirality. A combined calculation and experiment method was used the study the magnetic property of C-doped ZnO. Experimentally, anodic aluminum oxide (AAO) template was produced by a two-step anodization process. A novel electrical bridge model has been proposed to understand the self-assembly of the nanopores in the AAO. Then, AAO template was used to produce highly-ordered carbon nanotubes and metallic nanowires. Template-based synthesis illustrated that highly-ordered carbon nanotubes can be produced, which were found useful in the interconnection of nanodevices after studying their electronic properties. Single crystal metallic nanowires were obtained by template-synthesis. The single-crystalline Ni and Co nanowires showed better magnetic properties than poly-crystal nanowires. The nonlinear optical property of metallic nanowires was investigated. Thermal evaporation of semiconductor nanowires, i.e. Si, ZnO and Mg doped ZnO nanowires, demonstrated that catalyst-free growth is possible, which can be useful to remove the metal impurity in semiconductors induced by catalyst in the process of catalyst-assisted growth. Possible applications explored in the study, such as electroluminescence and photoluminescence, showed that these nanostructures can be used in nanodevices, optical devices and storage.

This study demonstrated that the research based on theoretical calculation and experimental method is efficient and fruitful to study nanostructures. And it is possible to extend the study to other systems.

LIST OF PUBLICATIONS

1. Hui Pan, Weizhe Chen, Yuanping Feng, Wei Ji, Jianyi Lin, Optical limiting of metal nanowires, ***Appl. Phy. Lett. 88, 223106 (2006)***. Also highlighted on ***Virtual Journal of Nanoscale science & Technology*** 13 (23) (Jun 12, 2006) and ***Photonics Spectra (Aug. 1, 2006)***.

2. Hui Pan, Yuanping Feng, Jianyi Lin, *Ab initio* study of single-wall BC_2N nanotubes, ***Phys. Rev. B 74, 045409 (2006)***. Also highlighted on Virtual ***Journal of Nanoscale science & Technology*** 14 (4) (Jul. 24, 2006).

3. Hui Pan, Yuanping Feng, Jianyi Lin, First-principles study of optical spectra of single-wall BC_2N nanotubes, ***Phys. Rev. B 73, 0345420 (2006)***. Also highlighted on Virtual ***Journal of Nanoscale science & Technology*** 13 (3) (Jan. 23, 2006).

4. Hui Pan, Zhenhua Ni, Han Sun, Yuanping Feng, Zexiang Shen, Jianyi Lin, Strong green emission of Mg doped ZnO nanowires, ***J. Nanoscience and Nanotechnology 6, 2529–2532 (2006).***

5. Hui Pan, Yanwu Zhu, Han Sun, Yuanping Feng, Chow Haur Sow, Jianyi Lin, Electroluminescence and Field emission properties of Mg doped ZnO tetrapods, ***Nanotechnology17, 5096-5100(2006).***

6. Hui Pan, Yuanping Feng, Jianyi Lin, Magnetic properties of carbon doped ZnO, ***to be submitted.***

7. Hui Pan, Han Sun, Yuanping Feng, Jianyi Lin, Hydrogen storage of ZnO and Mg doped ZnO nanowires, ***Nanotechnology 17, 2963(2006)***.

8. Yuanping Feng, Hui Pan, Rongqing Wu, Guowen Peng, Jianyi Lin, *Ab initio* study of functionalized nanotubes, ***Hard Nanomaterials***, edited by H. S. Nalwa, in press. (invited review)

9. Hui Pan, Cheekok Poh, Yuanping Feng, Jianyi Lin, Supercapacitor electrodes from carbon nanostructures, ***submitted***.

10. Hui Pan, Yuanping Feng, Jianyi Lin, *Ab initio* study of F, Cl-functionalized single wall carbon nanotubes, ***J. Phys: Conden. Mater. 18, 5175-5184(2006)***.

11. Hui Pan, Liying Tong, Yuan Ping Feng, Jianyi Lin, Enhancement of minority-carrier lifetime by an advanced high temperature annealing method, ***Thin Solid Films*** 504, 129-131 (2006).

12. Hui Pan, Yuanping Feng, Jianyi Lin, Ab initio study of electronic and optical properties of multiwall carbon nanotube structures made up of a single rolled-up graphite sheet, ***Phys. Rev. B 72, 085415 (2005)***. Also highlighted on Virtual ***Journal of Nanoscale science & Technology*** 12 (7) (Aug. 15, 2005).

13. Hui Pan, Binghai Liu, Jiabao Yi, Cheekoh Poh, Sanhua Lim, Jun Ding, Yuanping Feng and Jianyi Lin, Growth of single-crystalline Ni and Co nanowires via electrochemical deposition and their magnetic properties, ***J. Phys. Chem. B 109, 3094-3098 (2005).***

14. Hui Pan, Yanwu Zhu, Zhenhua Ni, Han Sun, Cheekok Poh, Sanhua Lim, Chornghaur Sow, Zexiang Shen, Yuanping Feng, Jianyi Lin, Optical and field emission properties of ZnO nanostructures, ***J. Nanoscience and Nanotechnology 5, 1683–1687 (2005)***.

15. Hui Pan, Han Sun, Cheekoh Poh, Yuanping Feng, Jianyi Lin, Single crystal growth of metal nanowires with preferred orientation, ***Nanotechnology 16, 1559-1564 (2005)***.

16. Hui Pan, Jianyi Lin, Weizhe Chen, Han Sun, Yuanping Feng, and Wei Ji, Optical limiting and hydrogen storage characterization of Cu, Cu_2O and CuO nanostructures, ***ICNT 2005 Proceeding***.

17. Hui Pan, Zhenhua Ni, Han Sun, Cheekoh Poh, Zhexiang Shen, Yuanping Feng, Jianyi Lin, Optical and Raman characterization of ZnO nanowires, ***poster presented in the 3rd ICMAT (2005)***.

18. Hui Pan, Weizhe Chen, Sanhua Lim, Cheekoh Poh, Xiaobing Wu, Yuanping Feng, Wei Ji, Jianyi Lin, Photoluminescence and optical limiting of Si nanowires, ***J. Nanoscience and Nanotechnology 5, 733-737 (2005).***

19. Hui Pan, J.B. Yi, B.H. Liu, S. Thongmee, J. Ding, Yuan Ping Feng, Jian Yi Lin, Magnetic properties of highly-ordered Ni, Co and their alloy nanowires in AAO templates, ***Solid state Phenomena, 111, p123 (2006)***.

20. Hui Pan, Sanhua Lim, Cheekoh Poh, Xiaobing Wu, Yuanping Feng, Jianyi Lin, Growth of Si nanowires by thermal evaporation, ***Nanotechnology 16, 417-421 (2005).***

21. Hui Pan, Yuanping Feng, Jianyi Lin, *Ab initio* study of OH-functionalized single wall carbon nanotubes, ***Phys. Rev. B 70, 245425 (2004)***. Also highlighted on Virtual ***Journal of Nanoscale science & Technology*** 11 (1) (Jan. 10, 2005).

22. Hui Pan, Jianyi Lin, Yuanping Feng, Han Gao, Electrical bridge model on the self-organized growth of nanopores in anodized Aluminum oxide, ***IEEE Trans. On Nanotechnology 3(4), 462-467 (2004)***.

23. Hui Pan, Han Gao, Sanhua Lim, Yuanping Feng and Jianyi Lin, Highly ordered carbon nanotubes based on porous aluminum oxide: fabrication and mechanism, ***J. Nanoscience and Nanotechnology 4 (8), 1014-1018 (2004)***.

24. Han Gao, Jianyi Lin, Hui Pan, Guotao Wu, Yuanping Feng, The growth of carbon nanotubes at predefined locations using nickel nanowires as templates**,** ***Chem. Phys. Lett. 393, 511 (2004).***

LIST OF PATENTS

1. Hui Pan, Jianyi Lin, Jun Ding, Yuanping Feng, "Single Crystal Growth of Magnetic Nanowires", **US Provisional Patent Application No. 60/607,111**.
2. Hui Pan, Jianyi Lin, Yuanping Feng, "Synthesis of Mg doped ZnO nanowires and their applications to optical devices and hydrogen storage", **US Provisional Patent Application No. 60/698,476**.
3. Hui Pan, Jianyi Lin, Yuanping Feng, "Supercapacitor from carbon tube-in-tube nanostructures", **US Provisional Patent Application No. 60/777,547**.
4. Jin Chua Soo, Hailong Zhou, Jianyi Lin, Hui Pan, "Method of ZnO film grown on the epitaxial lateral overgrowth GaN template", submitted.

LIST OF TABLES

LIST OF FIGURES

CHAPTER 1

INTRODUCTION

1.1 Background

Nanotechnology arises from the exploitation of physical, chemical, and biological properties of systems that are intermediate in size between isolated atoms/molecules and bulk materials, where phenomena length scales become comparable to the size of the structure. It is recognized as an emerging technology of the 21st century, along with the already established areas of computer/information technology and biotechnology. New experimental and simulation tools emerging in the last few years and the discovery of novel phenomena and processes at the "nano" scale have opened revolutionary opportunities for developments in nanoparticles, nanostructured materials, and nanodevices. Nanostructures, including nano-clusters, nano-layers, nano-tubes, nano-wires and two and three-dimensional structures in the size range between the dimensions of molecules and 50 nm (or in a broader sense, submicron sizes as a function of materials and targeted phenomena), are seen as tailored precursors for building up functional structures. The physical, chemical, and biological properties of these nanostructures may be significantly different from those of corresponding bulk materials, and desirable novel or enhanced properties may be obtained at this nanoscale. The two main reasons for this change in behaviour are an increased relative surface area, and the dominance of quantum effects. An increase in surface area (per unit mass) will result in a corresponding enhancement of chemical reactivity, making nanomaterials useful with higher efficiency. As the size of matter is reduced to nanometer scale, quantum effects can begin to play a role, and these can significantly change a material's electronic, optical, magnetic

properties. For example, the band gap of nanometer-scale semiconductor structures increases as the size of the microstructure decreases, raising expectations for many possible optical and photonic applications[1]. The emerging science of nanotechnology will affect not only the fundamental theories, but also the competitive global positions of companies. The potential impact is considerable -- nanostructured materials or nano-processed devices have broad applications from pharmaceuticals, bioengineering, pigments, and electronics to optical and magnetic devices and structures and coatings with special properties.

Research and development (R&D) in this field emphasize scientific discoveries in the generation of nanostructures with controlled characteristics; understanding of the physics of new phenomena and processes at nanoscales (1-100 nm); research on their processing into microstructured bulk materials with engineered properties and technological functions; and introduction of new device concepts and manufacturing methods. R&D in this field is stimulating the development of new modeling and experimental tools for the mentioned purposes. This thesis will focus on the theoretical and experimental study of one-dimension nanostructures to control their physical properties and investigate their possible applications.

One-dimensional nanostructures, nanotubes and nanowires, are of great interest in theoretical physics, solid state science and practical technological applications due to their periodic structure in one-direction, which can induce new physical phenomena[2,3,4]. These nanostructures are seen as precursors of devices with tailored properties. Among these one-dimension nanostructures, carbon nanotubes, metal nanowires and semiconductor

nanowires are very important to information technology in the future, for their applications in high-density storage devices, nanolaser, and spintronics[5,6,7]. Theoretical calculation and experimental study on these 1-D nanostuctures can reveal their physical properties, predict new materials and develop their applications.

Carbon nanotubes (CNTs)[8] are formed when a graphite sheet is curled up into cylinders. Generally, there are two kinds of CNTs: single-wall CNT (SWCNT) and multi-wall CNT (MWCNT). A SWCNT can be described as a single layer of a graphite crystal rolled up into a seamless cylinder, one atom thick, usually with a small number of carbon atoms along the circumference and a long length (microns) along the cylinder axis[9,10,11]. A carbon nanotube is specified by the chiral vector $\vec{C}_h$,

$$\vec{C}_h = n\vec{a}_1 + m\vec{a}_2 \equiv (n,m) \tag{1.1}$$

which is often described by the pair of indices (n, m) that denote the numbers of unit vectors $\vec{a}_1$ and $\vec{a}_2$ in the $\vec{C}_h$ vector of the hexagonal honeycomb lattice. The so-called zigzag nanotubes correspond to *n=0 or m=0*, whereas the so-called armchair nanotubes correspond to *n=m*, and the nanotube axis for the so-called chiral nanotubes correspond to n≠*m*≠*0*. The electronic properties of SWCNTs are correlated with their chirality and diameter. Armchair carbon nanotubes with the chiral index (n, n) are metallic[12,13], while zigzag carbon nanotubes (n, 0) are semiconductors except for the case of n=3k (k is an integer), which is narrow gap semiconductor due to the curvature if n is not large enough[14,15,16]. Chiral carbon nanotubes are mostly semiconductors except for the case of n-m=3k. The band gap of Chiral SWCNT is controlled by its diameter, $E_g \propto \frac{1}{d}$, where d is the diameter of the SWCNT[12,17].

There are two kinds of MWCNT, *i.e.*, Russian doll and Swiss scroll (carbon nanoscroll)[18]. Russian doll structure refers to the nested carbon nanotubes, while Swiss scroll structure represents the rolled-up graphene sheet[8,19]. Most studies of the MWCNT have focused on the Russian doll and revealed that the intershell spacing d_{002} ranges from 0.34 to 0.39 nm, increasing with decreasing tube diameter[20,21]. MWCNTs are metallic, except for some double- or trio-wall CNTs for which a gap or pseudo-gap can be induced due to the inter-tube interaction or the lowering of symmetry[21]. Even though there have been many studies on Russian doll structure, to date, there has not been any first-principles calculation reported on carbon nanoscrolls. Hence, theoretical study of carbon nanoscrolls becomes one of the objectives of the thesis.

The physical properties of CNT are greatly related to its size. Does metal nanowire have the same relations? Metal nanowires are one of the most attractive materials because of their unique properties that may lead to a variety of applications. Examples include interconnects for nanoelectronics, magnetic devices, chemical and biological sensors, and biological labels[22]. In terms of electron transport properties, metal nanowires can be described as classical wires or quantum wires. The electron transport in a classical wire obeys the classical relation:

$$G = \sigma \frac{A}{L} \tag{1.2}$$

where G is the conductance, and L and A are the length and the cross-sectional area of the wire, respectively. σ in Eq. (1.2) is the conductivity, which depends on the material of the wire. The classical behavior arises if the wires are much longer than the electron mean-free path, and much thicker than the electron Fermi wavelength. The Fermi wavelength is related to the size of the nanostructure (diameter and length). For example, The Fermi

wavelength of Co nanowire with a diameter of 100 nm is about 0.5 nm. The former condition means that conduction electrons experience many collisions with phonons, defects, and impurities when they traverse along a wire. The second condition smears out the effects due to the quantum-size confinement in the transverse direction of the wire.

When the wire is shorter than the electron mean-free path, the electron transport is ballistic, that is, without collisions along the wire. If, in addition, the diameter of the wire is comparable to the electron wavelength, quantum-size confinement becomes important in the transverse direction, which results in well-defined quantum modes. The conductance of the system measured between two bulk electrodes is described by the Landauer formula[23]

$$G = \frac{2e^2}{h} \sum_{i,j=1}^{N} T_{ij} \tag{1.3}$$

where e is the electron charge, h is Planck's constant, and T_{ij} is the transmission probability of an electron from ith mode at one side of the wire to the jth mode at the other side. The summation is over all the quantum modes, and N is the total number of modes with nonzero T_{ij} values, which is determined by the number of standing waves at the narrowest portion of the wire. In the ideal case, T_{ij} is 1 for $i = j$ and 0 for all other cases, so Eq. (1.3) is simplified as $G = NG_0$, where $G_0 = 2e^2/h \equiv 77.5$ μS is the conductance quantum. Thus the conductance is quantized and the wire is referred to as a quantum wire. A number of applications based on the phenomenon have been proposed and explored, such as analog and digital switches using atomic-scale point contacts formed between a Ni wire and a Au substrate[24].

Metal nanowires are attractive also because they can be readily fabricated with various techniques. An important fabrication technique is the electrochemical method based on template. This approach is promising for large-area ordered nanowires with high aspect ratio[25,26,27]. The arrays of metal nanowires have many potential technical applications, such as high-density magnetic recording and as sensors, and are scientifically interesting because they can be considered as model systems to study interaction processes and magnetic reversal in low-dimensional magnetic structures[28,29,30]. Many works were concerned with exploratory issues, such as establishing an easy axis for typical preparation conditions and the essential involvement of shape anisotropy, as opposed to magnetocrystalline anisotropy. More recently, attention has shifted towards the understanding of magnetization processes. Particularly interesting problems are the magnetic hysteresis of the wires and the time dependence of the magnetic reversal: it has become well known that simple reversal mechanisms, such as coherent rotation and curling, are unable to account for the observed hysteretic behavior. For example, the coercivity of the wire arrays is often greatly overestimated by those delocalized reversal modes. This failure originates from the neglect of morphological (real-structural) wire imperfections. Therefore, it is essential to produce highly ordered nanowires with prefect crystalline structure to investigate the mechanism.

Besides the metallic interconnections, the nanodevice needs semiconductor components to perform functions. It is necessary to investigate the properties of semiconductor nanostructures, especially Si and ZnO. Semiconductor nanowires exhibit novel electronic and optical properties owing to their unique structural one-dimensionality and possible quantum confinement effects in two dimensions. With a broad selection of compositions

and band structures, these one-dimensional semiconductor nanostructures are considered to be the critical components in a wide range of potential nanoscale device applications. To fully exploit these one-dimensional nanostructures, current researches have focused on rational synthetic control of one-dimensional nanoscale building blocks, novel properties characterization and device fabrication based on nanowire building blocks, and integration of nanowire elements into complex functional architectures.

A lot of semiconductor nanowires, including group IV, III-V compounds, and II-VI compounds, have been fabricated and investigated. For example, InP nanowire was synthesized via a laser-assisted catalytic growth and showed a striking anisotropy in the PL intensity recorded parallel and perpendicular to the long axis of an InP nanowire[31]. This intrinsic anisotropy can be used to create polarization sensitive nanoscale photodetectors that may prove useful in integrated photonic circuits, optical switches and interconnects, near-field imaging, and high resolution detectors. Among these semiconductor nanowires, Si and ZnO nanowires have received broad attention due to their distinguished performance in electronics, optics and photonics.

Silicon is one of the most important and fundamental electronic materials in computer and information technology (IT) industry. Recently, Si nanowires (SiNWs) have attracted great attention due to their potential applications in Si-based nanodevices[32,33], including optoelectronic nanodevices[34]. The band gap of Si nanowire was calculated to be direct and at the zone corner on the basis of first-principles calculations[35]. The blueshift of the optical absorption edge along with the intense red photoluminescence (PL) peak has been observed from micron-long crystalline silicon nanowires prepared by pulsed-laser

vaporization of heated Si (mixed with metal catalyst) targets due to quantum confinement effect[36]. Further calculations based on first-principles with Green function illustrated that quantum confinement becomes significant for d<2.2 nm (d is the diameter of Si nanowires), where the dielectric function exhibits strong anisotropy and new low-energy absorption peaks start to appear in the imaginary part of the dielectric function for polarization along the wire axis[37]. Therefore, it is necessary to develop a method to synthesis Si nanowires without catalyst to compare the experimental result with that of calculations because catalyst may contaminate Si nanowires and cover up their intrinsic properties.

ZnO possesses spectacular chemical, structural, electrical and optical properties that make it useful for a diverse range of technological applications. As a wide band gap semiconductor (3.37 eV at room temperature) with large exciton binding energy (60 meV), ZnO is of great interest for the applications in low-voltage and short-wavelength electric and photonic devices, such as blue and UV light emitting diodes for full-color display and room-temperature excitonic ultraviolet laser diodes for high density optical storage[38,39,40,41]. ZnO is a versatile functional material that has a diverse group of growth morphologies, such as nanocombs, nanorings, nanohelixes/nanosprings, nanobelts, nanowires and nanocage [42] . Visible luminescence was observed on these nanostructures[43,44]. The proposed mechanisms for the visible luminescence include the radiative recombination of the electrons from singly ionized oxygen vacancies and interstitial oxygen with the photo-generated holes or surface states[41,45,46], donor-acceptor and shallow donor-deep level transitions[47,48], Zn interstitials[49], and antisite oxygen[50]. And

it may be useful to grow ZnO nanostructures without catalyst because the atom species of the catalyst may exist in ZnO as impurities and affect the luminescence property.

1.2 Motivation

As nanostructures in various applications continue to become increasingly small in size, they approach a limit at which their behavior may become atomic in character, and study of the nanostructure then falls into the area of basic atomic, molecular, and quantum physics. Research in the nanostructures focuses on the interpretation of the internal structure and dynamics of atoms and molecules through application of the fundamentals of quantum mechanics and investigation of potential applications via theoretical simulation. Another important issue in the study and application of these 1D materials is how to assemble individual atoms into 1D nanostructure in an effective and controllable way. Nanostructure engineering involves the synthesis and processing of nanometer-sized materials with controlled properties for applications in advanced materials such as nanoelectronics, spintronics, optical structures, and semiconductors.

Nanotechnology is concerned with the structures, properties, and processes involving materials having organizational features on the spatial scale of 1 to 300 nm. This is bigger than simple molecules but smaller than the wavelength of visible light. At these scales there are new phenomena that provide opportunities for new levels of sensing, manipulation, and control. In addition, devices at this scale may lead to dramatically enhanced performance, sensitivity, and reliability with dramatically decreased size, weight, or cost. From the experimental point of view, the fundamental problem in nanoscale technology is that the units are too small to see and manipulate and too large

for single-pot synthesis from chemical precursors; consequently, most synthetic nanotechnologies focus on self-assembly of molecules. Anodic aluminum oxide (AAO) is an important self-organized template and particularly suitable for growing highly uniform ordered nanostructures. Another critical challenge in developing successful nanoscale technology is development of reliable simulation tools to guide the design, synthesis, monitoring, and testing of the nanoscale systems. This is critical for nanotechnology because we cannot "see" the consequences of experiments at the nanoscale. Thus it is essential to use first-principles calculation because the method based on density functional theory reliably predicts the chemical and physical properties of nanostructure.

1.3 Objectives

The purpose of the project is to use theoretical calculation and experimental method to study the physical properties and size effect of the nanostructures and investigate their potential applications. More specifically, the objectives are:

- To study the electronic and optical properties of carbon nanotubes by ab initio total energy method based on density functional theory. The theoretical calculations are performed on carbon nanoscrolls and OH-, Cl-, and F-functionalized SWCNTs to investigate their electronic and optical properties, which are difficult to be obtained in experiments.
- To study the electronic and optical properties of BC_2N nanotubes based on first-principles. The dependence of the band gap on the diameter and chirality of the nanotubes are calculated. The optical properties are investigated.

- To study the the magnetic property of C-doped ZnO based on the combined calculation and experiment method.
- To produce nanostructure in an effective and controllable way and investigate their growth mechanism and physical properties. A self-organized template, anodic aluminum oxide (AAO) is introduced. Highly ordered carbon nanotubes and metal nanowires with controllable diameter and length can be fabricated on the basis of AAO template.
- To produce semiconductor nanowires and investigate their growth mechanism and physical properties. A catalyst-free thermal evaporation method is employed. Si nanowires and ZnO nanostructures are produced by the thermal evaporation without metal contamination.

1.4 Organization of the Thesis

The thesis is organized into eleven chapters:

In chapter 2, a thorough but concise review on the first-principles total-energy calculation based on density function theory (DFT) will be presented.

In chapters 3 and 4, the carbon nanotubes will be studied based on ab initio calcultions. In particular, the structural and electronic properties of carbon nanoscrolls will be investigated in chapter 3. And the OH-, F- and Cl-functionalized single wall carbon nanotubes based on first-principles will be studied in chapter 4.

In chapter 5, the dependence of the band structure on the diameter and chirality of the single-wall BC_2N nanotubes will be discussed on the basis of first-principles. The dependence of the optical properties on the diameter and chirality are also investigated.

In chapter 6, the magnetic property of C-doped ZnO was studied based on the combined calculation and experiment method.

In chapter 7, a porous anodic aluminum oxide (AAO) consisting of closely packed nanopores, is introduced and served as a template for the nanotubes and nanowires in a controllable way. A novel electrical bridge model is firstly proposed to describe the self-organization of the nanopores. The template is used to produce highly ordered carbon nanotubes by chemical vapor deposition, as discussed in chapter 8, and metal nanowires including Ni, Co, Cu, Ag, Zn, Pd, Pt, et. by electrochemical deposition, as discussed in chapter 9. The magnetic and optical properties of the metal nanowires are discussed accordingly.

In chapter 10, a catalyst-free thermal evaporation method is used to produce Si and ZnO nanostructures. Si nanowires with good crystallinity are fabricated. The possible mechanism is discussed for their growth. And their optical property is studied. The optical properties of ZnO nanostructures with and without Mg doping, such as photoluminescence, electroluminescence, Raman scattering, and field emission, are studied.

Finally, in chapter 11, the dissertation will be wrapped up by providing a summary of the main findings of this research work. And, some directions for further research in the area will be provided.

References:

[1] Colvin, V., M. Schlamp, and P. Alivisatos, Nature 370, 6488 (1994).
[2] R. H. Baughman, A. A. Zakhidov, and W. A. de Heer, Science 297, 787 (2002).
[3] N. A. Melosh, A. Boukai, F. Diana, B. Gerardot, A. Badolato, P. M. Petroff, and J R. Heath, Science 300, 112 (2003).
[4] X. Duan, Y. Huang, Y. Cui, J. Wang, and C. M. Lieber, Nature 409, 66 (2001).
[5] M.H. Huang, S. Mao, H. Feick, H. Yan, Y. Wu, H. Kind, E. Weber, R. Russo, and P. Yang, Science 292, 1897 (2001).
[6] W. Wernsdorfer, E.B. Orzeo, K. hasselbach, A. Benoit, B. Barbara, N. Demoncy, A. Loiseau, H. Pascard, and D. Mailly, Phys. Rev. Lett. 78, 1791 (1997).
[7] S. W. Chung, J. Y. Yu, and J. R. Heath, Appl. Phys. Lett. 79, 2068 (2000).
[8] S. Iijima, Nature 354, 56 (1991).
[9] M. S. Dresselhaus, G. Dresselhaus, and P. C. Eklund, Science of Fullerenes and Carbon Nanotubes, 1996 (New York/San Diego: Academic).
[10] M. S. Dresselhaus, G. Dresselhaus, and G, R. Saito, Phys. Rev. B 45, 6234 (1992).
[11] R. Saito, G. Dresselhaus, and M. S. Dresselhaus, Physical Properties of Carbon Nanotubes, 1998 (London: Imp. Coll. Press).
[12] N. Hamada, S. Sawada, and A. Oshiyama, Phys. Rev. Lett. 68, 1579(1992).
[13] J.W. Mintwire, B.I. Dunlap, and C.T. White, Phys. Rev. Lett. 68, 631 (1992).
[14] A. Kleiner and S. Eggert, Phys. Rev. B 63, 073408 (2001).
[15] J.W. Mintmire and C.T. White, Phys. Rev. Lett. 81, 2506 (1998).
[16] O. Gulseren, T. Yildirim, and S. Ciraci, Phys. Rev. B 65, 153405 (2002).
[17] D. H. Oh and Y.H. Lee, Phys. Rev. B 58, 1687 (1998).
[18] Peter J.F. Harris., Carbon nanotubes and related structures: new materials for the 21st century, (New York: Cambridge University Press), 1999.
[19] S. Amelinckx, D. Bernaerts, X.B. Zhang, G.V. Tendeloo, and J.V. Landuyt, Science 267, 1334 (1995).
[20] C. H. Kiang, M. Endo, P. M. Ajayan, G. Dresselhaus, and M. S. Dresselhaus, Phys. Rev. Lett. 81, 1869 (1998).
[21] Y.-K Kown and D. Tomanek, Phys. Rev. B 58, R16001 (1998).
[22] D. H. Reich, M. Tanase, A. Hultgren, L. A. Bauer, C. S. Chen, and G. J. Meyer, J. Appl. Phys. 93, 7275 (2000). And references within.
[23] R. Landauer, IBM J. Res. Dev. 1, 223 (1957).
[24] D. P. E. Smith, Science 269, 371 (1995).
[25] H. Masuda and K. Fukuda K, Science 268, 1466 (1995).
[26] A. P. Li, F. Muller, A. Birner , K. Nielsch and U. Gosele, J. Appl. Phys. 84 , 6023 (1998).

[27] M. Zheng, L. Menon, H. Zeng, Y. Liu, S. Bandyopadhyay, R. D. Kirby and D. J. Sellmyer, Phys. Rev. B 62, 12 282 (2000).
[28] R. Skomski, H. Zeng, M. Zheng, and D. J. Sellmyer, Phys. Rev. B 65, 3900 (2000).
[29] W. Wernsdorfer, E. B. Orzeo, K. Hasselbach, A. Benoit, B. Barbara, N. Demoncy, A. Loiseau, H. Pascard, and D. Mailly, Phys. Rev. Lett. 78, 1791 (1997).
[30]J. G. S. Lok, A. K. Geim, J. C. Maan, S. V. Dubonos, L. Theil Kuhn and P. E. Lindelof, Phys. Rev. B 58, 12201 (1998).
[31] J. Wang, M. S. Gudiksen, X. Duan,1 Y. Cui, and C. M. Lieber, Science 293, 1455 (2001).
[32] S. Chung, J Yu and J. R. Heath, Appl. Phys. Lett. 76, 2068 (2000).
[33] A. Tilke, R. H. Blick, H. Lorenz, and J. P. Kotthaus, J. Appl. Phys. 89, 8159 (2001).
[34] D. P. Yu, Z. G. Bai, J. J. Wang, Y. H. Zou, W. Qian, J. S. Fu, H. Z. Zhang, Y. Ding, G. C. Xiong, L.P. You, J. Xu, and S. Q. Feng, Phys. Rev. B 59, R2498 (1999).
[35] A. J. Read, R. J. Needs, K. J. Nash, T. K. Canham, P. D. J. Calcott, and A. Oteish, Phys. Rev. Lett. 69, 1232 (1992).
[36] S. Bhattacharya and D. Banerjee, K. W. Adu, S. Samui and S. Bhattacharyya, Appl. Phys. Lett. 85, 2008 (2004).
[37] X. Zhao, C. M. Wei, L. Yang, and M. Y. Chou, Phys. Rev. Lett. 92, 236805 (2004).
[38]M.H. Huang, S. Mao, H. Feick, H. Yan, Y. Wu, H. Kind, E. Weber, R. Russo, and P. Yang, Science 292, 1897 (2001).
[39] D.M. Bagnall, Y.F. Chen, Z. Zhu, T. Yao, S. Koyama, M. Y. Shen, and T. Goto, Appl. Phys. Lett. 70, 2230 (1997).
[40] H. Cao, J.Y. Xu, D.Z. Zhang, S.-H. Chang, S.T. Ho, E.W. Seelig, X. Liu, and R.P.H. Chang , Phys. Rev. Lett. 84, 5584 (2000).
[41] M.H. Huang, Y.wu, H. Feick, N. Tran, E. Weber, and P. Yang, Adv. Mater. 13, 113 (2001).
[42] Z. L. Wang, J. Phys.: Condens. Matter 16, R829 (2004).
[43] N.E. Hsu, W.K. Hung, and Y.F. Chen, J. Appl. Phys. 96, 4671 (2004).
[44] A.B. Djurisic, Y.H. Leung, W.C.H. Choy, K.W. Cheah, and W.K. Chan, Appl. Phys. Lett. 84, 2635 (2004).
[45] K. Vanheusden, W.L. Warren, C.H. Seager, D.K. Tallant, J.A. Voigt, and B.E. Gnade, J. Appl. Phys. 79, 7983 (1996).
[46] X. Wang, Q. Li, Z. Liu, J. Zhang, Z. Liu, and R. Wang, Appl. Phys. Lett. 84, 4941 (2004).
[47] D.C. Reynolds, D.C. Look, and B. Jogai, J. Appl. Phys. 89, 6189 (2001).
[48] S.A. Studeniken and M. Cocivera, J. Appl. Phys. 91, 5060 (2002).
[49] M. Liu, A.H. Kitai, and P. Mascher, J. Lumin. 54, 35 (1992).
[50] B. Lin, Z. Fu, and Y. Jia, Appl. Phys. Lett. 79, 934 (2001).

CHAPTER 2

FIRST-PRINCIPLES THEORY

2.1 Introduction

First-principles (or *ab initio*) methods enable one to study the electronic structures of solids, surfaces, or clusters with moderate computational effort. Using *ab initio* molecular-dynamics methods, which calculate the forces exerted on atoms at each time step, one can simulate the evolution of atomic and electronic motions without assuming empirical parameters. The basis of the usual *ab initio* molecular-dynamics methods is the Born-Oppenheimer approximation, *i.e*. the nuclei are always in a steady state because the change in the electronic state occurs very rapidly compared to the nuclear motion. One can separate the calculation of the electronic structure from that of the ionic motion on the basis of the approximation. However, to treat the quantum states of many-electron systems is not easy and we have to use a methodology which is reliable but not exact.

There are many first-principles approaches for determining the ground state of many-body systems. These approaches are identified as three main groups. The first is an approach starting from the Hartree-Fock approximation, which offers a rigorous one-electron approximation. The second approach is based on the density functional theory (DFT), which offers an exact ground for the many-body problem but can be solved only approximately. The third approach is using quantum Monte Carlo methods. In this chapter, the first-principles total energy pseudopotential method based on DFT will be briefly discussed.

It is well-known that nearly all physical properties are related to total energy or to differences between total energies. If total energies can be calculated, any physical properties related to a total energy or to a difference between total energies can be determined computationally. Total energy techniques have been successfully used to predict with accuracy equilibrium lattice constants, bulk moduli, phonons, and phase-transition pressures and temperatures[1,2,3].

Any problem in the electronic structure of matter is covered by quantum mechanics. However, analytic solutions of the Schrödinger equation are not possible for many-body systems. So, approximations and numerical schemes are necessary. The "adiabatic principle", which treats the nuclei adiabatically based on Born-Oppenheimer approximation, reduces the many-body problem to the solution of the dynamics of the electrons in some frozen-in configuration of the nuclei. To perform the total energy calculation accurately and efficiently, further approximations schemes are introduced[4]. They include DFT to model the electron-electron interaction, psuedopotential to model the electron-ion interaction, supercell to model systems with aperiodic geometries, and iterative scheme to minimize the total energy function. These will be described in following sections.

2.2 The Schrödinger Equation

For an isolated N-electron atomic or molecular system in the Born-Oppenheimer non-relativistic approximation, the Schrödinger equation is given by

$$\hat{H}\Psi = E\Psi \tag{2.1}$$

where E is the electronic energy, $\Psi = \Psi(\vec{r}_1, \vec{r}_2, ..., \vec{r}_N)$ is the wave function, and $\hat{H}$ is the Hamiltonian operator,

$$\hat{H} = \sum_{i=1}^{N} (-\frac{\hbar^2}{2m} \nabla_i^2) + \sum_{i=1}^{N} U(\vec{r}_i) + V(\vec{r}_1, \vec{r}_2, ...\vec{r}_n) \tag{2.3}$$

in which

$$U(\vec{r}_i) = -\sum_a \frac{Z_a e}{r_{ia}} \tag{2.4}$$

is the "external" potential acting on electron *i*, the potential due to nuclei charge Z_a.

And,
$$V(\vec{r}_1, \vec{r}_2, ...\vec{r}_n) = \sum_{i<j}^{N} \frac{e^2}{|\vec{r}_i - \vec{r}_j|} \tag{2.5}$$

is the electron-electron repulsion energy.

The many-body wave function can be reduced to a product of single-particle functions based on Hartree's *independent electron approximation*[5]:

$$\Psi = \Psi(\vec{r}_1, \vec{r}_2, ..., \vec{r}_n) = \psi_1(\vec{r}_1)\psi_2(\vec{r}_2)\cdots\psi_n(\vec{r}_n) \tag{2.6}$$

And, each $\psi_i(\vec{r}_i)$ satisfies a one-electron Schrödinger equation with a potential term arising from the average field of the other electrons:

$$[-\frac{\hbar^2}{2m}\nabla^2 + V(r) + \sum_j{}' e^2 \int \frac{\psi_j^*(r')\psi_j(r')d\tau}{|r - r'|}]\psi_i(r) = \varepsilon_i \psi_i(r) \tag{2.7}$$

The sum is over all occupied states, except the state ψ_i. The ε_i are one-electron energy eigenvalues. Then, based on the variational principle, the total energy for the ground state in the system can be expressed as:

$$\frac{<\Psi|H|\Psi>}{<\Psi|\Psi>} = \sum_i \varepsilon_i - \frac{1}{2}\sum_{i,j}{}' e^2 \int \frac{\psi_j^*(r')\psi_j(r')\psi_i^*(r)\psi_i(r)d\tau d\tau'}{|r - r'|} \tag{2.8}$$

The equation can be solved self-consistently by iteration, *i.e*., assuming a particular set of approximation eigenstates, computing the potential, and recalculating the eigenstates. The improved estimates are then substituted, the potential recalculated, and the process repeated. Such a process converges and can lead to a set of states that are consistent with the potential[6,7,8].

2.3 The Hartree-Fock Approximation

The Hartree method does not consider the anti-symmetry of the wave function in a many-electron system. However, the wave function must be anti-symmetric under exchange of any two electrons because the electrons are fermions. The anti-symmetry of the wave function produces a spatial separation between electrons that have the same spin and thus reduces the Coulomb energy of the electronic system. The reduction in the energy of the anti-symmetry wave function is called the *exchange energy*. It is straightforward to include exchange in a total energy calculation, and this is generally referred to as the *Hartree-Fock approximation*[4].

Hartree's *independent electron approximation* was replaced by the *Slater determinant* in *Hartree-Fock approximation, i.e*.

$$\Psi_{HF} = \frac{1}{\sqrt{N!}} \det[\psi_1(\vec{r}_1), \psi_2(\vec{r}_2) ... \psi_N(\vec{r}_N)] \tag{2.9}$$

Thus, the wave function of a many-body system is anti-symmetric under exchange of any two electrons as demanded by the Pauli principle. The *Hartree-Fock approximation* is the method where-by the orthonormal orbitals ψ_i are found that minimize[9]

$$E(\Psi) = < \Psi | \hat{H} | \Psi > / < \Psi | \Psi > \tag{2.10}$$

The wave function Ψ_{HF} is normalized, and the energy expectation value is given by

$$E_{HF} = <\Psi_{HF} | \hat{H} | \Psi_{HF}> = \sum_{i=1}^{N} H_i + \frac{e^2}{2} \sum_{i,j=1}^{N} (J_{ij} - K_{ij}) \tag{2.11}$$

where

$$H_i = \int \psi_i^* [-\frac{\hbar^2}{2m} \nabla^2 + V(\vec{r})] \psi_i d\tau \tag{2.12}$$

$$J_{ij} = \iint \psi_i(\vec{r}^{\,'}) \psi_i^*(\vec{r}^{\,'}) \frac{1}{|\vec{r} - \vec{r}^{\,'}|} \psi_j(\vec{r}) \psi_j^*(\vec{r}) d\tau^{'} d\tau \tag{2.13}$$

$$K_{ij} = \iint \psi_i^*(\vec{r}^{\,'}) \psi_j(\vec{r}^{\,'}) \frac{1}{|\vec{r} - \vec{r}^{\,'}|} \psi_i(\vec{r}) \psi_j^*(\vec{r}) d\tau^{'} d\tau \tag{2.14}$$

These integrals are real, and $J_{ij} \geq K_{ij} \geq 0$. The J_{ij} are called *Coulomb integrals*, and the K_{ij} are called *exchange integrals*. And $J_{ii} = K_{ii}$. The term $(-\frac{e^2}{2} \sum_{i,j=1}^{N} K_{ij})$ in Eq. (2.11) is called *exchange energy*.

However, the exact wave function for a system of many interacting electrons is never a single determinant or a simple combination of a few determinants. The difference between the many-body energy of an electronic system and the energy of the system calculated in the Hartree-Fock approximation or the error in energy is called *correlation energy*[10] and defined to be negative,

$$E_{corr}^{HF} = E - E_{HF} \tag{2.15}$$

Correlation energy tends to remain constant for atomic and molecular changes that conserve the numbers and types of chemical bonds, but it can change drastically and become determinative when bonds changes. It is extremely difficult to calculate the correlation energy of a complex system, although some promising steps are being taken in

this direction using quantum Monte Carlo simulations of electron-gas dynamics[11,12]. At present these methods are not tractable in total-energy calculations of systems with any degree of complexity, and alternative methods are required to describe the effects of the electron-electron interaction[4]. The density functional theory is presently the most successful (and also the most promising) approach to model electron-electron interaction. Its applicability ranges from atoms, molecules and solids to nuclei and quantum and classical fluids.

2.4 Density Functional Theory

DFT takes a radically different approach than the foregoing wave function methods. It is both a profound, exact theory for interacting electrons[13], and a practical prescription in terms of single-electron equations[14]. This is a remarkable theory that allows one to replace the complicated N-electron wave function $\Psi = \Psi(\vec{r}_1, \vec{r}_2, ..., \vec{r}_N)$ and the associated Schrödinger equation by the much simpler *electron density* $n(\vec{r})$ and its associated calculational scheme. Since its formulation in the mid-1960s and early 1970s, DFT has been used extensively in condensed matter physics in almost all band-structure and electronic structure calculations. It has also been widely adopted in the quantum chemistry community, and has led to a computational revolution in that area[15]. It has become a runaway success, enabling great advances in practical first-principles calculations.

The history begins with the works of Thomas and Fermi in the 1920s[16,17,18,19]. The authors realized that statistical considerations can be used to approximate the distribution of electrons in an atom. The assumptions stated by Thomas include that “Electrons are

distributed uniformly in the six-dimensional phase space for the motion of an electron at the rate of two for each $\hbar^3$ of volume" and "There is an effective potential field determined by the nuclear charge and the distribution of electrons". In an electronic system, the number of electrons per unit volume in a given state is the *electron density* $n(\vec{r})$ for that state

$$n(\vec{r}) = 2\sum_i \ |\psi_i(\vec{r})|^2 \tag{2.16}$$

$$\int n(\vec{r})d\vec{r} = N \tag{2.17}$$

In this approximation, the electrons are treated as independent particles in a homogeneous electron gas. The Thomas-Fermi method contains all ingredients of a density functional theory. However, the approach treated the kinetic energy crudely, and neglected the exchange and correlation energies.

However, the situation changed with the publication of the landmark paper by Hohenberg and Kohn[13]. They provided the fundamental theorems showing that for ground states the Thomas-Fermi model may be regarded as an approximaton to an exact theory, the *density functional theory*. There exists an exact energy functional E[n], and also an exact variational principle.

2.4.1 The Hohenberg-Kohn Theorems

The first Hohenberg and Kohn theorem states that *the total energy including exchange and correlation of a system of electrons and nuclei, is a unique functional of the electron density* $n(\vec{r})$. Since $n(\vec{r})$ determines the number of electrons, it follows that $n(\vec{r})$ also determines the ground-state wave function Ψ and all other electronic properties of the

system. Thus, this theorem allows for the systematic formation of a many-body interacting electrons in an external potential (being from the nuclei in a solid) in terms of the $n(\vec{r})$ as the basic variable.

For a system of N electrons, the nonrelativistic, time-independent Hamiltonian based on Born-Oppenheimer approximation is expressed as

$$\hat{H} = \hat{T} + V_{ext} + V \tag{2.18}$$

where $\hat{T}$ is the kinetic energy operator, V_{ext} is the external potential being from the nuclei which couples to the density, and V is the two-body electron-electron interaction (the *Coulomb interaction*).

As stated, the density uniquely determines *N* and *potentials* (including external potential and coulomb energy) and hence all properties of the ground state, for example the kinetic energy $T[n(\vec{r})]$, the total energy $E[n(\vec{r})]$. We get the total energy formula in terms of *electron density* $n(\vec{r})$ alone

$$\begin{aligned} E = E[n(\vec{r})] &= T[n(\vec{r})] + E_{ne}[n(\vec{r})] + E_{ee}[n(\vec{r})] \\ &= \int n(\vec{r}) V_{ne}(\vec{r}) dr + F_{HK}[n(\vec{r})] + E_{corr}[n(\vec{r})] \end{aligned} \tag{2.19}$$

$$F_{HK}[n(\vec{r})] = T[n(\vec{r})] + E_{exch}[n(\vec{r})] + E_{coul}[n(\vec{r})] \tag{2.20}$$

where $T[n(\vec{r})]$ is the kinetic energy and $E_{ee}[n(\vec{r})]$ is the electron-electron interaction energy which contains the Coulomb interactions $E_{coul}[n(\vec{r})]$ which is given by:

$$E_{coul}[n(\vec{r})] = \frac{e^2}{2} \iint \frac{n(\vec{r}_1) n(\vec{r}_2)}{r_{12}} dr_1 dr_2 \tag{2.21}$$

The second Hohenberg and Kohn theorem provides the energy variational principle, *i.e.*, *the variational minimum of the energy is exactly equivalent to the true ground-state energy*. For a trial *electron density* $n(\vec{r})$, such that $n(\vec{r}) \geq 0$ and $\int n(\vec{r})d\vec{r} = N$,

$$E_0 = E[n_0(r)] \leq E[n(\vec{r})] \tag{2.22}$$

E_0 is the exact ground-state energy and $n_0(\vec{r})$ the ground-state *electron density*.

The energy functional in *electron density approximation* can be written as,

$$E[n(r)] \equiv <\psi[n(r)]\left|\hat{H}\right|\psi[n(r)]> = <\psi[n(r)]\left|\hat{T} + V_{ext} + V\right|\psi[n(r)]> \tag{2.23}$$

The ground-state energy can be found by varying the *electron density* $n(\vec{r})$ to minimize the energy, provided we know the form of the functional $E[n(r)]$, or at least have a good approximation for it.

2.4.2 The Kohn-Sham Equations

Accurate calculational implementations of the density functional theory are far from easy to achieve, because of the unfortunate (but challenging) fact that the functional $F_{HK}[n(\vec{r})]$ is hard to come by in explicit form. While the Hohrnberg-Kohn theorem rigorously established that we may use the density alone, as a variable to find the ground–state energy of an N-electron problem, it does not provide us with any useful computational scheme. Kohn and Sham showed that it is possible to replace the many-body problem by an exact equivalent set of self-consistent one-electron equations[14]. The Kohn-Sham total-energy functional for a set of doubly occupied electronic states ψ_i can be written[4]

$$E[\{\psi_i\}] = 2\sum_i \int \psi_i[-\frac{\hbar^2}{2m}]\nabla^2\psi_i d^3r + \int V_{ion}(r)n(r)d^3r$$

$$+\frac{e^2}{2}\int\frac{n(r)n(r')}{|r-r'|}d^3rd^3r'+E_{xc}[n(r)]+E_{ion}(\{\vec{R}_I\}) \tag{2.24}$$

where V_{ion} is the static total electron-ion potential, $E_{xc}[n(r)]$ is the exchange-correlation functional, and E_{ion} is the Coulomb energy associated with interactions among the nuclei (or ions) at positions $\{\vec{R}_I\}$.

It is necessary to determine the set of wave functions ψ_i that minimizes the Kohn-Sham total-energy functional. These are given by the self-consistent solutions to the Kohn-Sham equations (1965)[4]

$$[-\frac{\hbar^2}{2m}\nabla^2+V_{ion}(r)+V_H(r)+V_{xc}(r)]\psi_i(r)=\varepsilon_i\psi_i(r) \tag{2.25}$$

where $\psi_i(r)$ is the wave function of electronic state *i*, ε_i is the Kohn-Sham eigenvalue, and $V_H(r)$ is the Hartree potential of the electrons given by

$$V_H(r)=\int\frac{e^2n(r')}{|r-r'|}d^3r' \tag{2.26}$$

The exchange-correlation potential, $V_{xc}(r)$ is given by the functional derivative

$$V_{xc}(r)=\frac{\delta E_{xc}[n(r)]}{\delta n(r)} \tag{2.27}$$

In the Kohn-Sham equations, the effective potential is the Kohn-Sham potential:

$$V_{KS}(r)=V_H(r)+V_{xc}(r)=\int\frac{e^2n(r')d^3r'}{|r-r'|}+\frac{\delta E_{xc}[n(r)]}{\delta n(r)} \tag{2.28}$$

The Kohn-Sham equations represent a mapping of the interacting many-electron system onto a system of noninteracting electrons moving in an effective potential due to all the other electrons. If the exchange-correlation energy functional were known exactly, then

taking the functional derivative with respect to the density would produce an exchange-correlation potential that included the effects of exchange and correlation exactly. The Kohn-Sham equations must be solved self-consistently so that the occupied electronic states generate a charge density that produces the electronic potential that was used to construct the equations[4].

2.5 Local Density Approximation

The Hohenberg-Kohn theorem provides some motivation for using approximate methods to describe the exchange-correlation energy as a function of $n(\vec{r})$. However, the difficulty of the many-body problems is still present in the unknown functional $E_{xc}[n(\vec{r})]$. To overcome this, Kohn and Sham proposed a *local density approximation* (LDA)[14]. In the *local density approximation*, the exchange-correlation energy of an electronic system is constructed by assuming that the exchange-correlation energy per electron at the position $\vec{r}$ in the electron gas, $\varepsilon_{xc}(\vec{r})$ is equal to the exchange-correlation energy per electron in a homogeneous electron gas that has the same density as the electron gas at point $\vec{r}$. Thus

$$E_{xc}[n(\vec{r})] \approx E_{xc}^{LDA} = \int n(\vec{r})\varepsilon_{xc}(\vec{r})d\vec{r} \tag{2.29}$$

and

$$\varepsilon_{xc}(\vec{r}) = \varepsilon_{xc}^{\text{hom}}[n(\vec{r})] \tag{2.30}$$

$\varepsilon_{xc}[n(\vec{r})]$ can be further split into exchange and correlation contributions,

$$\varepsilon_{xc}[n(\vec{r})] = \varepsilon_{x}[n(\vec{r})] + \varepsilon_{c}[n(\vec{r})] \tag{2.31}$$

A Hartree-Fock description of the electron gas leads to a simple form of the exchange-only energy functional $E_x[n(\vec{r})] \propto n^{4/3}(\vec{r})$ [20]. A much more accurate exchange-correlation

energy for the homogeneous electron gas as a function of density may be derived from quantum Monte Carlo simulations[21] and used to construct exchange-correlation functionals within the framework of the LDA[22].

The local-density approximation assumes the exchange-correlation energy is purely local. Several parameterizations exist for the exchange-correlation energy of a homogeneous electron gas[14,23,24], all of which lead to total-energy results that are very similar. These parameterizations use interpolation formulas to link exact results for the exchange-correlation energy of high-density electron gases and calculations of the exchange-correlation energy of intermediate and low-density electron gases[4].

The LDA, in principle, ignores corrections to the exchange-correction energy at a point $\vec{r}$ due to the nearby inhomogeneities in the electron density. Considering the inexact nature of the approximation, it is remarkable that the calculations performed using the LDA have been so successful that it is almost universally used in total-energy pseudopotential calculations. Some work has shown that this success can be partially attributed to the fact that the local density approximation gives the correct sum rule for the exchange-correlation hole[4]. The LDA appears to give a single well-defined global minimum for the energy of a non-spin-polarized system of electrons in a fixed ionic potential. Therefore any energy minimization scheme will locate the global energy minimum of the electronic system.

2.6 Generalized-Gradient Approximation

As stated above, the LDA uses the exchange-correlation energy for the uniform electron gas at every point in the system regardless of the inhomogeneity of the real charge density. For nonuniform charge densities the exchange-correlation energy can deviate significantly from that of the uniform gas. This deviation can be expressed in terms of the gradient and higher spatial derivatives of the total charge density. In the *generalized gradient approximation* (GGA), there is an explicit dependence of the exchange-correlation functional on the gradient of the electron density[22].

The gradient expansion (GE), in which in addition to *n(r)* its gradients are used for the density functional representation of the exchange-correlation energy, is the most systematic nonlocal extension of the LDA. The lowest order contribution to the GE, depending on $\nabla n(\vec{r})$, is rigorously determined by the long wavelength limit of the linear response function of the homogeneous electron gas. The LDA can be considered to be the zeroth order approximation to the semi-classical expansion of the density matrix in terms of the density and its derivatives[25]. GGA can be interpreted as semi-empirical partial resummations of the complete GE, including only terms depending on $\nabla n(\vec{r})$, but no higher density gradients. Thus, we write the exchange-correlation energy in the following form termed generalized gradient approximation (GGA):

$$E_{xc}^{GGA} = \int n(\vec{r})\varepsilon_{xc}(n(\vec{r}), \nabla n(\vec{r}))d\vec{r} \tag{2.32}$$

where ε_{xc} at $\vec{r}$ depends on the density and its gradient (+ higher order terms) at $\vec{r}$.

As a straightforward expansion in terms of the gradient violates the sum-rules for the exchange hole, generalized gradient expansions corrected for the sum rules have been proposed by a number of authors[26]. However, at the moment there is as yet no consensus on the best GGA[22]. For solid-state applications, the GGAs proposed by Perdew and co-workers[27,28,29] have been widely used and have proved to be quite successful in correcting some of the deficiencies of the LDA. Density functional theory with the GGA, on the other hand, is essentially no more complicated than Hartree or LDA calculations.

2.7 Periodic Supercells

Although certain observables of the many-body problems can be mapped into equivalent observables in an effective single-particle problem, there still remains the formidable task of handling an infinite number of noninteracting electrons moving in the static potential of an infinite number of nuclei or ions. Two difficulties must be overcome: a wave function must be calculated for each of the infinite number of electrons in the system, and the basis set required to expand each wave function is infinite since each electronic wave function extends over the entire solid. Both problems can be surmounted by performing calculations on periodic systems and applying *Bloch's theorem* to the electronic wave functions[4].

2.7.1 Bloch's Theorem

Bloch's theorem states that each electronic wave function in a solid can be the product of a cell-periodic part and a wavelike part[4,30]

$$\psi_i(\vec{r}) = \exp(i\vec{k}\cdot\vec{r}) f_i(\vec{r}) \tag{2.33}$$

where $\vec{k}$ is wave vector of the plane wave. The cell-periodic part of the wave function can be expanded using a basis set consisting of a discrete set of plane waves whose wave vectors are reciprocal lattice vectors of the crystal,

$$f_i(\vec{r}) = \sum_{\vec{G}} c_{i,\vec{G}} \exp\left[i\vec{G} \cdot \vec{r} \right] \tag{2.34}$$

where the reciprocal lattice vectors $\vec{G}$ are defined by $\vec{G} \cdot \vec{R} = 2\pi m$ for all $\vec{R}$, where $\vec{R}$ is a lattice vector of the crystal and m is an integer, and $c_{i,\vec{G}}$ are the expansion coefficients. Therefore each electronic wave function can be written as a sum of plane waves,

$$\psi_i(\vec{r}) = \sum_{G} c_{i,k+G} \exp\left(i\left(\vec{k} + \vec{G}\right) \cdot \vec{r}\right) \tag{2.35}$$

2.7.2 $\vec{k}$ -Point Sampling

Electronic states are allowed only at a set of $\vec{k}$ points determined by the boundary conditions that apply to the bulk solid. The density of allowed $\vec{k}$ points is proportional to the volume of the solid. The infinite number of electrons in the solid is accounted for by an infinite number of $\vec{k}$ points, and only a finite number of electronic states are occupied at each $\vec{k}$ point. The Bloch's theorem changes the problem of calculating an infinite number of electronic wave functions to one of calculating a finite number of electronic wave functions at an infinite number of $\vec{k}$ points. The occupied states at each $\vec{k}$ point contribute to the electronic potential in the bulk solid so that an infinite number of calculations are needed to compute this potential. However, the electronic wave functions at $\vec{k}$ points that are very close together will be almost identical. Hence it is possible to represent the electronic wave functions over a region of k space by the wave functions at a single $\vec{k}$ point. In this case the electronic states at only a finite number of $\vec{k}$ points are required to calculate the electronic potential and hence determine the total energy of the solid. Methods, such as Monkhorst-Pack scheme[31], have been devised for obtaining very

accurate approximation of the electronic potential and the contribution to the total energy from a filled electronic band by calculating the electronic states at a special set of $\vec{k}$ points in the Brillouin Zone. Using these methods, one can obtain an accurate approximation for the electronic potential and the total energy by calculating the electronic states at a very small number of $\vec{k}$ points. The electronic potential and total energy are more difficult to calculate if the system is metallic because a dense set of $\vec{k}$ points is required to determine the Fermi surface precisely[4].

The magnitude of any error in the total energy due to the inadequacy of the $\vec{k}$-point sampling can always be reduced by using a denser set of $\vec{k}$ points. The computed total energy will converge as the density of $\vec{k}$ points increases, and the error due to the $\vec{k}$-point sampling then approaches zero. In principle, a converged electronic potential and total energy can always be obtained provided that the computational time is available to calculate the electronic wave functions at a sufficiently dense set of $\vec{k}$ points. The computational cost of performing a very dense sampling of $\vec{k}$ space can be significantly reduced by using the $\vec{k} \cdot \vec{p}$ perturbation method[32,33].

2.7.3 Plane Wave Basis Sets

Bloch's theorem states that the electronic wave functions at each $\vec{k}$ point can be expanded in terms of a discrete plane-wave basis set. In principle, an infinite plane wave basis set is required to expand the electronic wave functions. Since the coefficients $c_{i,\vec{k}+\vec{G}}$ for the plane-waves with small kinetic energy $\left(\hbar^2/2m\right)\left|\vec{k}+\vec{G}\right|^2$ are typically more important than

those with large kinetic energy, the plane-wave basis can be truncated to the plane waves that have kinetic energies less than some particular cutoff energy. Application of the Bloch theorem allows the electronic wave functions to be expanded in terms of a discrete set of plane waves. Introduction of an energy cutoff to the discrete plane wave basis set produces a finite basis set. But the truncation of the plane wave basis set at a finite cut-off kinetic energy will lead to an error in the total energy of the system. However, in principle it is possible to make this error arbitrarily small by increasing the size of the basis set by allowing a larger energy cut-off[4].

When plane wave functions are used as a basis set, the Kohn-Sham equations are simplified. Substitution of Equation (2.35) into (2.25) and integration over $\vec{r}$ gives

$$\sum_{\vec{G}'}[\frac{\hbar^2}{2m}\left|\vec{k}+\vec{G}\right|^2\delta_{\vec{G}\vec{G}'}+V_{ion}(\vec{G}-\vec{G}')+V_H(\vec{G}-\vec{G}')+V_{xc}(\vec{G}-\vec{G}')]c_{i,\vec{k}+\vec{G}'}=\varepsilon_i c_{i,\vec{k}+\vec{G}} \qquad (2.36)$$

In this form, the kinetic energy is diagonal, and the various potentials are described in terms of their Fourier transforms. Solution of Eq. (2.36) proceeds by diagonalization of the Hamiltonian matrix elements $H_{k+G,k+G'}$ given by the term in the brackets above. The size of the matrix is determined by the choice of cutoff energy $\left(\hbar^2/2m\right)\left|\vec{k}+\vec{G}_c\right|^2$, and will be intractably large for systems that contain both valence and core electrons. This is a severe problem, but can be overcome by use of the pseudopotential approximation[4].

2.8 Nonperiodic Systems

The Bloch theorem cannot be applied to a non-periodic system, such as single defect and surface, without a periodic supercell used because a continuous plane-wave basis set

would be required in the calculations. Calculations using finite plane-wave basis sets on non-periodic system need to apply a supercell.

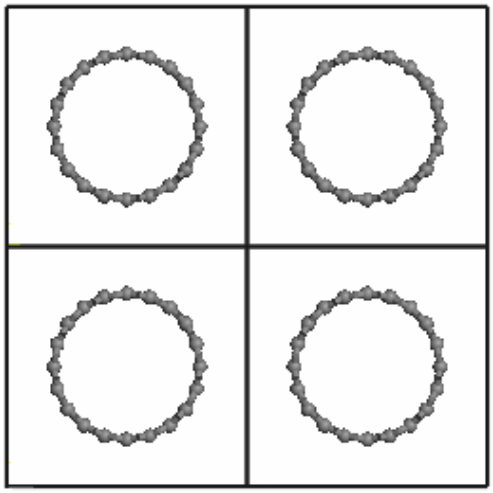

Fig. 2.1, Schematic illustration of a supercell geometry for an array of carbon nanotubes.

Figure 2.1 shows a supercell for carbon nanotube calculation. The supercell is periodic along the tube axis. The supercell is repeated over all space, so the total energy of an array of carbon nanotubes is calculated. To ensure that the results of the calculation accurately represent an isolated nanotube, the vacuum region must be wide enough so that nanotubes of adjacent supercells do not interact across the vacuum region.

2.9 Pseudopotential Method

Although Bloch theorem states that the discrete plane waves can be used as the electronic wave functions, a plane-wave basis set is very poorly suited to expanding electronic wave functions because a very large number of plane waves are needed to expand the tightly bound core orbitals and to follow the rapid oscillations of the wave functions of the valence electrons in the core region[4]. An extremely large plane-wave basis set would be required to perform an all-electron calculation and a vast amount of computational time

would be also required. Usually, the core electrons are not important in describing, for example, the nature of the bonding between atoms in a crystal; only the valence electrons surrounding the core region contribute to it. A convenient technique which neglects the core electrons completely in the calculation scheme is the "pseudopotential" approach[34,35]. In the scheme, the effective one-electron potential is given by the sum of the pseudopotential and Coulomb potential due to the average valence electron density.

The most general form for a pseudopotential is

$$V_{NL} = \sum_{lm} |lm> V_l < lm| \tag{2.37}$$

where $|lm>$ are the spherical harmonics and V_l is the pseudopotential for angular momentum l. Acting on the electronic wave function with this operator decomposes the wave function into spherical harmonics, each of which is then multiplied by the relevant pseudopotential V_l.

Modern pseudopotentials are constructed from first-principles. The main requirement of the pseudopotential approach is that it reproduces the valence charge density associated with chemical bonds. It has been shown that for pseudo and all-electron wave functions to be identical beyond the core radius, r_c, it is necessary for the integrals of squared amplitudes of the two functions to be the same[36]. This is equivalent to requiring norm-conservation from pseudo wave functions, *i.e.*, that each of them should carry exactly one electron. This condition ensures that the scattering properties of the pseudopotential are reproduced correctly. Various schemes have been suggested to improve convergence properties of norm-conserving pseudopotentials[37]. A more radical approach was suggested by Vanderbilt[38], which involves relaxing the norm conservation requirement in

order to generate much softer pseudopotentials. Ultrasoft potentials have another advantage besides being much softer than the norm-conserving potentials. The generation algorithm guarantees good scattering properties over a pre-specified energy range, which results in much better transferability and accuracy of the pseudopotentials. Ultrasoft potential usually also treats shallow core states as valences by including multiple sets of occupied states in each angular momentum channel. This also adds to high accuracy and transferability of the potentials, although at a price of computational efficiency.

2.10 Minimization of the Kohn-Sham Energy Functional

To perform a total energy pseudopotential calculation, it is necessary to find the electronic states that minimize the Kohn-Sham (KS) energy functional. Indirect searching for the self-consistent KS Hamiltonian can lead to instability because of the discontinuous changes in the KS Hamiltonian from iteration to iteration. These instabilities would be avoided if the KS energy functional were minimized directly because the KS energy functional normally has a single well-defined energy minimum[4]. It is necessary to find a computational method that allows direct minimization of the KS functional in a tractable and efficient way.

The conjugate-gradients (CG) technique provides a simple and effective procedure for the implementation of such a minimization approach. To locate the energy minimization, the initial search direction is taken to be the negative of the gradient at the starting point. A subsequent conjugate direction is then constructed from a linear combination of the new gradient and the previous direction that minimizes the functional. Although the CG technique provides an efficient method for locating the minimum of a general functional,

it is important to implement the technique in such a way as to maximize computational speed and to minimize the memory requirement. A GC method that fulfills these criteria has been developed by Teter et al[39].

2.11 CASTEP Code

CASTEP (CAmbridge Serial Total Energy Package)[4] [2.4] is a state of the art quantum mechanics based program designed specifically for solid state materials science. CASTEP employs the Density Functional Theory (DFT) plane-wave pseudopotential method which allows one to perform first-principles quantum mechanics calculations that explore the properties of crystals and surfaces in materials such as semiconductors, ceramics, metals, minerals and zeolites.

Typical applications involve studies of surface chemistry, structural properties, band structure, density of states and optical properties. CASTEP can also be used to study the spatial distribution of the charge density and wave functions of a system. In addition, CASTEP can be used effectively to study properties of point defects (vacancies, interstitials and substitutional impurities) and extended defects (e.g., grain boundaries and dislocations) in semiconductors and other materials. It can also be used to calculate the vibrational properties of solids (phonon dispersion, total and projected density of phonon states, thermodynamic properties) using the linear response methodology. These results can be used in various ways, e.g., to investigate the vibrational properties of adsorbates on surfaces, to interpret experimental neutron spectroscopy data or vibrational spectra, to study phase stability at high temperatures and pressures, etc.

In this thesis, the properties of nanostructures, such as carbon nanotubes, and carbon related nanostructures are studied using this CASTEP program code and discussed in following chapters.

References:

[1] M. L. Cohen, Phy. Rep. 110, 293 (1984).
[2] J. D. Joannopoulos, in Physics of disordered materials, edited by D. Adler, H. Fritzsche, and S. R. Ovshinsky, (Plenum, New York) p.19, 1985.
[3] W. Pickett, Comput. Phys. Rep. 9, 115 (1989).
[4] M. C. Payne, M. P. Teter, D. C. Allan, T. A. Arias and J. D. Joannopoulos Rev. Modern. Phys. 64, 1045 (1992).
[5] D. R. Hartree, Proceedings of the Cambridge Philosophical Society, 24, 89 (1928).
[6] H. Clark, *Solid State Physics: An introduction to its theory* (St Martin's, New York, 1968), p.7.
[7] W. A. Harrison, *Solid State Theory* (McGraw-Hill, New York, 1970), p.72.
[8] F. Seitz, *Modern Theory of Solids* (McGraw-Hill, New York, 1940), p.677.
[9] C. C. J. Roothaan, Rev. Mod. Phys. 23, 69 (1951).
[10] A. L. Fetter and J. D. Walecka, *Quantum Theory of Many-Particle Systems* (McGraw-Hill, New York, 1971), p.29.
[11] S. Fahy, X. W. Wang, and S. G. Louie, Phys. Rev. Lett. 61, 1631 (1988).
[12] X. P. Li, D. M. Ceperley, and R. M. Martin, Phys. Rev. B 44, 10929 (1991).
[13] P. Hohenberg and W. Kohn, Phys. Rev. 136, B864 (1964).
[14] W. Kohn and L. J. Sham, Phys. Rev. 140, A1133 (1965).
[15] P. L. Taylaor and O. Heinonen, *A Quantum Approach to Condensed Matter Physics* (Cambridge University Press, Cambridage, 2002), p.183.
[16] E. Fermi, Rend. Accad. Lincei 6, 602 (1927).
[17] E. Fermi, Rend. Accad. Lincei 7, 342 (1927).
[18] E. Fermi, Z. Phys. 48, 73 (1927).
[19] L. H. Thomas, Proc. Camb, Phil. Soc. 23, 542 (1927).
[20] J. Hafner, Acta. Mater. 48, 71 (2000).
[21] D. M. Ceperley and B. J. Alder, Phys. Rev. Lett. 45, 566 (1980).
[22] M. J. Gillan, in *Computer Simulation in Materials Science*, edited by M. Meyer and V. Pontikis (Dordrecht, Kluwer, 1991), p.257.
[23] S. H. Vosko, L. Wilk, and M. Nusair, Can. J. Phys. 58, 1200 (1980).
[24] J. P. Perdew and A. Zunger, Phys. Rev. B 23, 5048 (1981).
[25] R. M. Dreizler and E. K. U. Gross, *Density Functional Theory* (Spring Verlag, Berlin, 1990), p.-.
[26] J. Hafner, Acta. Mater. 48, 71 (2000).
[27] J. P. Perdew, A. Chevary, S. H. Vosko, K. A. Jackson, M. R. Pedersen, M. R. Singh, and C. Fiolhais, Phys. Rev. B 46, 6671 (1992).
[28] J. P. Perdew and Y. Wang, Phys. Rev. B 45, 13244 (1992).

[29] J. P. Perdew, K. Burke, and M. Ernzerhof, Phys. Rev. Lett. 77, 3865 (1996).
[30] N. W. Ashcroft and N. D. Mermin, *Solid State Physics*, (Holt Saunders, Pjiladelphia) 1976, p.113 .
[31] H. J. Monkhorst and J. D. Pack, Phys. Rev. B 13, 5188 (1976).
[32] I. J. Robertson and M. C. Payne, J. Phys.: Condens. Matter 2, 9837 (1990).
[33] I. J. Robertson and M. C. Payne, J. Phys.: Condens. Matter 3, 8841 (1991).
[34] W. A. Harrison, Solid State Theory, (McGraw-Hill, New York), 1970.
[35] W. A. Harrison, Pseudopotentials in the theory of metals (Benjamin/Cummings, Menlo Park, California), 1966.
[36] D. R. Hamann, M. Schluter, and C. Chiang, Phys. Rev. Lett. 43, 1494 (1979).
[37] N. Troullier and J. L. Martins, Phys. Rev. B 43, 1993 (1991).
[38] D. Vanderbilt, Phys. Rev. B 41, 7892 (1990).
[39] M. P. Teter, M. C. Payne, and D. C. Allan, Phys. Rev. B 40, 12255 (1989).

CHAPTER 3

CARBON NANOSCROLLS

3.1 Introduction

CNTs can be classified as single-wall CNT (SWCNT) (one cylinder of the graphene sheet) and multi-wall CNT (MWCNT). MWCNTs can be further divided into two categories, the Russian doll and the Swiss roll (carbon nanoscroll)[1]. The Russian doll structure consists of nested carbon tubes, while the Swiss scroll structure is made up of a single rolled-up graphene sheet[2,3,4,5]. The Swiss roll structures were first considered as defects in CNTs[4]. But their existence was demonstrated by X-ray diffraction[6]. Recently, Ruland *et al.* demonstrated that the Swiss roll structure has a uniform chirality[7]. More recently, Viculis *et. al*. proposed a simple chemical route to synthesis carbon nanoscroll[8]. Systematic investigation on the structural and electronic properties would be useful for understanding this type of interesting nanostructure and for exploring their potential applications, such as sensors, hydrogen storage and nanodevices.

Theoretical study on CNTs, particularly MWCNTs or nanoscrolls, is difficult due to the large number of atoms required to model the system. Initial calculations on carbon nanoscrolls were carried out using continuum elasticity theory[9,10,11,12] which cannot reveal atomic-level features of structure. Setton carried out a molecular mechanics calculation but used only a pairwise interaction[13]. More recently, Braga *et al.* performed molecular dynamics simulations to investigate formation, stability and the structural effect of carbon nanoscrolls due to charge injection[14], and found that carbon nanoscrolls automatically occur when a critical overlap between sheet layers is achieved for the partially curled

sheet, and charge injection causes them to unwind. However, to our knowledge, there has not been any systematic investigation on the electronic properties of such structures, particularly using first-principles methods. With unprecedented accuracy, first-principles calculations, as reviewed in Chapter 2, can be expected to reveal more details on the structure and properties of the carbon nanoscrolls and provide further understanding to this unique type of structures.

In this chapter, the electronic and optical properties of carbon nanoscrolls were investigated using first-principles method based on the density functional theory and local density approximation.

3.2 Calculation Details

A supercell of 25×25×2.438 Å was found sufficient to avoid interaction of the nanoscroll with its images and used for calculations. A cut-off energy of 310 eV was used for the plane wave expansion of the wave functions. The Monkhorst and Pack scheme for sampling of k points in the Brillouin-zone integrations was used[15]. 10 k points were used along the tube axis in the reciprocal space. Good convergence was obtained with these choices of parameters. The total energy was converged to 2.0×10^{-5} eV/atom while the Hellman-Feynman force is converged to 5.0×10^{-2} eV/Å.

Calculations were performed on two models, both have chirality equivalent to that of the armchair carbon nanotube, *i.e.* the carbon nanoscrolls are rolled up based on the armchair structure ($\vec{R}_n = n\vec{C}_1 + n\vec{C}_2$). The two models differ only in their sizes, with *n* being 14 for Model 1 and 24 for Model 2 to investigate the size effect. It can be seen that Model 2 is

large enough to test the interlayer interaction. The models are shown in Fig. 3.1a and Fig. 3.1b, respectively. Dangling bonds at the edges of the graphene sheet were saturated using hydrogen atoms which are shown using white balls in Fig. 3.1. Hydrogenation of edge carbon atoms is physically possible due to presence of hydrogen atoms in the growth process. The carbon nanoscrolls were constructed from a structurally optimized graphene sheet in which the C-C bond length is 1.41 Å. The distance between two adjacent graphene layers was 3.41 Å. The bond length in graphene is close to the experimental value of 1.42 Å. The atomic structures of the carbon nanoscrolls were then fully optimized by minimization of its total energy by means of the Hellman-Feynman forces, including Pulay-like corrections[16].

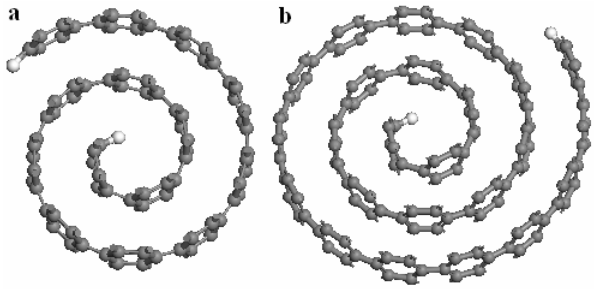

Fig. 3.1 Initial structures of (a) Model 1 and (b) Model 2 of carbon nanoscrolls. Black and white balls indicate carbon and hydrogen atoms, respectively.

3.3 Electronic Structures

3.3.1 Structural Properties

Figure 3.2 shows the atomic structures of the two models after geometry optimization. It is clear that the inner half-circle graphene sheet extends after the optimization, due to the relaxation of the stress. However, the outer parts of the nanoscroll extend outward slightly. The interlayer spacing is about 3.42 Å, which is similar to that of graphene or the Russia roll, except for the edges of the graphitic sheet. Near the inner edge, the interlayer

distance is shorter (3.13 Å) while it is larger near the open end (3.45 Å for Model 1 and 3.55 Å for Model 2) due to the extension of the graphitic sheet. Model 1 differs from Model 2 only in size. It is interesting to note that the structure of Model 1 is very similar to the equivalent section of Model 2. The C-C bond length remains constant (1.42 Å) except for the edges, where the bond stretches to 1.43 Å near the inner edge and 1.44 Å near the open edge. The bond angles also remain unchanged (~119^{o}) except for the edges, where the bond angle expands to about 122^{o} and there is essentially no difference between the inner edge and the open edge. The changes in bond length and bond angle near the free ends can be expected. Other than that, the structural properties of the nanoscroll are similar to those of SWCNTs and the Russia roll, and there is essentially no difference in interlayer spacing, bond lengths and bond angles between these structures. This is reasonable because the interlayer couplings in all these structures are weak and the properties of these structures are mainly determined by their chirality and curvature. Results of our calculation are consistent with the experimental results[7]. It should be pointed out that even though our structural optimization has converged, whether carbon nanoscrolls of such small sizes can be stable remains to be investigated. In the following, we focus on the electronic and optical properties of the carbon nanoscrolls.

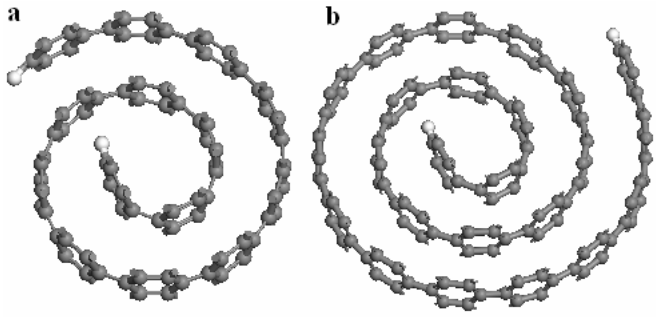

Fig. 3.3, Optimized structures of (a) Model 1 and (2) Model 2 of carbon nanoscrolls. Black and white balls indicate carbon and hydrogen atoms, respectively.

3.3.2 Electronic Properties

The symmetry of an achiral carbon nanotube, armchair (n, n) or zigzag (n, 0), is expressed by the direct product of groups $D_n \otimes C_i^4$, which depends on whether n is even or odd. When n is even, the product is D_{nh}; otherwise, it is D_{nd}. It is known that all armchair nanotubes are metallic with bands crossing the Fermi level at $k=\pm 2\pi/(3a)$, where a=2.47 Å is the lattice constant of graphene. The top valence band and the bottom conduction band are non-degenerate and form the big ppπ and ppπ^* states, respectively. Most of other energy levels are doubly degenerate. The symmetry of the nanoscroll is lower than that of the armchair, and it belongs to the point group of C_s. The big ppπ state is thus distorted, which results in the split of the degenerate states.

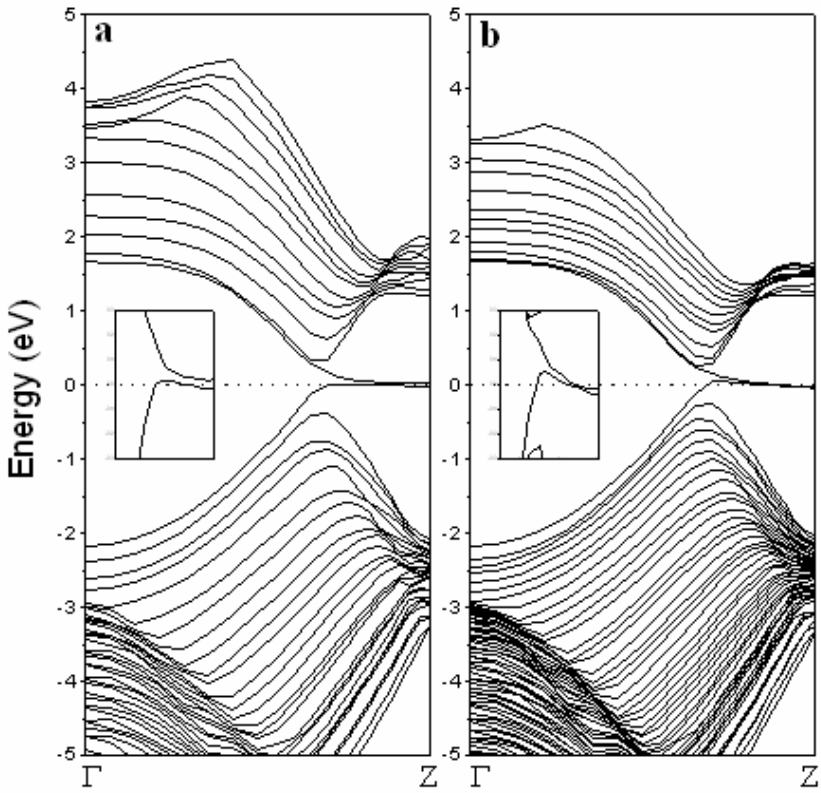

Fig. 3.4, Calculated band structures of (a) Model 1 and (b) Model 2 of the carbon nanoscrolls. The inserts are the fine structures of the valence band top and conduction band bottom near the Fermi level which is indicated by the dashed line.

Figure 3.3 shows the calculated band structures of the two models. All energy levels of the scroll structure are non-degenerate, due to the lower symmetry, in contrast to those of the tube structure. The overall band structures of the two models are similar. Compared to the band structure of a single wall armchair carbon nanotube[17], the two bands that cross each other now split, due to interlayer interaction. This is similar to that in a double wall carbon nanotube where the same two bands split due to intertube interaction and resulted in opening of pseudo energy gaps[18]. However, these two bands in the nanoscrolls remain close to each other near the Brillouin zone boundary. By considering scrolled carbon as a curled graphene sheet these two energy levels may result from the bonding unsaturation at the edges of the graphene sheet. They may be denoted as conduction band edge state (*ces* for the one above the Fermi level) and valence band edge state (*ves* for the one below the Fermi level). It is interesting to note that the *ces* level and the *ves* level of Model 1 come very close to each other but do not intersect, as shown in the inset of Fig. 3.3(a), indicating that the carbon nanoscroll is a semi-metal. But for Model 2, the same two energy levels cross each other, as shown in the inset of Fig. 3.3(b). The larger carbon nanoscroll appears to be metallic within LDA.

Figure 3.4 shows the total density of states (TDOS) of the two models. The peak around −6.0 eV in the TDOS of Model 1 (Fig. 3.4a) is mostly due to the ppσ bonds because the ppσ states are unchanged by the distortion of symmetry and dominate the bonding in the scroll. A small peak in the TDOS can be seen around the Fermi level, which is induced by the valence band edge state, as shown Fig. 3.3a. The general features of TDOS of Model 2 (Fig. 3.4b) are the same as those of Model 1.

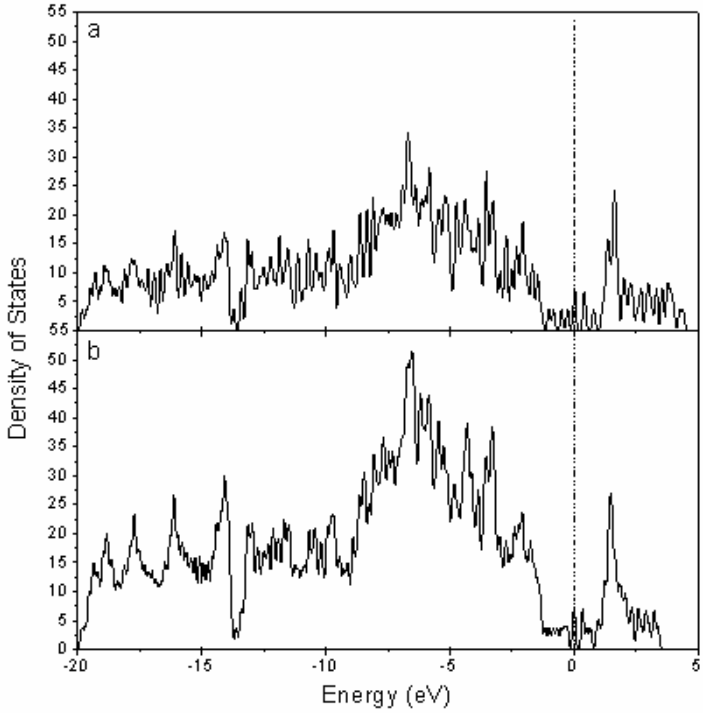

Fig. 3.4, Calculated total density of states for (a) Model 1 and (b) Model 2, respectively. The Fermi level is indicated by the dashed line.

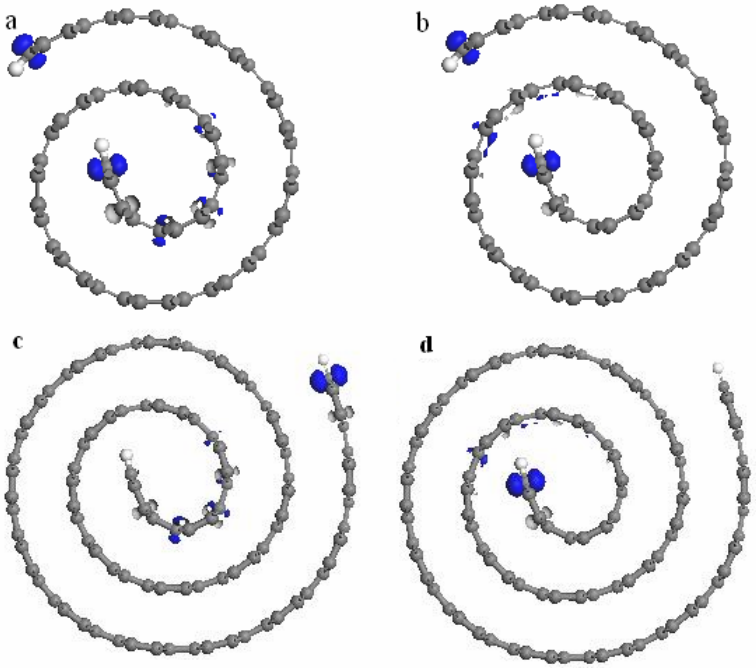

Fig. 3.5, The electron density of (a) the valence band edge state of Model 1; (b) the conduction band edge state of Model 1; (c) the valence band edge state of Model 2; (d) the conduction band edge state of Model 2.

Figure 3.5 shows the electron densities of the valence band edge state and the conduction band edge state of both models. The electron densities have been summed over all *k* points in the Brillouin zone. For Model 1, the *ves* and *ces* are mainly contributed by the *p* orbitals of the carbon atoms near the inner and outer edges. These *p* orbitals are perpendicular to the axis of the scroll and contribute to the formation of the big ppπ in the SWCNTs. In the scroll structure, the *p* orbitals of the carbon atoms near the edges separate from the big ppπ state and form π states along the scroll axis near the edges of the graphitic sheet. Both of the *ves* and *ces* are mainly contributed by the *p* electrons near the ends of the scroll (Figs. 3.5a and 3.5b). At the same time, the effect of the curvature leads to further splitting of the degenerate energy level. However, the effect of the curvatures at different positions makes the bands different. For Model 2, The electron densities of the same orbitals (Figs. 3.5c and 3.5d) show that the *ves* has its origin from the *p* orbital of the carbon atom at the open end of the nanoscroll (Fig. 3.5c), while the *ces* results mainly from the *p*-orbitals of the carbon atoms near the inner end of the graphitic sheet (Fig. 3.5d), which is different from Model 1. Comparing the charge densities corresponding to the *ves* and *ces* of the two models given in Fig. 3.6, we can see that *p* orbitals from carbon atoms near both ends of the nanoscroll in Model 1 contribute to these energy levels. However, in Model 2, the *p*-orbital of the carbon atoms near the open end is mostly filled with electrons while that near the inner end is largely unoccupied. Thus, increasing the size of the nanoscroll results in decoupling between the *p* orbitals at the two ends and reduces the effect of the curvature of the inner part that has the largest change during the geometry optimization process. It can be concluded that the effect of the inner part pushes the *ces* up and separates the *ves* and *ces*, but this effect diminishes with the increasing in size of the nanoscroll.

Compared to SWCNTs and MWCNTs, nanoscrolls show certain unique electronic properties. First of all, non-degenerate states dominate in nanoscrolls, in contrast to the doubly degenerate states in SWCNTs. Furthermore, for the small nanoscroll (Model 1), the *ves* and the *ces* are very close but remain on separate sides of the Fermi level, E_F, resulting in a pseudo-gap. It was reported that a gap or a pseudo-gap can be induced in MWCNTs composed of metallic armchair tubes due to intertube interaction or reduced symmetry[18]. Similarly, the pseudo-gap observed here in Model 1 can be attributed to the reduced symmetry and the curvature effect of the nanoscroll. The pseudo-gap disappears as the number of overlapping layers increases, as observed in Model 2. It is noted that the electronic properties of the nanoscroll are related to the number of overlapping layers in the scroll. The metallic property of the tube is restored when the number of overlapping layers reaches a certain value.

3.4 Optical Properties

Theoretical studies of the optical properties of SWCNTs and MWCNTs had been reported previously[19,20,21,22,23]. These studies revealed a special structure at $\omega \sim 2\gamma_0$ ($\gamma_0 \sim 2.4 - 3.0$ eV is the nearest-neighbor overlap integral[24]) for MWCNTs[21]. We compared the reflection spectra and loss function of two models to investigate the difference due to the size of the scroll. The imaginary part of the dielectric constant was calculated from

$$\varepsilon_2(q \to O_{\hat{u}}, \hbar\omega) = \frac{2e^2\pi}{\Omega\varepsilon_0} \sum_{k,v,c} |< \Psi_k^c \mid \hat{u} \cdot r \mid \Psi_k^v >|^2 \ \delta(E_k^c - E_k^v - E) \qquad (3.1)$$

where $\hat{u}$ is the vector defining the polarization of the incident electric field. This expression is similar to the Fermi's Golden rule for time dependent perturbations, and

$\varepsilon_2(\omega)$ can be thought of as detailing the real transitions between occupied and unoccupied electronic states. The real part, $\varepsilon_1(\omega)$, is obtained by the Kramers-Kronig relation[25]

$$\varepsilon_1(\omega) = \frac{2}{\pi} p\int_0^\infty \frac{\Omega\varepsilon_2(\Omega)}{\Omega^2 - \omega^2} d\Omega \tag{3.2}$$

where *p* denotes the Cauchy principle value of the integral, defined by,

$$p = \lim_{a\to 0} \int_{-\infty}^{\omega-a} \frac{\varepsilon(\Omega)}{\Omega - \omega^2} d\Omega + \int_{\omega+a}^{\infty} \frac{\varepsilon(\Omega)}{\Omega - \omega^2} d\Omega \tag{3.3}$$

The reflectance spectra were calculated from the macroscopic dielectric function ε(ω) for a periodic system by the relation

$$R(\omega) = |1 - \sqrt{\varepsilon(\omega)}|^2 \; / \; |1 + \sqrt{\varepsilon(\omega)}|^2 \tag{3.4}$$

$$\varepsilon(\omega) = \varepsilon_1(\omega) + i\varepsilon_2(\omega) \tag{3.5}$$

Figures 3.6a and 3.6b show the calculated reflectance spectra (*R*) for light polarization perpendicular and parallel to the axis of the nanoscroll, respectively. In the case of perpendicular light polarization, *R* decreases first, reaches a minimum, and then increases, as ω increases from zero to ω_0 (~1.1 eV). The reflectance spectrum reaches a peak at ω = ω_0. Beyond the peak, *R* decreases rapidly as a function of ω, reaches the second minimum, and then increases rapidly again, until reaching the second peak at $2\gamma_0$ (~4.9 eV in our calculation). With further increase in ω, *R* drops to 0 rapidly. The small peak at ω_0 is not apparent under the parallel light polarization, particularly for Model 2, as shown in Fig. 3.6b. Generally, the frequency-dependent reflectance spectrum of the nanoscroll is similar to that of MWCNTs[21], except the peak at ω_0. For example, the peak at $\omega=2\gamma_0$ and an abrupt π-plasmon edge at $\omega>2\gamma_0$ are typical features of reflectance spectra of MWCNTs. However, the peak at ω_0 is only observed in SWCNTs[23], and its position is up-shifted with the increase in the diameter of the SWCNTs. This low frequency peak

corresponds to the transition between DOS peaks of the tubes. In this aspect, the optical properties of carbon nanoscrolls are similar to those of the corresponding SWCNTs. Comparing the reflectance spectra of the two models, no major difference is observed, except the intensity of the spectrum, especially at ω_0.

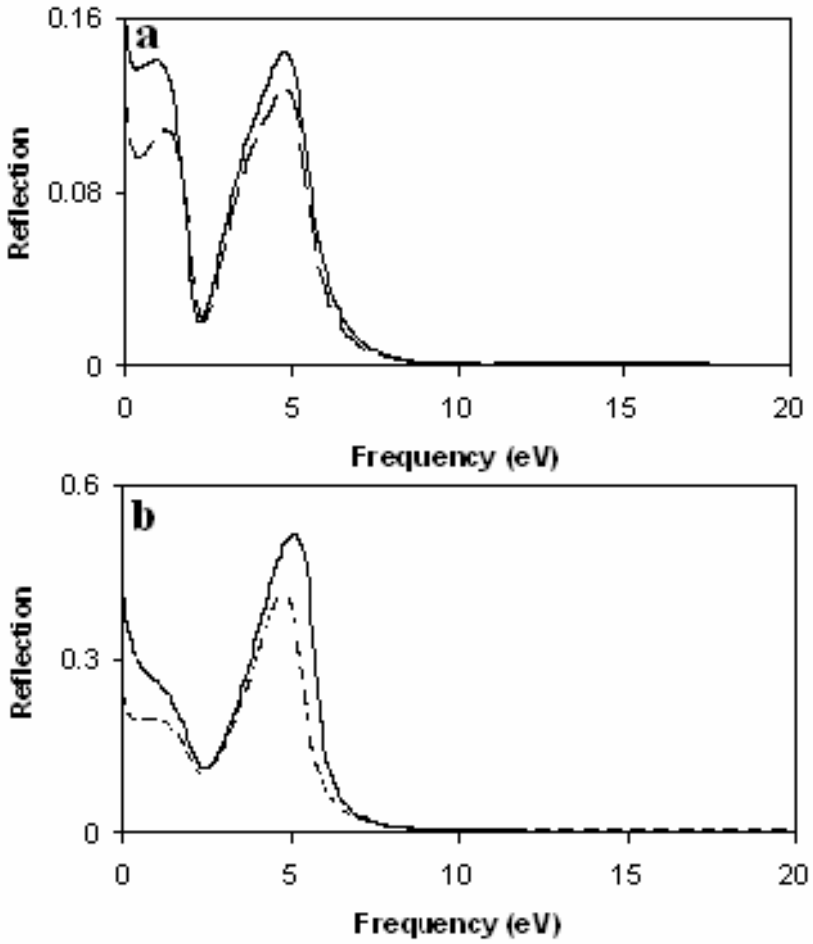

Fig. 3.6, Reflection spectra of the two models, (a) for the polarization perpendicular to the nanoscroll's axis; (b) for the polarization parallel to the nanoscroll's axis. The dashed line (solid line) is for Model 1 (Model 2).

The loss function was calculated using $\mathrm{Im}(-1/\varepsilon(\omega))$ at zero momentum transfer, and the results are shown in Figs. 3.7a and 3.7b, for polarization perpendicular and parallel to the axis of the scroll, respectively. Several peaks, including a pronounced one near $2\gamma_0$, can

be seen in the loss functions of both nanoscrolls. The pronounced peak at $\omega = 2\gamma_0$ can be attributed to the collective excitations of π electrons. The π plasmon is weaker for the perpendicular polarization than that for the parallel polarization, due to the fact that optical excitation is less effective in the perpendicular case. Under perpendicular light polarization, peaks are also observed in the high frequency region ($\omega \sim 13.5$ eV). These peaks are attributed to the high-frequency π+σ plasmon[20]. There exists another peak around $\omega \sim 2.0$ eV in the loss function of the nanoscroll, which is related to the inter-π-band excitation[26]. This low-frequency excitation, apparent in both polarization conditions, is also seen in the spectra of SWCNTs, but normally does not appear in the spectra of MWCNTs, except those consisting of a very few walls under perpendicular polarization[23,27]. In the latter, the strength of inter-π-band excitation reduces with the increase in the number of walls[27].

It is clear in Figs. 3.7a and 3.7b, particularly in the case of parallel light polarization, that the strength of the π plasmon increases and its peak position up-shifts with the increase of overlapping layers in the nanoscrolls which results from the increased number of carbon atoms and thus enhanced strength of the *p* orbitals. This is similar to the size effects in MWCNTs where the π plasma were also enhanced and up-shift with the increase in number of walls[27]. On the other hand, the inter-π-band excitation is also strengthened but the peak position slightly down-shifts as the overlapping layers increases. This is because the spacing between energy levels decreases with the increasing number of atoms due to the splitting of degenerate levels. The downward shift of the inter-π-band excitation peak is different from that in MWCNTs[27], but similar to the size effect in SWCNTs where the inter-π-band excitation is enhanced and down-shifted with the increase in tube diameter[22].

Therefore, the loss function of nanoscrolls behaves like MWCNTs except at low frequency region where it is similar to that of SWCNTs.

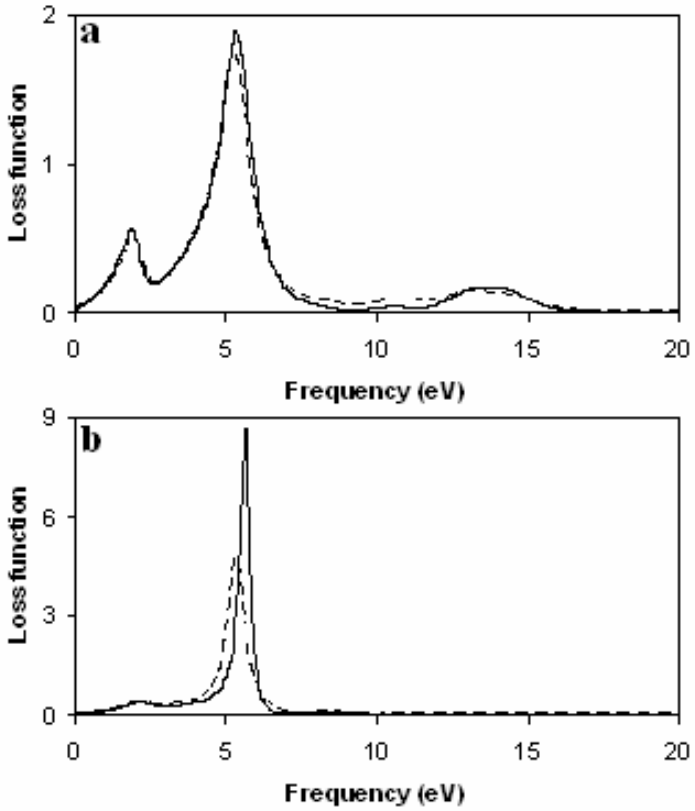

Fig. 3.7, Loss functions of the two models, (a) for the polarization perpendicular to the nanoscroll's axis; (b) for the polarization parallel to the nanoscroll's axis. The dashed line (solid line) is for Model 1 (Model 2).

3.5 Summary

In summary, the first-principles calculations on electronic and optical properties of the carbon nanoscrolls were performed. The results show that the electronic and optical properties of carbon nanoscrolls are different from those of nanotubes. The electronic properties of the scroll are closely related to the overlapping layers in the scroll. For the small scroll (Model 1), the valence band edge state and the conduction band edge state are very close but do not cross each other. But for the large scroll (Model 2), they are tangled

near the Fermi level. The nanoscrolls were found to be metallic/semimetallic within LDA. The results of the calculated optical properties give evidences of the anisotropic properties of the nanoscrolls. The analysis on the reflection and loss function showed that the nanoscroll structure share properties of both SWCNTs and MWCNTs.

The present work, i.e., *ab initio* study on carbon nanoscrolls, has indicated that the method is efficient and fruitful. These calculations demonstrated that *ab initio* method could be used to study such structures with reasonable computational resources. The experience obtained in the calculation of nano-scrolls such as testing of convergence, and determining equilibrium lattice constant and electronic properties will be valuable for applying the same method to the study of the functionalized CNTs, which will be discussed in next chapter.

References:

[1] Peter J.F. Harris, Carbon nanotubes and related structures: new materials for the 21st century, (New York: Cambridge University Press), 1999.
[2] S. Iijima, Nature 354, 56 (1991).
[3] S. Amelinckx, D. Bernaerts, X.B. Zhang, G.V. Tendeloo, and J.V. Landuyt, Science 267, 1334 (1995).
[4] O. Zhou, R.M. Fleming, D.W. Murphy, C.H. Chen, R.C. Haddon, and A.P. Ramirez, S.H. Glarum, Science 263, 1744 (1994).
[5] M. Liu and J. M. Cowley, Carbon 32, 393 (1994).
[6] G. Xu, Z. Feng, Z. Popovic, J. Lin, and J. J. Vittal, Adv. Mater. 13, 264 (2001).
[7] W. Ruland, A.K. Schaper, H. Hou, and A. Greiner, Carbon 41, 423(2003).
[8] L. M. Viculis, J. J. Mack, and R. B. Kaner, Science 299, 1361 (2003).
[9] J. G. Lavin, S. Subramoney, R. S. Ruoff, S. Berber, and D. Tomanek, Carbon 40, 1123 (2002).
[10] D. Tomanek, W. Zhong, and E. Krastev, Phys. Rev. B 48, 15461 (1993).
[11] D. Tomanek, Physica B 323, 86 (2002).
[12] M. Grundmann, Appl. Phys. Lett. 83, 2444 (2003).
[13] R. Setton, Carbon 34, 69 (1996).

[14] S. F. Braga, V. R. Coluci, S. B. Legoas, R. Giro, D. S. Galvao, and R. H. Baughman, Nano Lett. 4, 881 (2004).
[15] H.J. Monkhorst and J. Pack, Phys. Rev. B 23, 5188 (1976).
[16] P. Ordejon, E. Artacho, and J. M. Soler, Phys. Rev. B 53**,** R10 441 (1996).
[17] S. Reich, C. Thomsen, P. Ordejon, Phys. Rev. B 65, 155411 (2002).
[18] Y.-K Kown and D. Tomanek, Phys. Rev. B 58, R16001 (1998).
[19] F. J. Garcýa-Vidal, J. M. Pitarke, and J. B. Pendry, Phys. Rev. Lett. 78, 4289 (1997).
[20] A.G. Marinopoulos, L. Reining, A. Rubio, and N. Vast, Phys. Rev. Lett. 91, 046402 (2003).
[21] M. F. Lin, F. L. Shyu, and R. B. Chen, Phys. Rev. B 61, 14114 (2000).
[22] M. F. Lin, Phys. Rev. B 62, 13153 (2000).
[23] J. Hwang, H. H. Gommans, A. Ugawa, H. Tashiro, R. Haggenmueller, K. I. Winey, J. E. Fischer, D. B. Tanner, and A. G. Rinzler, Phys. Rev. B 62, R13310 (2000).
[24] J.W. Mintwire, B.I. Dunlap, and C.T. White, Phys. Rev. Lett. 68, 631 (1992).
[25] M. P. Marder, Condensed Matter Physics (John Willy & Sons, INC), 1999, p.570.
[26] T. Pichler, M. Knupfer, M. S. Golden, J. Fink, A. Rinzler, and R. E. Smalley, Phys. Rev. Lett. 80, 4729 (1998).
[27] F. L. Shyu and M. F. Lin, Phys. Rev. B 62, 8508 (2000).

CHAPTER 4

FUNCTIONALIZATION OF CARBON NANOTUBES

4.1 Introduction

Functionalization of single wall carbon nanotubes (SWCNTs) through chemical binding of atoms, molecules or molecular groups has attracted much attention, as it offers a possible way to modify the electronic, chemical, optical and mechanic properties of SWCNTs[1,2,3]. Experimentally, functionalization of SWCNTs can be realized by introducing molecules or molecular groups to their open ends or on their walls, through carbodiimide chemistry, or mixing the SWCNTs with an electrophilic reagent[2,3,4]. The functionalization may dramatically change the chemical, electronic, and transport properties of SWCNTs[5,6,7,8,9] and metal-nanotube contact properties[10,11,12,13,14]. Nguyen et al. reported that the nucleic acid functionalized carbon nanotube enhanced the reactivity by providing structural support to the CNTs and improved the chemical reactivity[5]. The C-H stretching mode of hydrogen functionalized carbon nanotubes was observed in Fourier transform infrared spectroscopy[6]. The characteristics of the carbon nanotube transistors could be controlled by the oxygen concentration[7]. Heinze et al. reported that the main effect of oxygen exposure is to change the work function of the CNTs and hence the contact potential in the metal-nanotubes Schottky barrier transistors[8]. Modeling of carbon nanotube Schottky barrier modulation under oxidizing conditions suggested that the role of oxygen molecules is to increase this potential drop with a negative oxygen charge, leading to a lower barrier in air[9]. Band-structure calculations show essentially no change in the nanotube band gap when NH_3 is boned to CNTs[10]. The binding of ammonia on carbon nanotubes is mostly electrostatic in nature and there is very little charge

transfer occurring. Theoretically, computational studies based on density functional theory have been carried out to investigate the mechanism behind the functionalization of SWCNTs by molecules or molecular groups[15,16,17,18,19]. It was found that the adsorbed molecules or atoms change the sp^2 local hybridization and lead to the formation of π-π conjugated bonds at the surface of the SWCNT. However, the DFT calculations on the effect of oxygen molecule on properties of CNTs have not been consistent. Calculations based on local-density approximation predicted a finite electron transfer from the carbon nanotube to the physisorbed oxygen molecule[11,13,17], while those based on generalized gradient approximation[20,21,22] and quantum chemistry calculations at the MP2 level[23,24] suggested that oxygen does not dope the CNT. Available experimental results support the latter and suggest that the main effect of oxygen adsorption is not to dope the bulk of the tube, but to change the work function of the metal contact, even though alkali metals like potassium act as dopants[7,8]. The discrepancy in the results of DFT calculations could be due to the different forms of exchange-correlation functional and the lack of explicit treatment of Van de Waals interaction. Nevertheless, first-principles method based on DFT does accurately describe chemisorption and produce very reliable results.

4.2 OH-Functionalization of Single-Wall Carbon Nanotubes

Recently, effects of OH groups on the electronic properties of SWCNTs were systematically investigated in our lab[25]. It was found that electronic and chemical properties of SWCNTs can be greatly changed due to the introduction of the OH group. OH-functionalized CNTs become soluble in water and many organic solvents. The OH doping largely reduces the work function of CNTs and changes the band gap of CNTs, which makes SWCNTs a possible candidate for biological sensors. It can be expected that

OH attached SWCNT bundles exhibit thermo-power effect due to the additional scattering channel for electrons in the tube wall.

To further understand the effect of OH doping on SWCNTs, we carried out *ab initio* total energy calculations[26] on the electrical and optical properties of single wall carbon nanotubes attached with OH groups. Semiconducting SWCNT was chosen in our calculations since the effects of OH groups would be more apparent for a semiconducting SWCNT than its metallic counterpart.

4.2.1 Calculation Details

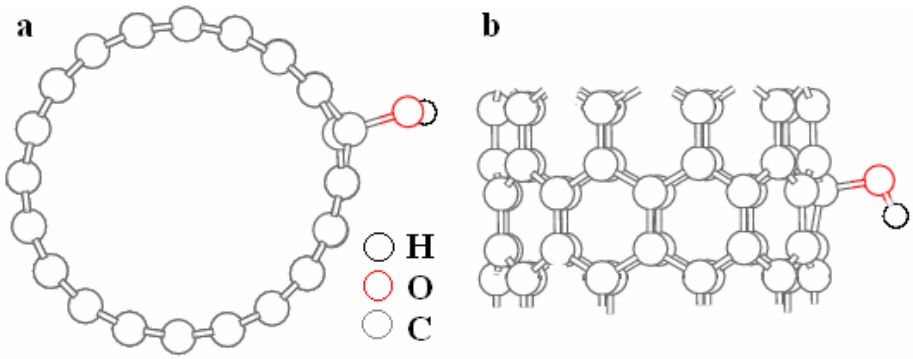

Fig. 4.1, Top (a) and side (b) views of the SWCNT-OH supercell used in our calculation. One OH group is attached on the wall of the SWCNT with the Oxygen atom connected to the carbon atom.

The first-principles method based on the density functional theory[27] and the generalized gradient approximation[28] are used in our study to investigate the structural and electronic properties of SWCNTs attached with OH groups. The details about the method have been given in Chapter 2. An energy cut-off of 400 eV and 6 k-points along the axis of the tube in the reciprocal space were used in our calculation. Good convergence was obtained with these parameters and the total energy was converged to 2.0×10^{-5}eV/atom. A large

supercell dimension in the plane perpendicular to the tube axis was used to avoid interaction between the carbon nanotube and its images in neighboring cells. The unit is periodic in the direction of the tube with a cell height of 4.24 Angstrom (see Fig. 4.1).

Calculations were carried out for a zigzag (10, 0) SWCNT, with and without the OH group, respectively. One OH group was included in each unit cell to simulate the adsorption and it was chemically attached to the wall of the nanotube. The geometry of the SWCNT, with and without the OH group, was fully optimized. Figure 4.1 shows the optimized structure of the OH functionalized SWCNT (10, 0) with an oxygen atom attached to the wall. Properties of the carbon nanotubes such as band structure, density of states (DOS) and population analysis were calculated for the optimized structure.

4.2.2 Binding Energy

The binding energy of the OH group was calculated according to the following formula

$$E_b = E_t(CNT + OH) - E_t(CNT) - E_t(OH) \tag{4.1}$$

where $E_t(CNT+OH)$ and $E_t(CNT)$ are the total energies of the tube, with and without the OH group, respectively, $E_t(OH)$ is the total energy of an isolated OH group. The binding energy was found to be 0.78 eV, which indicated that a stable chemical bond was formed between the tube and the OH group.

4.2.3 Electronic Properties

The band structure of the zigzag (10, 0) carbon nanotube, which has D_{10h} symmetry, is shown in Fig. 4.2. Most of the energy levels are doubly degenerate, which is a general property of the achiral carbon nanotubes due to the rotational point group C_n. Our

calculated result is very similar to that in Ref. 29. Figure 4.2b shows the fine structure of the bands near the Fermi level. It can be seen that there exists a band gap which is about 0.51 eV within GGA. The highest valence band consists of two degenerate levels, denoted as E_0 in Fig. 4.2b, which contributes to the big ppπ bond along the ring of the tube[30]. The bottom of the conduction band corresponds to the big π^* anti-bonding states.

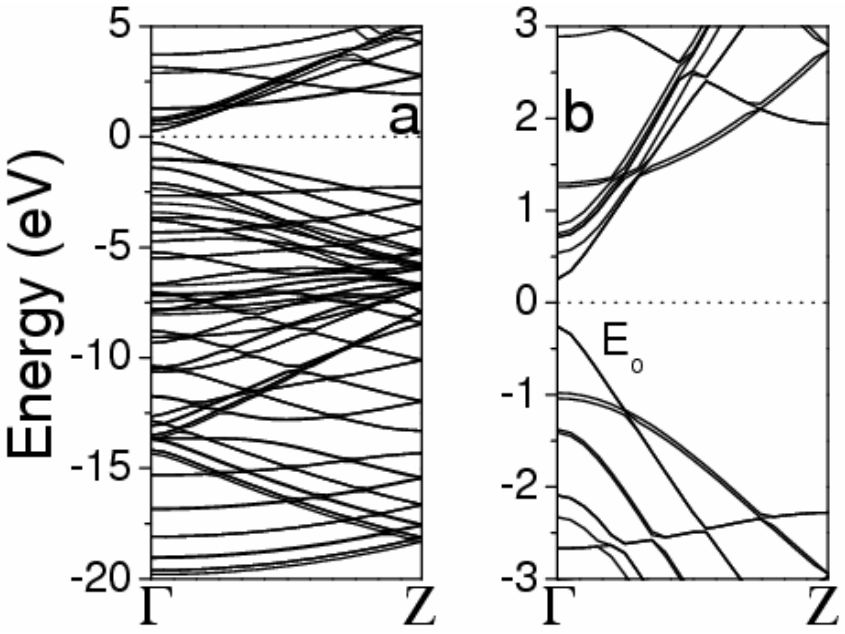

Fig. 4.2, Band structure of the zigzag (10, 0) SWCNT, (b) shows its details near the Fermi level (E_F=0eV).

In the optimized tube–OH system, the angle between the C-O bond and the O-H bond is about 100 degrees. It is well known that the three p orbitals of oxygen are perpendicular to each other. The bond of the sp hybridization formed by one p orbital (p_z) of oxygen and the s orbital of hydrogen is roughly perpendicular to the C-O bond because another p orbital (p_x) of oxygen forms a bond with one p orbital of the carbon. The angle is tilted due to the interaction of orbitals. By carefully analyzing the bonding around the carbon atom on which the OH group is attached, we found that the angles between the O-C bond and C-C bond fall in the range of 107 to 112 degrees, and are close to 109.5 degrees of

sp^3 hybridization. And the bond lengths are within 1.48 and 1.52 angstroms. It can be concluded that the local sp^2 hybridization was destroyed due to the introduction of the OH group, and a ppσ bond was formed between C and O. The local structure of the carbon nanotube is distorted due to the introduction of the OH group, and C-C bond becomes longer than that in a pure SWCNT (1.42 angstrom). This distortion and addition of the OH group lead to the differences in the electronic properties of the SWCNT–OH system and pure SWCNT.

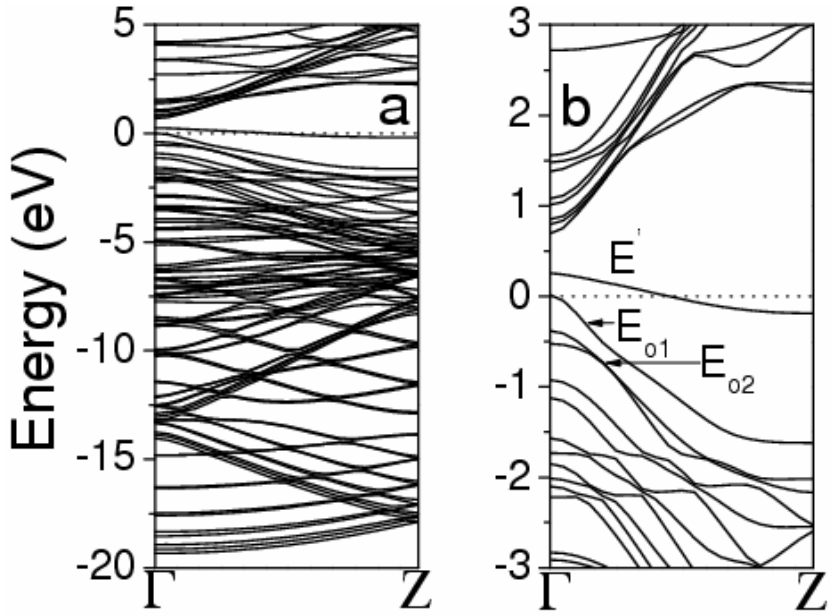

Fig. 4.3, Band structure of the SWCNT-OH system, (b) shows its details near the Fermi level (E_F=0eV).

The band structure of the carbon nanotube is changed significantly up on introducing the OH group, as can be seen in Fig. 4.3. It is clear that an energy level, *E′* crosses the Fermi level (E_F=0). The fine band structure near E_F (Fig. 4.3b) shows that the degenerate energy levels below the Fermi level split after the OH group is introduced to the tube (refer to Fig 4.2). The original doubly degenerate state (E_0) in the pure tube splits into two states E_{01} and E_{02} which are separated by 0.39 eV at the Γ point in the SWCNT–OH system. This

energy level separation is due to the reduced symmetry of the system after the OH group is introduced.

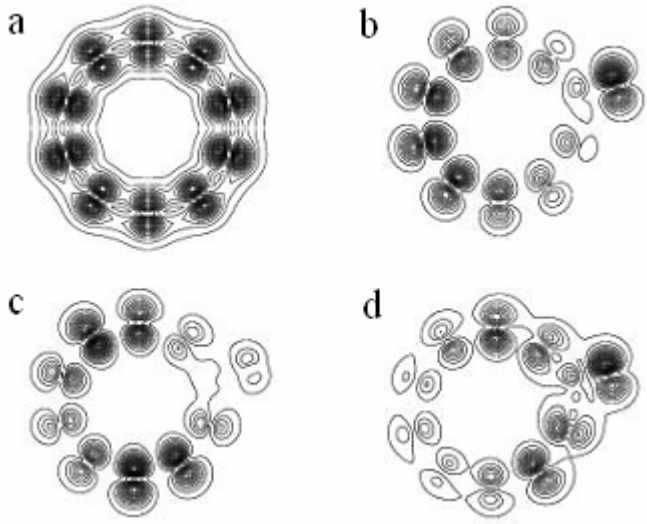

Fig. 4.4, Electron density corresponding to (a) the E_0 level in the pure tube; (b) the E′ level crossing the Fermi level; (c) the E_{01} level and (d) the E_{02} level in the tube–OH system, respectively.

The E_0 state consists of the big π bonding in the pure tube. Figure 4.4a shows the electron density of this orbital. The π bonding characteristics is clearly seen in the figure. Analysis of electron density of the corresponding orbital in the tube–OH system reveals the mechanism behind the separation of the doubly degenerate E_0 state. The E_0 state of the perfect tube (Fig. 4.4a) interacts with the fully occupied p orbital (p_y) of the oxygen, and results in the separation of E_0 into E_{01} and E_{02}, as shown in Fig. 4.3b. The electron densities of these orbitals show that E_{02} and E' are the coupling state and anti-coupling state between the E_0 and p_y orbital of oxygen, respectively, shown in Fig. 4.4d and 4.4b, respectively, while E_{01} is mainly contributed by the big π bond of the tube (Fig. 4.4c). This is different from the attachment of oxygen molecule[17].

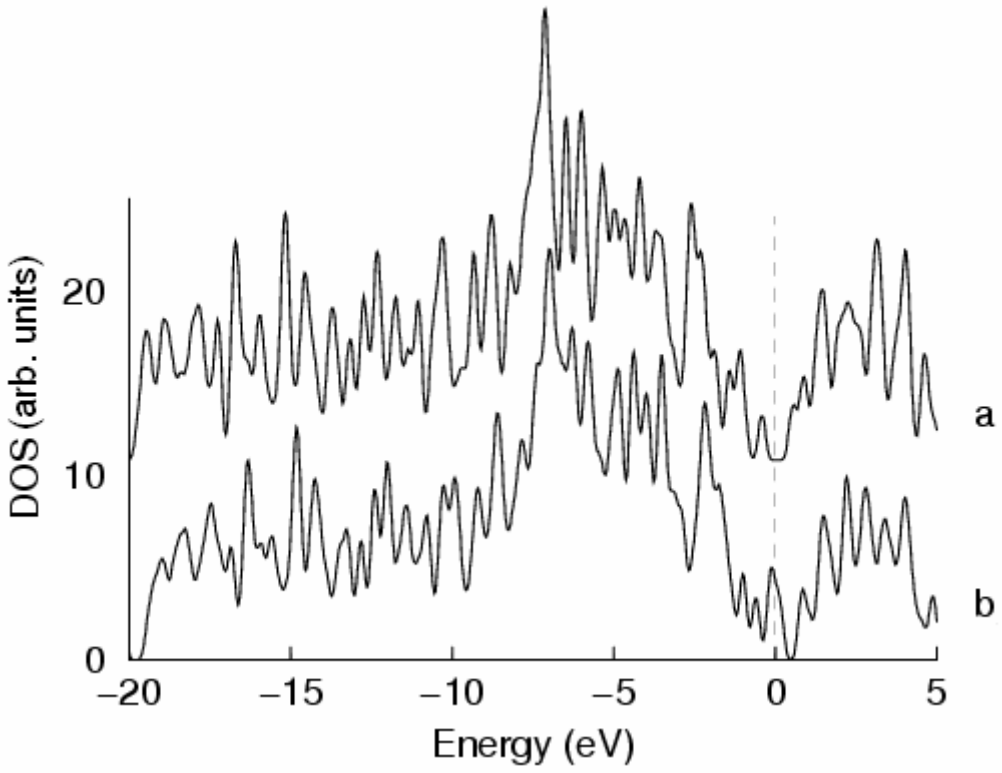

Fig. 4.5, Calculated (a) total DOS of the pure SWCNT, (b) total DOS of SWCNT-OH. The Fermi level is at 0 eV.

The calculated total density of states (TDOS) further revealed the separation of the degenerate states and the expansion of the DOS. Figure 4.5 shows the TDOS of the pure tube (a) and the TDOS of the tube–OH (b), respectively. Notable difference can be seen in the densities of states, which is a result of introducing the OH group to the nanotube. When the OH group is introduced to the tube wall, a peak in the DOS arises at the Fermi level and the energy gap is significantly reduced. This is due to the interaction between the tube and the oxygen because the p_y orbital of oxygen and the p orbital of one carbon atom form a bond, which makes the degenerate levels in the pure SWCNT to split. The OH group possesses an unpaired electron, which actively participates in hybridization near the C atom when it is attached to the tube. This can form an acceptor level and

enhance the conductivity of the CNT. Changes in the TDOS can also be seen in other ranges of energy but are minor. The main features in the TDOS of the pure tube remain in the TDOS of the tube-OH system, due to the fact that the TDOS in these regions are dominated by the carbon states.

When the OH group is attached to the tube wall, electrons are transferred from the tube to the OH group due to its large electronegativity. From the Mulliken population analysis, a charge transfer of 0.33e per O atom was found. It can therefore be concluded that semiconducting SWCNT can be functionalized and its band gap can be significant reduced by the attachment of organic molecules. This simulation results are in an excellent agreement with the experimental measurments in our lab, which show a band gap reduction from 0.1 to 0.05 eV due to OH functionalization. Also, it can be expected that metallic SWCNTs maintain their electronic properties due to hole carriers generated in the tube. The calculated length of the C-O bond is 1.52 angstrom, which is similar to the bond length of C-O in aromatic carbon[31]. This property shows that the functionalized SWCNTs can have good solubility and will be useful in biology and chemistry. In this calculation, there is only one OH group in each unit cell. If there was one OH group per six carbons, as in the aromatic carbon, the tube can be expected to be an aromatic tube.

4.2.4 Optical Properties

Optical absorption or electron energy loss spectroscopy is a direct probe to study the collective electron excitation of the system under consideration. They can be simulated by theoretical calculations. Theoretical studies of the optical and loss spectra of SWCNTs and MWCNTs have been reported previously[32,33,34,35,36]. In this section, theoretical

calculations were performed, using the procedure described on Page 46, to investigate how OH-functionalization may affect the optical properties of SWCNTs.

The loss function was calculated using $\mathrm{Im}(-1/\varepsilon(\omega))$ at zero momentum transfer from the macroscopic dielectric function ε(ω) ($\varepsilon(\omega) = \varepsilon_1(\omega) + i\varepsilon_2(\omega)$) for a periodic system.

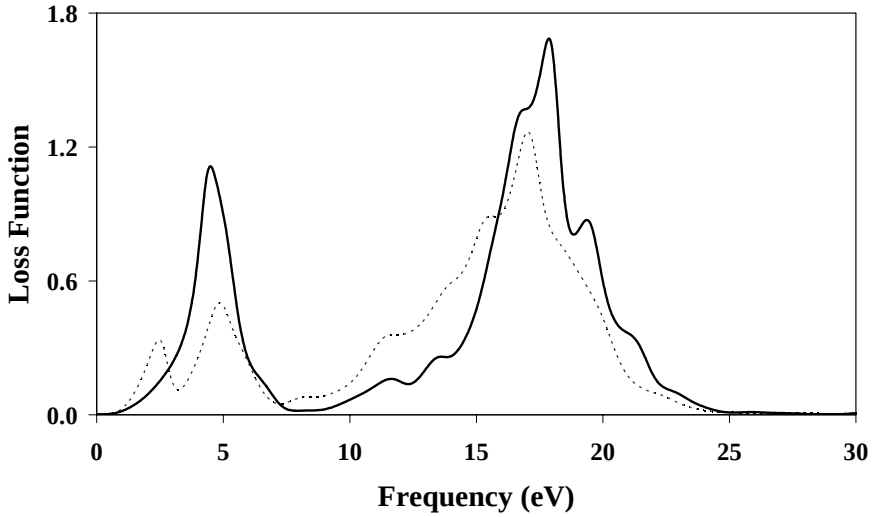

Fig. 4.6, Loss functions of zigzag (10, 0) SWCNT. The dotted line (solid line) corresponds to the case when the polarization direction is perpendicular (parallel) to the axis of the tube.

Figure 4.6 shows the loss function of the zigzag (10, 0) SWCNT. Several peaks are predicted, which are related to the 1D subbands with divergent density of states. One pronounced peak in the loss function is at $\omega \sim 2\gamma_0$, which can be attributed to the collective excitations of π electrons[34]. The π plasmon is weaker for the perpendicular polarization than for the parallel polarization, since the optical excitation is less effective in the perpendicular case. Another pronounced peak is at ω ~ 17.0 – 19.0 eV. The peak is attributed to the higher-frequency π+σ plasmon[33]. Under the perpendicular polarization,

there is a peak around ω ~ 2.6 eV. The lower-frequency excitation only exists in the SWCNTs, which is related to the inter-π-band excitation[37].

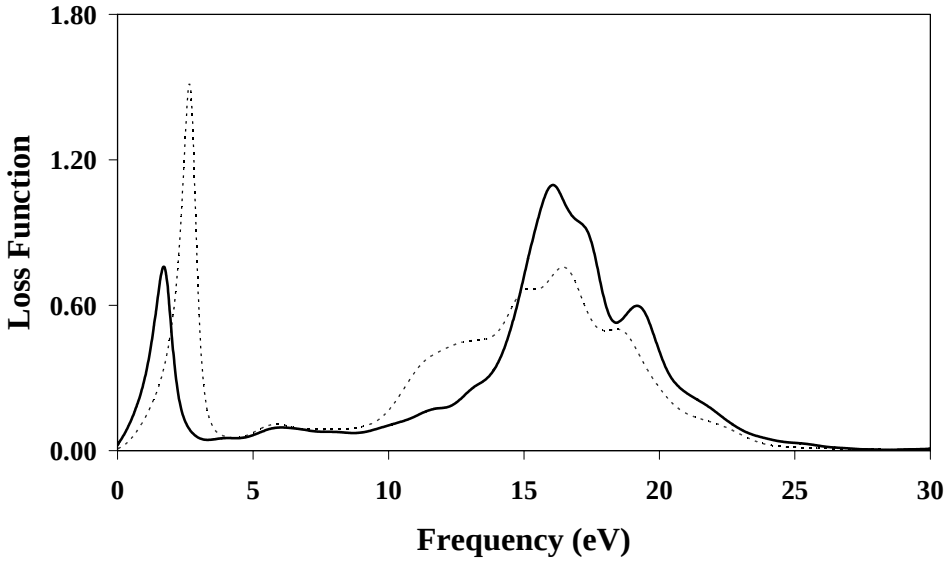

Fig. 4.7, Loss functions of the SWCNT–OH. The dotted line (solid line) corresponds to the case when the polarization direction is perpendicular (parallel) to the axis of the tube.

Figure 4.7 shows the loss function of the SWCNT–OH system. Significant differences can be observed when it is compared with Fig. 4.6. The π plasmon excitation disappears in the SWCNT–OH system. The inter-π-band excitation becomes stronger in both polarization conditions at the lower-frequency (ω ~ 1.8 – 2.7 eV). It is also noticed that the higher-frequency excitation is down-shifted to 16 – 18 eV with reduced strength. The reason behind these changes is the introduction of the OH group which distorted the symmetry of the tube and split the degenerate energy levels. The separation increases the number of energy levels and reduces the spacing of energy levels, which leads to more inter-π-band excitation and the down-shift of excitation energy. At the same time, the big π bonding was distorted due to the introduction of the OH that forms bond with the tube. The distortion disturbed the π electron gas and made the π plasmon to disappear. The

downshift and reduction of the higher-frequency π+σ plasmon can be attributed to the same reason.

4.3 F- and Cl-Functionalization of Single-Wall Carbon Nanotubes

The functionalization of nanotube actually started from the fluorination of SWCNTs[38]. Recently, it was demonstrated by Touhara and Okino that the halogen atoms were chemically absorbed on the wall of carbon nanotube which resulted in diverse electronic structures[39]. However, there have been few theoretical studies on functionalization of CNTs by F and other atoms such as Cl. Due to their large electronegativity, one can expect that such atoms will be chemically adsorbed on carbon nanotubes and affect the physical properties of the nanotubes. Here, we carried out *ab initio* total energy calculations on the electronic properties of single wall carbon nanotubes attached with F, or Cl. Semiconducting SWCNT was chosen in our calculations since the effects of F, or Cl would be more apparent for a semiconducting SWCNT than its metallic counterpart[17].

4.3.1 Calculation Details

Calculations were carried out for a zigzag (10, 0) SWCNT, with and without the functionalization, respectively, using a similar approach as OH-functionalized SWCNTs described in section 4.2. One F or Cl atom was included in each unit cell to simulate the functionalization and it was chemically attached to the wall of the nanotube. Due to the symmetry of CNT, the C=C bonds are symmetrically equivalent. The choice of attached carbon atom on the SWCNT should not affect the results of the calculation. The geometry of the SWCNT, with and without the functionalization, was fully optimized. Figure 4.8

shows the optimized structure of the Cl (Fig. 4.8a) and F (Fig. 4.8b) functionalized SWCNT (10, 0) with Cl or F atom attached to the wall. The properties of the carbon nanotubes such as band structure, density of states (DOS) and population analysis were calculated based on the optimized structures.

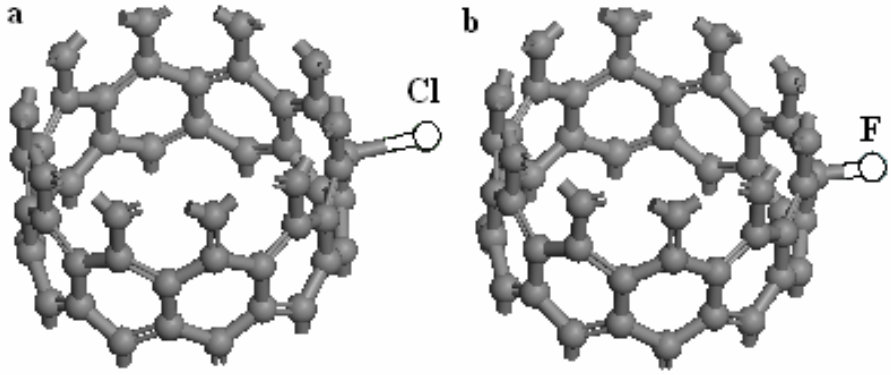

Fig. 4.8, The models of the SWCNT-Cl (a) and SWCNT–F (b) used in our calculation. One F or Cl is attached on the wall of the SWCNT.

4.3.2 Binding Energy

The binding energy of the attached F or Cl was calculated according to Eq. (4.1). The binding energies were found to be 0.98 eV and 0.93 eV, for Cl and F respectively.

4.3.3 Optimized Geometry

In the optimized tube–F and tube-Cl systems (Fig. 4.8), the local structure around the carbon atom attached with Cl or F is slightly distorted. One of p orbitals of Cl (or F) forms a bond with one of the carbon p orbitals. By carefully analyzing the bonding around the carbon atom on which the Cl (or F) was attached, we found that the angles between the Cl-C bond and C-C bond fall in the range of 100^{o} to 106^{o}. The angles between the C-C bonds around the distorted position fall in the range of 111^{o} to 116^{o}, which are around 119^{o} in the original tube. And the bond lengths are within 1.44 and 1.47

Å. It can be concluded that the local sp^2 hybridization was partially destroyed due to the introduction of Cl (or F) and a bond was formed between C and Cl (or F). The C-Cl and C-F bond lengths are 2.09 Å and 1.49 Å, respectively (see Table 4.1). The local structure of the carbon nanotube is distorted due to the introduction of Cl (or F), and C-C bond becomes longer (1.46 Å) than that in a pure SWCNT (1.42 Å).

System	Binding Energy (eV)	Bond length (Å)	Charge transfer (*e*)
SWCNT-Cl	0.98	2.09	0.23
SWCNT-F	0.93	1.49	0.41

Table 4.1, The calculated binding energy of halogen atom, equilibrium distance between the halogen atom and the tube, and the amount of charge transfer from the CNT to the halogen atom.

4.3.4 Electronic Properties

The calculated band structures of the pure tube and functionalized tubes are shown in Fig. 4.9. The highest valence band of the pure tube consists of two degenerate bands, denoted as E_0 in Fig 4.9a, which contributes to the big π bond along the ring of the tube[30]. The bottom of the conduction band corresponds to the big π^* anti-bonding states.

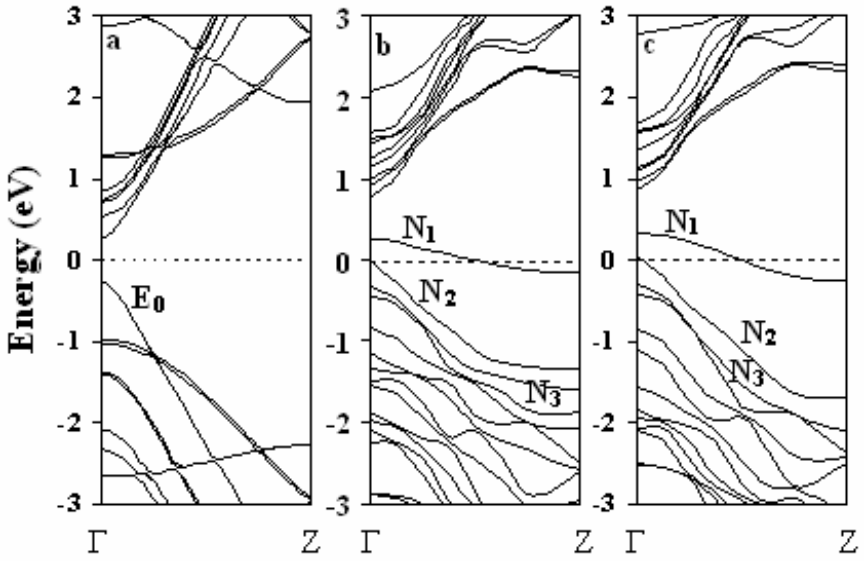

Fig. 4.9 (a) Band structure of the zigzag (10, 0) SWCNT near the Fermi level (E_F=0 eV); (b) band structure of the SWCNT-Cl system; (c) Band structure of the SWCNT-F system.

Introducing Cl or F to the tube results in significant changes in the band structure, as can be seen in Fig. 4.9b and 4.9c. It is clear that an energy level crosses the Fermi level (E_F=0). The fine band structure near E_F shows clearly that the energy levels below the Fermi level are separated after Cl or F is introduced to the tube. A single occupied molecular orbital (SOMO) is formed upon the addition of an atom according to radical organic chemistry. The original doubly degenerate state (E_0) in the pure tube splits. The energy difference between the two top valence levels is 0.32 eV in the SWCNT–Cl system and 0.34 eV in the SWCNT-F system at the Γ point. The separation of energy levels is due to the reduced symmetry of the system after the atom (Cl or F) was introduced.

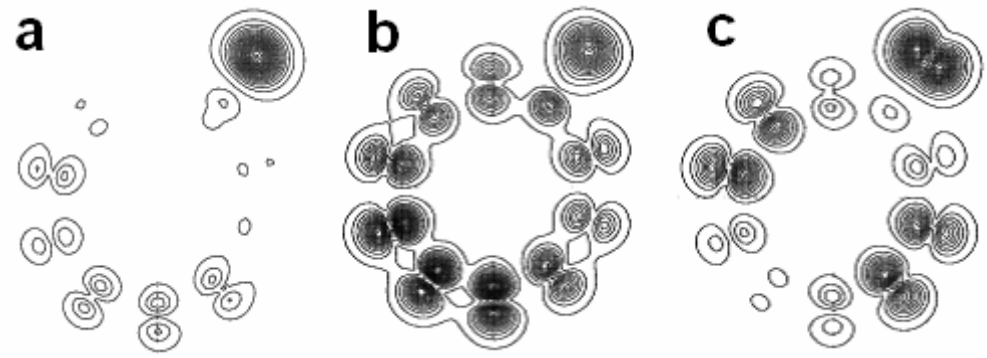

Fig. 4.10, Electron density of State of (a) the N_1 level cross the Fermi level; (b) the N_2 level and (c) the N_3 level in the tube–Cl system, respectively.

The E_0 state consists of the big π bonding in the pure tube (Fig. 4.4a). Analysis of electron density of the corresponding orbitals in the tube–Cl (or F) system reveals the mechanism behind the separation of the doubly degenerate E_0 state and the difference between two systems. In SWCNT-Cl system, the doubly degenerate E_0 state separates into two levels, which interacts with the two p orbitals of Cl. N_1, N_2, and N_3 (shown in Fig. 4.9b) are mainly corresponding to one p orbital of Cl (parallel to the tube) (Fig. 4.10a), the

coupling state between the p orbital and the big π orbital (Fig. 4.10b) and the anti-coupling state between another p orbital (perpendicular to the tube) and the big π orbital (Fig. 4.10c), respectively. However, in the SWCNT-F system, N_1, N_2, and N_3 (shown in Fig. 4.9c) are mainly corresponding to one separated E_0 state (Fig. 4.11a), the anti-coupling state between the p orbital (parallel to the tube) and the big π orbital (Fig. 4.11b) and the coupling state between the p orbital (parallel to the tube) and the big π orbital (Fig. 4.11c), respectively. The finite dispersion of N_1 state in the band structure of the SWCNT-F system (Fig. 4.9c) is attributed to the non-local E_0 state (Fig. 4.11a).

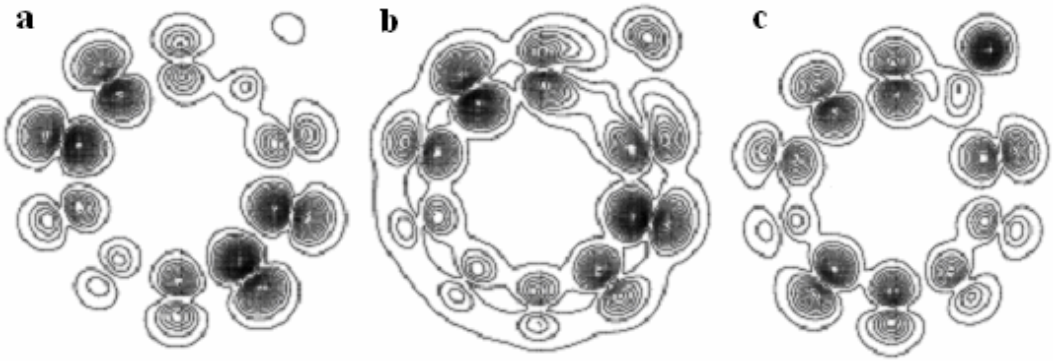

Fig. 4.11, Electron density of State of (a) the N_1 level cross the Fermi level; (b) the N_2 level and (c) the N_3 level in the tube–F system, respectively.

The calculated total DOS (TDOS) further revealed the separation of the degenerate states and the expansion of the DOS. Figure 4.12 shows the TDOS of the pure tube (Fig. 4.12a), the TDOS of the tube–Cl (Fig. 4.12b), and the TDOS of the tube–F (Fig. 4.12c). The TDOS of the SWCNT–Cl system and the SWCNT–F system are different from that of the perfect SWCNT. Introducing the atom (Cl or F) to the nanotube results in changes in the TDOS of the nanotube. When the atom is introduced to the tube wall, a peak in the TDOS arises near the Fermi level and the energy gap is reduced. This also can be seen in the band structures (Fig. 4.9b and 4.9c). The Cl or F possesses an unpaired electron, which

actively participates in hybridization near the C atom when it is attached to the tube. This can form an acceptor level and enhance the conductivity of the CNT, as indicated in the band structures (Fig. 4.9b and 4.9c), where the energy level crosses the Fermi level. Changes in the TDOS can also be seen in other ranges of energy but are minor. The main features in the TDOS of the pure tube remain in the TDOS of the tube- Cl or F system, due to the fact that the TDOS in these regions are dominated by the carbon states.

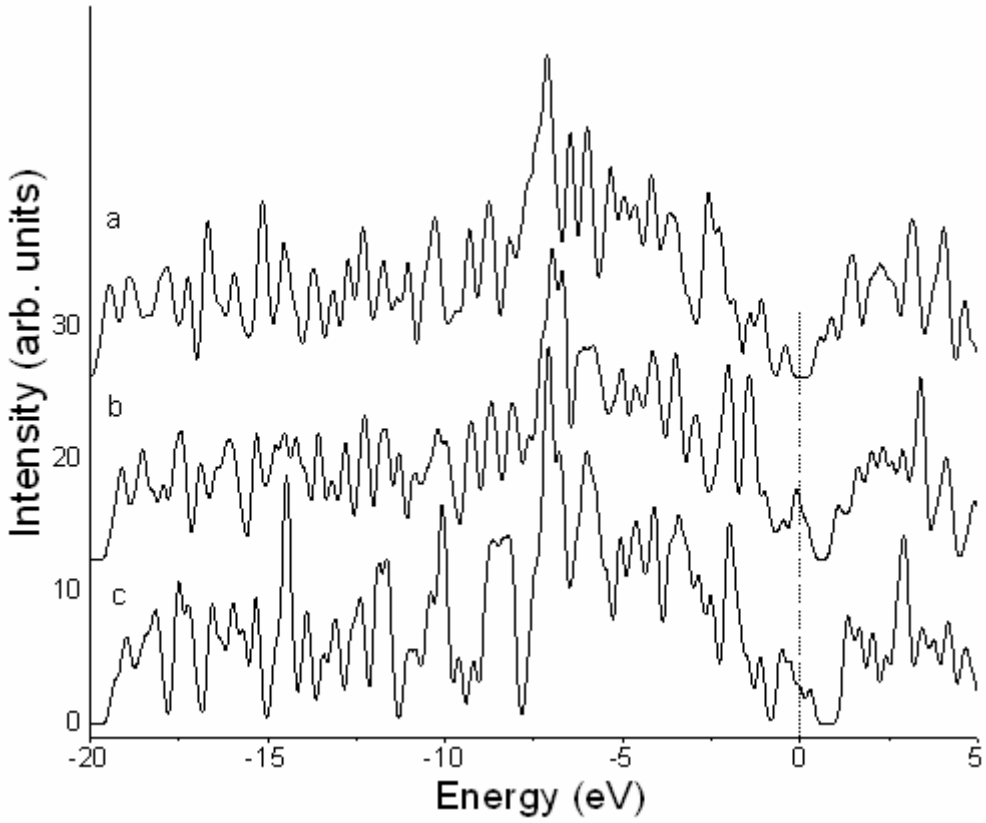

Fig. 4.12, Calculated (a) total DOS of the pure SWCNT; (b) total DOS of SWCNT-Cl and (c) total DOS of SWCNT-F. The Fermi level (dashed line) is at 0 eV.

When Cl or F is attached to the tube wall, electrons are transferred from the tube to the atom due to its large electronegativity. From the Mulliken population analysis, we found a charge transfer of 0.27 e per Cl atom, while 0.41 e per F atom (Table 4.1). The charge transfer did not occur in the physical adsorption of ammonia[10]. In the present cases, a

bond forms between the halogen atom (Cl or F) and one carbon atom in the tube. The charge transfer is induced by chemical adsorption. It is thus obvious that semiconducting SWCNTs can be functionalized.

4.4 Summary

In summary, the attachment of the atoms or chemical groups on the tube wall induces significant changes in the electronic properties of the semiconducting SWCNT. It can be expected that the charge transfer from carbon to the attached atoms results in the distortion of the local structure in the functionalized SWCNT systems. From the calculated band structures, an acceptor level in the SWCNT-OH, -Cl or -F system was found, which mainly comes from the interaction between the p orbital of the atom and carbon atom. This strongly suggests that the attached atoms accept electrons from the tube, which is in agreement with the band structure analysis. The interaction between the tube and atom makes the degenerate levels in the pure tube to split. The splitting of the degenerate E_0 states near the Fermi level was due to the coupling of the p orbitals of the atom with the big π orbital of the tube. Based on the results of our calculations, the atoms or chemical groups are expected to be good acceptors for hole doping. Introducing atoms can be an effective way of modifying the electronic properties of semiconducting SWCNTs.

The *ab initio* studies on carbon nanoscrolls and functionalized carbon nanotubes have indicated that the method is efficient in the research of nanostructures. These calculations demonstrated that *ab initio* method could be used to study such structures with reasonable computational resources. The experience obtained in the calculations will be valuable for

applying the same method to the study of the carbon-related nanotubes, *i.e*. boron carbonitride nanotubes, which will be discussed in next chapter.

References:

[1] C. Richard, F. Balavoine, P. Schultz, T. W. Ebbesen, and C. Mioskowski, Science 300, 775 (2003).
[2] J. Chen, M. A. Hamon, H. Hu, Y. Chen, A. M. Rao, Peter C. Eklund, and R. C. Haddon, Science 282, 95 (1998).
[3] S. S. Wong, E. Joselevich, A. T. Woolley, C. L Cheung, and C. M. Lieber, Nature 394, 52 (1998).
[4] J. Liu, A.G. Rinzler, H. Dai, J. H. Hafner, and R. K. Bradley, *et al*, Science 280, 1253 (1998).
[5] C. V. Nguyen, L. Delzeit, A. M. Cassell, J. Li, J. Han, and M. Meyyappan, Nano Lett. **2**, 1079 (2002).
[6] B. N. Khare, M. Meyyappan, A. M. Cassell, C, V. Nguyen, and J. Han, Nano Lett. **2**, 73 (2002).
[7] V. Derycke, R. Martel, J. Appenzeller, and Ph. Avouris, Appl. Phys. Lett. **80**, 2773 (2002).
[8] S. Heinze, J. Tersoff, R. Martel, V. Derycke, J. Appenzeller, and Ph. Avouris, Phys. Rev. Lett. 89, 106801 (2002).
[9] T. Yamada, Phys. Rev. B 69, 125408 (2004).
[10] C. W. Bauschlicher, Jr. and A. Ricca, Phys. Rev. B 70, 115409 (2004).
[11] S. Peng and K. Cho, Nanotechnology 11, 57 (2000).
[12] J. Kong, N. R. Franklin, C. Zhou, and M.G. Chapline, *et al.*, Science 287, 622 (2000).
[13] J. Zhao, A. Buldum, J. Han and J. P. Lu, Nanotechnology 13, 195 (2002).
[14] X. P. Tang, A. Kleinhammes, H. Shimoda, L. Fleming, K.Y. Bennoune, S. Sinha, C. Bower, O. Zhou, and Y. Wu, Science 288, 492 (2000).
[15] J. Zhao, J. P. Lu, J. Han, and C. K. Yang, Appl. Phys. Lett. 82, 3746 (2003).
[16] H. Chang, J. D. Lee, S. M. Lee and Y. Lee, Appl. Phys. Lett. 799, 3863 (2001).
[17] S. H. Jhi, Steven G. Louie, and M. L. Cohen, Phys. Rev. Lett. 85, 1710 (2000).
[18] E. C. Lee, Y. S. Kim, Y. -G. Jin, and K. J. Chang, Phys. Rev. B 66, 073415 (2002).
[19] D. J. Mann and D. Halls, J. Chem. Phys. 116, 9014 (2002).
[20] P. Giannozzi, R. Car, and G. Scoles, J. Chem. Phys. 118, 1003 (2003).
[21] D. C. Sorescu, K. D. Jordan, and P. Avouris, J. Phys. Chem. B 105, 11227 (2001).
[22] D. Lamoen and B. N. J. Persson, J. Chem. Phys. 108, 3332 (1998).
[23] A. Ricca and J. D. Drocco, Chem. Phys. Lett. 362, 271 (2002).
[24] A. Ricca, C. W. Bauschlicher, and A. Maiti, Phys. Rev. B, 68, 035433 (2003).
[25] To be published.
[26] M. D. Segall, P. J. D. Lindan, M. J. Probert, C. J. Pickard, P. J. Hasnip, S. J. Clark and M. C. Payne, J. Phys.: Condens. Matter 14, 2717 (2002).
[27] M. C. Payne, M. P. Teter, D. C. Allan, T. A. Arias and J. D. Joannopoulos, Rev. Modern. Phys. 64, 1045 (1992).

[28] J. P. Perdew and Y. Wang, Phys. Rev. B 46, 13244 (1992).
[29] S. Reich, C. Thomsen, and P. Ordejon, Phys. Rev. B 65, 155411 (2002).
[30] M. S. Dresselhaus, G. Dresslhaus, and P. C. Eklund, Science of fullerenes and Carbon nanotubes (Acadamic Press, San Diego, 1996).
[31] A. A. Askadskii, Computational Materials Science of Polymers (Cambridge International Science publishing, 2003).
[32] F. J. Garcýa-Vidal, J. M. Pitarke,and J. B. Pendry, Phys. Rev. Lett. 78, 4289 (1997).
[33] A. G. Marinopoulos, L. Reining, A. Rubio, and N. Vast, Phys. Rev. Lett. 91, 046402 (2003).
[34] M. F. Lin, F. L. Shyu, and R. B. Chen, Phys. Rev. B 61, 14114 (2000).
[35] M. F. Lin, Phys. Rev. B 62, 13153 (2000).
[36] J. W. Mintwire, B. I. Dunlap, and C. T. White, Phys. Rev. Lett. 68, 631 (1992).
[37] T. Pichler, M. Knupfer, M. S. Golden, J. Fink, A. Rinzler, and R. E. Smalley, Phys. Rev. Lett. 80**,** 4729 (1998).
[38] E. T. Michelson, C. B. Huffman, A. G. Rinzler, R. E. Smalley, R. H. Hauge, and J. L. Margrave, Chem. Phys. Lett. 296, 188 (1998).
[39] H. Touhara and F. Okino, Carbon 38, 241 (2000).

CHAPTER 5

BORON CABONITRIDE NANOTUBES

5.1 Introduction

Since its discovery, carbon nanotube has attracted ever increasing scientific interests, and has triggered search in other compound nanotubes[1]. A number of nanotubes based on first row elements, such as BN[2], BC_3[3], BC_2N[4], CN[5], and AlN[6] nanotubes, have been predicted theoretically, and some of them, *i.e.*, BN[7,8], BC_3, $B_xC_yN_z$[9,10] and AlN[11], have been successfully synthesized. It is well known that the electronic properties of carbon nanotubes depend on the size (radius) and chirality of the nanotubes[12,13,14]. In the case of BN nanotubes, previous calculations showed that the energy gap of zigzag BN nanotubes decreases rapidly with the decrease in radius, while that of the armchair BN nanotubes remain a constant[15]. Recently, Hernández et al. studied the elastic properties of $B_xC_yN_z$ and found that graphitic nanotubes were stiffer than any of the composite nanotubes considered[16]. As for BC_2N nanotubes, although an early study was carried out to investigate its electronic properties[4], there has been no detailed report on size and chirality dependence of their electronic properties. Therefore, it is necessary to investigate the chirality and radius dependence of electronic properties of the armchair and zigzag BC_2N nanotubes on the basis of ab initio method and to explore their applications in nanodevices.

5.2 Calculation Details

We carried out first-principles calculation based on the density functional theory and the generalized gradient approximation as stated in previous chapters. An energy cut-off of 310 eV and 10 k-points along the axis of the tube in the reciprocal space were used in our calculation. Good convergence was obtained with these parameters and the total energy was converged to 2.0×10^{-5} eV/atom. A large supercell dimension in the plane perpendicular to the tube axis was used to avoid interaction between the carbon nanotube and its images in neighboring cells. The unit is periodic in the direction of the tube.

5.3 Geometrical Properties

We start with atomic structures of BC_2N sheets. Using the first-principles total-energy calculations, various possible structures of BC_2N were considered and their total energies were calculated. The results show that the geometry given in Fig. 5.1 which consists of alternating zigzag C and BN lines is the most stable structure. The covalent bond lengths in the fully optimized BC_2N sheet are 1.42 Å for C-C bond, 1.56 Å for C-B bond, 1.43 Å for B-N, and 1.32 Å for C-N, respectively. The calculated band gap is 1.61 eV. These results are in good agreement with those reported in Refs[4,17].

Compared to carbon nanotube, many different nanotubes can be obtained by rolling up a flat BC_2N sheet due to its anisotropic geometry. If we follow the notation of carbon nanotubes and specify the nanotube in terms of the chiral vector (n, m)[14], we can get two kinds of zigzag BC_2N nanotubes by rolling up the BC_2N along a_1 and a_2 directions, respectively, and two kinds of armchair nanotubes by rolling up the BC_2N sheet along R_1 and R_2 directions, respectively (Fig. 5.1), depending on the choice of the basic vectors. In

this study, we focus on these four types of BC_2N nanotubes, and determine the chirality and diameter dependence of their electronic properties. For convenience, we refer the nanotubes obtained by rolling up the BC_2N sheet along direction of $\mathbf{a}_1$, $\mathbf{a}_2$, $\mathbf{R}_1$ and $\mathbf{R}_2$ as ZZ-1, ZZ-2, AC-1 and AC-2, respectively. The corresponding translational lattice vectors along the tube axes are T_{a1}, T_{a2}, T_{R1}, and T_{R2}, respectively, as shown in Fig. 5.1.

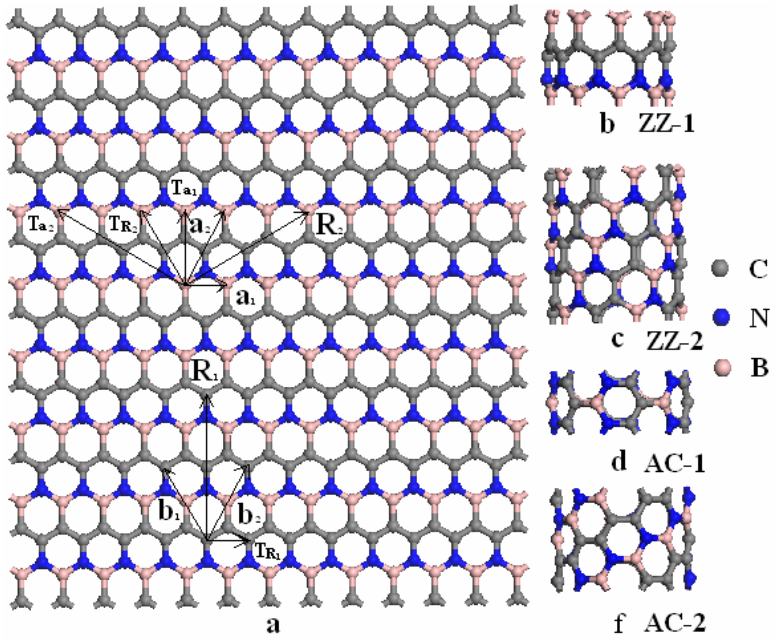

Fig. 5.1. Atomic configuration of a BC_2N sheet. Primitive and translational vectors are indicated.

To systematically study the chiral and diameter dependence of electronic properties of BC_2N nanotubes, ZZ-1 (n, 0) nanotubes with n =5−25, ZZ-2 (0, n) nanotubes with n=2−5, AC-1 (n, n) nanotubes with n=2−5, and AC-2 (n, n) with n=2−5, were considered. The structures of all nanotubes were fully relaxed through minimization of the Hellmann-Feynman forces acting on the atoms to within 0.05 eV/Å. The bond lengths in the optimized BC_2N nanotubes are $d_{C\text{-}C}$=1.42 Å, $d_{C\text{-}B}$=1.51 Å, $d_{C\text{-}N}$ =1.39 Å, and $d_{B\text{-}N}$=1.45 Å, respectively, which deviated slightly from those of the BC_2N sheet.

5.4 Convergence of Total Energy

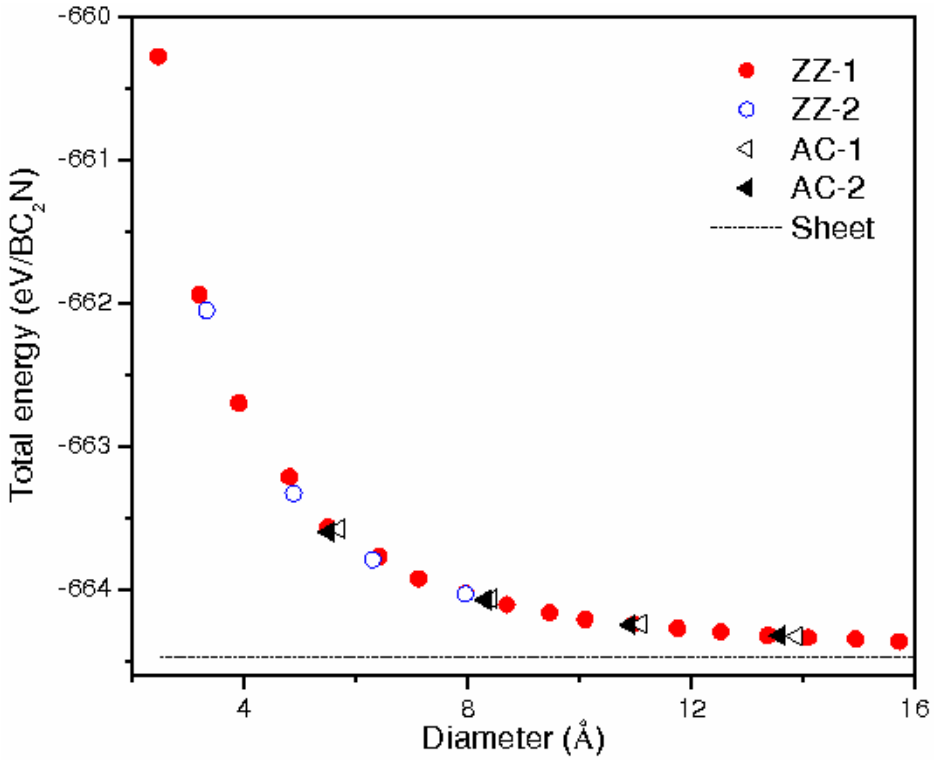

Fig. 5.2, The total energies of BC_2N nanotubes and a BC_2N sheet.

The total energies per BC_2N unit of the optimized BC_2N nanotubes are shown as a function of radius in Fig. 5.2. The energy of the corresponding BC_2N sheet is also shown for comparison. It is noted that the total energies of all four kinds of BC_2N nanotubes converge to that of the BC_2N sheet as the diameter of the tubes increases. Furthermore, the total energies per BC_2N unit of all four types of BC_2N nanotubes are essentially the same. This indicates that the strain energy of a BC_2N nanotube, defined as the energy difference between the BC_2N nanotube and the BC_2N sheet, depends only on its diameter, but not on its chirality, which is similar to the case of BN nanotubes[15]. Therefore, from the energy point of view, all four types of BC_2N nanotubes may be produced experimentally, although it is easier to grow BC_2N nanotubes with larger diameters.

5.5 Electronic Properties

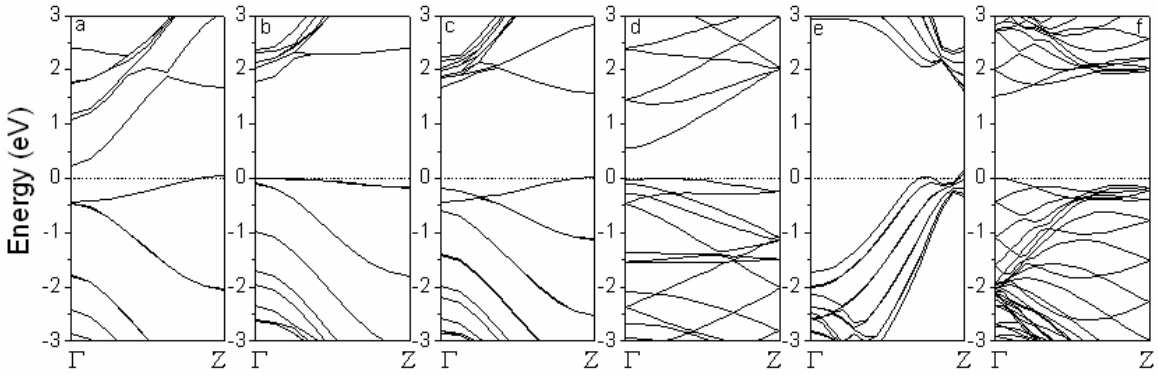

Fig. 5.3. The calculated band structures of (a) ZZ-1 (6, 0), (b) ZZ-1 (9, 0), (c) ZZ-1 (10, 0), (d) ZZ-2 (0, 3), (e) AC-1 (5, 5) and (f) AC-2 (5, 5).

Although the strain energy of the BC_2N nanotubes is independent of the chirality, our calculations show that the electronic properties of the BC_2N nanotubes are closely related to the chirality. Band structure was calculated for each optimized BC_2N nanotube. The calculated band gap energies are listed in Table 1. First of all, all BC_2N nanotubes, except the one with the smallest diameter, ZZ-1 (5, 0), are semiconductors. ZZ-1 (5, 0) is metallic within GGA, possibly due to the curvature effect. For the rest of the ZZ-1 (*n*, 0) nanotubes, their electronic properties depend on both chirality *n* and diameter. Figures 5.3a, 5.3b and 5.3c show three representative band structures of ZZ-1 (*n*, 0) nanotubes near the Fermi level. When *n* is even and greater than 8, both the bottom of the conduction level and the top of the valence level are located at the Brillouin zone boundary (Z). The nanotubes are direct gap semiconductors (see Fig. 5.3c) with a fairly constant energy gap (1.56 eV – 1.61 eV). However, ZZ-1 nanotubes with $n = 6$ or 8 are indirect gap semiconductors, with the bottom of the conduction level located at the Γ point but the top of the valence level at the Z point (Fig. 5.4(a)). For odd but small *n* (between 7 and 13), the ZZ-1 BC_2N nanotubes also show direct gap but both the bottom

of the conduction level and the top of the valence level are located at the Brillouin zone center (Γ). When n=15, the indirect band structure occurs similar to the cases with n=6 and 8. When *n* is greater than 15, the bottom of the conduction band shifts from Γ to Z and the band structures for nanotubes with odd *n* are essentially the same as those with even *n*. It was also found that the band gap of the ZZ-1 (*n*, 0) increases with the increase in the diameter. However, when *n* is large (>8), we observe an interesting oscillatory behavior for the *n*-dependence of the energy gap. The energy gap oscillates depending on whether *n* is even or odd (Fig. 5.4). With further increases in diameter of the tube, the energy gap converges to the value of BC_2N sheet (1.61 eV).

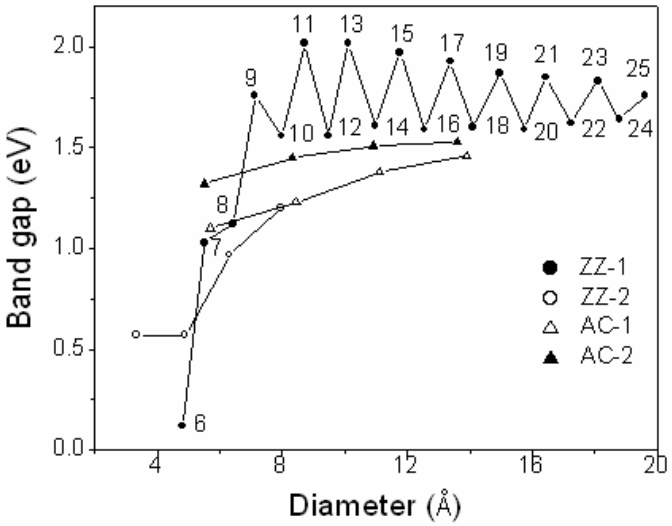

Fig. 5.4, The change of band gap with increase of the diameter.

Electron densities for the top valence band and the bottom conduction band for ZZ-1 (6, 0), ZZ-1 (9, 0) and ZZ-1 (12, 0) are shown in Fig. 5.5. It is clear that the *p* orbitals that are normal to the tube from carbon atom near the boron atom (position 1) contribute to the top valence band, while the *p* orbitals of carbon near nitrogen (position 2) contribute to the bottom conduction band. These *p* orbitals couple with the nearest boron or nitrogen atoms which could be the reason for the indirect band structure. The situation of ZZ-1 (9,

0) is similar. When *n* is even and greater than 8, the top valence band is solely contributed by the *p* orbitals of carbon at position 1 and the bottom conduction band by the *p* orbitals of carbon at position 2. However, the carbon *p* orbitals and nitrogen or boron orbitals are decoupled, as shown in Figs. 5.5e and 5.5f for ZZ-1 (12, 0). Furthermore, when *n* is odd and less than 15, only orbitals of atoms from one side of the nanotube are involved in the top valence band and bottom conduction band, as shown in Figs. 5.5c and 5.5d.

Type	(n, m)	E_g (eV)
ZZ-1	(5, 0)	0 (metallic)
	(6, 0)	0.12 (ind.)
	(7, 0)	1.03 (dir. Γ)
	(8, 0)	1.12 (ind.)
	(9, 0)	1.76 (dir. Γ)
	(10, 0)	1.56 (dir. Z)
	(11, 0)	2.02 (dir. Γ)
	(12, 0)	1.56 (dir. Z)
	(13, 0)	2.02 (dir. Γ)
	(14, 0)	1.61 (dir. Z)
	(15, 0)	1.99 (ind.)
	(16, 0)	1.59 (dir. Z)
	(17, 0)	1.93 (dir. Z)
	(18, 0)	1.60 (ind. Z)
	(19, 0)	1.87 (dir. Z)
	(20, 0)	1.59 (dir. Z)
	(21, 0)	1.86 (dir. Z)
	(23, 0)	1.83 (dir. Z)
	(25, 0)	1.77 (dir. Z)
ZZ-2	(0, 2)	0.57 (ind.)
	(0, 3)	0.57 (ind.)
	(0, 4)	0.97 (dir. Γ)
	(0, 5)	1.20 (dir. Γ)
AC-1	(2, 2)	1.10 (dir. Z)
	(3, 3)	1.23 (dir. Z)
	(4, 4)	1.38 (dir. Z)
	(5, 5)	1.46 (dir. Z)
AC-2	(2, 2)	1.32 (dir. Γ)
	(3, 3)	1.45 (dir. Γ)
	(4, 4)	1.51 (dir. Γ)
	(5, 5)	1.53 (dir. Γ)

Table 5.1, Calculated band gap energies of various BC_2N nanotubes.

When the diameter of the ZZ-2 (0, *n*) tube is small (*n*=2 and 3), the band gap is indirect, with the bottom of the conduction band located at the Γ point and the top of the valence

band at approximately 1/4 away from Γ. Figure 5.3d shows the band structure of ZZ-2 (0, 3). The GGA band gap is around 0.57 eV. As the diameter of the tube becomes larger (n>3), the top of the valence band shifts to the zone center and the energy gap becomes direct. The band gap energy increases with the increase in the diameter of the tube. Similar to the ZZ-1 (n, 0) nanotubes, the *p* orbitals of carbon atoms at position 1 and those at position 2, which are normal to the tube, contribute to the top valence band and the bottom conduction band, respectively. However, for ZZ-2 (0, 5), the top valence band is contributed by the *p* orbitals of carbon atoms (position 1) from one side of the nanotube while the bottom conduction band by those carbon atoms (position 2) from the opposite side of the tube.

All armchair nanotubes were found semiconducting. The gap of the AC-1 nanotubes is a minimum at the zone boundary (Fig. 5.3e), while the gap of the AC-2 nanotubes is the smallest at the zone center (Fig. 5.3f). The energy gap increases with increasing tube diameter and eventually approaches to that of the BC_2N sheet. The smallest AC-2 tube being considered, AC-2 (2, 2), has a band gap energy of 1.32 eV, which is close to the value given in Ref. 4. It is noted that the band gap of AC-2 is slightly lager than that of AC-1 of the same index (n, n), although the tube diameter of AC-1 (n, n) is slightly lager than that of AC-2 (n, n). Again, the *p* orbitals of carbon atoms at position 1 and position 2 contribute to the top valence band and the bottom conduction, respectively.

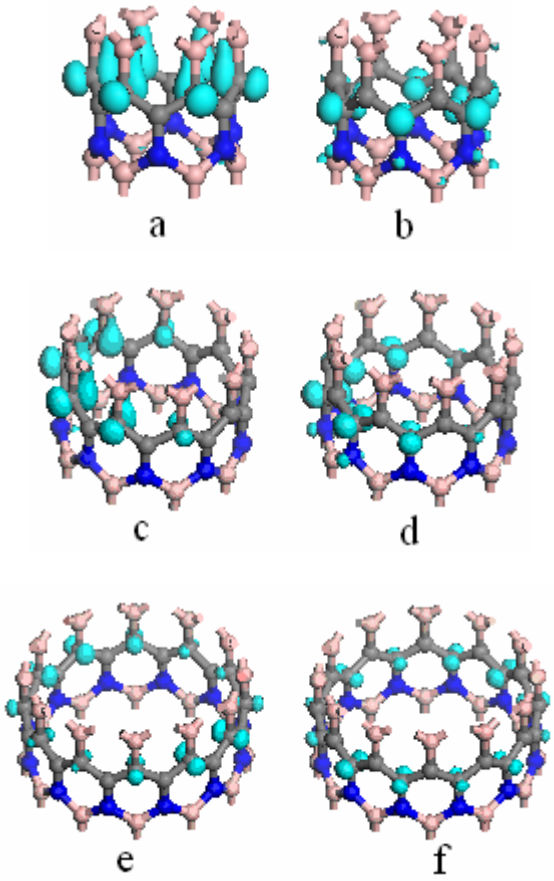

Fig. 5.5, Electron densities of (a) the top valence band and (b) the bottom conduction band of ZZ-1 (6, 0); (c) the top valence band and (d) the bottom conduction band of ZZ-1 (9, 0); (e) the top valence band and (f) the bottom conduction band of ZZ-1 (12, 0).

5.6 Optical Properties

Optical characterization is an important technique to understand the physical properties of nanostructures. It is possible to find a unique mapping to the measured electronic and vibrational properties of the nanotubes onto the index (n, m) and the optical applications. To date, the optical properties of BC_2N nanotubes have not been investigated. Here, the first-principles study on the optical properties of BC_2N nanotubes was carried out. It was pursued to find the relationship between the optical properties (absorption, loss spectra, and reflection) and the geometry (diameter and chirality).

The imaginary part of the dielectric constant was calculated from Eq. (3.1). The real part, $\varepsilon_1(\omega)$, is obtained by the Kramers-Kronig relation, as discussed in section 3.4.

5.6.1 Chirality and Size Dependence of Absorption Spectra

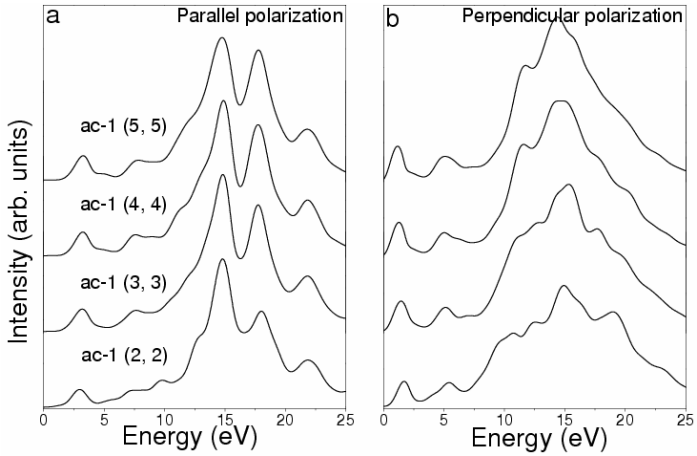

Fig. 5.6, Absorption spectra of AC-1 (n, n): (a) for parallel light polarization and (b) for perpendicular light polarization. The curves are displaced vertically for clarity (also applies to other figures).

Figure 5.6 shows the absorption spectra of AC-1 type BC_2N nanotubes of different diameters. First of all, optical anisotropy can be clearly seen. The absorption spectra under parallel and perpendicular light polarizations show clearly different features. For parallel light polarization, the first peak is at ~3.1 eV (Fig. 2a), which is mainly attributed to the inter-π band transitions. This low-energy absorption peak was not observed in the absorption spectra of boron nitride nanotubes[18], but was present in the absorption spectra of carbon nanotubes[19]. With the increase of the tube diameter (or *n* from 2 to 5), the peak is slightly blue-shifted (from 2.94 eV to 3.31 eV). The π band to π^* band transition at ~7.5 eV is also blue-shifted from 7.11 eV to 7.71 eV when the diameter of the tube increases, *i.e.*, *n* increases from 2 to 5. The peaks above 10.0 eV are enhanced in larger tubes,

especially the peak around 18.0 eV. The position of the peak around 14.8 eV remains the same with the change of tube size. But the peaks around 18.0 eV and 21.8 eV slightly red-shift with the increase of the tube size. The peaks above 10.0 eV are attributed to the inter-σ band transitions. The range of the σ band transition is wider than that of the π band transition. The situation is different for the perpendicular light polarization (Fig. 2b). Here the first absorption peak is around 1.5 eV and it red-shifts from 1.66 eV to 1.16 eV with the increase of the tube diameter (*n* from 2 to 5). There exists another weak peak around 5.2 eV which gains strength and red-shifts with increasing tube diameter. The broad σ band transitions above 10.0 eV red-shift with increasing tube diameter.

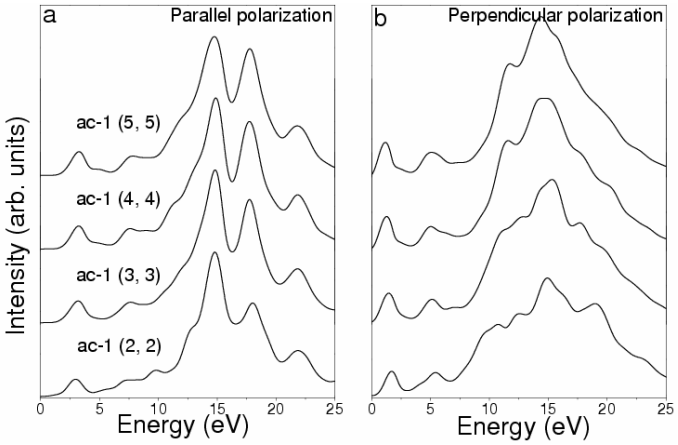

Fig. 5.7, Absorption spectra of AC-2 (m, m): (a) for parallel light polarization and (b) for perpendicular light polarization.

The absorption spectra of the AC-2 type nanotubes are shown in Fig. 5.7. For light polarization parallel to the tube axis, the main absorption peak is located near 14.5 eV (Fig. 5.7a). As the diameter of the tube increases, *i.e.*, *n* increases from 2 to 5, this pronounced σ band absorption peak red-shifts from 14.64 eV to 14.32 eV. There exist other peaks in the low-energy wavelength. The π band transition around 2.3 eV is blue-

shifted, suppressed with increasing tube diameter and almost disappears in AC-2 (5, 5). The π band transition around 5.5 eV red-shifts and gains strength as the diameter of the tube increases. Compared to the AC-1 tube, only one dominant peak for the σ band transition exists in the parallel polarization absorption spectrum of AC-2. In the case of perpendicular light polarization, the main absorption peak is located around 14.6 eV and is slightly red-shifted from 14.69 eV to 14.43 eV when *n* increases from 2 to 5 (Fig. 5.7b). A nearby peak, around 12.5 eV, gains strength and red-shifts from 12.76 eV to 11.94 eV as *n* varies from 2 to 5. The peak around 1.5 eV corresponds to the π band transition. It is slightly red-shifted.

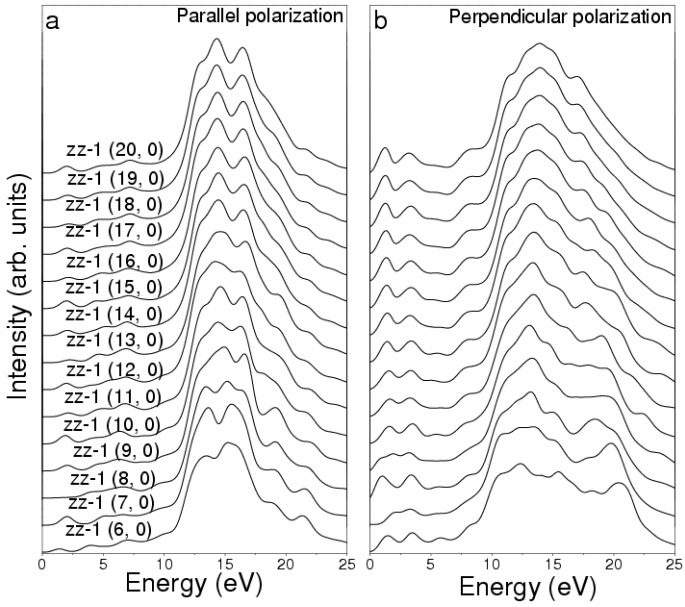

Fig. 5.8, Absorption spectra of ZZ-1 (n, 0): (a) for parallel light polarization and (b) for perpendicular light polarization.

Figure 5.8 shows the absorption spectra of the ZZ-1 type BC_2N nanotubes. For light polarization parallel to the tube axis, the main absorption peaks are within the range of 10.0 eV to 20.0 eV, corresponding to σ band transitions. Two of the peaks are prominent and shift in opposite directions with increasing tube size. The peak around 14.5 eV red-

shifts from 14.83 eV to 14.25 eV when *n* increases from 12 to 20. The peak around 16.5 eV blue-shifts from 16.35 eV to 16.55 eV when *n* increases from 13 to 20 (Fig. 5.8a). The shoulder-like structures on both sides of the above peaks suggest existence of two weak peaks, the one at higher energy red-shifts and is suppressed, but the one at lower energy essentially remains where it is as the size of the tube increases. Absorption peaks are also observed in the low energy range. The peak around 2.0 eV remains at the same energy, but the peak at 7.0 eV is blue-shift from 6.32 eV to 7.24 eV with *n* increasing from 8 to 20. Several absorption peaks are observed in the case of perpendicular light polarization. The first absorption peak red-shifts from 1.53 eV to 1.18 eV with *n* increasing from 10 to 20 (Fig. 5.8b). The peak around 3.3 eV red-shifts slightly and becomes more intense with the increase of the tube size. The σ band transitions above 9.7 eV blue-shift to certain degrees, and one of them vanishes gradually with increasing tube diameter.

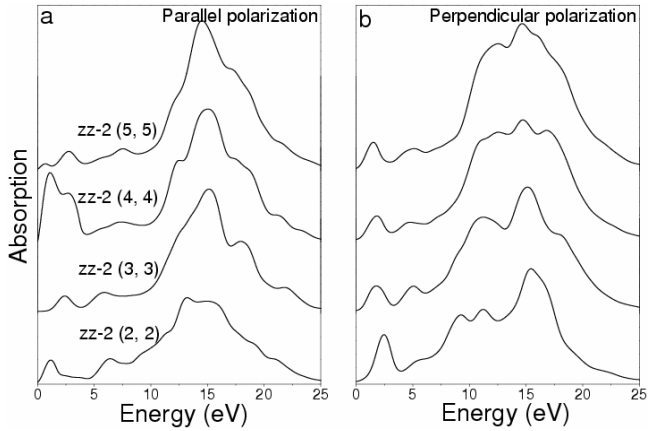

Fig. 5.9, Absorption spectra of ZZ-2 (0, m): (a) for parallel light polarization and (b) for perpendicular light polarization.

For the ZZ-2 type BC_2N nanotubes (Fig. 5.9), the pronounced absorption corresponding to the σ band transitions is broad and centers around 15.0 eV, which red-shifts from 15.56 eV to 14.58 eV as the diameter of the tube increases in the case of parallel light

polarization (Fig. 5.9a). The π band transition below 5.0 eV for ZZ-2 (4, 4) is broad and different from that of ZZ-2 (*n*, *n*) (*n*≠4). For light polarization perpendicular to the tube axis, the σ band transitions center around 15.0 eV, which red-shifts from 15.44 eV to 14.71 eV as the diameter of the tube increases in the case of parallel light polarization (Fig. 5.9b). The first π band transition around 2.0 eV red-shifts from 2.45 eV to 1.47 eV as the tube diameter increases. No noticeable shift was found for the second π band transition around 5.0 eV.

The absorption spectra of the four series of BC_2N nanotubes given above show clear optical anisotropy with respect to light polarization. This can be attributed to the local field effect due to depolarization. It is also shown that the absorption spectra are chirality and size dependent. For a given chirality, red- or blue-shift in the position of the absorption peak is possible with increase in the tube diameter, which is due to the competition between the size effect and π orbitals overlapping[20]. The optical gap will eventually saturate when the tube diameter reaches a certain value, due to the reduction of curvature induced hybridization effect[21]. It is noted that the first absorption peak, which should corresponds to the optical gap, is above 2.5 eV and is larger than the calculated energy gap (about 1.6 eV).

5.6.2 Chirality and Size Dependence of Loss Function

The loss function is a direct probe of collective excitation of the system under consideration. We have calculated the loss functions of the BC_2N nanotubes using $\mathrm{Im}(-1/\varepsilon(\omega))$ at zero momentum transfer from the macroscopic dielectric function

$\varepsilon(\omega) = \varepsilon_1(\omega) + i\varepsilon_2(\omega)$. The calculated loss functions of the AC-1 type BC_2N nanotubes are shown in Fig. 5.10. Several peaks are observed, which are related to the 1D subbands with divergent density of states. Under parallel light polarization, the first peak in the loss function is around 3.5 eV (Fig. 5.10a), which can be attributed to the inter-π transition. The peak blue-shifts from 3.25 eV to 3.64 eV with the increase of the tube diameter. Another peak is located around 7.5 eV which is contributed to the collective excitation π electrons and becomes apparent with increasing tube diameter. Three peaks above 12.0 eV are contributed to π+σ plasmon[22]. And the peak at 18.6 eV gains strength with the increase of the tube size. In the case of perpendicular polarization, the main peak is around 2.0 eV which is attributed to the inter-band transition[23] and shifts from 2.12 eV to 1.72 eV as the tube diameter increases (Fig.5.10b). The peak around 5.3 eV is due to the collective excitation of π electrons. Peaks are also observed above 10.0 eV, which are attributed to the higher-frequency π+σ plasmon[22]. Generally, the higher-frequency π+σ plasmon is stronger that the collective excitation π electrons because the density of π+σ electrons is larger than that of π electrons.

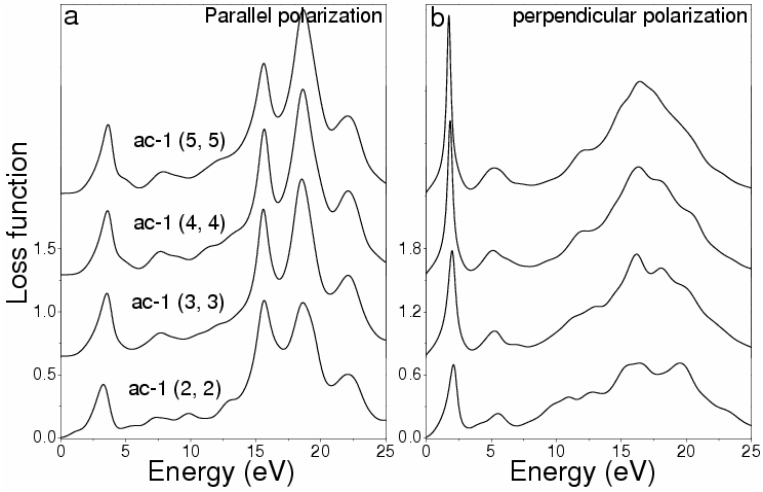

Fig. 5.10, Loss functions of AC-1 (n, n): (a) for parallel light polarization and (b) for perpendicular light polarization.

Figure 5.11 shows the loss functions of the AC-2 type BC_2N nanotubes under different polarizations. In the case of parallel polarization, the inter-π transition red-shifts slightly from 2.38 eV to 2.27 eV with the strength suppressed as the diameter of the tube increases (Fig. 5.11a). The collective excitation of π electrons around 5.8 eV remains there and gains strength as the diameter of the tube increases. High-frequency π+σ plasma is in the range of 12.0 eV to 22.0 eV and its peak slightly blue-shifts as the diameter of the tube increases. For perpendicular polarization, the weak π plasma excitation occurs around 7.5 eV (Fig. 5.11b). The inter-band transition peak located around 2.0 eV shifts from 2.18 eV to 1.85 eV with the incrase of the tube diameter. High-frequency π+σ plasma with broad band excitation are also observed above 10.0 eV.

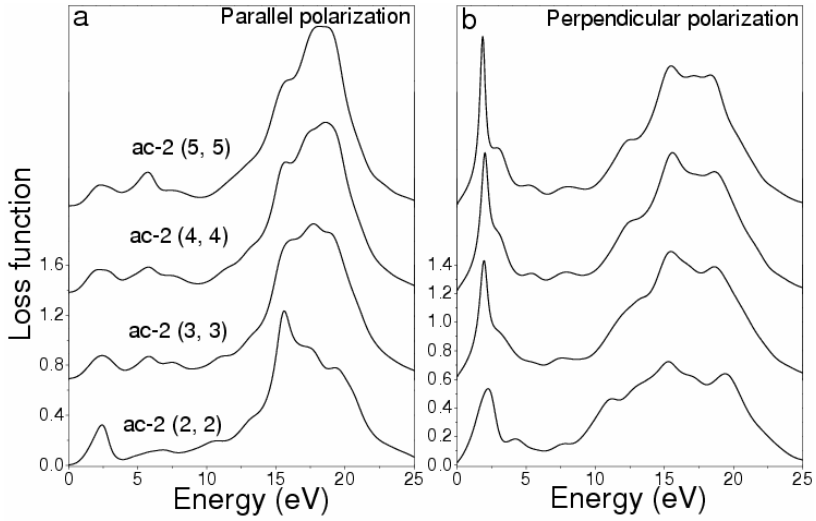

Fig. 5.11, Loss functions of AC-2 (m, m): (a) for parallel light polarization and (b) for perpendicular light polarization.

The loss functions of the ZZ-1 type BC_2N nanotubes under parallel light polarization are showed in Fig. 5.12a. The inter-π transition red-shifts slightly from 2.28 eV to 2.17 eV as *n* increases from 7 to 20. The weak collective excitation of π electrons is located around 7.1 eV and blue-shifts slightly as the diameter of the tube increases. High-frequency π+σ

plasma is in the range of 12.0 eV to 22.0 eV and its peak slightly blue-shifts as the diameter of the tube increases. For perpendicular polarization, the weak π plasma excitation occurs around 8.2 eV (Fig. 5.12b). The inter-band transition peaks located within the range of 0 eV to 5 eV. The lower-energy inter-band transition around 1.7 eV gains strength with the increase of the tube diameter. High-frequency π+σ plasma with broad band excitation are also observed above 10.0 eV. Two excitation peaks remain prominent as the diameter increases.

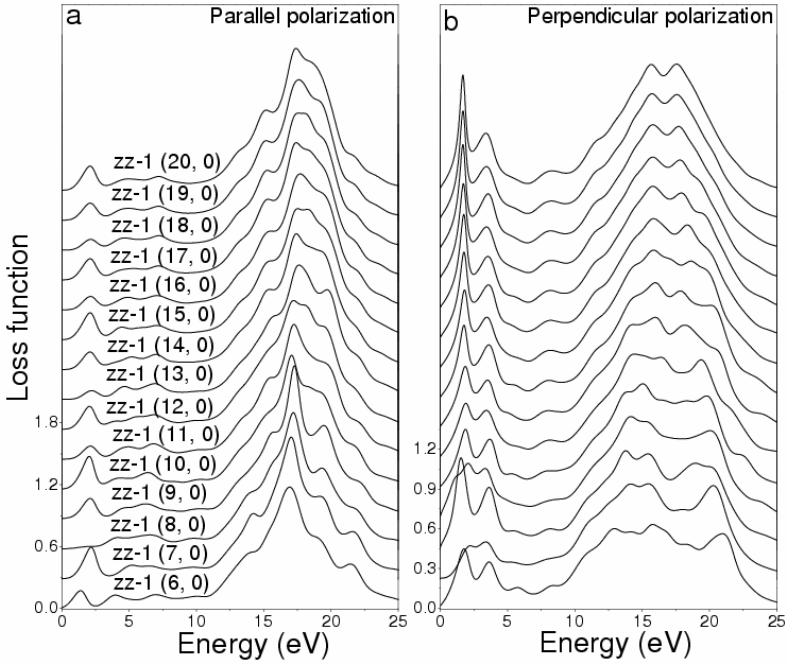

Fig. 5.12, Loss functions of ZZ-1 (n, 0): (a) for parallel light polarization and (b) for perpendicular light polarization.

The loss functions of the ZZ-2 type BC_2N nanotubes are shown in Fig. 5.13. For parallel polarization, the π+σ plasma is in the range of 12.0 ~ 20.0 eV and blue-shift with the increase in the diameter of the tube (Fig. 5.13a). The inter-π-band transition around 3.7 eV is very strong for zz-2 (4, 4). The weak π plasma around 7.0 eV blue-shifts as the tube diameter increases. Under perpendicular polarization, the the π+σ plasma is within 9.0 ~

20.0 eV (Fig. 5.13b) and blue-shifts as the tube diameter increases. The inter-π-band transition around 2.0 eV red-shifts from 3.06 eV to 1.89 eV as the tube diameter increases. The π plasma around 5.0 eV red-shifts slightly as the tube diameter increases.

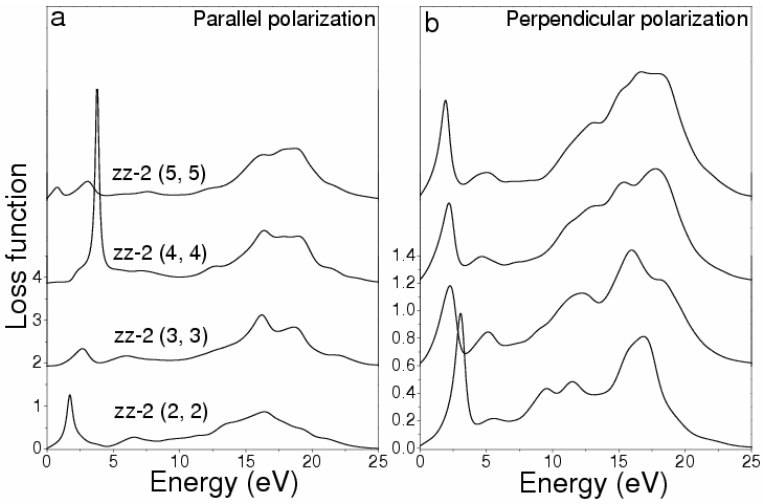

Fig. 5.13, Loss functions of ZZ-2 (0, n): (a) for parallel light polarization and (b) for perpendicular light polarization.

From the above, we can see that the loss functions of the BC_2N nanotubes have anisotropy in the plasma excitation with different light polarizations. Generally, the inter-π-band excitation energy is less than 5.0 eV. The π plasmon excitation energy is within the range of 5.0 eV to 9.0 eV. The high-frequency π+σ plasmon is observable above 10.0 eV. The intensity of π plasma is much weaker than that of π+σ plasma because the density of π+σ electrons is larger than that of π electrons. The peaks shift slightly with the increase of the tube diameter.

5.8 Summary

To summarize, we systematically investigated the structural, electronic, and optical properties of BC_2N nanotubes using first-principles method.

It was found that the strain energy of the BC_2N nanotubes depends only on the diameter of the tube. But the electronic properties of the BC_2N nanotubes are closely related to both diameter and charility. Generally, most of BC_2N nanotubes, except a few with very small diameter, are direct band gap semiconductors although there is difference in details. The band gap can be tuned by varying the diameter of the nanotubes and chirality. The band gap of ZZ-1 (n,0) type nanotubes show an interesting oscillatory behaviour as the diameter of the nanotube increases. The valence band top and conduction band bottom consist of mainly *p* orbitals of carbon atoms.

It was found that the absorption spectra and loss functions of the BC_2N nanotubes are closely related to their diameter and charility. Optical anisotropy is observed for different light polarizations. The absorption spectra indicate that the optical gap can redshift or blueshift with the increase in the tube diameter, depending on the charility. The observation of low-energy absorption in BC_2N nanotubes indicate that BC_2N nanotubes have similar optical properties as carbon nanotubes to some extent due to their similar π bonding consisting of carbon *p* orbitals. The pronounced peaks in the loss function spectra are mainly induced by the collective excitation of π electrons below 10.0 eV and the high-frequency $\pi+\sigma$ plasmon above 10.0 eV. The collective excitation of π electrons is much weaker than that of the high-frequency $\pi+\sigma$ plasmon. It is noted that due to the well know fact that DFT/GGA underestimates band gap of semiconductors, a systematic shift for the peak positions may be necessary in the calculated optical spectra. However, the dependence of the optical properties of BC_2N naotubes on their size and charility are valid.

The *ab initio* studies on carbon nanoscrolls, functionalized carbon nanotubes, and boron carbonitride nanotubes have indicated that the method is efficient in the research of nanostructures. In next chapter, a combined calculation and experiment method will be used to study the carbon doped ZnO.

References:

[1] S. Iijima, Nature 354, 56 (1991).
[2] A. Rubio, J. L. Corkill, and M. L. Cohen, Phys. Rev. B 49, 5081 (1994).
[3] Y. Miyamoto, A. Rubio, S. G. Louie, and M. L. Cohen, Phys. Rev. B 50, 18 360 (1994).
[4] Y. Miyamoto, A. Rubio, M. L. Cohen, and S. G. Louie, Phys. Rev. B 50, 4976 (1994).
[5] Y. Miyamoto, M. L. Cohen, and S. G. Louie, Solid State Commun. 102, 605 (1997).
[6] M. Zhao, Y. Xia, D. Zhang, and L. Mei, Phys. Rev. B 68, 235415 (2003).
[7] G. Chopra, R. J. Luyken, K. Cherrey, V. H. Crespi, M. L. Cohen, S. G. Louie, and A. Zettl, Science 269, 966 (1995).
[8] A. Loiseau, F. Willaime, N. Demoncy, G. Hug, and H. Pascard, Phys. Rev. Lett. 76, 4737 (1996).
[9] Z. Weng-Sieh, K. Cherrey, N. G. Chopra, X. Blase, Y. Miyamoto, A. Rubio, M. L. Chen, S. G. Louie, A. Zettl, and R. Gronsky, Phys. Rev. B 51, 11 229 (1995).
[10] K. Suenaga, C. Colliex, N. Demoncy, A. Loiseau, H. Pascard, and F. Willaime, Science 278, 653 (1997).
[11] Q. Wu, Z. Hu, X. Wang, Y. Lu, X. Chen, H. Xu and Y. Chen, J. Am. Chem. Soc. 125, 10176(2003).
[12] N. Hamada, S. Sawada, and A. Oshiyama, Phys. Rev. Lett. 68, 1579 (1992).
[13] M. S. Dresselhaus, G. Dresselhaus, and R. Saito, Solid State Commun, 84, 201 (1992).
[14] M. S. Dresselhaus, G. Dresslhaus, and P. C. Eklund, Science of fullerenes and Carbon nanotubes (Acadamic Press, San Diego, 1996), p804.
[15] H. J. Xiang, J. Yang, J. G. Hou, and Q. Zhu, Phys. Rev. B 68, 035427 (2003).
[16] E. Hernández, C. Goze, P. Bernier, and A. Rubio, Phys. Rev. Lett. 80, 4502 (1998).
[17] A. Y. Liu, R. M. Wentzcovitch, and M. L. Cohen, Phys. Rev. 39, 1760 (1989).
[18] M-F. Ng and R. Q. Zhang, Phys. Rev. B 69, 115417 (2004).
[19]M. F. Lin, Phys. Rev. B 62, 13153 (2000).
[20] W. Z. Liang, X. J. Wang, S. Yokojima, and G. H. Chen, J. Am. Chem. Soc. 122, 11129 (2000).
[21] A. Zunger, A. Katzir, and A. Halperin, Phys. Rev. B 13, 5560 (1974).
[22] A. G. Marinopoulos, L. Reining, A. Rubio, and N. Vast, Phys. Rev. Lett. 91, 046402 (2003).
[23] M. F. Lin, F. L. Shyu, and R. B. Chen, Phys. Rev. B 61, 14114 (2000).

CHAPTER 6

CARBON DOPED ZnO

6.1 Introduction

Diluted magnetic semiconductors (DMS) have attracted intense interest, because it brings the possibility of devices which combine information processing and storage functionalities in one material[1,2]. Alternatively, control of spin state of carriers may be realized by injecting spin-polarized current into semiconductors, which can be useful for carrying out quantum bit (qubit) operations required for quantum computing[3]. To date, most of the attention on DMS has been focused on doping semiconductors such as GaAs, GaN and InAs with magnetic element such as Mn[4,5]. As a wide and direct band gap semiconductor (3.37 eV at room temperature) with large exciton binding energy (60 meV), ZnO has been widely used in low-voltage and short-wavelength electronic and photonic devices[6]. Recently, it was demonstrated that ZnO can be a high-Curie-temperature magnetic semiconductor when doped with Ni, Sc, Ti, V, Fe, or Co[7,8,9]. For II-VI semiconductors, the valence of the cations matches that of the common magnetic ions which makes it more difficult to dope such materials to create *p*- and *n*-type devices. In this case, it may be useful to go beyond magnetic elements and to consider unconventional doping elements. Since the discovery of carbon nanotubes[10], carbon has shown to be an amazing material and it has various interesting properties. For example, all-carbon system consisting of polymerized C_{60} shows weak ferromagnetism at room-temperature[11]. Carbon adatom and carbon vacancy in graphite sheet and carbon nanotube, and carbon doping of graphitic-BN sheet and BN nanotube all result in magnetization[12,13]. Even though integrating these nanostructures into devices still remains a challenge, the

magnetism in these systems motivated us to consider C-doping of ZnO as a possible way of producing magnetic semicondutors which may find applications in spintronics, spin-field effect transistors (FETs), and spin-light emitting diodes (LEDs). In this chapter theoretical calculation and experimental results on the C-doped ZnO are briefly summarized. Theoretical calculations indicate that magnetic property can result from the carbon substitution at anion sites in ZnO. Indeed C-doped ZnO prepared by pulse laser deposition was shown to possess magnetic property with Curie temperature of ~673 K. XPS analysis has confirmed the carbon substitution in ZnO anion lattice sites. These excellent agreements between the theoretical prediction and experimental confirmation show the success and power of combining theoretical and experimental studies.

6.2 Calculation Details

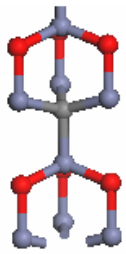

Fig. 6.1 Local structures for carbon substitution at O site.

First-principles method based on DFT and the local spin density approximation (LSDA) was used in our theoretical investigation of carbon doping of ZnO, as described in chapter 2. The system was modeled with a periodic supercell of 9.787×9.787×10.411 $Å^3$ with 18 formula units of wurzite ZnO, which is sufficient to avoid interaction of C atom with its images in neighboring supercells. An energy cut-off of 380 eV was used for the plane wave expansion of the electronic wave function. Special k points were generated with a

5×5×5 grid based on Monkhorst-Pack scheme. Three types of carbon doping, including carbon interstitial (C_I), carbon substitution at Zn site (C_{Zn}) and carbon substitution at oxygen site (C_O), were considered. The local structures for the carbon substitution at O site cases were shown in Fig. 6.1.

6.3 Calculation Results and Discussion

The four-atom wurzite unit cell of ZnO was optimized first. The lattice constants of the optimized structure (a=3.25 Å, c=5.20 Å) within LSDA are in good agreement with the experiment values (a=3.25 Å, c=5.21 Å)[14]. The calculated band gap is 1.13 eV within LSDA, which is consistent with the results of other previous studies[15,16].

6.3.1 System Energy and Defect Stability

Formation energy (E_d) is calculated using the following equation:

$$E_d = E(b+C) - E(b) - E(C) \text{ or } E_d = E(b+C) - E(b) - E(C) - E(S) \quad (6.1)$$

where E(b) is the total energy of bulk ZnO, E(C) the energy of one carbon atom, E(S) the energy of one oxygen/zine atom and E(b+C) is the total energy of doped ZnO.

The calculated formation energies are 3.121, 3.502 and 10.305 eV for ZnO-C_I, ZnO-C_O and ZnO-C_{Zn}, respectively. In the view of energy, ZnO-C_I and ZnO-C_O are energetically more stable and hence easier to be produced experimentally.

6.3.2 Magnetic Properties

The calculations indicated that only C substitution at O site in ZnO show magnetic. Figure 6.2 shows the calculated band structure of ZnO with C substituted O (ZnO-C_O).

An important feature of the band structure is the occurrence of nearly flat bands over the whole Brillouin zone near the Fermi level. These bands are attributed to the carbon. The corresponding charges are highly localized. Importantly, Fermi level in the spin-down band structure is within the impurity bands. Therefore, charge carriers within the impurity bands are sufficiently mobile. The introduction of C did not spin-polarize the valence band noticeably, but caused a non-negligible spin polarization of the conduction band. Figure 6.3 shows the calculated densities of states, which further indicates the magnetic property of the system. Spin-up defect levels are fully occupied. Spin-down defect levels are partially occupied. The calculated local magnetic moment of C is 1.26 μ_B while those on the neighboring O and Zn atoms are 0.48 and 0.12 μ_B, respectively. All moments are positive.

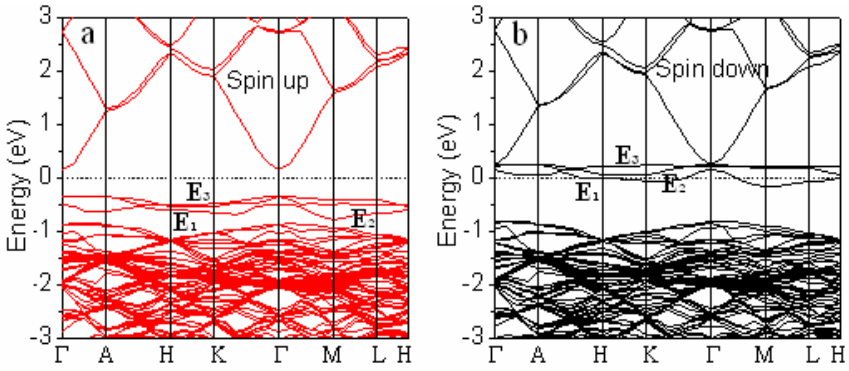

Fig. 6.2, Calculated band structure of ZnO-C_O. The dotted line is the Fermi level.

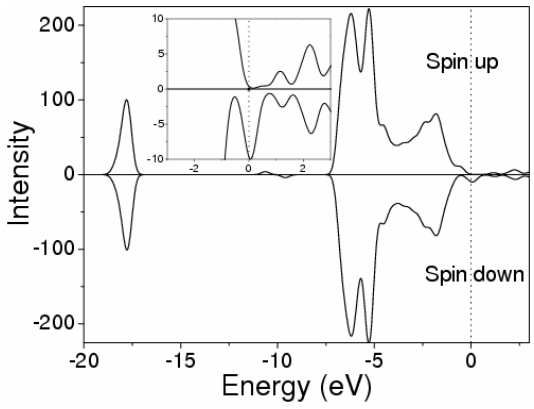

Fig. 6.3, Majority and minority spin DOS of ZnO-C_O. The dotted line is the Fermi level.

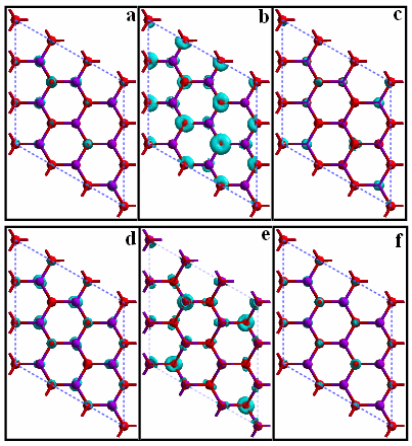

Fig. 6.4, Electron densities of orbitals for ZnO-C_O: (a)-(c) corresponding to energy levels E1-E3 for spin up, respectively; (e)-(f) corresponding to energy levels E1-E3 for spin down, respectively.

It is noticed that the local magnetic moment of an element is determined by two factors: (a) the occupation of the corresponding spin-up and spin-down bands and (b) the hybridization of the states with other occupied and unoccupied states[17]. Carbon and Zinc are diamagnetic elements, while oxygen is paramagnetic. For spin-up of ZnO-C_O, three orbital levels below Fermi level are mainly contributed to the p orbitals of carbon or oxygen atoms (Figs. 6.4a-c). For spin-down states of ZnO-C_O, the three levels above the Fermi level are mainly contributed to the p orbitals of oxygen atoms (Figs. 6.4d-f). It is interesting to note that the carbon doping can produce electrons which could be bound impurity states in the close proximity of the C impurity. And, the local magnetic moment is induced by the local impurity potential, which is large enough to strongly bind the charge to nearest neighbor atoms[18].

6.4 Experimental Details

The C-doped ZnO sample was prepared by conventional pulsed-laser deposition (PLD) in a high vacuum chamber with base pressure better than $1x10^{-8}$ torr. The C-ZnO films were

deposited on sapphire (100) substrate using a KrF excimer laser operating at 248 nm and a fluence of 1.8 J cm^{-2}. The ZnO/C targets were prepared by sintering mixed ZnO and carbon powders in nitrogen atmosphere at 1273 K at molar ratio of 1%. No ferromagnetism could be found in the high purity powders of ZnO and carbon as measured by superconducting quantum interference devices (SQUID, MPMS XL, Quantum Design, USA). The films were deposited at 673 K and 10^{-3} torr O_2 pressure. The thickness of the ZnO films was measured by a profilometer (P-12, Tencor Instruments, USA). X-ray diffractometry (XRD, Bruker, D8 Advance, USA), Atomic Force Microscope (AFM), Secondary Ion Mass Spectrometry (SIMS), Raman spectrometry (LabRam HR800, Jobin Yvon Horiba Inc. USA), Transmission electron microscopy (TEM, JEOL, JEM3010) and SQUID were used to study these films.

6.5 Experimental Results

6.5.1 Characterization of C-doped ZnO

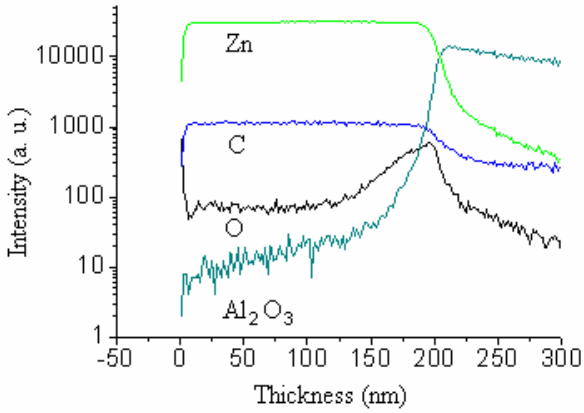

Fig. 6.5, SIMS result of ZnO doped with 1 at% carbon.

SIMS study shows that Zn and O are uniformly distributed in the film (Fig. 6.5). XPS results are shown in Fig. 6.6. The C1s spectrum of the pristine ZnO film is characteristic

of carbon contaminations on the ZnO surface, including adventitious carbon at 284.6 eV, and trace of carbonylic and carboxylic species at 286.5 and 288 eV binding energy. After the carbon doping, new carbon species with C1s binding energy between 280 and 284 eV is observed suggesting that the doped carbon may exist in a carbide state [19,20] The carbide state of carbon is due to the replacement of carbon to oxygen in the ZnO lattice, which is consistent with the first-principles calculations. Zn2p peak displays little change (spectrum not shown). But O1s peak shows a strong shoulder at higher binding energy side between 531 and 533 eV. This appears to indicate that some oxygen ions may be squeezed by doped carbon and further away from the Zn sites.

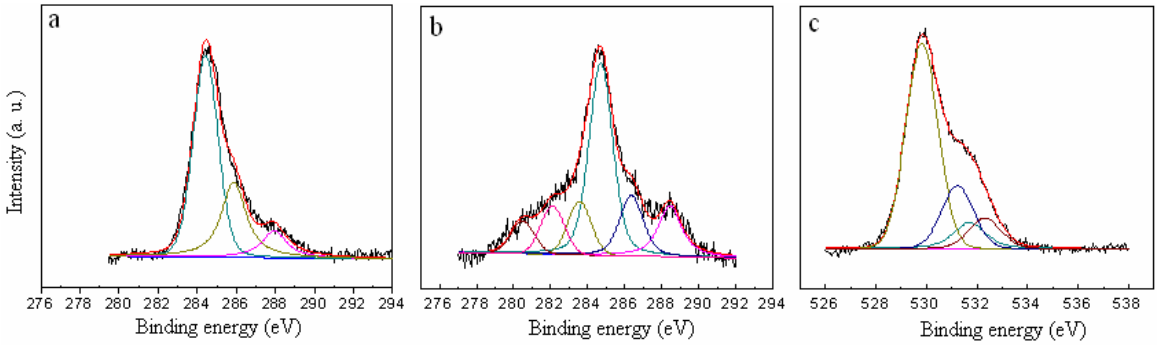

Fig. 6.6, XPS spectra of (a) carbon in ZnO without doping, (b) carbon in ZnO doped with 1% carbon, and (c) oxygen in ZnO doped with 1% carbon.

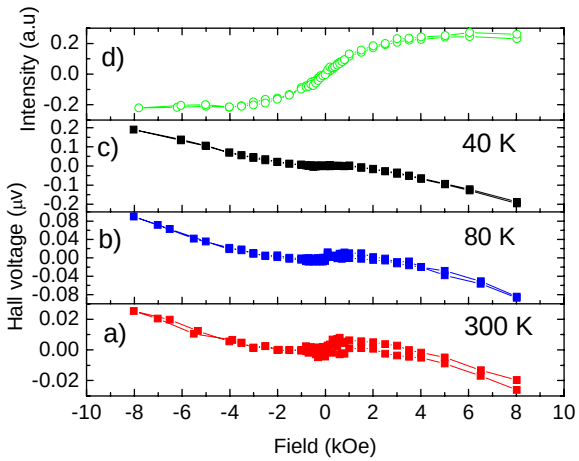

Fig. 6.7, Hall effect at different temperature of 1% C doped ZnO, a) 300 K; b) 80 K; c) 40 K; d) Hall effect of c) after deduction of abnormal part.

Figure 6.7 shows the abnormal Hall effect full loops of 1%C doped ZnO at different temperature. The curves indicate that the films are n-type semiconductor from the normal Hall effect part, which is consistent with our calculations. The Hall voltage strongly increases with the decreasing of temperature. This is because when the temperature decreases, the carrier density n decreases and the ordinary Hall voltage dominated. Hence, the Hall voltage will strongly increase.

6.5.2 Feromagnetism in C-doped ZnO

Pristine ZnO film without C doping showed no feremagnetism. But the C-doped ZnO showed ferromagnetism at room temperature. The hysteresis loop of 1%C-ZnO at room temperature is shown in Fig. 6.7. The loop at 5 K has the similar shape to that taken at 300 K except with a larger magnetization and coercivity (60 Oe). The loops are performed with Brillouin type magnetization. The magnetization of the film has a strong temperature dependence (the inset of Fig. 6.10). This is different from other DMSs [21,22], in which the magnetization is contributed by the defects and remains almost constant in the whole temperature range. The magnetization at 400 K is approximately 3.4 emu/cm^3, indicating that the Curie temperature of the film is higher than 400 K. The Curie temperature cannot be directly determined due to the instrument limitation. However, by fitting the magnetization-temperature curve (see the inset of Fig. 6.7) with Bloch law. $1-\frac{M_a}{M_{(0)}}=BT^{\frac{3}{2}}$, where M_a is the magnetization at different temperature. $M_{(0)}$ is the saturation magnetization of the film, B is the constant, and T is the temperature, we can obtain B=5.73×10-5; $M_{(0)}$=7.26 emu/cm^3. The Curie temperature of the film is estimated to be approximately 673 K.

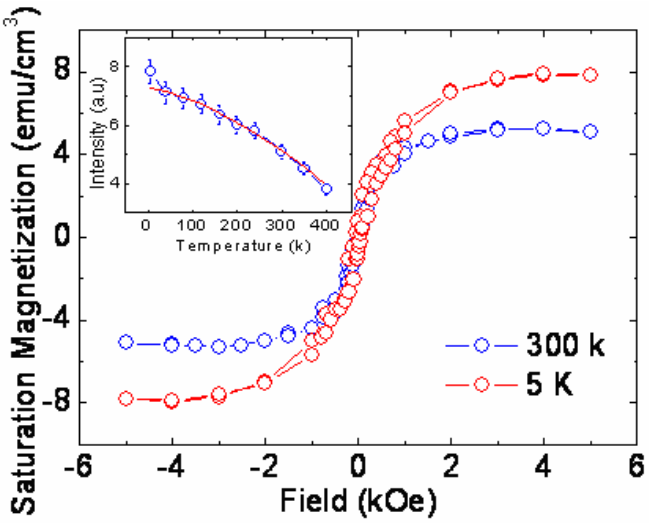

Fig. 6.8, Hysteresis loop of ZnO+1%C at 5 K and 300 K. The inset is the magnetization dependence on temperature, which can be fitted with Block law $(1-M/M_a)=BT^{3/2}$.

6.6 Summary

In summary, the magnetic property of C-doped ZnO was investigated by the combined calculation and experiment method. The calculations indicated that the carbon doping in ZnO, such as substituted oxygen, can confine the compensating charges in the molecular orbitals formed by carbon or oxygen orbitals on the nearest neighbors. The local magnetic moment under certain conditions can be formed due to the coupling between the impurity potential and the charges on the nearest neighbors. The experiment demonstrated that ferromagnetism does exist in the C-doped ZnO. The C-doped ZnO film showed room temperature ferromagnetism. This is the first non-metal doped DMS. Its high currie temperature (>400K) makes a potentially useful material for spintonics devices.

Our *ab initio* studies on nanotubes and C-doped ZnO, has indicated that the method is efficient in the research of nanostructures. These calculations demonstrated that *ab initio* method is a reliable simulation tool to study such structures with reasonable

computational resources. However, from the experimental point of view, the fundamental problem in nanoscale technology is how to produce high quantity nanostuctures for the study on physical properties and how to assembly these nanostructures together for their applications in devices. Two methods, template-synthesis and thermal evaporation, will be discussed in next chapters for these purposes.

References:

[1] H. Ohno, Science 281, 951 (1998).
[2] F. Matsukura, H. Ohno, A. Shen, Y. Sugamara, Phys. Rev. B 57, R2037 (1998).
[3] D. P. DiVincenzo, Science 270, 255 (1995).
[4] H. Akai, Phys. Rev. Lett. 63, 1849 (1998).
[5] M. J. Reed, F. E. Arkun, E. A. Berkman, and N. A. Elmasry, J. Zavada, M. O. Luen, M. L. Reed, and S. M. Bedair, Appl. Phys. Lett. 86, 102504 (2005).
[6] D. M. Bagnall, Y.F. Chen, Z. Zhu, T. Yao, S. Koyama, M. Y. Shen, and T. Goto, Appl. Phys. Lett. 70, 2230 (1997).
[7] D. A. Schwartz, K. R. Kittilstved, and D. R. Gamelin, Appl. Phys. Lett. 85, 1395 (2004).
[8] K. R. Kittilstevd, N. S. Norberg, and D. R. Gamelin, Phys. Rev. Lett. 94, 147209 (2005).
[9] M. H. F. Sluiter, Y. Kawazoe, P. Sharma, A. Inoue, A. R. Raju, C. Rout, and U. V. Waghmare, Phys. Rev. Lett. 94, 187204 (2005).
[10] S. Iijima, Nature 354, 56 (1991).
[11] T. L. Makarova, B. Sundqvist, R. Höhne, P. Esquinazi, Y. Kopelevich, P. Scharff, V.A. Davydov, L. S. Kashevarova, and A. V. Rakhmanina, Nature 413, 716 (2001).
[12] P. O. Lehtinen, A. S. Foster, A. Ayuela, A. Krasheninnikov, K. Nordlund and R. M. Nieminen, Phys. Rev. Lett. 91, 017202 (2004).
[13] R. Q. Wu, L. Liu, G. W. Peng, and Y. P. Feng, Appl. Phys. Lett. 86, 122510 (2005).
[14] O. Madelung, M. Schulz, and H. Weiss, Numerical Data and Functional Relationships in Science and Technology, (Springer-Verlag, Berlin, 1982), Vol. 17.
[15] A. F. Kohan, G. Ceder, D. Morgan, and Chris G. Van de Walle, Phys. Rev. B, 62, 15019 (2000).
[16] Y. N. Xu and W. Y. Ching, Phys. Rev. B 48, 4335(1993).
[17] S. H. Wei, X. G. Gong, G. M. Dapain, and S. H. Wei, Phys. Rev. B 71, 144409 (2005).
[18] I. S. Elfimov, S. Yunoki, and G. A. Sawatzky, Phys. Rev. Lett. 89, 216403 (2002).
[19] L. Ramqvist, K. Hamrin, G. Johansson, A. Fahlman, and C. Nordling, J. Phys. Chem. Solids 30, 1835, (1969).
[20] A. A. Galuska, J. C. Uht, and N. Marquez, J. Vac. Sci. Technol. A 6, 110 (1988).
[21] J. M. D. Coey, M. Venkatesan, P. Stamenov, C. B. Fitzgerald, and L. S. Dorneles, Phys. Rev. B **72**, 024450 (2005).
[22] M. Venkatesan, C. B. Fitzgerald, and J. M. D. Coey, Nature, 430, 630 (2004).

CHAPTER 7

POROUS ANODIC ALUMINUM OXIDE (AAO) — AN IDEAL TEMPLATE FOR THE SYNTHESIS OF NANOSTRUCTURES

7.1 Introduction

An important issue in the study and application of nanostructures is how to assemble individual atoms into a unique 1D nanostructure in an effective and controllable way. A general requirement for any successful preparative methodology is to be able to achieve nanometer scale control in diameter during anisotropic crystal growth while maintaining a good overall crystallinity. During the past decades, many methodologies have been developed to synthesize one-dimensional nanostructures[1,2,3,4,5,6,7,8]. Overall, they can be categorized into two major categories based on the reaction media used during the preparation: solution-based approaches and gas-phase growth methods.

7.1.1 Solution-Based Approaches

Solution-based approaches include solution-liquid-solid (SLS) method, solvothermal chemical synthesis, and template-directed synthesis. Highly crystalline semiconductor nanostructures, such as InP, InAs, and GaAs, have been obtained on the basis of SLS mechanism at low temperatures[7]. This approach uses simple, low-temperature (less than or equal to 200 ^{o}C) solution phase reactions. The materials are produced as fibers or whiskers having widths of 10 to 150 nanometers and lengths of up to several micrometers. The processes are analogous to vapor-liquid-solid (VLS) growth that can

operate at low temperatures. Solvothermal methodology has been extensively examined as one possible route to produce semiconductor nanowires and nanorods. In these processes, a solvent is mixed with certain metal precursors and possibly a crystal growth regulating or templating agent such as amines. This solution mixture is then placed in an autoclave and kept at relatively high temperature and pressure to carry out the crystal growth and assembly process. This methodology seems to be quite versatile and has been demonstrated to be able to produce many different crystalline semiconductor nanorods and nanowires[9,10]. The products are usually not pure and the monodispersity of the sample is also far from ideal. Template-based synthesis represents a convenient and versatile method for generating 1D nanostructures. In this technique, the template simply serves as a scaffold against which other kinds of materials with similar morphologies are synthesized. These templates could be nanoscale channels within mesoporous materials such as porous alumina and polycarbonate membranes. These nanoscale channels can be filled with solution, or sol-gel and electrochemical processes can be used to generate 1D nanoscale objects. The produced nanowires can then be released from the templates by selectively removing the host matrix[11,12,13,14].

7.1.2 Gas-Phase Growth Methods

Gas-phase growth methods include: Vapor-liquid-solid (VLS) growth, Oxide-assisted growth, and Vapor-solid (VS) growth. Studies of the VLS nanowire growth indicate that one can achieve controlled growth of nanowires at different levels. First of all, one can, in principle, synthesize nanowires of different compositions by choosing suitable catalysts and growth temperature. A good catalyst should be able to form liquid alloy with the desired nanowire material, ideally they should be able to form eutectic. Meanwhile, the

growth temperature should be set between the eutectic point and the melting point of the nanowire material. Both physical methods (laser ablation, arc discharge, thermal evaporation) and chemical methods (metal organic chemical vapor transport and deposition) can be used to generate the vapor species required during the nanowire growth[3,7,15,16,17,18,19,20,21,22,23]. Oxide-assisted method for the synthesis of nanowires has the advantage of requiring neither a metal catalyst nor a template, which simplifies the purification and subsequent application of the wires. For example, GaAs nanowires obtained by oxide-assisted laser ablation of a mixture of GaAs and Ga_2O_3, where Ga_2O_3 served as the nucleus[24]. Vapor-Solid (VS) method for whiskers growth also merits attention for the growth of nanometer 1D materials. In this process, vapor is first generated by evaporation, chemical reduction or gaseous reaction. The vapor is subsequently transported and condensed onto a substrate. The VS method has been used to prepare oxide or metal whiskers. The size of the whiskers can be controlled by supersaturation, nucleation sizes and the growth time, etc. As an example, Wang et al. recently reported the synthesis of oxide nanobelts by simply evaporating and condensing the commercial metal oxide powders[25,26].

7.1.3 Anodic Aluminum Oxide

Generally, the template method is cheap and easy to operate, which can produce nanowires with uniform diameters ranging from several nanometers to hundreds nanometer in large area. A number of temlpates have been extensively used in the templating process. One of them is micro and nanoporous polymeric filtration membrane that has been prepared via the “track-etch" method. Membranes with a wide range of pore diameters (down to 10 nm) and pore densities approaching 10^9 pores/cm^2 are available

commercially. Porous anodic aluminum oxide (AAO) is another excellent host materials. This template is prepared electrochemically from aluminum metal. The pores in these templates are arranged in a regular hexagonal lattice. Pore densities as high as 10^{11} pores/cm^2 can be achieved. AAO as an important template stands out for its salient properties, such as stability, insulating properties, the minimal size, density and uniformity of the nanopores, the ability to integrate the AAO template into a device or chip, corrosion resistance and decorative properties, and the nanopore regularity which can be improved by a two-step anodization process[27,28].

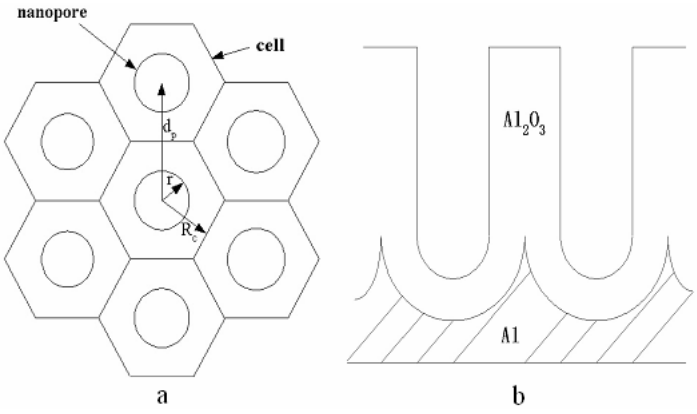

Fig. 7.1, Schematic drawing of the idealized hexagonal structure of anodic porous alumina. (a) top view; (b) side view.

When aluminum metal is anodically oxidized, Al_2O_3 is produced in the form of a film on the surface of aluminum. Anodic alumina is usually classified as non-porous (barrier type) or porous. Barrier type films grow in neural or basic electrolytes (PH>5), such as boric acid, ammonium borate, or tararte aqueous solution, where the Al_2O_3 has very low or no solubility. Aluminum anodized in electrolytes, such as oxalic, sulfuric, or phosphoric acids, which dissolve Al_2O_3, yields a porous type structure. The structure of the porous type Al_2O_3 has been characterized by a closely-packed array of columnar hexagonal cells, each containing a central pore, approximately cylindrical, normal to the

substrate surface and separated from the substrate by a barrier type film, which was first proposed by Keller in 1953[29], as shown in Fig. 7.1. Also, these nanopores are separated by oxide barrier walls.

7.2 Two-Step Process of AAO Growth

The two-step anodization method for the AAO growth was first described in 1996[27]. An aluminum sheet (99.999%) with diameter of 5-6 cm was first cut from a big aluminum foil. Then, the sheet was degreased in acetone with ultrasound and rinsed in an ethanol solution. Subsequently, the aluminum sheet was dried. After that, it was annealed at 600^{o}C in argon gas atmosphere for 1h with the flow speed of gas in 100 ml/min. Then, the annealed sheet was deoxidized in 2 M/l NaOH solution. Subsequently, the aluminum sheet was electrochemical polished in a mixture of pherchoric acid and ethanol (1:4 in volume) to obtain a mirror surface on the aluminum sheet. Then, the two-step anodization was performed on the polished aluminum sheet. The Al sheet was anodized at 40 V in a 3% wt oxalic acid solution at room temperature for 6 h. Then, the oxide film was chemically etched in a mixture of phosphoric acid and chromic acid (3:1 in weight) at 60^{o}C. The second anodization was performed under the same conditions as the first anodization for 1 h. After the process, highly ordered nanopores were formed in the AAO template.

7.3 General Descriptions

After the two-step anodiztion, hexagonally ordered channel arrays were formed in the AAO template. These nanopores have a diameter ranging from 10 to 60 nm and up to a few microns in depth depending on the electrolyte used, each containing a central pore,

approximately cylindrical, normal to the substrate surface and separated from the substrate by a barrier type film, as schematically shown in Fig. 7.1a and 7.1b. The SEM image shows the average diameter of nanopores and the interpore distance are 30 nm and 100 nm, respectively, in our experiments (Fig 7.2). The size of domain is up to several microns.

Porous oxide growth consists of several stages that can be observed from the characteristic behavior of current versus time for potentiostatic anodization[30]. When an anodic voltage is applied, a barrier oxide layer starts to form on the surface of the aluminum with the decrease of current. Tiny cracks appear at the oxide/electrolyte (o/e) interface prior to any true pore formation. Further anodization results in propagation of individual paths and widening of cracks to form nanopores. Finally, these nanopores attain a constant dissolution speed at the o/e interface and accumulation speed at the metal/oxide (m/o) interface. A steady-state pore structure is then formed by closely packed cylindrical cells, each containing a pore at the center and separated from the aluminum metal by a layer of scalloped hemispherical barrier oxide (see Fig. 7.1b). The geometrical dimension and size of these nanopores depend on the anodizing conditions. The reaction occurring at the o/e interface is electrical field enhanced chemical dissolution and the metal dissolution at the m/o interface is due to charge transfer or electrochemical reaction. The local electrical field is the key variable along the interfaces, which determines the reaction rate or speed of the interfaces. The electrical fields at the o/e and the m/o interfaces, in turn, depend on the shape or topography of the interfaces.

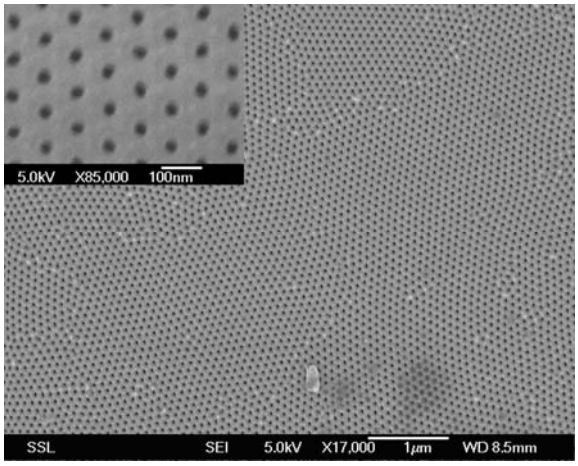

Fig. 7.2, The SEM image shows the morphology of the AAO template. The diameter of nanopore is about 30 nm, and the interpore distance is about 100 nm. The anodization was carried out in 3%w oxalic acid, at 40 V and room temperature.

The drift of ions such as Al^{3+}, OH^- and O^{2-} in the oxide layer plays an essential role for the formation of nanopores[31]. Two opposite reactions of formation (due to the arrival of OH^- and O^{2-} ions) and dissolution (due to the emission of Al^{3+} ions) of aluminum oxide take place at the interfaces between o/e and m/o layer, respectively. These two processes are balanced by the steady growth of the nanopores so that the thickness of the oxide layer is maintained as constant.

Many researches have been focused onto the growth mechanism of porous anodic aluminum oxide (AAO)[32,33,34]. A theoretical model based on well-developed nanopores and the electrical field distribution predicted a linear dependence of nanopore size on the applied voltage[35,36]. However, the models in these studies did not tolerate extensive lateral adjustment for the ordering of nanopores. The nanopore formation dynamics involved with moving boundary problem was discussed by a theoretical analysis[37], which predicted that the ratio of nanopore-diameter to nanopore-separation would be independent of the

applied voltage but vary with the pH values of electrolytes. Both the predicted pH range and pore dimensions were comparable to experimental data. It was shown that hexagonally ordered pore domains occurred under some specific conditions and the spatial order increased with increasing first anodization time, which indicates that a self-organization of nanopores existes[38]. The spatial ordering of nanopores was investigated in a number of experimental and theoretical studies. The ordering of the pores is affected by anodizing conditions, extrinsic factors (electrolytes, applied voltage and temperature) and intrinsic factors (defects and grain boundaries)[39,40]. A stress model and radial distribution function model were proposed to explain the self-organization behavior[39,40,41,42,43]. Recently, a 10% porosity rule had been proposed by Nielsch *et al.*[44]. However, these models cannot explain the hexagonal arrangement of nanopores in AAO template.

7.4 Electrical Bridge Model for Self-Organization of AAO

An electrical bridge model based on circuit theory is proposed here to explain the correlation among nanopores and the hexagonal arrangement of the nanopores. In this model, the anodization system is analogous to an electrical feedback system, and the spatial ordering of nanopores is achieved by self-adjustment among nanopores through the feedback of the electric bridge. And the effect of anodizing conditions, such as temperature, electrolytes and applied voltage, are discussed according to the variation of bridge resistances. Based on this model it is concluded that the hexagonal arrangement is more stable than other geometrical arrangements. And the formation of highly ordered nanopores in AAO is a self-assembly process.

The first anodization plays an essential role in the formation of uniform pattern with the same size (R_c) on the aluminum surface. This scalloped pattern determines the growth of highly ordered nanopores in the second anodization. Highly uniform pattern can be realized by the prolonged first anodization. Considering two neighboring nanopores, illustrated in Fig. 7.3, the bottoms of the nanopores can be considered as semi-spheres in shape, with radii of R_{c1} and R_{c2}, respectively. The experimental results show that these nanopores are not highly ordered at the initial stage of the first anodization, especially within the first minutes. With the prolonged first-step anodization, self-organization occurs, the sizes of nanopores approach uniformity, and the ordered domains expand. Therefore, it is reasonable to assume that R_{c1} is not equal to R_{c2}, as shown in Fig 7.3. R_{c1} and R_{c2} approach to each other by the self-organization as the first anodization continues. The process is similar to an electrical feedback system, which reaches stability by self-feedback or self-adjustment. The process of the AAO growth is self-adjusted or self-organized, *i.e.*, the highly ordered nanopores are correlated in the anodizing process. Every nanopore tries to adjust itself to match others.

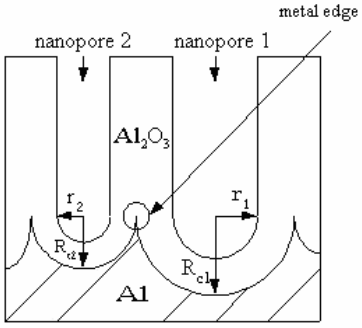

Fig. 7.3, Schematic drawing of the cross section of the nanopores with different sizes. The metal edge is illustrated for discussion.

The electrical bridge, also called Wheatstone Bridge, is fundamental to electrical system, such as circuits, and had been extensively studied[45]. The electrical bridge is shown in Fig.

7.4a, where R_1 and R_2 are two constant resistors, R_v is a variable resistor, and R_x is a unknown resistor. A is an Ampeimeter, which detects the current across the bridge. U is the applied voltage. In most cases, the bridge is used to determine the resistance of R_x by varying R_v with R_1 equal to R_2. The equilibrium condition, *i.e.*, no current along the bridge, is $R_v = R_x$. If this condition is not satisfied, there is a current along the bridge, which can be detected by A. By adjusting R_v and making the current through the bridge zero, the resistance of R_x is equal to R_v according to the equilibrium condition.

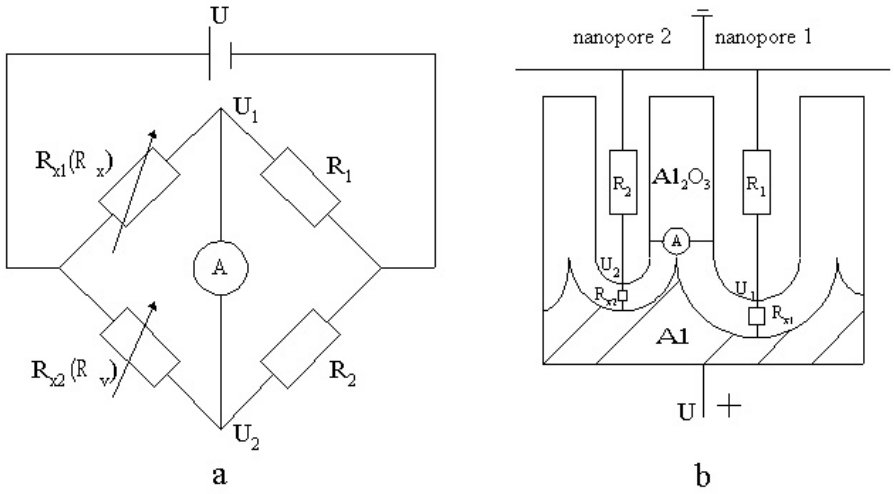

Fig. 7.4, (a) an electrical bridge model, where R_1 and R_2 are constant resistors and equal, corresponding to the resistances of electrolytes in different nanopores. U_i (i=1,2) is the potential at the end of bridge. R_x and R_v are the unknown resistor and variant resistor, respectively, corresponding to R_{xi} (i=1,2) -- the resistance of oxide layer. (b) schematic representation of corresponding electrical bridge model for two neighboring nanopores compared to (a). U_i (x=1,2) is the potential at the e/o interface.

The AAO self-organization growth can be modeled by the electrical bridge circuit as illustrated in Fig. 7.4b. Here, R_1 and R_2 represent the resistances of electrolyte within different nanopores (only two nanopores are drawn in Fig. 7.4b for simplicity). As a simple approximation, we can assume that R_1 is equal to R_2, because the resistance of the system was totally determined by the oxide layer and the resistance of the electrolyte can

be negligible. R_{x1} and R_{x2} are the resistances of the scalloped oxide layer at the bottoms of nanopores, which separates the electrolyte and the aluminum. Also, we assume that the thickness of the oxide layer is uniform at the bottom of every nanopore, but it may vary from nanopore to nanopore. In Fig. 7.4b, an imaginary Ampeimeter (A) was inserted to "detect" the current between two nanopores. R_{x1} and R_{x2} depend on the size of nanopore, *i.e.*, the thickness of the oxide layer at the bottoms of nanopores. Here, the resistance of the oxide layer is determined exclusively by the properties of the oxide layer. Other factors are expected to have little effect and are neglected for simplicity. Therefore, R_{x1} and R_{x2} change with the thickness of the oxide layer and the ion drift induced thermally. U_1 and U_2 are potentials at the two ends of the bridge and correspond to potentials at the o/e interface on the oxide layer in Fig. 7.4b. If $(U-U_1)$ is lager than $(U-U_2)$ or $U_1 < U_2$, R_{x1} is lager than R_{x2}. Thus, the thickness of oxide layer (h) at the bottom of nanopore 1 is thicker than that of nanopore 2, $h_1>h_2$ (the effect of anodizing conditions will be discussed later).

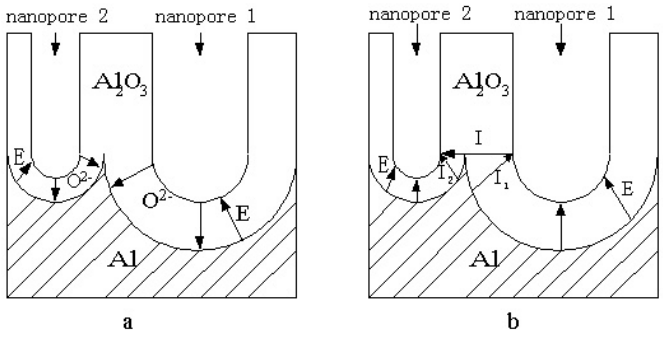

Fig. 7.5, Schematic representation of the cross section of the barrier layer where the oxide formation zone and the oxide dissolution zone adjacent to the m/o interface and the e/o interface, respectively, and the ionic movement and the electric field are shown (a). The current model corresponding to the ionic drift is illustrated in (b).

The sizes of the nanopore and cell are proportional to the applied voltage and the ratio of R_c to r ($G=R_c/r$) is independent of the applied voltage[37]. The voltage difference between the two sides of the oxide layer determines the sizes of the nanopore and the cell. If the sizes of nanopores are different, the voltage drops in these oxide layers at the bottoms of nanopores are different under constant applied voltage. Smaller U_i (i=1, 2) or larger ($U-U_i$) results in nanopores with larger R_c and r. Both R_c and r increase with the increase of the voltage drop ($U-U_i$). Therefore, the oxide layer ($h=R_c-r$) increases with the increase of voltage drop on the layer. Thicker oxide layer results in lager voltage drop due to higher resistance. As shown in Fig. 7.5a, assuming $R_{c1}>R_{c2}$ and $r_1>r_2$, then, $(U-U_1) > (U-U_2)$ or $U_1<U_2$. Therefore, there is a current (I) across the bridge, as shown in Fig. 7.5b. That is a current from nanopore 2 to nanopore 1. O^{2-} ions are considered as the electrical carriers in our system for simplicity (Al^{3+} drifts in the opposite direction of O^{2-}. That is the same to the current direction.). Thus, the flow of O^{2-} ions from nanopore 1 to nanopore 2 forms the current across the bridge. Therefore, more O^{2-} ions contribute to the oxidization of aluminum at the bottom of nanopore 2 compared with that of aluminum oxidization at nanopore 1 due to the thin oxide layer and strong electrical field. In this case, the current (I_2) induced by O^{2-} in oxide layer of nanopore 2 is lager than that in nanopore 1. There is a current through the bridge by the vector rule, $I=I_2-I_1$ (Fig. 7.5b). The metallic oxidization at the bottom of nanopore 2 accelerates due to the strong electrical field. And the metal edge shifts toward nanopore 1. Nanopore 2 expands and nanopore 1 shrinks. This bridge plays a role of feedback. If the size of nanopore 2 is larger than that of nanopore 1, the current direction will reverse. This is, therefore, a dynamic process. R_{c1} may be larger than R_{c2} or $R_{c2}>R_{c1}$ in the process of anodization. As the anodization continues, the difference between the resistances, $|R_{c1}-R_{c2}|$, will decreases by the self-

feedback via the electrical bridge. Nanopore 1 and nanopore 2 reach uniform size by self-adjustment via the electrical bridge. In a real system of the aluminum anodization, every nanopore is surrounded by six neighbors. Thus, there is a network of electrical bridges. All of them are correlated. This correlation leads to the self-organization of ordered nanopores and the formation of big domain.

In the above discussion, we analyzed the self-organization of the pores during the anodizing process based on the electrical bridge model at constant anodization conditions (for example, 3% oxalic acid, 25^{o}C, and 40V) and did not consider the effect of anodizing conditions. It is noticed that the ordering of the pores is closely related to anodizing parameters. And this self-organization is greatly affected by the extrinsic (electrolytes, temperature, and applied voltage) and intrinsic (grain boundary) factors. The ion diffusion and volume expansion change with the factors. For example, the diffusion coefficient is related to the temperature. The effect can lead to the fluctuation of the bridge resistances and distort the correct feedback according to the bridge model.

7.4.1 Effect of Temperature

The current depends on the local temperature at the bottom of nanopore and can be expressed as:

$$I = f(E,T) \qquad (1)$$

where E is the electrical field and T the local temperature. If T fluctuates strongly, the steady state is destroyed and it is difficult for nanopores to get the correct feedback induced by the change of the size of nanopore because of the fluctuated drift of ions induced thermally. Therefore, it is important to keep the temperature constant during the

process of anodization. Our observation showed that the ordering of nanopores cannot be achieved by increasing the temperature (20^{o}C to 60^{o}C) during the anodization (keeping other parameters constant). We also carried out experiments at T=0 ^{o}C, 25 ^{o}C and 50 ^{o}C (V=40 V, 3 % oxalic acid), respectively. It was noticed that anodizing current increases with the temperature. The best ordering occurs at T=25 ^{o}C with the current equal to 40 mA. At higher temperature (50 ^{o}C), the diameter of the pores is larger than that at lower temperature due to higher dissolution rate of oxide induced by the fast drift of ion. Therefore, the volume expansion is small and the oxide layer is thinned, which leads to the reduction of the bridge resistances and confused the feedback. At lower temperature (0^{o}C), the volume of oxide expands and the bridge resistances increase, which results in the breakdown of the correlation between two pores and the cut of the bridge due to the negligible feedback current. Under both conditions, the feedback current is out of the range of sensibility of the system. The system is broken and the ordering is worse.

7.4.2 Effect of Applied Voltage

The oxide layer at the bottoms of pores increases with the applied voltage (U). Based on the bridge model, if U changes during the anodization process, the ordering is distorted due to the incorrect feedback. Our experiments demonstrated that the ordering cannot be achieved when U increases linearly from 20 V to 60 V (25 ^{o}C, 3 % oxalic acid). Experiments were also carried out at U=20 V, 40 V, and 60 V (25 ^{o}C, 3 % oxalic acid), respectively. The current increases with U. The best ordering is at U=40 V. The resistance (R_x) is related to the oxide layer (h) and the applied voltage, expressed as:

$$R_x = R_{opt} + \Delta R \qquad (2)$$

where R_{opt} is the resistance of the oxide layer, corresponding to the steady state at constant anodization conditions. ΔR is the fluctuation. At higher U, R_{opt} is large and $\Delta R << R_{opt}$. Therefore, it is difficult to detect the varying current due to the smaller ΔR. At lower U, R_{opt} is small and $\Delta R \sim R_{opt}$. The lager ΔR does not really reflect the change of the pores. It is similar to an electrical system. Its sensibility is limited to a range. Exceeding the range, the feedback is broken.

7.4.3 Effect of Acid Concentration

The concentration of the oxalic acid in the range of 1% to 8% was used to investigate its effect on the ordering (25^{o}C, 40V). The best ordering occurs in the range of 3% to 5%, corresponding to the current of 40 mA to 50 mA. The current increases with the concentration of the acid. The ion drift and volume expansion are related to the concentration. Higher concentration results in a larger expansion, which reduces the correlation between the pores. And lower concentration leads to a small expansion, which amplifies the feedback. These reasons are similar to the effect of the applied voltage due to the limited sensibility of the system.

7.4.4 Effect of Annealing

Annealing process had been employed to study the effect of grain boundaries in our experiments. It was found that the ordered domains in annealed Al sheet are lager than those in non-annealed Al. The ordering of the pores is greatly affected by the grain boundaries because of current concentration around the surface defects. As the anodization continues, the defected regions are replaced by oxide, and their effect on the overall ordering diminishes[39,40]. Based on the bridge model, the boundaries affect the

bridge resistances, especially ΔR, which results in the noise during the feedback. With the prolonged anodization, the effect of the boundaries is diminished and the variation of the resistances reduces. This provides better feedback for the self-adjustment of the pores.

The effect of anodizing conditions on the ordering based on the bridge model is consistent with those according to the stress model[37,38], radial distribution function[39,40] or 10% rule[44]. Here, the variation of anodizing conditions affects the correct feedback of the bridge, cutting, amplifying or noising the feedback. The best ordering occurs at the optimal anodizing conditions, *i.e.*, the variation of the resistances is within the sensibility of the system.

7.5 Morphological Symmetry of AAO

The nanopores in AAO arrange hexagonally, as shown in Fig. 7.1a. The arrangement of nanopores keeps every nanopore surrounded by six nearest-neighbors and the electrical field at the bottoms of nanopores is uniformly distributed. The electrical field at the interfaces can be written as in the hemispherical case[35]:

$$E_e = \frac{U/h}{r/R_c}$$
$$E_m = \frac{U}{h} \times \frac{r}{R_c} \tag{7.3}$$

where E_e and E_m are the electrical fields at the electrolyte/oxide interface, and metal/oxide interface, respectively. $h=R_c-r$ is the thickness of oxide layer, as shown in Fig. 7.1a. U is the applied voltage. r/R_c is independent of the applied voltage (U)[37]. In the hexagonal arrangement, the thickness of oxide layer along six directions is uniform, which keeps the distribution of electrical field isotropic under steady growth state. If the thickness of the oxide layer at one direction is larger or less than other directions, this variation leads to

the change of electrical field at the bottom of the nanopore. The nanopore may adjust itself via the electrical bridge within the nanopore or among nanopores to improve the variation and reach the uniform distribution.

The electrical bridge model also suggests that other arrangements of nanopores are unstable. For example, the square arrangement of nanopores may be a possible arrangement, where every nanopore surrounded by four nearest-nanopores and four next nearest-nanopores. If the distance between two nearest-neighbors is d, then the distance between two next nearest-neighbors is $\sqrt{2}$ d. Therefore, the thicknesses of the oxide layer at these two directions, $\sqrt{2}$ d/2-r and d/2-r (r is the radius of the nanopore) are not the same. The electrical fields in these two directions are not isotropic. To reach the same potential, the nanopore would adjust itself via the electrical bridge. This adjustment would destroy the square arrangement. Based on the electrical bridge model, it is required that the distance between the nearest nanopores on the circle is equal to the radius of the circle, *i.e.*, $2\pi r/N=r$ (r is the radius of the circle, N the number of nanopores on the circle). Then N is equal to 6.

The prolonged first anodization process gives nanopores enough time to adjust themselves by the electrical bridge. The dynamical process arranges the nanopores hexagonally under the steady growth state. The local temperature vibration would destroy the state and induce defects. The self-repair of ordered pattern provides an evidence for the stable hexagonal arrangement of pores in AAO[46].

7.6 Summary

In summary, the hexagonal arrangement of nanopores in AAO suggested the self-organization growth and the correlation among nanopores. We discussed the naturally occurred self-organization process based on the electrical bridge model. The thickness of oxide layer at the bottom of nanopore determines the electrical field distribution, thicker layer resulting in weaker field and vise verse. The distribution made the rate of accumulation of oxide at the m/o interface different at different directions. Thus, the currents at different directions differ. The current vector rule gives out a bridge current between different parts at the bottom of nanopore. For two nearest nanopores, they were closely correlated through the electrical bridge. The electrical bridge equilibrium resulted in the steady state growth of self-organized nanopores. The difference among nanopores in sizes of cell and nanopore introduces the bridge current among nanopores. The dynamic process by adjusting the bridge current results in the self-organization of nanopores. The process was improved by prolonged first anodization for the ordering of nanopores increases with the increase of the prolonged first anodization time. Based on the model, the effect of anodizing conditions on the ordering was analyzed. And the optimal anodizing conditions can be explained. The electrical bridge model also suggested the hexagonal morphology is stable. This natural process is slightly different from the “artificial” patterning, where the “artificial” mask dominates the growth of pores. It would be possible to grow other morphologies, such as square, by one-step anodization in an artificial way. However, the hexagonal morphology is more stable in the natural way.

AAO as an important template is an excellent material for the growth of highly-ordered nanotubes or nanowires due to its salient properties, such as stability, insulating properties, the minimal size, density and uniformity of the nanopores, the ability to integrate the AAO template into a device or chip, and corrosion resistance. In next chapters, this template is used to fabricate highly ordered carbon nanotubes and metal nanowires.

References:

[1] Y. Wu and P. Yang, Chem. Mater. 12, 605 (2000).
[2] M. H. Huang, Y. Wu, H. Feick, E. Webber, and P. Yang, Adv. Mater. 13, 113 (2000).
[3] A. M. Morales and C. M. Lieber, Science 279, 208 (1998).
[4] C. R. Martin, Science 266, 1961 (1994).
[5] D. Almawlawi, C. Z. Liu, and M. Moskovits, J. Mater. Res. 9, 1014 (1994).
[6] W. Han, S. Fan, W. Li, and Y. Hu, Science 277, 1287 (1997).
[7] T. J. Trentler, K. M. Hickman, S. C. Geol, A. M. Viano, P. C. Gibbons, and W. E. Buhro, Science 270, 1791 (1995).
[8] X. Duan and C. M. Lieber, Adv. Mater. 12, 298 (2000).
[9] Y. F. Liu, J. H. Zeng, W. X. Zhang, W. C. Yu, Y. T. Qian, J. B. Cao, and W. Q. Zhang, J. Mater. Res. 16, 3361 (2001).
[10] X. Jiang, Y. Xie, J. Lu, L. Y. Zhu, W. He and Y. T. Qian, Chem. Mater. 13, 1213 (2001).
[11] C. G. Wu and T. Bein, Science 266, 1013 (1994).
[12] T. Huczko, Appl. Phys. A: Mater. 70, 365 (2000).
[13] A. L. Prieto, M. S. Sander, M. S. Martin-Gonzalez, R. Gronsky, T. Sands, and A. M. Stacy, J. Am. Chem. Soc. 123, 7160 (2001).
[14] T. E. Huber, M. J. Graf, C. A. Foss, and P. Constant, J. Mater. Res. 15, 1816 (2000).
[15] Y. Wu and P. Yang, J. Am. Chem. Soc. 123, 3165 (2001).
[16] M. S. Gudiksen and C. M. Lieber, J. Am. Chem. Soc. 122, 8801 (2000).
[17] C. C. Chen, C. C. Yeh, C. H. Chen, M. Y. Yu, H. L. Liu, J. J. Wu, K. H. Chen, L. C. Chen, J. Y. Peng, and Y. F. Chen, J. Am. Chem. Soc. 123, 2791 (2001).
[18] X. F. Duan and C. M. Lieber, J. Am. Chem. Soc. 122, 188 (2000).
[19] W. S. Shi, H. Y. Peng, Y. F. Zheng, N. Wang, N. G. Shang, Z. W. Pan, C. S. Lee, and S. T. Lee, Adv. Mater. 12, 1343 (2000).
[20] C. C. Tang, S. S. Fan, M. L. de la Chapelle, H. Y. Dang, and P. Li, Adv. Mater. 12, 1346 (2000).
[21] G. Gu, M. Burghard, G. T. Kim, G. S. Dusberg, P. W. Chiu, V. Krstic, S. Roth, and W. Q. Han, J. Appl. Phys. 90, 5747 (2001).

[22] Z. W. Pan, H. L. Lai, F. C. K. Au, X. F. Duan, W. Y. Zhou, W. S. Shi, N. Wang, C. S. Lee, N. B. Wong, S. T. Lee, and S. S. Xie, Adv. Mater. 12, 1186 (2000).
[23] Y. Wu, B. Messer, and P. Yang, Adv. Mater. 13, 1487 (2001).
[24] S. T. Lee, N. Wang, Y. F. Zhang, and Y. H. Tang, MRS Bulletin 24, 36 (1999).
[25] Z. W. Pan, Z. R. Dai, and Z. L. Wang, Science 291, 1947 (2001).
[26] Z. R. Dai, Z. W. Pan, and Z. L. Wang, Solid State Commun. 118, 351 (2001).
[27] H. Masuda and K. Fukuda, Science, 268, 1466 (1995).
[28] H. Masuda and M. Satoh, Jpn. J. Appl. Phys. 35, L126 (1996).
[29] F. Keller, M. S. Hunter, and D. L. Robinson, J. Electrochem. Soc. 100, 411 (1953).
[30] V.P Parkhutik, Corros. Sci. 26, 295 (1986).
[31] G. E. Thomopson, R. C. Furneaux, G. C. Wood, J. A. Richardson, and J. S. Goode, Nature 272, 433 (1978).
[32] G. Patermarakis and H. S. Karayannis, Electrochima. Acta 40, 2647 (1995).
[33] G. Patermarakis and K. Moussoutzanis, Electrochima. Acta 40, 699 (1995).
[34] G. Patermarakis, P. Lenas, Ch. Karavassilis and G. Papayiannis, Electrochima. Acta 36, 709 (1991).
[35] V. P. Parkhutik and V. I. Shershulsky, J. Phys. D 25, 1258 (1992).
[36] V. P. Parkhutik and V. I. Shershulsky, J. Phys. D 25, 1258 (1992).
[37] S. K. Thamida and H-S. Chang, Chaos 12, 240 (2002).
[38] S. Shingubara, O. Okino, Y. Sayama, H. Sakaue and T. Takahagi, Jpn. J. Appl. Phys. 36, 7791 (1997).
[39] J. F. Behnke and T. Sands, J. Appl. Phys. 88, 6875 (2000).
[40] F. Li, L. Zhang, and R. M. Metzgar, Chem. Mater., 10, 2470 (1998).
[41] A. P. Li, F. Muller, A. Birner, K. Nielsch, and U. Gosele, J. Appl. Phys. 84, 6023 (1998).
[42] A. P. Li, F. Muller, A. Birner, K. Nielsch, and U. Gosele, J. Vac. Sci. Technol. A 17, 1428 (1999).
[43] O. Jessensky, F. Muller, and U. Gosele, Appl. Phys. Lett. 72, 1173 (1998).
[44] K. Nielsch, J. Choi, K. Schwirn, R.B. Wehrpohn, and U. Gosele, Nano Lett. 2, 677 (2002).
[45] J. W. Nilsson, Electric circuits, 4th ed., Addison-Welsay Publishing Company, 1993, p. 69.
[46] H. Masuda, M. Yotsuya, M. Asano, K. Nishio, M. Nakao, A. Yokoo, and T. Tamamura, Appl. Phys. Lett. 78, 826 (2001).

CHAPTER 8

CARBON NANOTUBES BASED ON AAO TEMPLATE

8.1 Introduction

Carbon nanotubes (CNTs) have attracted extensive attention since their discovery[1] for their intriguing and potentially useful structural, electrical and mechanical properties. Although, in recent years, significant progress has been made in controlling the growth of CNTs[2,3,4,5], the full potential of CNTs for application will not be realized until the growth of CNTs can be further optimized and controlled. The application of CNT in device integration is one special example. Electromigration is a fundamental factor limiting the further miniaturization of metallic wires in nanodevices, while CNTs have higher current carrying capacities[6,7] and can be used as interconnections in nanodevices. Template-synthesis of CNTs, as a convenient method for these purposes, has increasingly attracted wide interests. Anodic aluminum oxide (AAO) is an important template. Among other salient properties, such as corrosion resistance and decorative properties, AAO template method is particularly suitable for growing highly ordered CNTs which can serve as inter-layer connections integrated with Si technology in the microelectronics. The AAO-based synthesis of CNTs was first proposed by Martin et al[8] and developed by Lee et al[9,10,11,12]. Highly ordered CNTs can be produced in large-scale by this method, with the size of CNTs varying over a wide range depending on the template. Two models, *i.e.*, bottom-growth- and tip-growth-mode, have been proposed[9] to explain the growth of CNTs within

or out of the nanopores of the AAO template. Nevertheless the detailed mechanism of the AAO-based synthesis of CNTs still remains open for discussion.

In this chapter, the AAO-template growth of CNTs was systematically studied, and the conditions for the graphitization of CNTs grown within or out of the AAO nanopores were discussed.

8.2 Experimental Details

8.2.1 The Preparation of the AAO Template

The AAO template growth technique is described in Chapter 6 in detail. Briefly, high purity (99.999%) aluminum foil as the starting material was annealed under the argon atmosphere at 500-600^{o}C for couples of hour, in order to increase the grain size of the aluminum metal and to ensure the homogeneous growth of nanopores over a large area. After degreased with acetone, and rinsed with ethanol, the Al foil was electrochemically polished in a mixture of perchloric acid and ethanol (1:4 in volume) under constant voltage (20 V) at 0 ^{o}C for 4 min. Two-step anodization was utilized to prepare an ordered AAO template[13,14]. The first anodization of the Al foil was performed at 40 V in an oxalic acid solution of 3 wt% at about 25 ^{o}C for 6 h. It was then chemically etched in a mixed solution of phosphoric acid and chromic acid (3:1 in weight) at 60 ^{o}C. The second anodization was performed at the same conditions. Various time periods between 10 min and 2 h was applied to produce AAO templates with different thickness (1-2 μm for 10 min and 10 μm for 2 h) for comparative experiments.

8.2.2 The Deposition of Co Catalysts on AAO Template

In order to facilitate the deposition of the Co catalyst for the CNTs growth, the AAO template was etched in phosphoric acid (5 wt%) to thin the barrier layer at the bottom of the nanopore arrays. Cobalt particles were electrochemically deposited at the bottom of nanopores at 10 V ac at room temperature, using a Co sulfate electrolyte (240 g $CoSO_4 \cdot 7H_2O$: 45 g $CoCl_2 \cdot 6H_2O$: 40 g $H_3BO_3 \cdot 2H_2O$).

8.2.3 The Growth of CNTs

Generally, the growth of CNT was carried out in a quartz reactor at high temperatures under a flow of Ar (95%) and H_2 (5%) gas mixture at 100 sccm, by the pyrolysis of a hydrocarbon gas (acetylene or ethylene at 16 sccm) with or without Co catalysts. In the case that the Co catalyst was employed, the catalyst was first reduced at 600^{o}C for 150 min, followed by the hydrocarbon pyrolysis at high temperatures for 40 min. After stopping the flow of the hydrocarbon, the samples were cooled in the atmosphere of the mixture of H_2 and Ar. In order to study the mechanism and graphitization of AAO-based CNTs, nine samples were prepared at different conditions. According to the AAO anodization time period (hence the AAO thickness) , the usage and preparation of Co catalysts, the choice of hydrocarbon feedstock, and the temperature of pyrolysis, samples are labeled as Sample 1 (AAO tinckness-1 μm, hydrocarbon-C_2H_2, Co catalyst-electrodeposited, pyrolysis temperature-650^{o}C), Sample 2 (10 μm, C_2H_2, Co electrodeposited, 650^{o}C), Sample 3 (10 μm, C_2H_2, no catalyst, 650^{o}C), Sample 4 (1 μm, C_2H_2, Co electrodeposited, 750^{o}C), Sample 5 (1 μm, C_2H_4, Co electrodeposited, 750^{o}C), Sample 6 (10 μm, C_2H_4, Co electrodeposited, 750^{o}C), Sample 7 (10 μm, C_2H_4, Co catalyst deposited by traditional impregnation procedures, 750^{o}C), Sample 8 (10 μm,

C_2H_4, no Co catalyst, 750°C) and Sample 9 (10 μm, C_2H_4, no Co catalyst, 930°C). (See Table 8.1)

8.2.4 Characterization

The morphology of the carbon nanotubes was observed by scanning electron microscope (SEM, JEOL JSM-6700F). Also, the as-grown carbon nanotubes were characterized by Raman scattering (Renishaw 2000 system with 1 cm^{-1} resolution and 0.4 cm^{-1} reproducibility, at the excitation source of 514.5 nm).

8.3 Results and Discussions

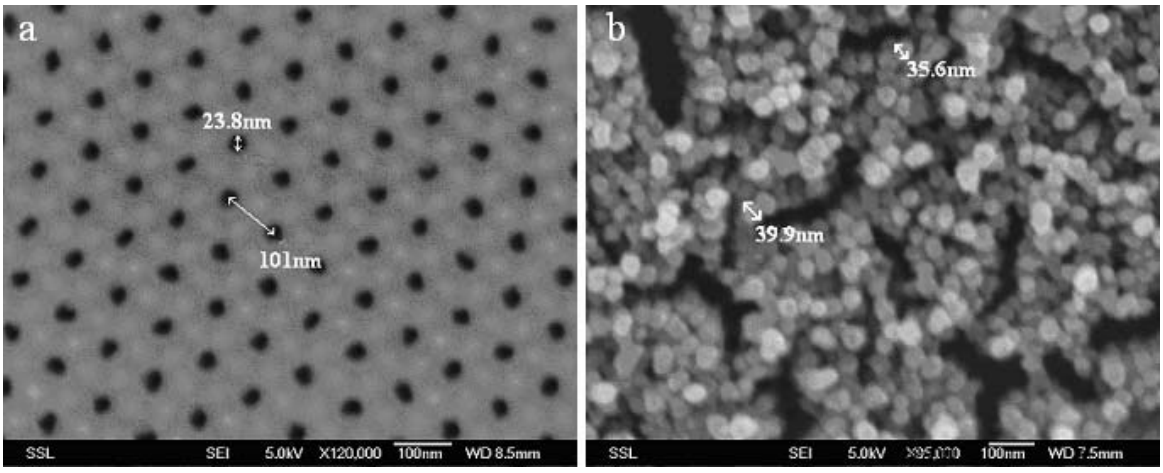

Fig. 8.1, (a) The SEM image of a typical AAO template prepared by the two-step anodization at 23°C using 3%w oxalic acid and 40 V voltage and (b) the SEM image of Co particles with the diameter around 40 nm. The AAO template has been removed by phosphoric and chromic acids.

A typical AAO template image shown in Fig. 8.1a indicates that the nanopores in AAO template are hexagonally arranged and highly ordered. The average diameter and interpore distance are approximately 30 nm and 100 nm, respectively. Straight parallel nanopores were obtained, which were perpendicular to the AAO template surface. Co

particles deposited at the bottom of the nanopores have uniform size of ~ 35-40 nm, as illustrated in Fig. 8.1b. They became observable under SEM after the alumina layer being removed in a mixed solution of phosphoric and chromic acids.

Sample	Gas source	Catalyst (Co)	Thickness (μm)	Temperature (^oC)	Results of SEM
1	C_2H_2	Deposited	1-2	650	out of nanopores
2	C_2H_2	Deposited	10	650	within nanopores
3	C_2H_2	No	10	650	within nanopores
4	C_2H_2	Deposited	10	750	within nanopores
5	C_2H_4	Deposited	1-2	750	out of nanopores
6	C_2H_4	Deposited	10	750	within nanopores
7	C_2H_4	Immersed	10	750	within nanopores
8	C_2H_4	No	10	750	No CNTs
9	C_2H_4	No	10	900	within nanopores

Table 8.1, Conditions for the growth of CNTs based on AAO template and the results of SEM.

The growth of CNTs was found to strongly depend on the pyrolysis temperature. As shown in Table 8.1, below 650^{o}C no CNTs were observable. The growth was also dependent on the type of hydrocarbon. C_2H_4 requires higher decomposition temperature as compared to C_2H_2 (by ~100 degree under identical conditions). The usage of Co catalysts can reduce the pyrolysis temperature. CNTs were not formed at 750^{o}C without Co (Sample 8) whereas they were observable with Co under otherwise identical conditions (750^{o}C, Samples 5-7). However the usage of Co is not a necessary condition. Our experiments showed that CNTs can be produced within the AAO nanopores from the acetylene pyrolysis at 650^{o}C without the presence of Co catalysts (see Fig. 8.2a for Sample 3 after the AAO being totally dissolved). Similar result was observed for Sample 9 (C_2H_4, no Co catalyst), though much higher temperature (up to 900^{o}C) was required (see table 8.1). Obviously the inner wall of the alumina nanopores plays a role as the catalyst for the hydrocarbon pyrolysis.

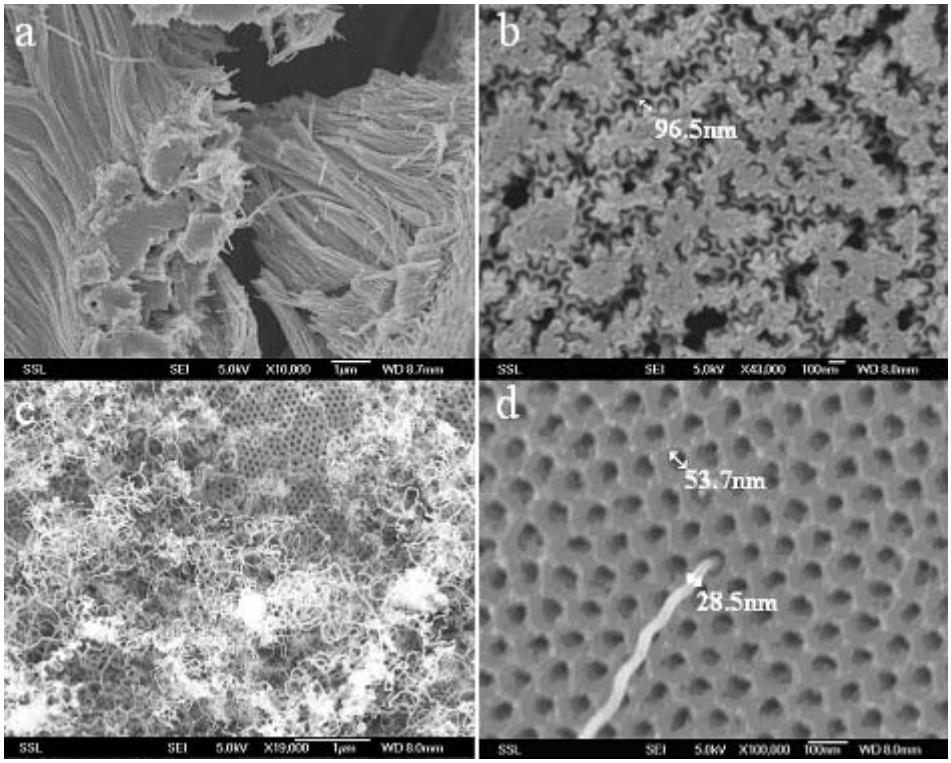

Fig. 8.2, SEM images of CNTs based on AAO template: (a) CNTs formed within nanopores of a thick AAO template without the presence of Co (Sample 3). (b) CNTs formed within nanopores of a thick AAO template (Sample 2). (c) CNTs growing out of nanopores on an AAO template with short pore length (Sample 1); (d) A CNT with a diameter of 28nm growing out of the nanopore on an AAO template with large diameter (around 50nm) (Sample 1).

CNTs were normally confined within the pore channels. Figure 8.2b is the SEM image of CNTs produced on Sample 2. The AAO template was partially etched by phosphoric and chromic acids at 60^{o}C for 5 min. As a result, the nanopores were widened, and the CNTs were exposed. The exposed tips of the CNTs have equal length and are tangled together. However, without the above acid etching, no CNTs were observed out of the nanopores on thick (e.g. 10 μm) AAO templates. So, it can be concluded that the CNTs are not easy to grow out of the nanopores if the channel is long. It is possible to observe CNTs growing out of the nanopores of Co-deposited AAO samples, only if the nanopore length

is short or if the nanopore diameter is big. Fig. 8.2c is obtained from as-prepared Sample 1 (1 μm channel length), where CNTs growing out of the pores are tangled together. Figure 8.2d shows a CNT growing out of a wide (54 nm) nanopore. It is understandable that the hydrocarbon gas molecules can easily reach the Co catalyst on the bottom of nanopores without being decomposed on the inner wall, if the channel is short or the pore diameter is large. With sufficient supply of the feedstock hydrocarbon CNTs can continuously grow from the Co catalyst and out of the channels. Note that the extension of the CNTs out of the pores is normally thinner than the pore size. For thick AAO template (nanopore length ~ 10 μm), it is difficult for CNTs to grow out of the nanopores, because longer alumina inner wall has more chances to decompose the hydrocarbon, which may prevent the approaching of hydrocarbon molecules to the Co catalysts and the outgrowth of CNTs from the Co catalyst. In literature the growth of CNTs on Co (or Fe, Ni) catalysts could follow either top-mode or bottom-mode, depending on the local situation during the growth. Nevertheless for the CNTs grown out of long nanopores, the tip-mode would appear to be dominant. If it is not so, the growth of CNTs will stop at any stage when the earlier formed carbon tubes may block the pore and prevent hydrocarbon molecules from approaching the catalyst particles at the bottom.

The extent of graphitization of the AAO-grown CNTs depends strongly on the growth conditions. Raman spectra in Fig. 8.3 show two peaks characteristic of multiwalled carbon Nanotubes, i.e. the G-band at 1580cm^{-1} and the D band at 1340cm^{-1}, for all the samples except Sample 8 (10 μm, C_2H_4, no Co catalyst, 750^{o}C).

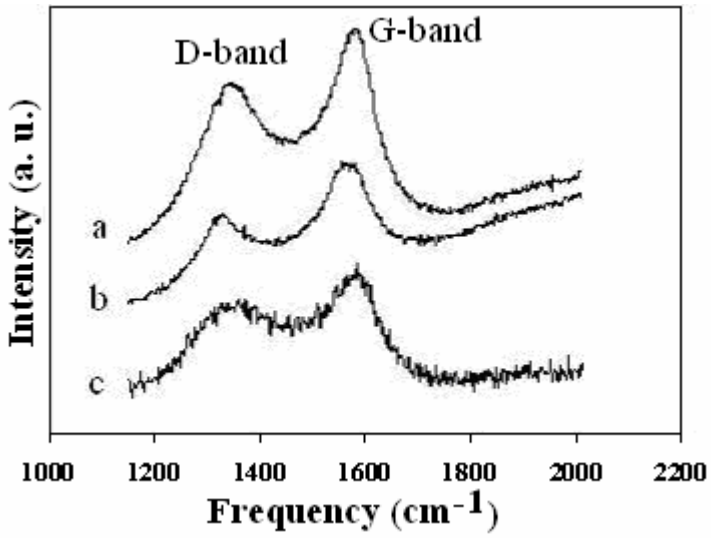

Fig. 8.3, Raman spectra of the AAO-template-grown CNTs samples: (a) from Samples 5 and 6 by using ethylene as the hydrocarbon source with the presence of electrodeposited Co catalysts; (b) from Samples 1, 2, and 4 by using acetylene and electrodeposited Co catalysts; (c) From Samples 3, 7 and 9 without Co catalysts.

G-band is related to the hybridization of sp^3 and D band to sp^2. The graphitization of CNTs can be estimated by the intensity ratio of the D band vs G band (I_D/I_G). The smaller the I_D/I_G ratio is, the higher the graphitization of CNTs. Obviously the graphitization of all the samples is not high. Nevertheless, in Fig. 8.3, the CNTs produced from ethylene are generally better in graphitization than those from acetylene, and the CNTs grown with the presence of Co catalysts better than those without Co catalysts. Figure 8.3a is the Raman spectrum for Samples 5-6, for which C_2H_4 was pyrolized at 750 ^oC on the electrodeposited Co catalyst. Obviously the I_D/I_G ratio is lesser than that of Fig. 3b for the pyrolysis of C_2H_2 at 650 ^oC on Co catalysts (Samples 1-2 and 4). Without Co catalysts (for Samples 3 and 9) Figure 3c shows high I_D/I_G ratio and hence poorer graphitization. The pyrolysis of acetylene produced a lot of amorphous carbon particles attached on the inner walls of the nanopores and reduced the extent of the graphitization of CNTs. It is

worth to mention that for Sample 7 the Co particles were deposited on the entire inner walls of nanopores by traditional impregnation. The spectrum of Sample 7 is similar to that of Samples 3 and 9 without Co catalysts. It appears that the Co catalysts coated on the inner wall of nanopores give rise to a lot of carbon nucleation sites and thus reduce the graphitization extent. The growth temperature does not seem to be an important factor for the graphitization. The CNTs produced from C_2H_4 at 900 ^oC without Co (Sample 9) show poorer graphitization than that of Sample5 (C_2H_4 at 750 ^oC with Co). It can be concluded that CNTs grown from ethylene with the presence of electro-deposited Co catalysts have the highest graphitization.

8.4 Summary

In summary, the AAO template growth is an effective method for producing highly ordered CNTs. In this research, the ordered CNTs were produced from the hydrocarbon (C_2H_2 or C_2H_4) pyrolysis at temperatures of 650 ^oC or above on the AAO templates. C_2H_4 normally requires a pyrolysis temperature 100 ^oC higher than C_2H_2 under otherwise identical conditions. The growth of CNTs can be performed without Co catalysts, indicating that the inner wall of alumina nanopores can catalyze the pyrolysis of hydrocarbons. Nevertheless the pyrolysis temperature is greatly reduced with the presence of Co catalysts. Normally CNTs are confined within the nanopores, but they can grow out of the nanopores with Co particles present at the bottom of the nanopores. But the out-growth of CNTs depends on the competition between nanopore inner wall and catalysts. In the cases that the pore diameter is large or the pore length is short, where the Co catalytic effect is dominant, the outgrowth of CNTs is observable. In other cases (e.g. long nanopores) where the inner wall of the nanopores plays an important role on the

growth of CNTs, the out-growth of CNTs from Co catalysts is hindered by the CNTs grown from the wall. The graphitization of AAO-template grown CNTs depends on growth conditions. The CNTs produced from ethylene are generally better in graphitization than those from acetylene, and the CNTs grown with the presence of Co catalysts deposited at the bottom of nanopores are better than those without Co catalysts or with Co catalysts coated on the entire inner wall of nanopores. The growth temperature is found not to play a critical role in graphitization.

This AAO-based method may be an alternative way for the scale-up production of CNTs for nano-device applications based on the above study. Another important component of nano-device is the metallic part, such as interconnection and magnetic storage. In next chapter, AAO-based growth of metal nanowires is studied and their applications in magnetic storage devices and optical limiter are explored.

References:

[1] S. Iijima, Nature 354, 56 (1991).
[2] A. Thess, R. Lee, P. Nikolaev, H. Dai, P. Petit, J. Robert, C. Xu, Y. H. Lee, S. G. Kim, A. G. Rinzler, D. T. Colbert, G. E. Scuseria, D. Tománek, J. E. Fischer, and R. E. Smalley, Science 273, 483 (1996).
[3] W. Z. Li, S. S. Xie, L. X. Qian, B. H. Chang, B. S Zou, W. Y. Zhou, R. A. Zhao, and G. Wang, Science 274, 1701 (1996).
[4] Z. F. Ren, Z. P. Huang, J. W. Xu, J. H. Wang, P. Bush, M. P. Siegal, and P. N. Provencio, Science 282, 1105 (1998).
[5] S. Fan, M.C. Chapline, N.R. Franklin, T.W. Tomnler, A.M. Cassell, H. Dai, Science 283, 512 (1999).
[6] B. Q. Wei, R. Vajtai, and P. M. Ajayan, Appl. Phys. Lett. 79, 1172 (2001).
[7] Philip G. Collins, M. Hersam, M. Arnold, R. Martel, and Ph. Avouris, Phys. Rev. Lett. 86, 3128 (2001).
[8] R. V. Parthasarathy, K. L. N. Phani, and C.R. Martin, Adv. Mater. 7, 896 (1995).
[9] S-H. Jeong, O-J. Lee, K.-H. Lee, S. H. Oh, and C.-G. Park, Chem. Mater.14, 4003 (2002).

[10] S-H. Jeong, O-J. Lee, and K-H. Lee, Chem. Mater. 14, 1859 (2002).
[11] Y. C. Sui, B. Z. Cui, R. Guardian, D. R. Acosta, and L. Martinez, R. Perez, Carbon 40, 1011 (2002).
[12] Y. Zhang, L.D. Zhang, G. H. Li, and L. X. Zhao, Mater. Sci. Eng. A308, 9 (2001).
[13] H. Gao, C. Mu, F. Wang, D. Xu, K. Wu, Y. Xie, S. Liu, E. Wang, J. Xu, and D. Yu, J. Appl. Phys. 93, 5602 (2003).
[14] H. Masuda and K. Fukuda, Science 268, 1466 (1995).

CHAPTER 9

METAL NANOWIRES BASED ON AAO TEMPLATE

9.1 Introduction

Metal nanowires are of great interests in theoretical physics, solid state science and practical technological applications[1,2,3]. Among the nanometric materials, the one-dimensional nanostructures have attracted great attention because of their potential applications to future ultra-high-density magnetic recording media, magnetic devices and materials for optical, microwave applications[4,5]. Methods used to produce the metallic nanowires include lithographic patterning[6,7], which is comparatively cumbersome, expensive and not suitable for large scale production, and "template-synthesis"[4,8,9,10,11], which involves electrochemically depositing metal into nanopores in the template. Generally, the template method is cheap and easy to operate, which can be used to produce nanowires with uniform diameters ranging from several nanometers to hundreds nanometer in large area. Commonly used template is anodic aluminum oxide (AAO), which as an important template stands out for its salient properties. To date, most metallic nanowires were produced based on AAO template, such as Au, Ag, Zn and Ni nanowires[10,12,13,14,15]. Highly ordered nanowires with uniform diameter, deposited in the AAO template, are essential to study their properties and for the application. The physical properties of nanowires, such as magnetic property, are greatly related to their structures and arrangement, such as length, diameter and inter-distance[12]. Most of researches have been focused on the effect of the arrangement of the nanowires. Successful growth of single crystal nanowires of low melting point metals have been reported[16], but growth of single crystal nanowires of high-melting-point metals was claimed to be very difficult if

not impossible[16]. Single crystal Fe or Ni nanowires were reported in literature[10,17]. But the single-crystalline size was rather small, around 40 nm along the wire axis, and there was no discussion on the mechanism of the single crystal growth and the effect of single crystallinity on their magnetic properties. However, the structure of the nanowire plays an important role on the electronic, optical and magnetic properties. The single-crystal structure is essential to compare the experimental results with the theoretical study. And, the conditions employed in the deposition process, such as pH value, deposition voltage, and temperature, are responsible for the structure control of the metal nanowires.

In this chapter, it is demonstrated that single crystalline Ni, Co, Zn, and Ag nanowires with preferred orientation can be successfully produced based on the AAO template. These nanowires show excellent magnetic and optical limiting properties. The effects of deposition conditions on the structures of the nanowires were investigated. The experimental results were presented and the optimal deposition conditions for the single crystal growth of metal nanowires were proposed. The mechanism for the single crystal growth of metal nanowires was investigated.

9.2 Experimental Details

The AAO template was prepared following the two-step anodization procedure as discussed in previous chapter. After the two-step anodiztion, the remaining Al on the AAO template was removed in $CuCl_2$ solution. The oxide layer at the bottoms of the pores was removed in acid. To facilitate electrodeposition, a Pt layer was sputtered to the back of the AAO as the electrode. A Ni sulfate electrolyte (240 g $NiSO_4 \cdot 7H_2O$: 45g $NiCl_2 \cdot 6H_2O$: 40g $H_3BO_3 \cdot 2H_2O$) with the pH value of 2.5 was used. DC electrodeposition

was performed at various applied voltages ranging from 0.4 V to 4.0 V and temperatures ranging from 25^{o}C to 60^{o}C to investigate their effects on the structures and magnetic properties of Ni nanowires. The pH value was in the range of 2.0 to 6.0 adjusted by the NaOH solution. Seven Ni samples were prepared at different electro-deposition conditions. These samples were labeled as Ni-1 (an applied voltage of 0.4 V, pH=2 and room temperature (RT)), Ni-2 (1.0 V, 2, RT), Ni-3 (4.0 V, 2, RT), Ni-4 (1.0 V, 2, 40^{o}C), Ni-5 (1.0 V, 2, 60^{o}C), Ni-6 (4.0 V, 2, 60^{o}C) and Ni-7 (4.0 V, 6, RT). To keep the length of nanowires equal in all the samples, long deposition time was applied at low electrodeposition voltages, and the AAO used were prepared under the same anodizing conditions so that they have the same pore structures. Following the same principles single-crystalline Co nanowires have been fabricated using a Co sulfate electrolyte (270 g $CoSO_4 \cdot 7H_2O$: 50g $CoCl_2 \cdot 6H_2O$: 40g $H_3BO_3 \cdot 2H_2O$) with the pH value of 2.5 at room temperature and 1.0 V (Co-1) or 4.0 V (Co-2). And a Zn sulfate electrolyte (250 g/l $ZnSO_4 \cdot 7H_2O$: 30g/l $ZnCl_2 \cdot 6H_2O$) and Ag sulfate electrolyte (10 g/l $AgSO_4$) were used to produce Zn nanowires (Zn-1) and Ag nanowires (Ag-1). The samples were prepared at 1.0 V, pH=3, and room temperature.

The morphology of the deposited Ni nanowires was observed by scanning electron microscope (SEM, JEOL JSM-6700F). The structure of the nanowires was characterized by HRTEM and XRD (Brucker AXS D8).

9.3 Single Crystal Growth of Metal Nanowires

A typical AAO template image shown in Fig. 7.1a indicates that the nanopores in AAO template are hexagonally arranged and highly ordered.

By the DC electrochemical deposition, metal was homogeneously filled into the nanopores of the AAO template. In order to visualize the nanowires, the AAO template was immersed in phosphoric acid to slightly remove the alumina surface and expose the nanowires. Figure 9.1 shows a typical arrangement of nanowires. The nanopores are almost 100% filled. These metal nanowires are embedded into the porous alumina matrix, which are highly ordered and confined by the hexagonal structure. The nanowires with diameter of 50 nm are separated by the alumina with inter distance of 100 nm. The diameter of the nanowires is larger than that of the original nanopores (Fig. 9.1) because of the widening effects of acid during the procedure of removing the oxide layer at the bottoms of the nanopores.

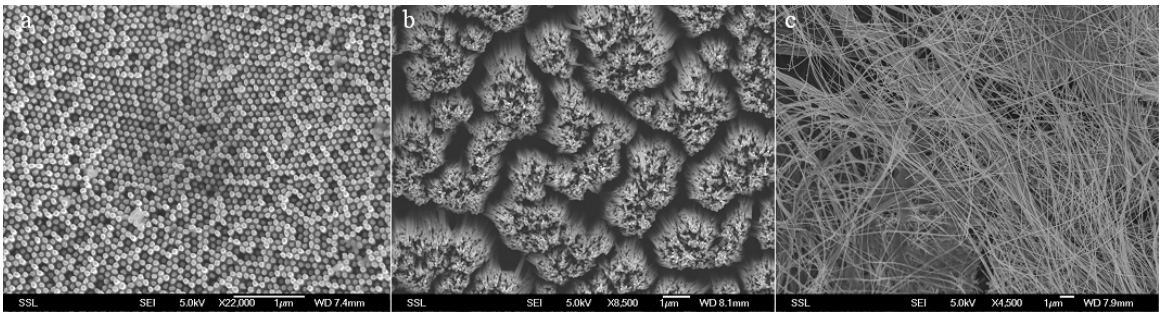

Fig. 9.1, SEM images of Ni nanowires (a) with the alumina partially and (b) with the alumina completely removed, and c) dispersed on Si substrate.

9.3.1 Ni Nanowires

Figure 9.2 displays the XRD patterns of the above-mentioned seven Ni samples. All Ni samples exhibit the fcc structure. The samples, Ni-2, -3, -6 and -7 (see Figs. 9.2b, 9.2c, 9.2f and 9.2g) have a preferred orientation along [220] direction, with little intensity at the (111) and (200) reflection. The strength at (111) exceeds that at (220) with the increase of the deposition temperature from room temperature to 40-60^{o}C (see Figs. 9.2d and 9.2e) at the applied voltage of 1.0 V. Decreasing the applied voltage also makes the (111) peak

stronger although (220) remains dominant (see Fig. 9.2a), while increasing the applied voltage suppresses other peaks than (220), even at high deposition temperature (60^{o}C) (see Fig. 9.2f). The pH value has no big impact on the structure of the Ni nanowires with the range from 2 to 6. If pH value is higher than 7, $Ni(OH)_2$ appears which prevents the formation of the Ni nanowires.

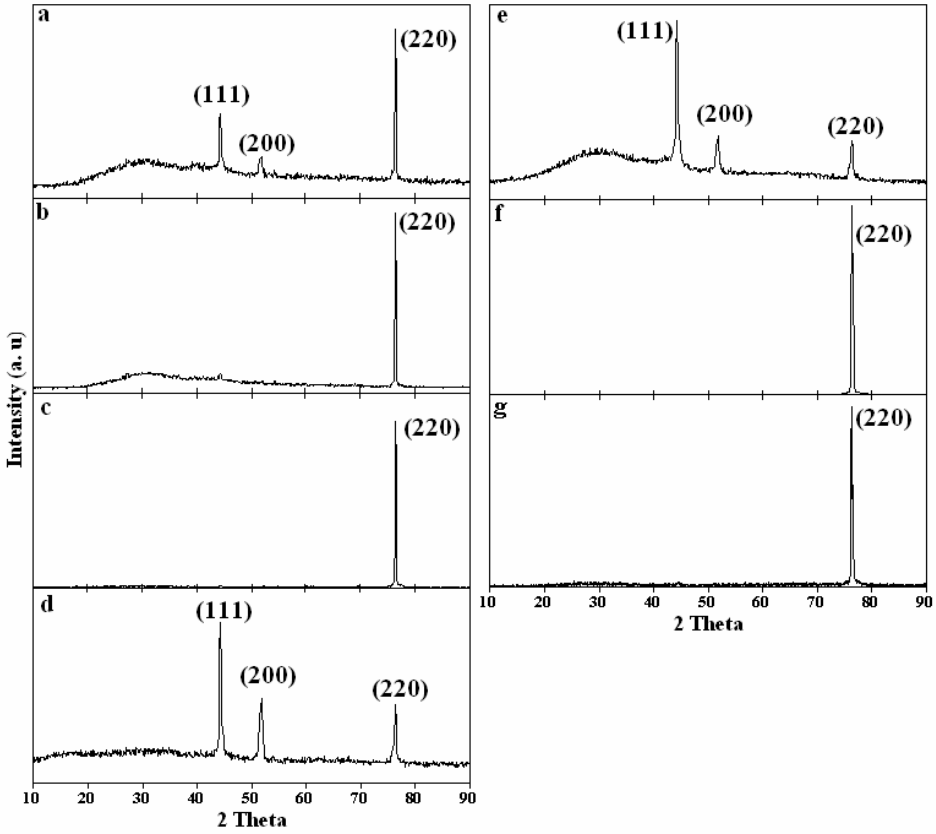

Fig. 9.2, XRD patterns for (a) Ni-1, (b) Ni-2, (c) Ni-3, (d) Ni-4, (e) Ni-5, (f) Ni-6 and (g) Ni-7.

The single- and poly-crystal structures were further confirmed by HRTEM and selected area electron diffraction (SAED). In Figs. 9.3a-b the single crystal structure of Ni-3 (Ni-2, Ni-6, and Ni-7 give similar images and patterns.) is clearly illustrated by SAED and HRTEM. As shown in Fig. 9.3a the diffraction pattern was taken from a selected area covering an as long as 2.0 micron segment of the nanowire, with uniform diameter 50 nm,

indicating the single crystallinity of Ni-2, -3, -6 and -7. The HRTEM image with [110] zone axis in Fig. 9.3b clearly shows lattice fringes of (111), ($\bar{1}\bar{1}1$) and (100) planes, suggesting single crystalline structure of the nanowire. The spotty diffraction rings in Fig. 9.3c and the dark contrast of the small crystals in Fig. 9.3d inset show the poly-crystalline nature of the Ni nanowires in Ni-1, -4, and -5. The crystalline grain size in these samples is about 5-10nm. Figure 9.4 clearly demonstrates that high-quality single crystal Ni nanowires can be fabricated by the AAO-template electrochemical deposition under controlled conditions.

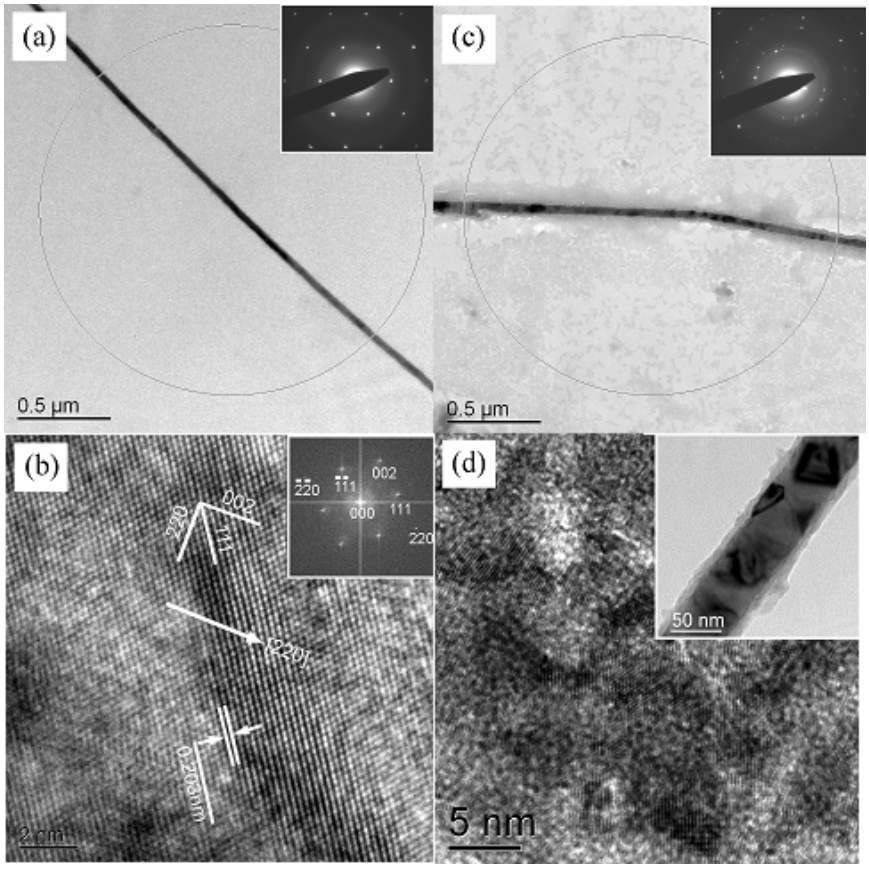

Fig. 9.3, TEM images and selective area electron diffraction patterns of Ni nanowires: (a) a Ni nanowire in Ni-3: the inset is the corresponding selective area ED, and the circle indicates that the size of selected area is as large as ~2.0 μ.; (b) HRTEM of Ni-3: the 0.203 nm interlayer spacing is characteristic of Ni (111) planes, and [220] is along the nanowire long axis; (c) Ni nanowires in Ni-4, and d) HRTEM images of Ni-4.

9.3.2 Co Nanowires

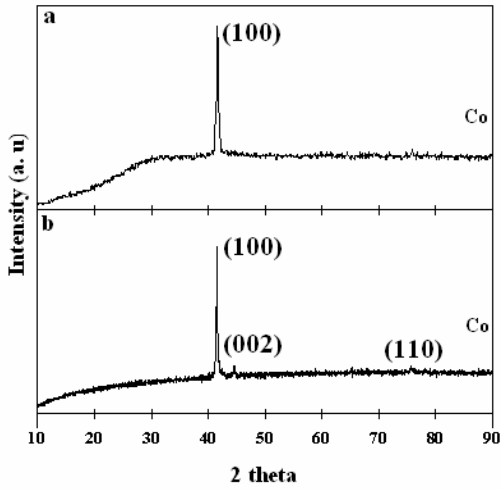

Fig. 9.4, XRD patterns for Co samples (a) Co-1; (b) Co-2.

The crystalline structure of Co nanowires greatly depends on the pH value of the electrolyte[18,19]. Co nanowires with fcc or hexagonal close-packed (hcp) structures can be produced by changing the pH value. In our experiments, Co nanowires have the hcp structure, as shown in Fig. 9.4. The strong (100) peak in the XRD pattern (see Fig. 9.4a) indicates that the Co-1 are [100]-preferred-oriented. As shown in Fig. 9.4b the (002) and (110) diffractions of sample Co-2 which are not observable in Fig. 9.4a are now observed, though in very low intensity.

9.3.3 Ag Nanowires

Figure 9.5a shows the XRD pattern of the Ag nanowires. The Ag-1 exhibits the fcc structure with a preferred orientation along [220] direction and little intensity at other directions, which is similar to Ni-2, -3, -6 and -7. The TEM image (Fig. 9.5b) and SAED pattern (the inset in Fig. 9.5b) indicated the single crystal structure of Ag nanowires.

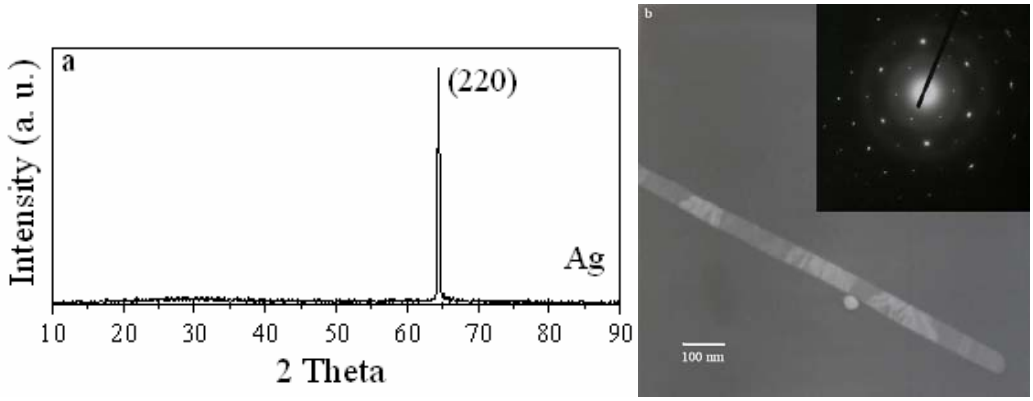

Fig. 9.5, XRD pattern for Ag-1 (a) and TEM image (b) with the SAED inserted.

9.3.4 Zn Nanowires

The XRD pattern of Zn nanowires is shown in Fig. 9.6. The Zn-1 shows the hcp structure with a preferred orientation along [220] direction and a little intensity at the (002) reflection. The TEM and SAED pattern are not available at present because the Zn nanowires are very easily oxidized in the distilled water when they freed from the template.

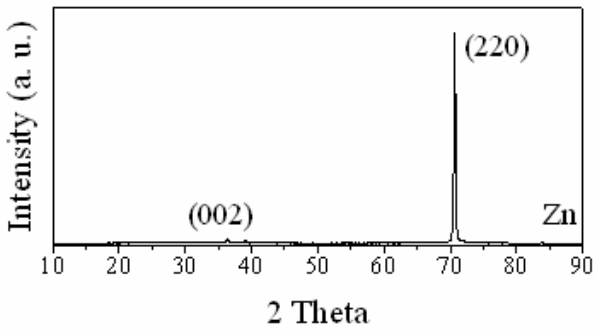

Fig. 9.6, XRD pattern for Zn-1.

9.3.5 Growth Mechanism

The electrodeposition is a complicated process and involves charge transfer, diffusion, reaction, adsorption and substrate. Therefore, the structure of the deposited nanowire is closely related to the deposition conditions and growth modes. Generally, three different

growth modes can be distinguished as schematically illustrated in Fig. 9.7 depending on the binding energy of metal atom on substrate (γ_{ms}) compared with that of metal atoms on native substrate (γ_{mm}), and on the crystallographic misfit characterized by interatomic distances d_m and d_s of 3D metal and substrate bulk phases, respectively[20]. Tian *et al*. attributed the single-crystal structure of electrodeposited low melting point metallic nanowires, such as Au, Ag and Cu, to the 2D-like nucleus[16], as shown in Fig. 9.7b. The crystalline nanowires will grow after the nucleus size exceeds the critical dimension N_c[16]. N_c for a 2D-like growth is expressed as:

$$N_c = \frac{bs\varepsilon^2}{(ze\eta)^2} \tag{1}$$

where s, ε, z and b are the area occupied by one metallic atom on the surface of the nucleus, the edge energy, the effective electron number, and a constant, respectively. And η is the overpotential and defined as:

$$\eta = E(I) - E_0 \tag{2}$$

where $E(I)$ and E_0 are the external current induced potential and the equilibrium potential of the electrode (potential in the absence of the external current), respectively. For 3D-like nucleus, N_c is expressed as:

$$N_c = \frac{8BV_m^2\sigma^3}{27(ze|\eta|)^3} \tag{3}$$

One possible reason for the single crystal growth of nanowires is the 2D-like nucleus[16] under lower overpotential because the smaller the overpotential, the larger N_c is, then the more favorable for a single crystal growth of nanowire. If only this mechanism is involved, it is difficult to explain the single crystal growth of higher melting point metal nanowires because N_c is smaller for 2D nucleation and favors the 3D cluster, as suggested in literature[16].

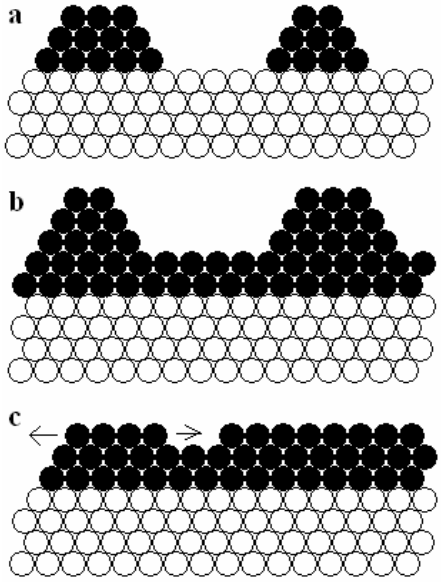

Fig. 9.7, Schematic representation of different growth modes in metal deposition on foreign substrate depending on the binding energy of metal atom on substrate (γ_{ms}), compared to that of metal atoms on native substrate (γ_{mm}), and on the crystallographic misfit characterized by interatomic distances d_m and d_s of 3D metal and substrate bulk phases, respectively. (a) "Volmer-Weber" growth mode (3D metal island formation) for $\gamma_{ms}<<\gamma_{mm}$ independent of the ratio $(d_m-d_s)/d_s$. (b) "Stranski-Krastanov" growth mode (metal layer-by-layer formation) for $\gamma_{ms}>>\gamma_{mm}$ and the ratio $(d_m-d_s)/d_s<0$ (negative misfit) or $(d_m-d_s)/d_s>0$ (positive misfit). (c) "Frank-van der Merwe" growth mode (metal layer-by-layer formation) for $\gamma_{ms}>>\gamma_{mm}$ and the ratio $(d_m-d_s)/d_s\approx0$.

In our cases, the metal nanowires were deposited on an amorphous substrate because the Pt film was sputtered on the back of AAO. An amorphous substrate is without an epitaxial influence and is inert with respect to the growth process of the deposit[21], although it would lead to growth of a specific lattice orientation under some specific cases. In the initial stages of the nanowire growth, the orientation of individual 3D nuclei is random and a newly coalesced compact deposit has perfectly random orientation. The texture of thicker metal deposits is a result of competitive growth mechanism occurring in a stage of growth subsequent to the coalescence stage. The low-surface-energy grains

grow easier than the high-energy grains do. The rapid growth of the low-surface-energy grains at the expense of the high-energy grains results in an increase in grain size and favors the formation of columnar grain. Figure 9.8 shows a columnar microstructure, which can be interpreted on the basis of the growth competition between adjacent grains as that of texture[22]. The development of the texture or columnar structure depends on the composition, substrate, overpotential and deposition conditions. As shown in Figs. 9.2a, 9.2b and 9.2c for Ni nanowires deposited at 25^{o}C with different applied voltage, only at high applied voltage (≥1.0 V) can the single crystal be produced. And the increase of the deposition temperature results in the formation of poly-crystal at lower overpotential. As expressed in Eq. (1) or (3), N_c decreases with the increase of the overpotential. N_c is not large enough to satisfy the 2D nucleus (Fig. 9.7b), as discussed in literature[16]. The single-crystal formation of Ni nanowires should be related to the model suggested in Fig. 9.8. The formation of columnar grain in the nanopore of AAO provides a possibility for the Ni single crystal due to the confinement of the nanopores after the competition between adjacent grains. However, the change of deposition temperature makes the appearance of polycrystal because the thermal energy distorts the competition between adjacent grains at constant overpotential. It was noticed that the strength of (111) peaks increases with the increase of the deposition temperature. The higher deposition temperature at constant overpotential (1.0 V) favors the growth of crystal with the orientation along [111]. But at larger overpotential (4.0 V), the single crystal structure can be produced even at higher temperature, as suggested in Fig. 9.2f. It is because the competition between the adsorption and desorption of H ions at the frontier growth surfaces of the nanowires, as discussed below.

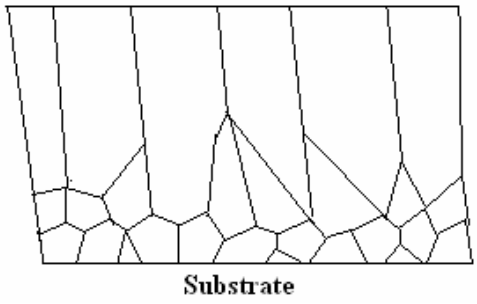

Fig. 9.8, Schematic cross section (perpendicular to the substrate) of the columnar deposition.

It was found that the overpotential and deposition temperature not only affect the crystallinity of the metal nanowires but also their structure. The metal naowires, produced in our experiments, prefer [220] direction. For Ni, the surface energy decreases along (110), (100) and (111). In electrochemistry, the low-surface-energy face more easily appears during the deposition. However, the preferred orientation not only depends on the native properties of the materials, but also on the deposition conditions, such as the overpotential, temperature, and electrolyte. For the deposition of Ni, the adsorption of H ions on the cathode stabilizes the (110) face[23]. And the higher overpotential induces the thermodynamics to kinetic transition in electrodeposition[24]. As illustrated in Fig. 9.2, (220) peak easily appears in our experiment. For single crystal structure, the preferred [220] direction is stable. For the preferred (220) growth of the single-crystal Ni nanowires, the model shown in Fig. 9.8 can be employed to understand the mechanism combining with the electrochemistry. For lower overpotential, (111) is preferred due to its low surface energy. However, the competition between (220) and (111) makes the formation of polycrystal due to the adsorption of H ions. The slightly higher overpotential kinetically favors the formation of (220) and the H adsorption stabilizes the process. This is the reason that (220) is preferred in the deposition of Ni nanowires. Also, the increase of the deposition temperature reduces the crystallinity of Ni nanowires, because the

temperature induces the change of the adsorption and the overpotential. At larger applied voltage, the effect of H-adsorption is dominant and can suppress that of the temperature (see Fig. 9.2f for Ni-6). Even with the increased pH value, the single crystal Ni nanowires can be produced (Fig. 9.2g). The same situation is suited to Ag nanowires (Fig. 9.5), where Ag single crystalline nanowires with the preferred orientation along [200] is observable. For Zn, the (001) surface energy is less than (220) surface energy. However, the preferred orientation [220] observed (Fig. 9.6) should be attributed to the same mechanism as discussed for Ni nanowires.

9.4 Magnetic Properties of Ni and Co Nanowires

The magnetic properties of nanowires embedded in the AAO template were measured by a vibrating sample magnetometer (Oxford Instruments) at room temperature.

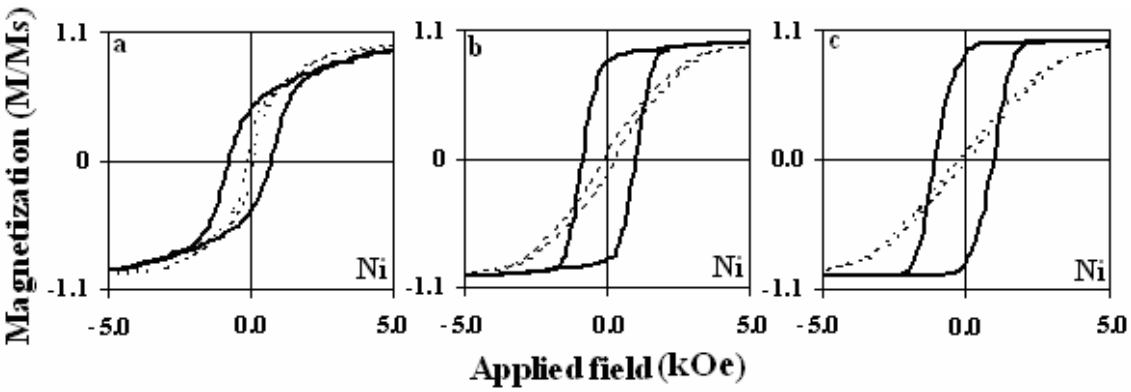

Fig. 9.9, Magnetization curves of the Ni nanowires embedded in the AAO template: (a) Ni-1, (b) Ni-2, (c) Ni-3. Solid line is for the applied magnetic field parallel to the long axis while dashed line for the perpendicular field.

The magnetic properties of Ni nanowires embedded in an AAO template are closely related to their physical properties, and therefore to the growth conditions. It is well known that reducing the nanowire diameter could improve the squareness of the

magnetization hysteresis, and raise the coercivity of nanowires[12]. Additionally the coercivity of the nanowires can be enhanced by increasing the nanowire length, which becomes saturated when the length exceeds a critical value at a constant diameter[2].

Our work has demonstrated that the crystallinity of the nanowires can greatly affect their magnetic properties. The magnetization hysteresis loops in Fig. 9.9 were measured for our Ni nanowires embedded in the AAO template at two different magnetic field directions, parallel (out-of-plane of the AAO template) or perpendicular to the nanowire long axis (in-plane of the AAO template). At the parallel direction Ni-2 which was prepared at an applied voltage of 1.0 V and a temperature of 25^{o}C has its coercivity H_c ($H_c^{\parallel}$) = 1000 Oe and the remanent magnetization M_r ($M_r^{\parallel}$) 88.6% of the saturated M_s, in other words, the squareness of the hysteresis of the Ni nanowires is about 0.886. The H_c and M_r values are both rather low at perpendicular direction, indicating an evident perpendicular anisotropy of the nanowires. When the single crystalinity is further improved in Ni-3 by increasing the applied electrodeposition voltage from 1 to 4 V while keeping the deposition at room temperature, the squareness of Ni-3 is enhanced to 93.7%. Note that the coercivity of Ni-3 remains at 1000 Oe, while its Mr increases up to saturated value of 93.7% of the saturated value. On the other hand, polycrystalline Ni-1, -4 and -5 have smaller $H_c^{\parallel}$, $M_r^{\parallel}$ and the squareness of the hysteresis than those of Ni-2 (see Table 9.1). The reduction of $H_c^{\parallel}$ (1000Oe→740Oe) is not as much as that of $M_r^{\parallel}$ and the squareness (94%→36%). It is worthy to note that our sample 3 has much higher magnetic squarness compared to the sample B in Ref. 12 (94% vs 86%). The Sample B in Ref. 12 is smaller in diameter (40 nm), but our sample is 50 nm in diameter. So the better magnetic squareness must be due to better single crystallinity of Ni-3. All these results indicate that

the crystalline structure and arrangements of Ni nanowirs can greatly affect the magnetic properties. Hence by controlling the growth condition we are able to prepare high quality single crystalline Ni nanowires with excellent magnetic properties.

Sample	H_c (Oe) (perpendicular)	H_c (Oe) (parallel)	M_r/M_s (perpendicular)	M_r/M_s(parallel)
Ni-1	182	746	0.094	0.369
Ni-2	193	1000	0.066	0.887
Ni-3	101	1000	0.045	0.937
Ni-4	159	764	0.091	0.453
Ni-5	147	857	0.148	0.639
Ni-6	101	1000	0.045	0.937
Ni-7	101	1000	0.045	0.937
Co-1	353	1800	0.056	0.808
Co-2	775	1680	0.117	0.678

Table 9.1, Coercivity H_c and squarness of Ni and Co nanowires.

The magnetic anisotropy of the nanowires results from the interplay of a series of effects: the macroscopic demagnetization field ($H_d=-6\pi M_s P$[25], P is the porosity of the template and M_s=500 emu/cm^3 for the Ni bulk value of the saturation magnetization; for Ni nanowires with the diameter of 50 nm, P=22.6% and H_d=-2130 Oe), the form effect of individual nanowire ($H_f=2\pi M_s$; for Ni nanowires, H_f=3140 Oe), and magnetocrystalline anisotropy energy ($H_m=\frac{-2k_1}{\mu_0 M_s}$, k_1 is the magnetocrystalline anisotropy coefficient; for Ni nanowires, H_m=140 Oe along [111] direction). By neglecting H_m, the theoretical effective coercive field of the nanowires is given by $H_c^{\parallel} = H_f - H_d$. For Ni nanowires with the diameter of 50 nm, $H_c^{\parallel}$=1010 Oe. The measured $H_c^{\parallel}$(=1000 Oe) is consistent with the theoretical result.

The magnetization hysteresis loops in Fig. 9.10a were measured for Co-1, i.e. the Co nanowires embedded in the AAO template (50 nm diameter and 100 nm interpore

spacing) at two different magnetic field directions, parallel or perpendicular to the nanowires' long axis, respectively. For Co-1, the coercivity H_c ($H_c^{\parallel}$) = 1800 Oe, and the remanent magnetization M_r ($M_r^{\parallel}$) equals 80.8% of the saturated M_s. The H_c and M_r values are both rather low at perpendicular field direction. It is worthy to note that the coercivity and magnetic squareness of Co-1 are comparable to the best sample (pH=6.4) in Ref 18 although the diameter of our Co-1 (50 nm) is much larger than that of their sample in Ref 18 (30 nm). The possible reason should attribute to the much better crystallinity in our samples. For Co-2, the coercivity H_c ($H_c^{\parallel}$) = 1620 Oe and the remanent magnetization M_r ($M_r^{\parallel}$)/M_s =67.8% (Fig. 9.10b). Both are lower than those of Co-1 due to the reduction of single crystallinity in Co-2. It should be noted that the easy magnetic axis of bulk Co is [001] so that the magnetic properties (remanence and coercivity) of Co nanowires would be further improved when [001]-oriented Co nanowires were fabricated.

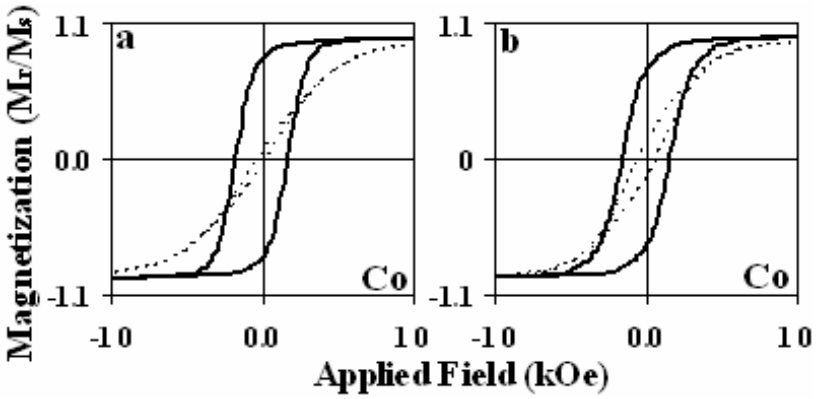

Fig. 9.10, Magnetization curves of the Co nanowires embedded in the AAO template: (a) Co-1 and (b) Co-2. Solid line is for the applied magnetic field parallel to the long axis while dashed line for the perpendicular field.

For Co nanowires with the diameter of 50 nm, H_d=5960 Oe (M_s=1400 emu/cm^3 the Co bulk value of the saturation magnetization), H_f=8790 Oe, and average magnetocrystalline anisotropy energy (H_m=6400 Oe). Physically, the theoretical effective coercive field of

the Co nanowires is given by $H_c^{\parallel} = H_f - H_d$. For Co nanowires with the diameter of 50 nm, $H_c^{\parallel}$=2830 Oe. The measured $H_c^{\parallel}$ (=1800 Oe) is smaller than the theoretical result because of the strong dipolar interactions among the nanowires.

9.5 Optical Limiting of Metal Nanowires

To study the optical limiting properties of metal nanowires, more metal nanowires were fabricated. Other metal nanowires were prepared at the same electro-deposition conditions as the Ni deposition, using a corresponding sulfate or chloride electrolyte. The MNWs prepared and studied include Ni nanowires (NiNW), Pd nanowires, (PdNW), Pt nanowires (PtNW), Ag nanowires (AgNW), Cu nanowires (CuNW) and Co nanowires (CoNW).

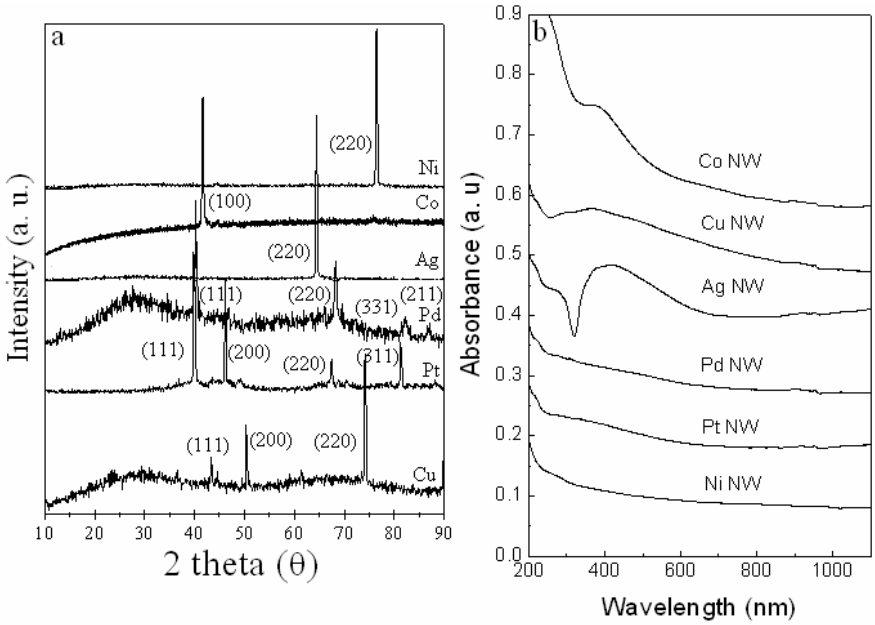

Fig. 9.11, (a) The XRD patterns of the MNWs and (b) the optical absorption spectra of the MNWs.

Figure 9.11a displays the XRD patterns of the MNWs. The Ni, Co and Ag nanowires each exhibit only one diffraction peak at the orientation along [220], [100] and [220],

respectively. They are single crystals. For Pd, Pt and Cu nanowires, the characteristic peaks are observable in their XRD patterns. The high intensity and small peak width indicate the good crystallinity of the nanowires. HRTEM confirms that the Pd, Pt, and Cu nanowires are polycrystalline.

For optical measurements, the MNWs were totally liberated from AAO template (using 1 M NaOH solution), cleaned in distilled water till pH = 7, and suspended in distilled water. All six samples have similar diameter and length because of identical AAO template and deposition conditions. In the optical absorption spectra shown in Fig. 9.11b, absorption bands around 250-600 nm are noticed, particularly for Co, Cu and Ag nanowires. There is a dip in the absorption spectrum at 320 nm (3.8 eV) for Ag nanowire solution. According to literature[26] this is photon-induced Ag-bulk-plasmon emission. The broad band of the absorption around 430 nm (2.9 eV) in the Ag spectrum is therefore attributed to surface plasmon resonance[27] and its long-wave-length tail is due to d-sp interband transitions[26]. Similar assignments can be applied to the absorption bands for Cu and Co nanowires[27]. The optical absorption is weak for Ni, Pd and Pt nanowire solutions in the entire range between 300-1100 nm. It seems that the latter group of metals has higher values of work function and first ionization potential[28] and their plasmon resonance would be in the shorter wavelength range[29].

Their optical limiting properties were studied by fluence-dependent transmission measurements, using 7-ns light pulses generated from a frequency-doubled Q-switched Nd:YAG laser (Spectra Physics DCR3), at two different wavelengths (532-nm and 1064-nm). The laser pulses were produced at 10 Hz repetition rate; and were focused on the

central point of the quartz cell with a spot radius of 30 μm. The nonlinear scattering measurements were conducted with the detector set at various angles from the propagation axis of the transmitted laser pulses. An aperture was placed in front of the detector. The radius of the aperture was adjusted so that a solid angle for collecting the scattered light was 0.015 rad. To study the nonlinear optical (NLO) response of the MNWs, the fluence-dependent light transmission measurements were conducted on the six samples under the same conditions at two wavelengths, 532 nm (see Fig. 9.12a) and 1064 nm (Fig. 9.12b) respectively. Nevertheless the concentration of the MNWs in the tested solutions could be different, adjusted in such a way that their linear transmittances are all 80%. In Fig. 9.13a the energy transmittance at the light fluences less than 0.08 J/cm^2 is constant for all the samples. However, in excess of 0.08 J/cm^2, the transmittance decreases as the incident fluence increases, a typical limiting property for all nanowires. The limiting threshold, defined as the incident fluence at which the transmittance falls to 50% of the normalized linear transmittance[30], is different for different metal nanowire samples. The limiting threshold at 532 nm is 0.9, 1.2, 1.3, 1.7, 2.5 and 4.2 J/cm^2 for Pd, Ni, Pt, Ag, Cu and Co nanowires, respectively. The nonlinear optical limiting responses of Pd, Ni, Pt and Ag nanowires are comparable to or slightly better than those of single-wall and multi-wall carbon nanotubes[31,32] (Table 9.2), whereas CuNWs and CoNWs are slightly poorer. Figure 9.13b shows similar optical limiting properties of MNWs at 1064 nm. The optical limiting of Pd, Pt, Ni and Ag nanowires is better than or comparable to those of carbon nanotubes at 1064 nm whereas Cu and Co nanowires are slightly poorer. The limiting threshold at 1064 nm radiation is 8, 8, 8, and 10.8 J/cm^2 for Pd, Pt, Ag, and Ni nanowires and larger than 30 J/cm^2 for Cu and Co nanowires, respectively. Obviously the nonlinear optical limiting is much weaker at 1064 nm as compared to that at 532 nm.

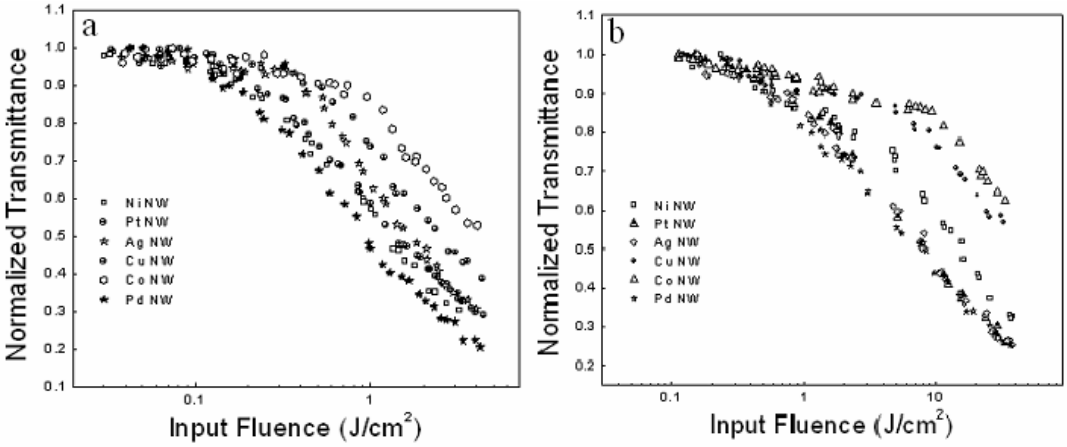

Fig. 9.12, The optical limiting response of the MNWs measured with 7-ns laser pulses at (a) 532-nm; and (b) 1064-nm wavelength.

Samples	F_{th} at 532 nm (J/cm^2)	F_{th} at 1064 nm (J/cm^2)
PdNWs	0.9	8
NiNWs	1.2	8
PtNWs	1.3	8
AgNWs	1.7	10.8
CuNWs	2.5	>30
CoNWs	4.2	>30
MWNTs	1.0 (Ref. 33)[33]	10.0 (Ref. 33)[33]

Table 9.2, The limiting threshold of metal nanowires at 532 nm and 1064 nm. The limiting threshold of multi-wall carbon nanotubes (MWNTs) is also listed for comparison.

There are several mechanisms proposed for optical limiting, including two-phonon absorption (TPA), free-carrier absorption (FCA) associated with TPA, reverse-saturable absorption (RSA), self-focusing/defocusing, thermal blooming and nonlinear scattering[34,35]. The observation of nonlinear limiting for all the MNWs at 1064 nm laser incidence in this work unambiguously shows that nonlinear scattering is a major mechanism responsible for the nonlinear limiting of the metal nanowires, since the energy of 1064 nm laser light is too low (1.16 eV) for single-photon excitation which generally

requires much higher photon energy (e.g. 2.15 eV for Cu and 3.6 eV for Ag)[26]. In nonlinear scattering, the key mechanism is the photon-induced ionization and excitation of the metal atoms in MNW suspensions. This leads to the formation of rapidly expanding micro-plasmas, which strongly scatter the incident light and results in the limiting behavior[31,32]. The response of the optical limiting induced by the nonlinear scattering is related to the ability of the photoionization of the atoms and the subsequent expansion of the micro-plasmas, as previously observed in different carbon nanotubes[31,32]. Because of the observation of the optical limiting in all the MNWs with the 1064 nm laser, the ionization must be a two-photon or multiple-photon process. Therefore, the light scattering by these samples is nonlinear, rapidly increasing with increasing light intensity[35,36]. Cu and Co nanowires have shown optical absorption at relatively long wave lengths (300-600 nm) (see Fig. 9.12) and hence have weaker nonlinear limiting ability due to saturable absorption[37]. Moreover, the nonlinear scattering, measured at 532 nm for all the MNWs, becomes stronger with increasing incident energy. One of these measurements at an angle of 10^{o} is displayed in Fig. 9.13. The nonlinear scattering is confined in the forward direction; and the scattered light energy decreases as the scattered angle arises, as shown in the inset of Fig. 9.13. Similarity in nonlinear scattering between the MNWs and MWNT strongly indicates that nonlinear scattering is dominant for the optical limiting observed in the MNWs. On the other hand, Pd and Pt are expected to have optical absorption only at shorter wavelengths (<200nm) due to higher surface plasmon resonance and their nonlinear limiting properties is more evident, slightly better than carbon nanotubes. For the nonlinear limiting of MNWs at 532 nm (2.32 eV) laser incidence, some d-sp interband or near-fermi-level intraband transitions may become possible and other mechanisms than nonlinear scattering may also contribute to the

nonlinear limiting. If the light absorption of the electrons in the excited levels is of greater probability than that of the ground state, nonlinear reverse-saturable absorption (RSA) would occur and its characteristic absorption would increase with light intensity. Nevertheless the fact that MNWs samples have similar optical limiting response in the two laser energies (532 and 1064 nm) seems to indicate that nonlinear scattering is the dominant mechanism.

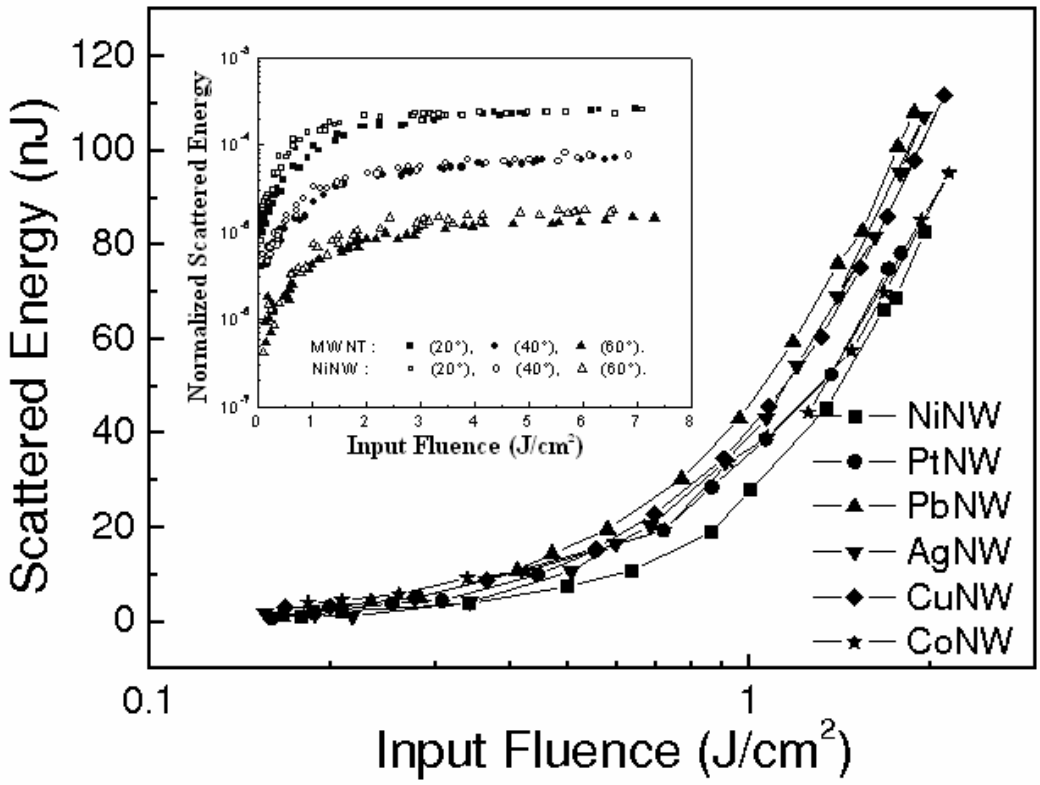

Fig. 9.13 Nonlinear scattering measured with 532-nm, 7-ns laser pulses at a forward angle of 10º with a solid angle of 0.015 rad. The inset shows the scattered energy of the NiNW and the MWNT as a function of the input fluence at various forward angles.

9.6 Summary

In summary, metal nanowires, Ni, Ag, Cu, Zn, Co, Pt, and Pd, were produced based on the AAO template via the electrodeposition. The Ni, Ag, and Zn nanowires prefer the

[220] orientation, while Co nanowires prefer the [100] direction under proper deposition conditions. By changing the deposition conditions, overpotential, pH value and temperature, polycrystal nanowires were produced. Thermodynamic and electrochemical analysis revealed that the crystallinity of the metal nanowires were closely related to the deposition conditions. Magnetic study shows that the single crystalline Ni and Co have larger coercivity, higher magnetization squareness and significant anisotropy. The optical limiting properties of Pt, Ni, Pd and Ag nanowires are better than those of Cu and Co nanowires. With the observation of optical limiting both at 532 nm and 1064 nm, nonlinear scattering is believed to make a dominant contribution to the limiting performance of metal nanowires.

References:

[1] E. Z. da Silva, F.D. Novaes, A. J. R. da Silva, and A. Fazzio, Phys. Rev. B 69, 115411 (2004).
[2] F. Favier, E. C. Walter, M. P. Zach, T. Benter, and R. M. Penner, Science 293, 2227 (2001).
[3] S. Ciraci, A. Buldum and I. P. Batra, J. Phys.: Condens. Matter 13**,** R537 (2001).
[4] T. M. Whitney, J. S Jiang, P. C. Searson and C. L. Chein, Science 261, 1316 (1993).
[5] S. Y. Chou, M. S. Wei, P. R. Krauss, and P. B. Fischer, J. Appl. Phys. 76, 6673 (1994).
[6] W. Wu, B. Cui, X. Sun, W. Zhang, L. Zhuang, L. Kong, and S. Y. Chou, J. Vac. Sci. Technol. B 16, 3825 (1998).
[7] G. M. McClelland, M. W. Hart, C.T. Rettner, M. E. Best, K. R. Carter, and B.D. Terris, 81, 1483 (2002).
[8] J. M. Garcya, A. Asenjo, J. Velazquez, D. Garcýa, M. Vazquez, P. Aranda and E. Ruiz-Hitzky, J. Appl. Phys. 85, 5480(1999).
[9] G. C. Han, B. Y. Zong, and Y. H. Wu, IEEE Trans. on Magn. 38, 2562 (2002).
[10] D.J. Sellmyer, M. Zheng and R. Skomski, J. Phys.: Condens. Matter 13, R433 (2001).
[11] R. Skomski, R.D. Kirby and D.J. Sellmyer, J. Appl. Phys. 85, 5069 (1999).
[12] K. Nielsch, R.B. Wehrspphn, J. Barthel, J. Kirschner, U. Gosele, S.F. Ficher, and H. Kronmuller, Appl. Phys. Lett. 79, 1360 (2001).
[13] G. Sauer, G. Brehm, S. Schneider, K. Nielsch, R. B. Wehrspohn, J. Choi, H. Hofmeister, and U. Gosele, J Appl. Phys. 91, 3243 (2002)
[14] A. J. Yin, J. Li, W. Jian, A. J. Bennett, and J. M. Xu, Appl. Phys. Lett. 79, 1039 (2001).

[15] Y. Li, G. W. Meng, and L. D. Zhang, and F. Phillipp, Appl. Phys. Lett. 76, 2011 (2000).
[16] M. Tian, J. Wang, J. Kurtz, T. E. Mallouk, and M. H. W. Chan, Nano Lett. 3, 919 (2003).
[17] C. G. Jin, W. F. Liu, C. Jia, X. Q. Xiang, W. L. Cai, L. Z. Yao, and X. G. Li, J. of Crystal Growth 258, 337 (2003).
[18] M. Darques, A. Encinas, L. Vila and L. Piraux, J. Phys. D: Appl. Phys. 37, 1411 (2004).
[19] F. Li, T. Wang, L. Ren and J. Sun, J. Phys.: Condens. Matter 16, 8053 (2004).
[20] M. Paunovic and M. Schleinger, Fundamentals of Electrochemical Deposition, John Wiley & Sons, 1998, p125.
[21] J. Amblart, M. Froment, G. Maurin, N. Spyrellis, and E. T. Trevisan-Souteyrand, Electronchim. Acta 28, 909 (1983).
[22] D. J. Srolovitz, A. Mazor, and G. G. Bukiet, J. Vac. Sci. Technol. A 6, 2371 (1988).
[23] E. Budevski, G. Staikov, and W. J. Lorenz, Electrochemical Phase Formation and Growth: An introduction to the initial stage of metal deposition, VCH, 1996, p267.
[24] J. A. Switzer, H. M. Kothari, and E. W. Bohannan, J. Phys. Chem. B 106, 4027 (2002).
[25] A. Encinas-Oropesa, M. Demand, L. Piraux, I. Huynen, U. Ebels, Phys. Rev. B 63, 104415 (2001).
[26] G. T. Boyd, Z. H. Yu, and Y. R. Shen, Phys. Rev. B 33, 7923 (1986).
[27] J-Y Bigot, V. Halte, J-C Merle and A. Daunois, Chem. Phys. 251, 181 (2000).
[28] H.B. Michaelson, IBM J. Res. Develop. 22, 72 (1978).
[29] M.A. Ordal et al Appl. Optics 22, 1099 (1983).
[30] X. Sun, Y. Xiong, P. Chen, J. Lin, W. Ji, J.H. Lim, S.S. Yang, D. J. Hagan and E.W. Van Stryland, Appl Optics 39, 1998 (2000).
[31] P. Chen, X. Wu, X. Sun, J. Lin, W. Ji and K.L. Tan, Phys. Rev. Lett. 82, 2548 (1998).
[32] D.G. Mclean, R.L. Sutherland, M.C. Brant, D.M. Brandelik, P.A. Fleitz and T. Pottenger, Optics Lett.18, 858 (1993).
[33] X. Sun, R. Q. Yu, G. Q. Xu, T. S. A. Hor, and W. Ji, Appl. Phys. Lett. 73, 3632 (1998).
[34] L.W. Tutt and T.F. Boggess, Prog. Quant. Electr. 17, 299 (1993).
[35] M.A. El-Sayed, Acc. Chem. Res. 34, 257 (2001).
[36] P.V. Kamat, M. Flumiani and G.V. Hartland J. Phys. Chem. B 102, 3123 (1998).
[37] R. Philip, G. R. Kumar, N. Sandhyarani and T. Pradeep, Phys. Rev. B 62, 13160 (2000).

CHAPTER 10

SEMICONDUCTOR NANOSTRUCTURES BY THERMAL EVAPORATION

10.1 Introduction: Thermal Evaporation Method

As one kind of gas-phase growth method, thermal evaporation is the simplest method to produce nanostructures. In this process, vapor is first generated by thermal evaporation. The vapor is subsequently transported and condensed onto a substrate. The method has been used to prepare oxide, metal whiskers with micrometer diameters. The size of the whiskers can be controlled by supersaturation, nucleation sizes, pressure and the growth time, etc.

The schematic diagram of the apparatus used in our experiments is illustrated in Fig. 10.1, which is very similar to that used in the laser ablation method[5]. A quartz tube of 1.2m in length was mounted inside a high temperature furnace.

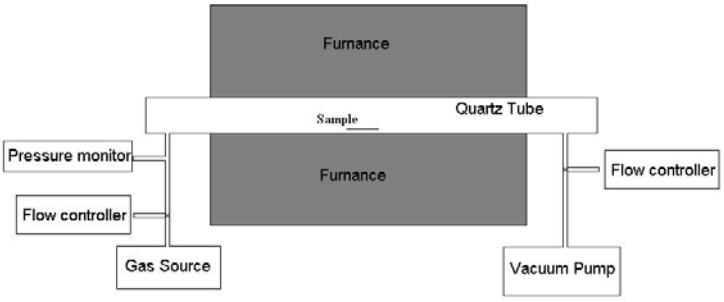

Fig. 10.1, The schematic diagram of the thermal-evaporation growth apparatus.

Generally, after the furnace temperature reaches the designed temperature at a designed heating rate, the temperature is kept constant for a period. After the growth process, the

furnace was cooled down to room temperature slowly. During the process, high purity Helium or Argon is used as protective gas at a designed flow rate. The growth conditions, such temperature, pressure, gas flow rate, and gas source, can be controlled to produce a varieties of nanostructures, as indicated in Fig. 10.1.

In this chapter, a thermal evaporation method was proposed to produce SiNWs and ZnO nanostructures without catalyst. The optical properties of SiNWs, including photoluminescence and optical limiting, were investigated. The field emission, hydrogen storage and optical properties of ZnO nanostructures were studied to explore their potential applications in nanodevices and energy.

10.2 Si Nanowires Based on Thermal Evaporation

10.2.1 Silicon Nanowires

Silicon is one of the most important and fundamental electronic materials in computer and information technology (IT) industry. Recently, Si nanowires (SiNWs) have attracted great attention due to their potential applications in Si-based nanodevices[1,2], including optoelectronic nanodevices[3]. A variety of techniques on the synthesis of SiNWs have been developed, such as electrochemical and chemical dissolution of wafers[4], laser ablation[5,6,7], nano-lithography[8,9], thermal vaporization[10], carbon-thermal synthesis[11] and field vaporization[12]. Usually, the growth of SiNWs needs the assistance of catalysts such as Fe, Co, Ni, Zn, Ti, Au, Ga, C or SiO, SiO_2[1-12,13]. However, the catalysts used in the growth may contaminate SiNWs and reduce the performance of devices. Therefore, growing SiNWs without catalyst is desired.

10.2.2 Experimental Details

To produce SiNWs, the commercial boron doped Si (111) substrate (1~3Ω·cm) with one surface polished was used, which was cut to small pieces before loading into the furnace. Some pieces were immersed in HF solution to remove oxide and contamination on the surfaces (samples A). Some were oxidized in air at high temperature to produce a layer of silicon oxide on Si surfaces to study the effect of the oxide layer on the growth of SiNWs (samples B). The acid-treated Si pieces (Samples A) were transferred to the quartz tube quickly, which was evacuated by a mechanical rotary pump to 1 Pa. High purity Helium was then introduced into the quartz tube at a flow rate of 100 standard cubic centimeters per second (sccm). The total tube pressure was kept at 50 Pa. After the furnace temperature had reached to 1100^{o}C, the pressure was kept to 4000 Pa. To investigate the effects of pressure and temperature, the growth conditions were changed in a pressure range from 50 Pa to one bar and a temperature range from 800 to 1100^{o}C. After three-hour growth process, the furnace was cooled down to room temperature slowly.

The morphology of SiNWs on the Si substrate was directly observed on scanning electron microscope (SEM, JEOL JSM-6700F). Some nanowires were scratched from the substrate and dispersed in ethanol, and then dropped onto a copper grid of holey carbon film destined by high resolution transmission electron microscope (HRTEM, JEOL 2010) at 200kv acceleration voltage at room temperature. The structure of nanowires was further characterized by XRD (Brucker AXS D8). Raman scattering measurements of the as-grown SiNWs were performed by using the micro-Raman Renishaw 2000 system (with 1cm^{-1} resolution and 0.4 cm^{-1} reproducibility, at the excitation source of 514.5 nm) at room temperature.

10.2.3 Characterization of SiNWs

The samples were taken out of the quartz tube after the furnace temperature reached the room temperature. For the acid (HF) -treated samples (samples A), the surfaces were black and turned to gray after exposed in the air due to the oxidation of SiNWs' surfaces. One piece of the samples (sample A1) was firstly immersed in HF solution, cleaned in distilled water and characterized by SEM. Another piece (sample A2) was directly observed by SEM. SiNWs were observed on both pieces, which indicates that SiNWs were really produced. But for the oxidized samples (samples B), no nanowires were observed on the surfaces. It can be concluded that the thicker oxide layer (SiO_2) prevents the formation of SiNWs during the thermal process.

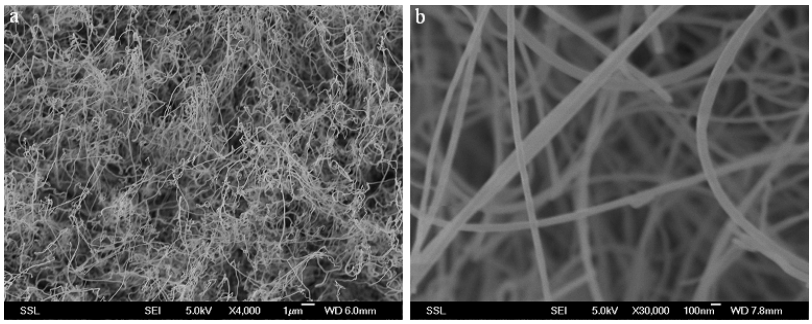

Fig. 10.2, The SEM images of SiNWs produced by thermal-evaporation based on Si substrate. (a) A typical SEM image of SiNWs at the center of the Si substrate; (b) A local view of the SiNWs.

The SEM images of the representative morphology of SiNWs are shown in Fig. 10.2. In Fig. 10.2a, dense nanowires can be observed. The sample consists of SiNWs with diameters ranging from 10 to 100 nm and length up to a few hundreds of μm. The SiNWs were tangled together above the Si substrate. And most of SiNWs are smoothly curved with straight sections along the nanowires, as shown in Fig. 10.2b. The SEM observation of SiNWs' roots remaining on the substrate proves that the nanowires were grown directly from the substrate.

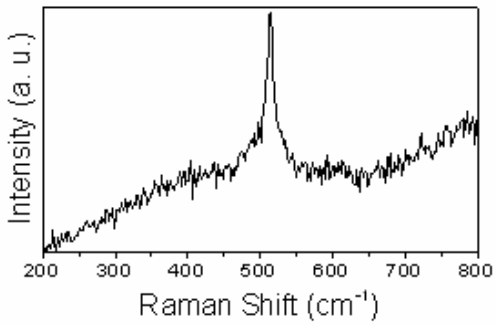

Fig. 10.3, The Raman shift of SiNWs measured at room temperature.

Raman spectroscopy is very sensitive to the lattice structure and the crystal symmetry. Raman study of SiNWs had been reported in details in literature[14]. Raman spectroscopy (peak energy, peak width, and symmetry) of nano-Si changes with the reduction of the size. The first-order Raman peak of Si crystal at 521cm^{-1} is symmetric. The Raman spectrum of Si nanowires is asymmetric centered at 512cm^{-1} in our experiments with an extended tails at low frequency (Fig. 10.3), which is attributed to the nanosize effect and internal structural defects of Si nanowires. The Raman spectroscopy confirms that the SiNWs were produced.

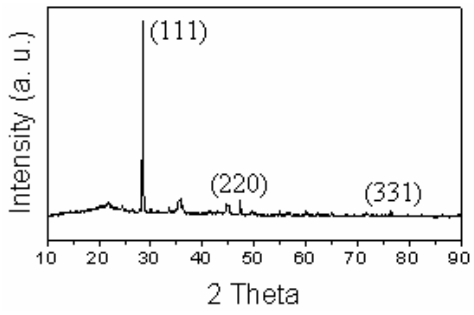

Fig. 10.4, The XRD spectrum of SiNWs measured at room temperature.

The structure of nanowires was characterized by XRD and HRTEM. In Fig. 10.4, the diffraction peaks for the Si (111), (220) and (331) planes are observable. Note that the diffraction intensity of (220) and (311) is extremely low for our SiNWs sample. Usually

for polycrystalline Si powders and for the Si nanowires prepared by laser ablation[6] the diffraction intensity of (220), (311) and other higher lattice index are evidently observable, being 50%, 20% as strong as that of the (111) diffraction. This reveals the one-orientation growth of our SiNWs sample. The TEM image of SiNWs is presented in Fig. 10.5a. The image confirms that the nanowires, produced in our experiments, are with diameters ranging from 10 to 100 nm. Selected-area electron diffraction (SEAD) patterns (Fig. 10.5b and 10.5c) reveal different crystallizations for SiNWs with different diameter. The bright spots (Fig. 10.5b), taken from SiNWs with smaller diameter, suggest the crystal structure of the nanowire. But a diffractive ring pattern in Fig. 10.5c, taken from SiNWs with larger diameter, reveals that the nanowire is in an amorphous state.

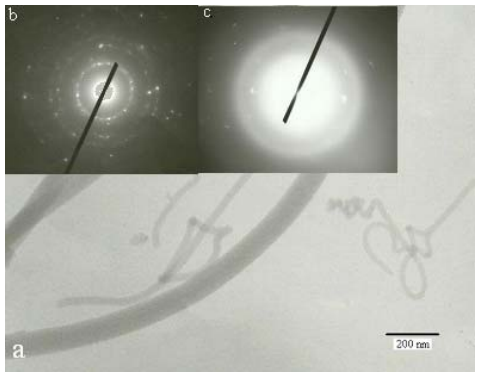

Fig. 10.5, (a) TEM micrograph showing the morphology of Si nanowires grown on Si substrate; (b) the SEAD pattern taken from the nanowires located at the center of the substrate; (c) the SEAD pattern taken from the nanowires located at the edge of the substrate.

10.2.4 Effects of Growth Conditions

The quality and production of SiNWs are greatly related to the growth conditions. In our experiments, SiNWs cannot be produced if the temperature is less than 1100^{o}C. SEM images (Fig. 10.6) are taken from three samples, Fig. 10.6a at lower pressure (50 Pa), Fig. 10.6b at 8000Pa, and Fig. 10.6c at atmosphere pressure, which clearly illustrates the effect of the pressure. At very lower or higher pressure, the production of SiNWs is less

than that at 4000 Pa (Fig. 10.2a). At lower pressure, the SiNWs are smaller (20nm in diameter) due to the escape of Si atoms. And at higher pressure, the SiNWs are bigger (100 nm). At atmosphere pressure, the textured surface appears on the Si substrate, but SiNWs cannot be observed. It can be concluded that the production and diameter of SiNWs can be controlled by the pressure.

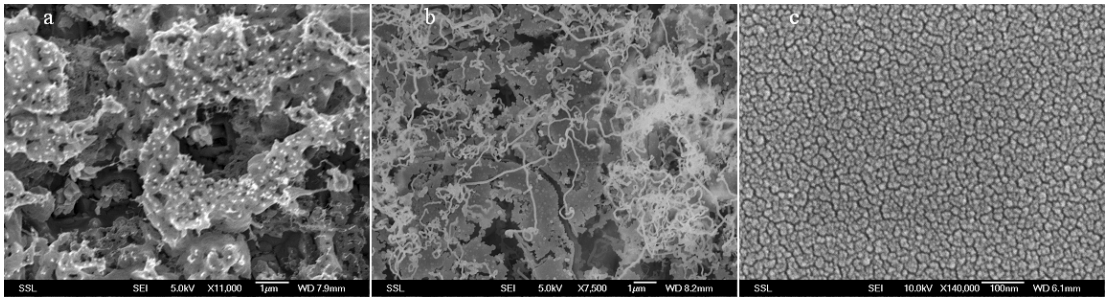

Fig, 10.6, SEM image of SiNWs produced at a pressure of (a) 50 Pa, (b) 8000 Pa and (c) atmosphere pressure.

10.2.5 Growth Mechanism of SiNWs

For catalyst-assisted growth of SiNWs, a model had been proposed by Lieber *et al.*[5]. It was noticed that SiO_x can assist the growth of SiNWs[15]. In our cases, no catalyst is involved in the process. Therefore, the growth of SiNWs should be based on following two possible mechanisms. One possible reason is the Oxygen-assisted growth under sub-ambience. The oxygen may come from the Si substrate, or trace impurity in He gas. And the oxygen atoms form SiO_x with thermal evaporated Si atoms. The SiO_x at the Si surface serves as seeds and enhances the growth of SiNWs, which is similar to SiO_x-enhanced vapor-solid mechanism[15,16,17,18]. Another possible reason is the non-uniform melting and the low pressure ambience. In details, the melting Si surface provides the source for the formation of SiNWs. With the formation of liquid Si at the surface and the non-uniform melting, some solid Si particles are surrounded by the liquid Si. These particles play a

role of seeds. In our case, the seeds were pushed upward tilted to the He flow induced by the low pressure. Figure 10.7a gives a picture of the growth of SiNWs at the center. It is observed that some SiNWs shared one seed (head), just like "Octopus". Some have one seed per SiNW. The "Octopus" structure is caused by the abundant supply of melting Si, which makes a bigger wire separated to reduce the effect of the gravity. For single head SiNWs, it is possibly due to the low supply of the melting Si. The growth of SiNWs in this way is mainly solid-liquid-solid (SLS) mode. This should be the reason that the preferred orientation is (111) because (111) Si substrate was used.

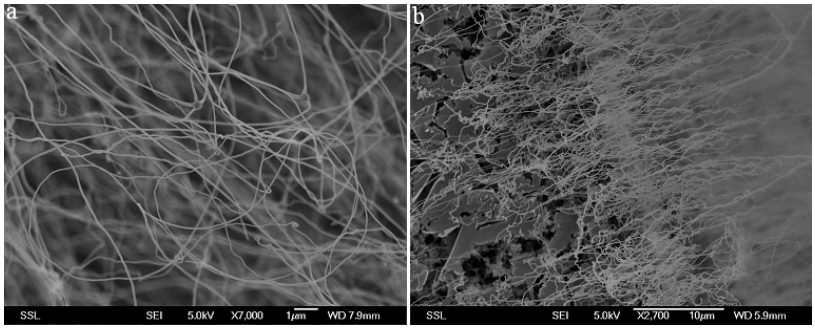

Fig. 10.7, (a) The "Octopus" structure of SiNWs at the center of the Si substrate and (b) SiNWs at the edge of the Si substrate.

Figure 10.7b shows the SiNWs growing at the edge down of the gas flow. The direction of SiNWs is parallel to that of the gas flow. The SiNWs are rooted at the edge of the substrate. The surface of the Si substrate near the edge became rough, where the cracks appeared on the surface due to the thermal evaporation. The formation of SiNWs rooted at the edge is mostly contributed to the Si vapor caused by the thermal process. These Si atoms flowed with the He and some of them were captured by the edge of the substrate down of the flow due to the edge effect which has more chances to trap atoms than the flat plane or corner because of the larger contact area. With the formation of the nucleation, more Si atoms attached on the tips of the nucleation, which leads to the

formation of nanowires. At the same time, the Si atoms attached on the surfaces of SiNWs making the SiNWs' diameter increase. The process is similar to the vapor-liquid-solid (VLS) model[17]. However, the liquid state is transient. Exactly, the real process is the vapor-solid (VS).

10.2.6 Optical Properties of SiNWs

In order to understand the electronic structure of our SiNWs, photoluminescence (PL) study was performed at room temperature on Cary Eclipse with a high intensity Xenon lamp at 265 nm (4.65 eV). To gain better insight of the nonlinear optical (NLO) response of SiNWs, we performed the fluence-dependent transmission measurement on our SiNWs and commercial Si powder (SiPW, 2-10 micrometer in size) samples, which were suspended in water, using 532-nm, 7-ns light pulses generated from a frequency-doubled Q-switched Nd:YAG laser.

10.2.6.1 Photoluminescence of SiNWs

As shown in Fig. 10.8 the strongest PL peak appears at 521 nm (2.37 eV). With much lower intensity there are five discrete peaks observable at 781 nm (1.58 eV), 573 nm (2.17 eV), 460 nm (2.69 eV), 423 nm (2.93 eV) and 400 nm (3.1 eV) respectively. According to literature[19,20] we attribute the green 521 nm (2.37 eV) and 570 nm (2.17 eV) peaks to the radiative recombination of confined electronic states in the form of Si-Si dimmer on the surface of SiNWs. Optical absorption in Si-Si dimmer leads to the excitation of one electron to the excited state, resulting in self-trapped exciton (STE) at a larger Si-Si distance and smaller luminescence energy. They are likely favored at surfaces where the elastic response of the environment (to the Si-Si distance change) is likely to be

weaker than in the bulk. Therefore, STEs may exist only for small enough crystallites and hence are quantum-confined, observable only in nanosized crystallites. Light emission from these trapped excitons is predicted to be possible in the visible/infrared region either by direct radiative recombination or by indirect recombination via quantum tunneling and thermal activation[19,20]. At high temperature the recombination could be at some intermediate coordinate with a smaller lifetime and a larger emission energy (than those of next-nearest-neighbor interspacing). In other words, at room temperature this kind of luminescence can emit light with energy fairly close to the optical absorption energy.

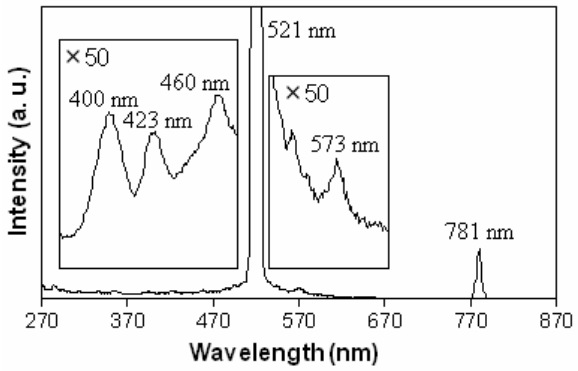

Fig. 10.8, The photoluminescence (PL) spectrum of the SiNWs recorded at room temperature with using a high intensity Xenon lamp as excitation source.

In Ref. 3, the 515 nm PL peak disappeared when the SiNWs were completely oxidized to silicon oxides. This observation would be better understood as the indication that the 515 nm peak is an intrinsic SiNWs' PL peak, probably due to surface Si-Si dimmers, rather than SiO defects. The second strongest PL peak of our SiNWs is located at 781 nm (1.58 eV) in Fig. 10.8. In agreement to experimental observation[3] as well as theoretical calculation based on the first principles model in reference[21,22], this peak is ascribed to the band-to-band radiative recombination of electron-hole pairs. It is blue-shifted from the indirect 1.1 eV band gap of bulk Si due to the nanosized confinement in SiNWs, similar

to many other experimental reports[3,23,24]. Though the average size of our SiNWs seems to be larger than theoretically predicted minimum value, the quantum confinement effect has been confirmed to play a role in our SiNWs sample by Raman signal downshift in Fig. 10.3. It may appear to mean that smaller-sized nanowires do exist in our SiNWs sample in which the quantum confinement effect occurs. The blue peaks around 460, 423 and 400 nm have been observed in completely or partly oxidized SiNWs samples[3,25,26,27] and should be attributed to radiative recombination which involves a free hole and an electron trapped by Si=O bonds or oxygen vacancy defects at the Si-SiO_2 interface (producing localized states in the band), since the wire would be coated by more or less silicon oxides.

10.2.6.2 Optical Limiting of SiNWs

So far no NLO study has been reported on SiNWs in literature. To gain better insight of the NLO response of SiNWs, the NLO response of multiwall carbon nanotubes and C_{60} were used as references[28,29]. The energy-dependent transmission results of the samples are displayed in Fig. 10.9a. At incident fluences of less than 3 J/cm^2 the energy transmittance is a constant. However, in excess of 3 J/cm^2, the transmittance decreases as the incident fluence increases, a typical limiting property for both SiNWs and SiPW. The experiments were conducted on the two samples under the same conditions, while the concentration of the SiPW in the test solutions has been adjusted in such a way that its linear transmittance is 70% at 532 nm, close to that of SiNWs. The limiting threshold, defined as the incident fluence at which the transmittance falls to 80% of the linear transmittance, is around 5.0 J/cm^2 for the SiNWs sample vs. 9.0 J/cm^2 of SiPW. Figure 10.9b clearly demonstrates that SiNWs and SiPW are both a broadband limiter up to 1064 nm, with SiNWs having

lower threshold value (10 vs. 20 J/cm^2 for SiPW). There are several mechanisms proposed for optical limiting, including reverse saturable absorption (RSA), nonlinear scattering, thermal blooming and multiphoton absorption[30]. Since the photoluminescence of our SiNWs was detected only between 400-780 nm (higher energy compared to 1064 nm), which means that the energy of the 1064 nm (1.16 eV) laser light is too low to excite the electron from its ground state to excited states, the RSA mechanism could be excluded in this case. Experimentally we found that nonlinear scattering is stronger with increasing incident energy. Hence the observation of limiting behavior of the two Si samples at 1064 nm laser incidence unambiguously shows the mechanism for the limiting behavior of the two Si samples is mainly due to nonlinear scattering. The fact that limiting performance is stronger for SiNWs than SiPW (see Fig. 10.9) is understandable, since two orders of magnitude smaller thermal conductivity has been measured on silicon nanowires compared to bulk Si[31]. This strong size-dependent thermal conductivity in SiNWs was ascribed to the increased role of boundary phonon [lattice vibration] scattering[31]. In Fig. 10.9a, however, the energy of incident light (530 nm or 2.32 eV) suffice the excitation of the electron in ground state into its excited states. For larger sized SiPW the optical absorption is indirect and hence less efficient, whereas for nanosized SiNWs the band-to-band excitation becomes direct and more efficient due to the quantum confinement of the free charge carriers. As shown in Refs [19, 20], along with the radiative recombination and relaxation into the ground state, the electron in the excited states can possibly be excited into higher excited states or be above-barrier-excited into self-trapped exciton states of surface Si-Si dimmers. If the absorption of the electrons in the excited levels is greater than that of the ground state, reversible saturation absorption (RSA) would occur and with its characteristic absorption increasing with light intensity.

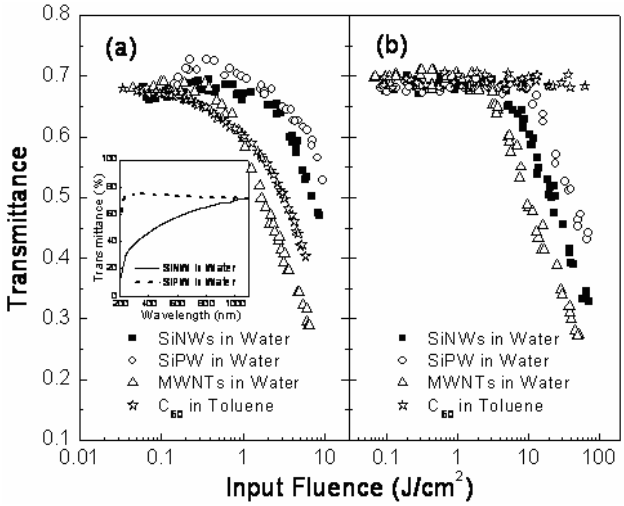

Fig. 10.9, The optical limiting measurements of the SiNWs and SiPW measured with 7-ns laser pulses at (a) 532-nm; and (b) 1064-nm wavelength. Both multiwalled carbon nanotubes (MWNTs) and C_{60} samples are used as the reference samples. The inset shows the optical transmission spectra for the SiNWs and SiPW.

Based on this analysis, RSA could occur in SiNWs. It is noted that in Fig. 10.9 the transmittance of SiNWs at 10 J/cm^2 is 0.45 in Fig. 10.9a (532 nm) vs. 0.6 in Fig. 10.9b (1064 nm), which means that the nonlinear limiting is more remarkable with 532-nm laser pulses than 1064-nm light pulses. This extra nonlinear limiting (Fig. 10.9a vs. Fig. 10.9b) could be contributed by RSA. SiNWs are a better optical limiter than SiPW since it is better in both nonlinear scattering and RSA effects due to the quantum confinement effects. The inset of Fig. 10.9a shows the optical transmission spectra recorded in the wavelengths between 200 and 1200 nm for the SiNWs and SiPW suspended in water. Obviously while SiPW absorbs lights only in the region between 200-250 nm the SiNWs does at wide range between 200-1000 nm with higher absorbance.

10.2.7 Summary

A new approach to grow SiNWs was proposed. The SEM and TEM images reveal that SiNWs can be produced with the absence of catalyst. XRD shows that the preferred

orientation is the same as that of the substrate. Our method proved that the catalyst is not essential to grow SiNWs, which can be self-induced, or oxygen-assisted. Photoluminescence study shows that the Si band-to-band gap increases from 1.1 eV for bulk Si to 1.56 eV for our SiNWs due to quantum confinement effect. Upon optical absorption self-trapped surface Si-Si dimmers could occur, which may be the origin of the strong PL peak at 521 nm and play an role in optical limiting of SiNWs with 532-nm, nanosecond laser pulses. With the observation of optical limiting at 1064 nm, nonlinear scattering is believed to make dominant contribution to the limiting performance of SiNWs. The method may be useful to the SiNW's' devices because the metallic catalyst can reduce the performance of nano-devices, such as mobility.

10.3 ZnO Nanostructures Based on Thermal Evaporation

10.3.1 ZnO Nanostructures

ZnO possesses spectacular chemical, structural, electrical and optical properties that make it useful for a diverse range of technological applications. As a wide band gap semiconductor (3.37 eV at room temperature) with large exciton binding energy (60 meV), ZnO is of great interest for the applications in low-voltage and short-wavelength electric and photonic devices, such as blue and UV light emitting diodes for full-color display and room-temperature excitonic ultraviolet laser diodes for high density optical storage[32,33,34,35]. Like many semiconductor materials, nanoanostructured ZnO may have superior optical properties than bulk crystals because of the quantum size effects[32,35,36,37,38,39]. Therefore the study of nanostructured ZnO has received increasing attention. A variety of ZnO nanostructures (ZnONs) morphologies have been reported, including nanowires[32], nanobelts[40], nanocombs[41], nanosprings[42], nanorings[43], nanotubes[44] and

nanocrystals[45]. Many methods have been employed in the synthesis of nanostructured ZnO, such as template (anodic aluminum oxide) growth[46], catalytic vapor phase transport process[47,48], solution deposition[35,45,49,50], thermal evaporation and condensation of Zn-containing materials (ZnO[51], zinc halide[52], or metallic Zn powder in the presence of oxygen[53]), metal organic vapor deposition[54,55], laser molecular beam epitaxy[56], plasma-enhanced molecular beam epitaxy[33] and ion sputter deposition[57], etc. When the thermal evaporation and condensation process was used, the structure and morphology of ZnO were found to depend on the location of deposition[51].

10.3.2 Experimental Details

Nanostructured ZnO was prepared by thermal vaporization and condensation of Zn (99.9 % purity) powder in the presence of oxygen. The alumina boat with Zn powder was placed at the center of a quartz tube reactor (Fig. 10.1). The tube was purged by a Helium (99.999 % purity) flow with 100 standard cubic centimeters per minute (sccm). The furnace temperature was increased to 850 ^{o}C, and an oxygen (99.99 % purity) flow was introduced to the tube reactor at a flow rate of 10 sccm. The mixed O_2 and He gas was maintained throughout the whole reaction process, which usually takes 30 minutes. After the reaction, the O_2 flow was switched off. The reactor was cooled down to room temperature with the protective He flow. The samples were collected from the inner wall of the quartz tube.

The characterization process was stated in section 10.2.1, such as TEM, SEM, XRD, photoluminescence and Raman. The measurements of field emission (FE) properties of ZnONMs were carried out using two-parallel-plate set-up in a high vacuum of about 5 ×

10^{-7} Torr[58]. The peeled ZnON films were adhered onto the Cu substrate, which serves as cathode, by double-sided copper tape. Indium tin oxide (ITO) glass covered with a layer of phosphor was employed as the anode. A cover glass plate was used as a spacer and the distance between the electrodes was kept at 100 μm. A Keithley 237 high voltage source measurement unit (SMU) was used to apply a voltage from 0 to 1100 V and to measure the emission current at the same time. All the measurements were performed at room temperature.

10.3.3 Characterization of ZnO Nanostructures

The ZnO nanostructures (ZnONs) were obtained at two different locations. ZnON-A was deposited on the reactor wall in the zone close to the center of the reaction tube (around 750 ^{o}C) while ZnON-B was produced in the zone close to the gas exit (around 200 ^{o}C). Figure 10.10a shows a SEM image of ZnON-A. The pike-shaped structure is observable, with a hexagonal bottom of about 200 nm in diameter and a sharp tip of less than 50 nm in diameter (see the inset in Fig. 10.10a). The average length of the ZnON-A pikes is about 1.5 μm. The X-ray diffraction pattern in Fig. 10.11a is characteristic of the wurtzite-structure ZnO. The selected-area electron diffraction (SAED) taken from one isolated ZnO nanofibre under TEM (see Fig. 10.12) indicates that the ZnON-A is basically single crystalline with some polycrystalline mixture. Figure 10.10b shows the SEM image of ZnON-B, in which the nano-pikes become thinner with the tip less than 10 nm in diameter (see the inset in Fig. 10.10b) and mixed with leaf-shaped ZnO. The XRD pattern of ZnON-B in Fig. 10.11b shows that the ZnON-B sample possesses wurtzite structure. However several weak peaks in Fig. 10.11b indicate the existence of Zn particles in ZnON-B. This is understandable since ZnON-B was collected from the

reactor wall away from the center of the furnace, where the temperature was relatively low. The zinc vapor may not be fully oxidized and the nano ZnO pikes formed are thinner. At the place close to the center of the reactor, the temperature is high with sufficient Zn vapor and O_2, so that larger nano ZnO pikes of higher crystalline quality were produced.

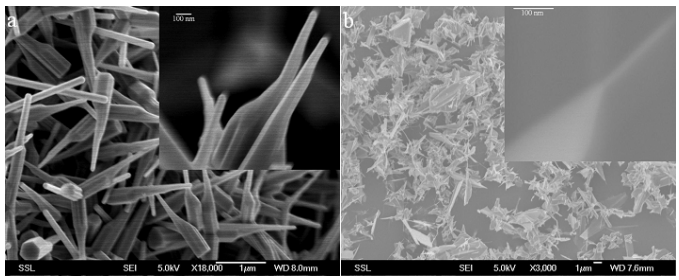

Fig. 10.10, SEM images of ZnON: (a) ZnON-A and (b) ZnON-B. The insets in the figures show close-up view of the pike tip at higher magnifications.

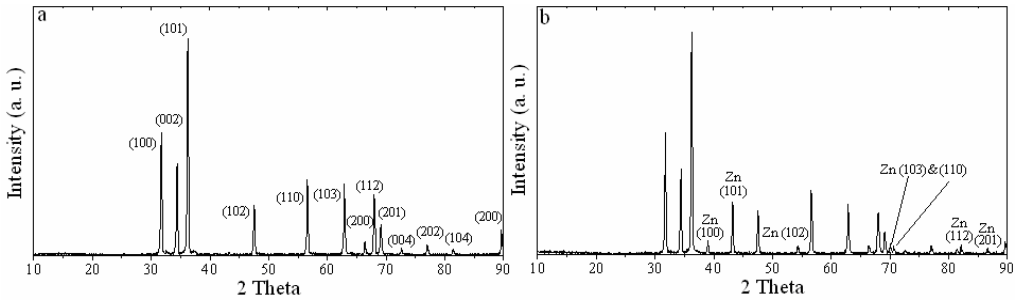

Fig. 10.11, XRD patterns for: (a) ZnON-A and (b) ZnON-B.

Fig. 10.12, Selective area electron diffraction pattern of ZnON-A.

Raman scattering spectra are shown in Figs. 10.13a and 10.13b. According to Group theory[59,60,61] zinc oxide with hexagonal wurtzite structure belongs to C^4_{6v} ($P6_3mc$) space

group and may have the following normal lattice vibration modes: $\Gamma_{opt} = A_1 + 2B_1 + E_1 + 2E_2$. Among them A_1, E_1 and E_2 are Raman active whereas B_1 is forbidden. From selection rules, only A_1 and E_2 modes can be observed in unpolarized Raman spectra. Hence the peaks at 332 cm^{-1}, 381 cm^{-1}, and 437 cm^{-1} in Fig. 10.13a for ZnON-A can be assigned to E_2(low), A_1, and E_2 (high), respectively[61]. In Fig. 10.13b ZnON-B produces a broad strong band around 570 cm^{-1}. This Raman band is known to be related to the E_1 mode due to the oxygen deficiency[62,63]. The Raman spectra of the samples further confirmed the oxygen vacancies in ZnON-B.

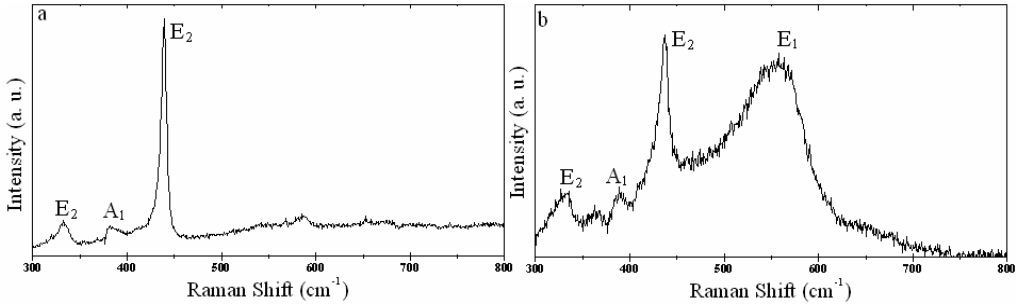

Fig. 10.13, Raman spectra with the excitation of 514.5 nm laser light for: (a) ZnON-A and (b) ZnON-B.

10.3.4 Photoluminescence of ZnO Nanostructures

The photoluminescence (PL) of ZnONMs at room temperature is shown in Fig. 10.14a and 10.14b with the excitation wavelength of 325 nm. For ZnON-A, one dominant peak at 383 nm (corresponding to 3.26 eV) is observable (Fig. 10.14a). This UV emission band can be attributed to the ZnO near-band exciton emission. This peak is similar to the P peak previously reported on high-quality ZnO crystals at higher temperature[39,64,65,66]. When the ZnO crystal is warmed, the shallow bound excitons de-trap thermally, and the inelastic scattering of the free excitons would result in the observation of the P peak[66]. For ZnON-B, in addition to the above two PL peaks, a very strong and broad band is centered at 500 nm. This green emission (around 2.46 eV) was proposed to be due to deep centers

(oxygen vacancies [39,50,67,68] or antisites[69]) which trap electrons (or holes). Because ZnON-B was collected in the zone close to the gas exit (around 200 ^{o}C) and the reaction time is around 30 min, the annealing effect is negligible and the antisite should not easily occur. However, the Raman scattering indicated that the existence of a lot of oxygen vacancies[65,66], which should be the dominant mechanism for the green emission of ZnON-B. These defects may largely occur in the imperfect grain boundary sites as well as other interstitial defects in ZnO. ZnON-B which was formed from the incomplete oxidation of zinc vapor is expected to consist of large amount of defects and hence shows very strong green PL emission. ZnON-A shows no green PL emission.

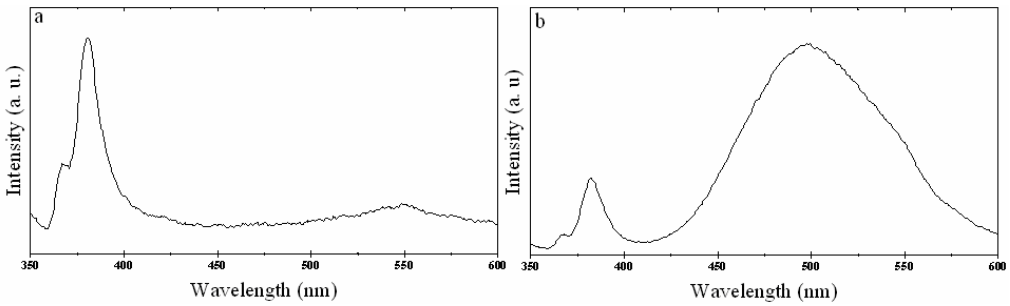

Fig. 10.14, Photoluminescence spectra obtained using Xenon lamp at 160 W as excitation source for: (a) ZnON-A and (b) ZnON-B;

10.3.5 Field Emission of ZnO Nanostructures

The field emission current density as a function of the macroscopic electric field is shown in Fig. 10.15. The turn-on fields for the two samples are 5.0 V/μm (ZnON-A) and 4.5 V/μm (ZnON-B), respectively. The emission current density reached 0.07 mA/cm^2 for ZnON-B at 7 V/μm, which is much higher than that of ZnON-A (0.02 mA/cm^2 at 11 V/μm).

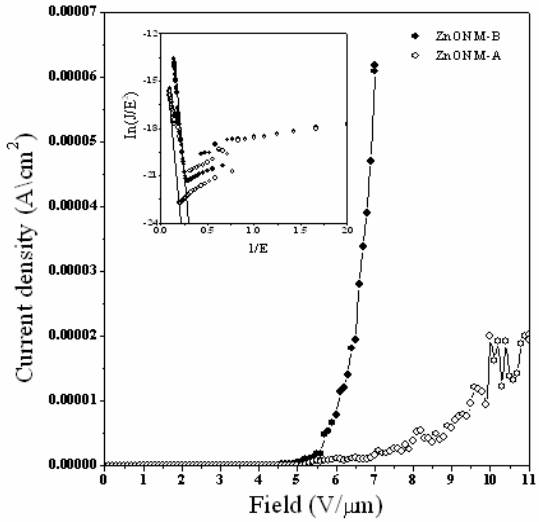

Fig. 10.15, Field emission measurement for ZnON-A (open symbols) and ZnON-B (solid symbols).

The Fowler–Nordheim (FN) plots for the measured samples are shown in the inset in Fig. 10.15. It is clear that the measured data fit well with the FN equation[70]:

$$\ln(\frac{J}{E^2}) = \ln(\frac{A\beta^2}{\varphi}) - \frac{B\varphi^{3/2}}{\beta E} \tag{10.1}$$

where J is the emission current density *(*A cm^{-2}*)*, *E* is the applied field (V μm^{-1}), *A*=1.543×10^{-6} A eV V^{-2}, *B*=6.833×10^3 eV$^{-3/2}$ V μm^{-1}, β is the field enhancement factor, and φ is the work function of emitter material (5.3 eV for ZnO[71]). The calculated field enhancement factor β from the slope of the inset in Fig. 10.15 is 1320 for ZnON-A and 1370 for ZnON-B, respectively. The β value of nanostructural ZnO is related to the geometry, crystal structure, conductivity, work function, and nanostructure density. The field emission current density of the ZnON-B is better than or at least comparable with those reported in literature for well-aligned ZnO nanofibers (β= 847)[70], although our samples were randomly oriented[71]. It should be mentioned that our field emission results are worse than those of ZnO nanowires on carbon fibers[72] with enhanced conductivity and alignment. The nanopikes in ZnON-B exhibit very sharp tip (Fig. 10.10b). The oxygen

deficiency as indicated from the PL (Fig. 10.14b) and Raman spectra (Fig. 10.13b) may enhance the conductivity of the ZnON-B (the measured resistance of ZnON-B is much smaller than that of ZnO-A). And the density of ZnON-B is lower than that of ZnON-A. All these factors contribute to the high emission current density and high field enhancement factor of ZnON-B.

10.3.6 Summary

ZnO nano-pike structures were produced by oxidative evaporation and condensation of Zn powders. The purity and crystalline structures of the ZnONs samples were related to the deposition positions. High quality crystalline ZnONs were produced at the place close to the center of the reactor. They have the PL and Raman spectra characteristic of perfect ZnO crystals. The ZnON-B produced at the place close to the gas exit has oxygen vacancies as indicated by the additional peaks in PL and Raman spectra due to insufficient oxidation of Zn vapor. ZnON-B gives a strong green PL emission and exhibits excellent field emission properties with high emission current density and lower turn-on field.

10.4 Mg Doped ZnO Nanowires

Doping has been widely used to improve the electrical and optical properties of semiconductors. It has been reported to introduce defects to ZnO and modify their luminescence properties[73,74]. Gallium doped ZnO nanofiber arrays showed a low threshold of electrical field in the field emission measurement[74]. Alloying ZnO with MgO (E_g=7.8 eV) permits the band gap to be controlled, which facilitates the band gap engineering[75]. Mg ions have radius (0.057nm) similar to Zn ions (0.060nm) so that Mg-

doped ZnO thin films are found to be a single phase alloy in a wide range of Mg doping levels. Their green photoluminescence have been carefully studied[75,76,77]. Nevertheless the Mg doped ZnO nanowires have not been available to date.

10.4.1 Experimental Details

Mg-doped ZnONW was prepared by oxidative vapor condensation. The alumina boat with Zn and Mg powders (2:1 in atomic ratio) were placed at the center of a quartz tube reactor as shown in Fig. 10.1. The powders were heated to 820 ^{o}C at a speed of 10 ^{o}C/min in a protective Helium flow with a flow rate of 100 standard cubic centimeters per minutes (sccm). Then, Oxygen flow at a speed of 10 sccm was introduced to the reactor after the designed furnace temperature reached. The mixed gas, O_2 and He, was maintained throughout the whole reaction process, which usually takes 30 minutes. After the reaction, the O_2 flow was switched off. The reactor was cooled down to room temperature with the protective He flow.

The characterization of morphologies, such as SEM, and structures, including XRD and Raman, is similar to those as stated in previous sections. X-ray photoelectron spectroscopy (XPS) was applied to study the Mg doping and chemical composition of Mg-ZnONWs. Optical transmittance and photoluminescence spectroscopies were recorded on a UV-visible spectrophotometer (Shimadzu UV-1700) and spectrofluorometer (Jasco FP-6300), respectively. Electroluminescence (EL) spectrum was measured by a home-made set-up with a fiber light detector (see Fig. 10.).

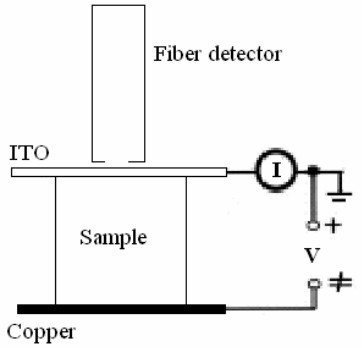

Fig. 10.16, Setup of the EL measurement.

10.4.2 Characterization of Mg Doped ZnO Nanowires (Mg-ZnONWs)

Figs. 10.17a and b show the SEM images of the Mg-ZnONWs sample taken from the quartz-tube wall close to the center of the tube. The Mg-ZnONWs have diameter ranging from 50 to 100 nm and length up to a few hundreds of μm. The XRD pattern in Fig. 10.18 can be indexed to ZnO wurtzite structure with strong [101] orientation. The strong sharp peaks indicate the high crystalline quality of the alloy samples. No appearance of MgO peaks in the XRD pattern indicates that the content (x) of Mg in the single-phase $Mg_xZn_{(1-x)}O$ alloy nanowires is <0.1[75] and Mg doping did not change the hexagonal atomic arrangement of ZnO. The presence of the Mg dopant in Mg-ZnONWs is further confirmed by the observation of XPS Mg 2p (at binding energy 50.5 eV) and KLL peaks (at bonding energies between 300-350 eV with Mg K_α photon source) as shown in Fig. 10.19.

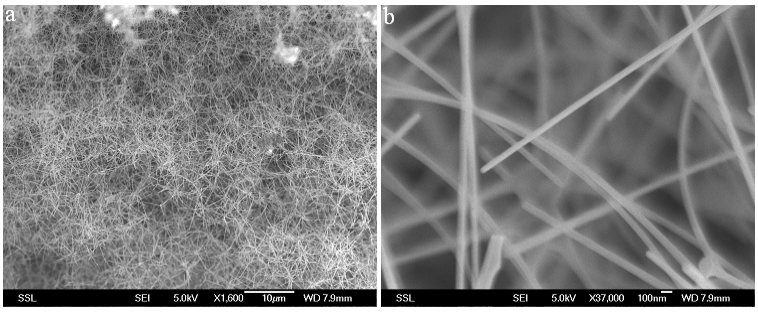

Fig. 10.17, SEM images of Mg-ZnONWs in (a) large scale and (b) local scale.

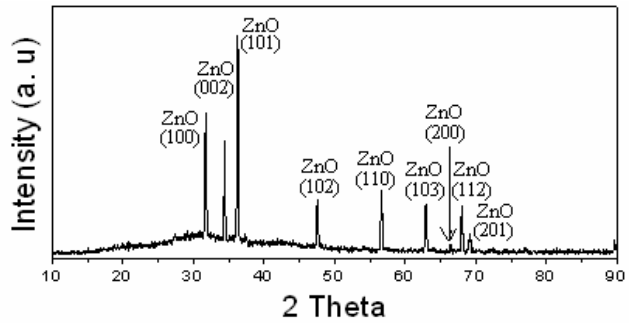

Fig. 10.18, XRD pattern of Mg-ZnONWs.

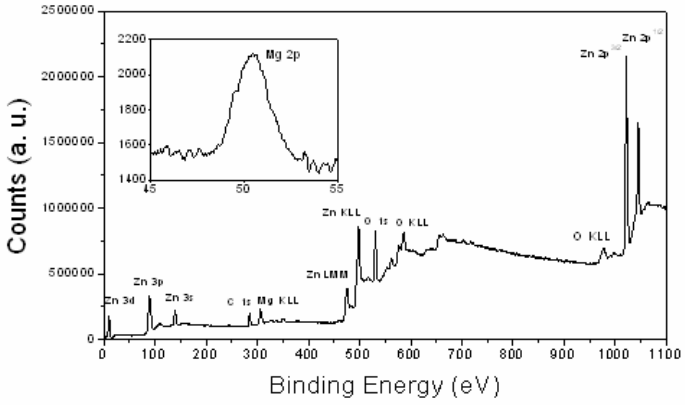

Fig. 10.19, XPS spectrum of Mg-ZnONWs.

Raman scattering spectrum is shown in Fig. 10.20. Zinc oxide with hexagonal structure belongs to C^4_{6v} space group. The normal lattice vibration modes can be predicted from group theory: $\Gamma_{opt} = A_1 + 2B_1 + E_1 + 2E_2$ where A_1, E_1 and E_2 are Raman active and B_1 forbidden. From the selection rules, only A_1 and E_2 modes can be observed in unpolarized Raman spectra. The peaks at 334, 380 and 437 cm^{-1} correspond to E_2(Low), A_1, and E_2 (High) respectively. It can be seen that the vibrational modes of Mg-ZnONWs are related to the modes of pure ZnO and no peak was observed at 560 cm^{-1}. Contrarily the 560 cm^{-1} peak is very strong in Zn-accessed ZnONWs (Fig. 10.13b). This peak is known to be due to oxygen vacancies. Therefore Raman scattering studies show that there do not exist large number of oxygen vacancies in the Mg-ZnONWs samples. The observation of strong green photoluminescence should be induced by other types of defects as discussed in the sections below.

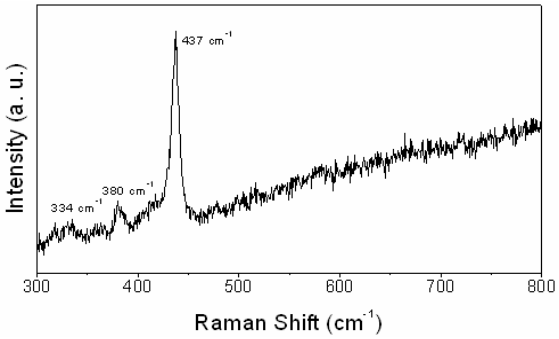

Fig. 10.20, Raman spectra of Mg-ZnONWs.

10.4.3 Optical Properties of Mg-ZnONWs

The UV-visible transmittance spectra in Fig. 10.21a show an absorption peak at 366.5 nm (3.39 eV) for Mg-ZnONWs (Red line) and 377.5 nm (3.29 eV) for pure ZnO (black line) respectively. By considering the excitonic binding energy of ZnO (60 meV), the measured band gap of Mg-ZnONWs is 3.45 eV, which is about 0.1 eV larger than that of pure ZnO (3.35 eV). The content (x) of Mg in the Mg-ZnONWs ($Zn_{(1-x)}Mg_xO$) is estimated from the relationship between the band gap and x ($E_{MgO} \times x + E_{ZnO} \times (1-x) = E_{Zn_{(1-x)}Mg_xO}$), and is about 0.023, which is consistent with the reported results[75,76].

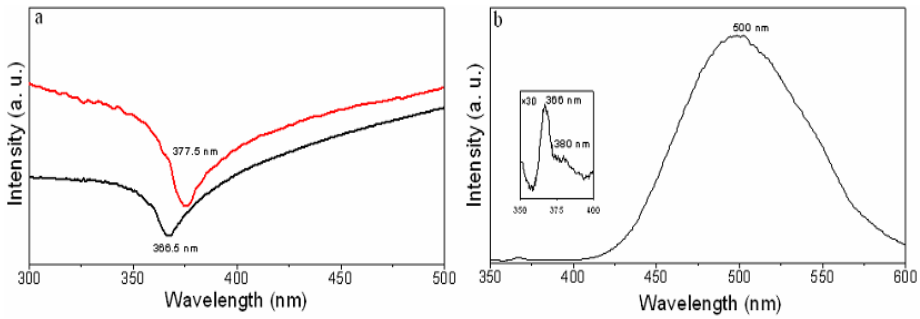

Fig. 10.21, Optical spectra of Mg-ZnONWs (a) transmittance and (b) photoluminescence.

The photoluminescence (PL) of Mg-ZnONWs at room temperature is shown in Fig. 10.21b at the excitation wavelength of 325 nm. A low intensity PL peak at 366 nm (3.36

eV) with a shoulder around 380 nm (3.25 eV) is observable for Mg-doped ZnONW. These UV emission bands can be observed in pure ZnONWs and Zn-access ZnONW too, with the reversed intensity ratio, i.e. the peak at 380 nm much stronger than that at 366 nm. The 3.25-eV peak is assigned to the bound exciton emission, i.e. the optical transitions from a shallow donor impurity levels to a shallow acceptor level while the peak at 3.39 eV is attributed to the de-exidation of electrons from the conduction band to the top valence band. The fact that 3.39 eV peak of the Mg-doped ZnONWs becomes stronger may be due to the screen effect where excitons are no longer trapped at intrinsic impurities because the Mg ions become the major impurity[75]. For pure ZnONWs without Mg doping there is little luminescence in the long wave length region. However a broad dominant peak at 500 nm which corresponds to a green emission band at 2.48 eV is observable for Mg-doped and Zn-access ZnONWs (Fig. 10.14b) probably due to the defects. We can use digital camera to record the green luminescence when the Mg-ZnONWs is stimulated by plasma in a plasma sputtering coater (JEOL JFC-1600), as shown in Fig. 10.22. This broad light emission peak originates from an inhomogeneous distribution of the various types defects in ZnO, such as interstitial Zn ions (Zn_i), monoionic Zn ions (Zn^+), Zn vacancies (V_{Zn+}, V_{Zn++}), substitutional Mg ions (Mg^{++}), interstitial Mg ions (Mg_i), monoionic oxygen ions (O^-), neutral oxygen atoms (O^*) and oxygen vacancies ($V_{o=}$) etc. Raman spectrum (Fig. 10.20) excluded the oxygen vacancy as a mechanism for the green emission in the Mg-ZnONWs samples. XPS (Fig. 10. 19) indicated the existence of Mg doping (substitution and interstitial). The Mg doping induced a lot of defects in the ZnO, which form defect energy levels, such as interstitial Mg ions, in the forbidden band, play a role in the radiative recombination or capture centers and leads to the strong green emission .The emission may include the capture of

excess electrons by deep donors, the capture of access holes by acceptors, the radiative recombination of free electrons and bound holes, radiative recombination in donor-acceptor pair and thermal release of bound hole to the valence band[78].

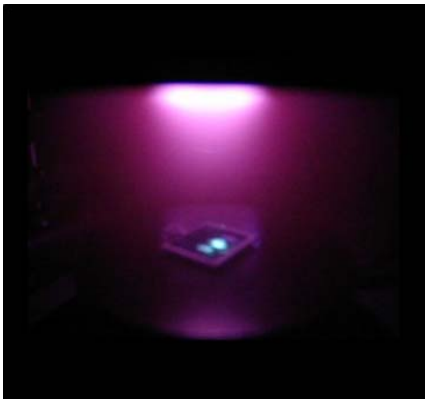

Fig. 10.22, Direct view of green light emission from Mg-ZnONWs.

Note that the nature of the oxygen defects in Zn-accessed ZnONWs and in Mg-doped ZnONWs could be very different based on the Raman spectra in Fig. 10.19 and 10.13b. There exist a large number of oxygen vacancies in the Zn-accessed-ZnONWs, but little in Mg-doped ZnONWs, which indicated that there do not exist a large number of oxygen vacancies in our Mg-ZnONWs samples. The Mg doping induced a lot of defects in the ZnO, which form defect energy levels, such as interstitial Mg ions, in the forbidden band, play a role in the radiative recombination or capture centers and leads to the strong green emission. The long-life light emission should be related to a second MgO phase, as observed using a digital camera[79]. During evaporation, MgO is excessive on the Mg-ZnONW surface, although it was not observed in XRD patterns. Electrons and holes created in ZnO phase by plasma can be trapped by defects from MgO precipitates on the surface. When they come back to ZnO phase and recombine with the emission centers, emission takes place again[79].

10.4.4 Electroluminescence of Mg-ZnONWs

Figure 10.23 shows the EL spectrum of Mg-ZnONWs with an applied electrical field of 1.6 V/μm at room temperature in atmosphere. The strongest peak at 500 nm with broad band is observable, which is related to the green emission. Another peak with low intensity is at 389 nm, corresponding to blue emission. The injected electron at the applied DC field takes part in a radiative recombination and hence gives rise to an emitted photon. The radiative recombination processes include interband transitions and impurity center recombination. The relative weak UV peak at 389 nm (3.20 eV) is related to the inter-band radiative recombination (directly from the valance band to conduction band). The interband transition is slightly less than the band gap (3.45 eV) due to the thermal excitation. The green light emission at 500 nm (2.43 eV) is contributed to the impurity center recombination.

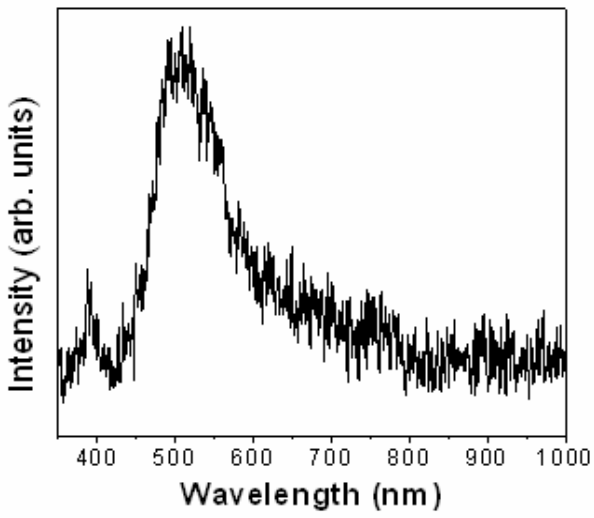

Fig. 10.23, Electroluminescence spectrum of Mg-ZnONWs with an applied field of 1.6 V/μm.

10.4.5 Summary

Mg-ZnONWs were produced by thermally oxidizing Zn and Mg powders. A strong peak at 500 nm was observed in PL and EL spectra. Raman scattering excludes oxygen

deficiency as a dominant mechanism for the green emission. Mg doping may induce charged oxygen defects. The electron trapped in these centers is in a multiplet (e.g. triplet) state. The transition from it to singlet ground state is forbidden, resulting in high efficient phosphorescence. This may be a strategic procedure in energy band engineering for long-lived charge separation.

10.5 Hydrogen Absorption of ZnO and Mg-ZnO Nanowires

10.5.1 Experimental Details

The hydrogen storage PCI of the ZnO and Mg-ZnO nanowires (ZnON and Mg-ZnON) was measured using a volumetric gas reaction controller[80,81] (AMC gas reaction controller) at room temperature up to 860 psi (1 pound per square inch). The samples (0.2 g) were evacuated and heated at 300 °C for 2 h prior to the measurement. Highly purified hydrogen (99.999% purity) was admitted and the isotherm at room temperature was recorded in the pressure range between 1 and 860 psi.

9.5.2 Hydrogen Storage

Hydrogen adsorption and desorption isotherms at room temperature are shown in Fig. 10.24. For a comparison, the hydrogen storage capacity of a commercial pure ZnO sample (com-ZnO) consisting of nanopowders (30 nm in diameter) was also measured. It shows 1.05 wt % uptake capacity at 860 psi and 65.2 % of which can be released upon de-pressure release. (Fig. 10.24 blue-color curves). Mg-ZnON gives the highest uptake of 2.79 wt % at 860 psi, with a total release of 1.95 wt %, i.e. 70.1% of the stored hydrogen can be released at ambient pressure. For ZnON, the ZnO nanostructures without the Mg doping, the uptake capacity is 2.57 wt% with 68.3 % release, indicating that our samples

can uptake many more hydrogen than commercial ZnO under identical conditions. At a medium pressure equivalent to that reported in Ref 17 (3.03 MPa), the uptake capacities of Mg-ZnON (0.99 wt %) and ZnON (0.91 wt %) are both larger than the reported result (0.83 wt %)[82].

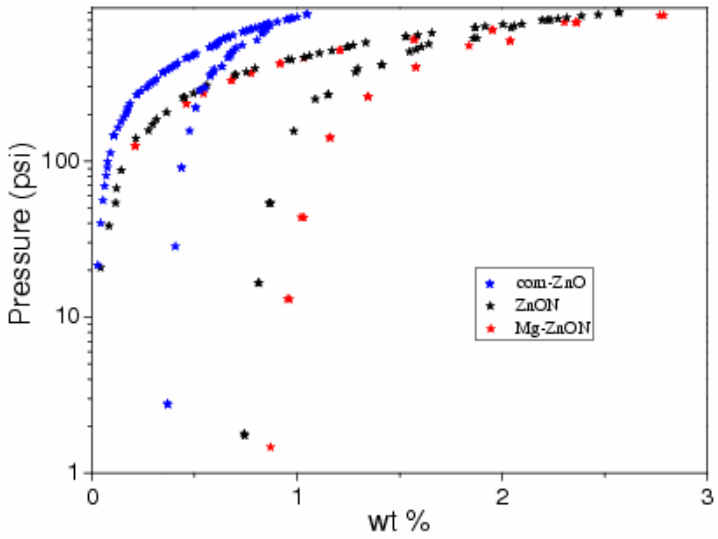

Fig. 10.24, The pressure-composition isotherms of the three samples, i.e. commercial ZnO, ZnON and Mg-ZnON, taken at room temperature.

In Fig. 10.25 temperature-programmed desorption (TPD) shows a H_2 desorption peak at ca. 140 ^oC for ZnON (red line in Fig. 10.24). For Mg-ZnON the peak is stronger, extending to higher desorption temperatures. By peak deconvorlusion, an extra peak around 170 ^oC can be expected (black line in Fig. 10.25). This strongly suggests that some hydrogen molecules were chemisorbed onto both Mg-ZnON and ZnON, and therefore would not be released at room temperature so that the PCI desorption curves do not follow the adsorption curve. Using a simple relation $E_d \sim 0.06\ T_p$[83] where E_d is the desoprtion energy and T_p the temperature at the TPD peak maximum, it can be estimated that the desorption energy is 24-27 Kcal/mol (ca. 1.1-1.2 eV).

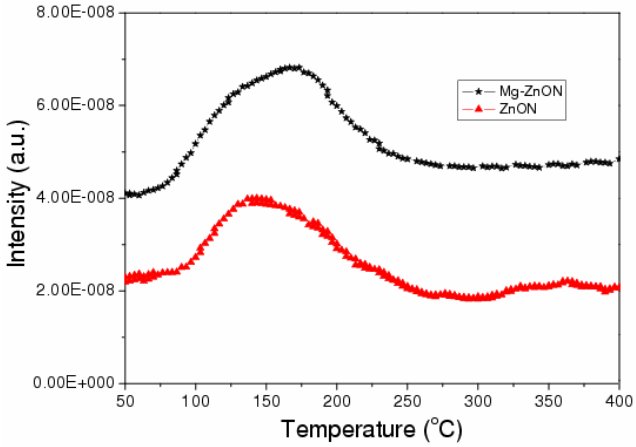

Fig. 10.25, TPD profiles of hydrogen-saturated Mg-ZnON and ZnON from room temperature to 350°C, ramp rate = 10°C/min, using argon as carrier.

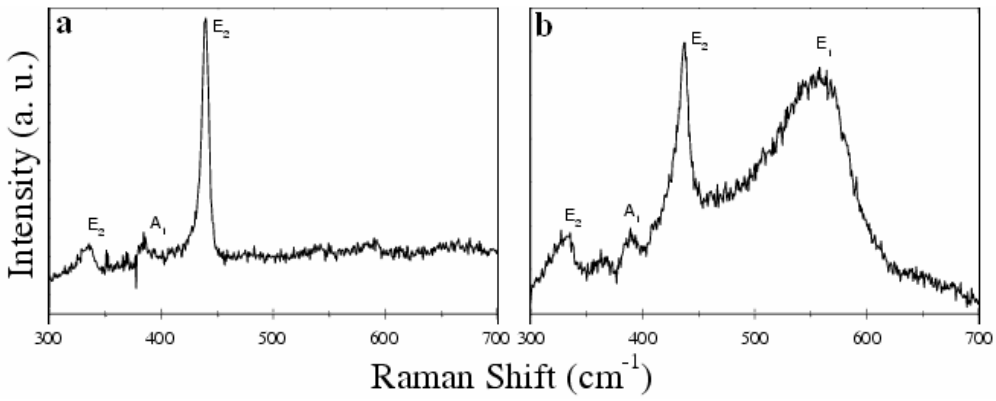

Fig. 10.26, Raman scattering for (a) com-ZnO, (b) ZnON.

Figure 10.26 displays the Raman scattering spectra of the samples. For commercial ZnO sample (com-ZnO) the peaks around 334, 380 and 438 cm^{-1} correspond to the Raman-active modes E_2(M), A_1, and E_2 (high) of the perfect wurzite ZnO crystal, respectively (see Fig. 10.26). For the ZnO nanowires (Fig. 10.26b) an extra Raman band around 580 cm^{-1} is known to be related to the E_1 mode due to the oxygen deficiency, indicating the presence of oxygen vacancies in the ZnO nanowires.

Based on a recent first-principle density function calculation, Van de Walle showed that hydrogen could incorporate in ZnO in high concentrations. The absorbed hydrogen could be located in various ZnO lattice sites (see Fig. 10.27, sites 1-5 which are similar to AB_O, AB_{Zn}, BC etc in Fig. 1 of Ref[84]) and in a few different forms including H^+, H^-, neutral atomic hydrogen H^o and H_2.

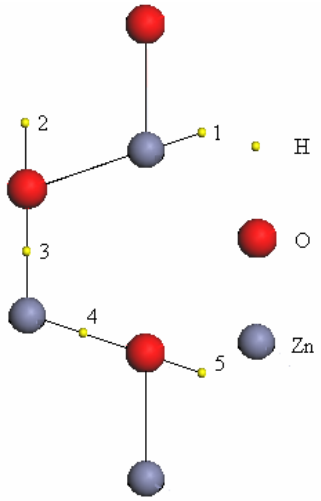

Fig. 10.27, Schematic diagram of wurtzite structured ZnO: 1-5 are possible sites of hydrogen absorption which are similar to AB_O, AB_{Zn}, BC etc in Fig. 1 of Ref [83].

The calculated formation energy of the absorbed H in reference[84] is strongly dependent on the position of the Fermi level in the ZnO band gap. If ZnO is n-type and the Fermi level is 2 eV above the top valence band, as observed in most cases, the H^+, H_2, H^o and H^- have the formation energy ca. -0.3, 0.8, 1.0 and 2.0 eV respectively[84]. This indicates that H^+ is absorbed at oxygen sites, forming O-H bond. The formation of O-H bonds with negative formation energy is the main driving force of the ZnO hydrogen uptake. It leads to the irreversible hydrogen uptake, so that ca. 25 % of the stored hydrogen can be released only upon heating. On the other hand the absorbed H_2, H^o and H^- in ZnO, which have positive formation energy, are energetically meta-stable so that can be released at ambient

conditions. The calculation also concluded that H_2 prefers a location in the interstitial channel, centered at site 1 (see Fig. 10.27) which is similar to AB_{Zn} sites in reference[84]. H^- may be most probably located near Zn^{++} ions (sites 3 and 4 in Fig. 10.27) as observed from secondary ion mass spectroscopic studies[85]. The calculation[84] also demonstrated that oxygen vacancies may form in ZnO in large concentration and the hydrogen atomes located at the oxygen vacancies are energetically meta-stable. This may explain the fact that the hydrogen storage capacity is affected by the crystallinity of ZnO samples. The better crystalline commercial ZnO sample hence showed lower hydrogen storage capacity. For the ZnON sample without Mg doping, the low growth temperature results in the larger quantity of oxygen vacancies, which should be responsible to the high uptake capability. Mg doping move the Fermi level down, closer to the valence band so that the H^+ formation energy increased[84], which slightly enhanced the hydrogen uptake capability.

10.5.3 Summary

In summary, ZnO nanostructures without and with Mg doping were fabricated by a simple thermal oxidation method. Both ZnON and Mg-ZnON possess wurtzite crystalline structure. Hydrogen absorption measurements reveal that Mg-ZnON has the highest uptake and release capability (2.79wt% and 1.95wt% at room temperature respectively). ZnON gives 2.57wt% and 68.3wt% hydrogen uptake and release, which are still much better than commercial ZnO measured under identical conditions. The hydrogen absorption is driven by the formation of O-H bond. Doping and lattice defects may be responsible for higher hydrogen uptake on ZnON and Mg-ZnON.

References:

[1] S. Chung, J Yu and J. R. Heath, Appl. Phys. Lett. 76, 2068 (2000).
[2] A. Tilke, R. H. Blick, H. Lorenz, and J. P. Kotthaus, J. Appl. Phys. 89, 8159 (2001).
[3] D. P. Yu, Z. G. Bai, J. J. Wang, Y. H. Zou, W. Qian, J. S. Fu, H. Z. Zhang, Y. Ding, G. C. Xiong, L. P. You, J. Xu, and S. Q. Feng, Phys. Rev. B 59, R2498 (1999).
[4] L. T. Canham, Appl. Phys. Lett. 57, 1046 (1990).
[5] M. M. Alfredo and C .M. Lieber, Science 279, 208 (1998).
[6] Y. F. Zhang, Y. H. Tang, N. Wang, D. P. Yu, C. S. Lee, I. Bello, and S. T. Lee, Appl. Phys. Lett. 72, 1835 (1998).
[7] Y. H Tang, Y. F. Zhang, H. Y. Peng, N. Wang, C. S. Lee, and S. T. Lee, Chem. Phys. Lett. 314, 16 (1999).
[8] H. Namatsu, S. Horiguchi, M. Nagase, and K. Kurihara, J. Vac. Sci. Technol. B 15, 1688 (1997).
[9] H. Namatsu, Y. Watanabe, K. Yamazaki, T. Yamaguchi, M. Nagase, Y. Ono, A. Fujiwara, and S. Horiguchi, J. Vac. Sci. Technol. B 21, 1 (2003).
[10] D. P. Yu, Z. G. Bai, Y. Ding, Q. L. Hang, H. Z. Zhang, J. J. Wang, Y. H. Zou, W. Qian, G. C. Xiong, H. T. Zhou, and S. Q. Feng, Appl. Phys. Lett. 72, 3458 (1998).
[11] G. Gundiah, F. L. Deepak, A. Govindaraj, and C. N. R. Rao, Chem. Phys. Lett. 381, 579 (2003).
[12] T. Ono, H. Saitoh, and M. Esashi, Appl. Phys. Lett. 70, 1852 (1997).
[13] Y. J. Xing, D. P. Yu, Z. H. Xi, and Z. G. Xue, Appl. Phys. A 76, 551 (2003).
[14] B. Li, D. Yu, and S. Zhang, Phys. Rev. B 59, 1645 (1999).
[15] N. Wang, Y. H. Tang, Y. F. Zhang, C. S. Lee and S.T. Lee, Phys. Rev. B 58, R16024 (1998).
[16] R. Q. Zhang, T. S. Chu, H. F. Cheung, N. Wang and S. T. Lee, Mater. Sci. & Eng. C 16, 31 (2001).
[17] E. I Givargizov, J. Cryst. Grow. 31, 20 (1975).
[18] W. Shi, H. Peng, Y. Zheng, N. Wang, N. Shang, Z. Pan, C. Lee and S. T. Lee, Adv. Mater. 12, 1343 (2000).
[19] G. Allan, C. Delerue and M. Lannoo, Phys. Rev. Lett. 76, 2961 (1996).
[20] M. H. Nayfeh, N. Rigakis and Z. Yamani, Phys. Rev. B 56, 2079 (1997).
[21] F. Buda, J. Kohanoff and M. Parrinello, Phys. Rev. Lett. 69, 1272 (1992).
[22] X. Zhao, C. M. Wei, L. Yang and M. Y. Chou, Phys. Rev. Lett. 92, 236805 (2004).
[23] S. T. Lee, N. Wang and C. S. Lee, Mater Sci & Eng A, 286, 16 (2000).
[24] Y. F. Zhang, Y. H. Tang, H. Y. Peng, N. Wang, C. S. Lee, I. Bello and S. T. Lee, Appl. Phys. Lett. 75, 1842 (1999).
[25] D. Nesheva, C. Raptis, A. Perakis, I. Bineva, Z. Aneva, Z. Levi, S. Alexandrova, and H. Hofmeister, J. Appl. Phys. 92, 4678 (2002).
[26] Y. W. Wang, C. H. Liang, G. W. Meng, X. S. Peng and L. D. Zhang, J. Mater. Chem. 12, 651 (2002).
[27] J. Wu, T. Wong and C. Yu, Adv. Mater. 22, 1643 (2002).
[28] P. Chen, X. Wu, X. Sun, J. Lin, W. Ji and K. L. Tan, Phys. Rev. Lett. 82, 2548 (1999).
[29] X. Sun, Y. Xiong, P. Chen, J. Lin, W. Ji, J.H. Lim, S.S. Yang, D. J. Hagan and E.W. Van Stryland, Appl Optics 39, 1998 (2000).
[30] D.G. Mclean, R.L. Sutherland, M.C. Brant, D.M. Brandelik, P.A. Fleitz and T. Pottenger, Optics Lett.18, 858 (1993).

[31] D. Y. Li, Y. Wu, R. Fan, P. D. Yang and A. Majumdar, Appl. Phys. Lett. *83*, 3186 (2003).
[32] M. H. Huang, S. Mao, H. Feick, H. Yan, Y. Wu, H. Kind, E. Weber, R. Russo, and P. Yang, Science 292, 1897 (2001).
[33] D. M. Bagnall, Y. F. Chen, Z. Zhu, T. Yao, S. Koyama, M. Y. Shen, and T. Goto, Appl. Phys. Lett. 70, 2230 (1997).
[34] H. Cao, J. Y. Xu, D. Z. Zhang, S. -H. Chang, S. T. Ho, E. W. Seelig, X. Liu, and R. P. H. Chang , Phys. Rev. Lett. 84, 5584 (2000).
[35] M. H. Huang, Y. Wu, H. Feick, N. Tran, E. Weber, and P. Yang, Adv. Mater. 13, 113 (2001).
[36] E. M. Wong and P. C. Searson, Appl. Phys. Lett. 74, 2939 (1999).
[37] B. J. Jin, S. H. Bae, S. Y. Lee, and S. Im, Mater. Sci. Eng. B 71, 301 (2000).
[38] C. Pieralli and M. Hoummady, Appl. Phys. A 66, 377 (1998).
[39] Y. Gu, I. L. Kuskovsky, M. Yin, S. OBrien, and G. F. Neumark, Appl. Phys. Letts. 85, 3833 (2004).
[40] Z. W. Pan, Z. R. Dai and Z. L. Wang, Science 291, 1947 (2001).
[41] S. Hashimoto and A. Yamaguchi, J. Am. Ceram. Soc. 79, 1121 (1996).
[42] X. Y. Kong and Z. L. Wang, Nano Lett. 3, 1625 (2003).
[43] X. Y. Kong, Y. Ding, R. S. Yang and Z. L. Wang, Science 303, 1348 (2004).
[44] J. Zhang, L. Sun, C. Liao and C. Yan, Chem. Commun. 262 (2002).
[45] R. Viswanatha, S. Sapra, B. Satpati, P. V. Satyam, B.N. Dev and D.D. Sarma, J. Mater. Chem. 14, 661 (2004).
[46] Y. Li, G. M. Meng, L. D. Zhang, and F. Phillipp, Appl. Phys. Lett. 76, 2011 (2000).
[47] Y. W. Wang, L. D. Zhang, G. Z. Wang, X. S. Peng, Z. Q. Chu, and C. H.Liang, J. Cryst. Growth 234, 171 (2002).
[48] C. N. R. Rao, G. Gundiah, F. L. Deepak, A. Govindaraj and A. K. Cheetham, J. Mater. Chem. 14, 440 (2004).
[49] D. S. Boyle, K. Govender, P. O'Brien, Chem. Commun. 80 (2002).
[50] M. Yin, Y. Gu, I. L. Kuskovsky, T. Andelman, Y. Zhu, G. F. Neumark, and S. OBrien, J. Am. Chem. Soc. 126, 6206 (2004).
[51] J. Lee, K. Park, M. Kang, I. Park, S. Kim, W. K. Cho, H. S. Han and S. Kim, J. Crystal Growth 254, 423 (2003).
[52] K. Omichi, N. Takahashi, T. Nakamura, M. Yoshioka, S. Okamoto and H. Yamamoto, J. Mater. Chem. 11, 3158 (2001).
[53] H. Yan, R. He, J. Johnson, M. Law, R. J. Saykally, and P. Yang, J. Am. Chem. Soc. 125, 4728 (2003).
[54] B. P. Zhang, N. T. Binh, Y. Segawa, Y. Kashiwaba, and K. Haga, Appl. Phys. Lett 84, 586 (2004).
[55] B. Zhao, H. Yang, G. Du, X. Fang, D. Liu, C. Gao, X. Liu and B. Xie, Semicond. Sci. Technol. 19, 770 (2004).
[56] C. H. Chia, T. Makino, K. Tamura, Y. Segawa, M. Kawasaki, A. Ohtomo, and H. Koinuma, Appl. Phys. Lett. 82, 1848 (2003).
[57] W. Chiou, W. Wu, and J. Ting, Diamond and Related Materials 12, 1841 (2003).
[58] Y. W. Zhu, T. Yu, F. C. Cheong, X. J. Xu, C. T. Lim, V. B. C Tan, J. T. L. Thong and C.H. Sow, Nanotechnology 16, 88 (2005).

[59] A. Kaschner, U. Haboeck, M. Strassburg, G. Kaczmarczyk, A. Hoffmann, C. Thomsen, A. Zeuner, H. R. Alves, D. M. Hofmann, and B. K. Meyer, Appl. Phys. Lett. 80, 1909 (2002).
[60] M. Tzolov, N. Tzenov, D. D. Malinovska, M. Kalitzova, C. Pizzuto, G. Vitali, G. Zollo, and I. Ivanov, Thin Solid Films 379, 28 (2000).
[61] F. Decremps, J. P. Porres, A. M. Saitta, J. C. Chervin, and A. Polian, Phys. Rev. B 65, 092101 (2002).
[62] X. L. Xu, S. P. Lau, J. S. Chen, G. Y. Che, and B. K. Tay, J. Cryst. Growth 223, 201 (2001).
[63] J. J. Wu and S. C. Liu, J. Phys. Chem. B 106, 9546 (2002).
[64] Y. C. Kong, D. P. Yu, B. Zhang, W. Fang, and S. Q. Feng, Appl. Phys. Lett. 78, 407 (2001).
[65] B. P. Zhang, K. Wakatsuki, N. T. Binh, Y. Segawa, and N. Usami, J. Appl. Phys. 96, 340 (2004).
[66] J. Wilkinson, G. Xiong, K. B. Ucer and R. T. Williams, J. of Nonlinear Optics 29, 529 (2002).
[67] K. Vanheusden, W. L. Warren, C. H. Seager, D. K. Tallant, J. A. Voigt, and B. E. Gnade, J. Appl. Phys. 79, 7983 (1996).
[68] D. Li, Y. H. Leung, A. B. Djurisic, Z. T. Liu, M. H. Xie, S. L. Shi, S. J. Xu, and W. K. Chan, Appl. Phys. Lett. 85, 1601 (2004).
[69] B. Lin, Z. Fu, and Y. Jia, Appl. Phys. Lett. 79, 943 (2001).
[70] C. J. Lee, T. J. Lee, S. C. Lyu, Y. Zhang, H. Ruh and H. J. Lee, Appl. Phys. Lett. 81, 3648 (2002).
[71] C. C. Tang and Y. Bando, Appl. Phys. Lett. 83, 659 (2003).
[72] D. Banerjee, S.H. Jo, Z.F. Ren, Adv. Mater. 16, 2028 (2004).
[73] B. K. Meyer, H. Alves, D. M. Hofmann, W. Kriegseis, D. Forster, F. Bertram, J. Christen, A. Hoffmann, M. Straßburg, M. Dworzak, U. Haboeck, A. V. Rodina, Phys. Stat. Sol. 241, 231 (2004).
[74] C. X. Xu, X. W. Sun, and B. J. Chen, Appl. Phys. Lett. 84, 1540 (2004).
[75] A. Ohtomo, M. Kawasaki, T. Koida, K. Masubuchi, H. Koinuma, Y. Sakurai, Y. Yoshida, T. Yasuda, and Y. Segawa, Appl. Phys. Lett. 72, 2466 (1998).
[76] D. Zhao, Y. Liu, D. Shen, Y. Lu, J. Zhang, X. Fan, J. Appl. Phys. 90, 5561 (2001).
[77] F. K. Fan, B. I. Kim, G. X. Liu, Z. F. Liu, J. Y. sohn, W. J. Lee, B. C. Shin, and Y. S. Yu, J. Appl. Phys. 95, 4772 (2004).
[78] M. A. Reshchikov, G. C. Yi and B.W. Wessels, Phys. Rev. B 59, 13176 (1999).
[79] J. Zhang, Z. Zhang, T. Wang, Chem. Mater. 16, 768 (2004).
[80] G. G. Tibbetts, G. P. Meisner, and C. H. Olk, Carbon 39, 2291 (2001).
[81] T. Kiyobayashi, H. T. Takeshita, H. Tanaka, N. Takeichi, A. Zuttel, L.Schlapbach, and N. Kuriyama, J. Alloys Compd. 330–332, 666 (2002).
[82] Q. Wan, C. L. Lin, X. B. Yu, T. H. Wang, Appl. Phys. Lett. 84, 124 (2004).
[83] R. I. Masel, in "Principles of adsorption and reaction on solid surfaces", John Wiley&Son, 1996, Inc (New York), p513.
[84] C. G. van de Walle, Phys. Rev. lett. 85, 1012 (2000).
[85] H. Chen, L. Chen, J. Y. Lin, K. L. Tan and J. Li, J. Phys. Chem. B 102, 1994 (1998).

CHAPTER 11

CONCLUSIONS AND RECOMMENDATIONS

Nanoscience and nanotechnology are concerned with the structures, properties, and processes involving materials having organizational features on the spatial nanoscale. From the experimental point of view, the fundamental problem in nanoscale technology is how to synthesis these nanostructures from chemical precursors and assemble them for the purposes of application. Another critical challenge in developing successful nanoscale technology is development of reliable simulation tools to guide the design, synthesis, monitoring, and testing of the nanoscale systems. In this thesis, theoretical method based on density functional theory and experimental methods including template method and thermal evaporation were employed to reach the goals.

In this chapter, the dissertation is wrapped up by providing a summary of the main findings of this research work. And, we provide some directions for further research in the area.

11.1 Contributions

In this thesis, the theoretical calculation and experimental method were carried out to study nanostructured materials and explore their possible applications. The results demonstrated that this research is efficient and fruitful. More specifically, carbon and carbon-related nanotubes, including carbon nanoscrolls, highly-ordered carbon nanotubes, boron carbonitride nanotubes and functionalized carbon nanotubes, and semiconductor

nanostructures, including Si nanowires and ZnO nanostuctures were investigated. In detail, the main findings include:

- The first-principles calculations on electronic and optical properties of the carbon nanoscrolls were performed. The results show that the electronic and optical properties of carbon nanoscrolls are different from those of nanotubes. The electronic properties of the scroll are closely related to the overlapping layers in the scroll. The nanoscrolls were found to be metallic/semimetallic within LDA. The analysis on the reflection and loss function showed that the nanoscroll structure share properties of both SWCNTs and MWCNTs.
- The functionalization of SWCNTs gave rise to significant changes in the electronic and optical properties of the semiconducting SWCNT on the basis of first-principles calculation. It has been found that the charge transfer from the carbon to the attached atoms or chemical groups. An acceptor level in the functionalized-SWCNT system was found due to the hole doping. It was found that the functionalization can be an effective way of modifying the electronic properties of semiconducting SWCNTs.
- The electronic, optical and symmetrical properties of BC_2N nanotubes were systematically investigated using first-principles method. The electronic properties of the BC_2N nanotubes are closely related to both diameter and charility. Generally, most of BC_2N nanotubes, except several smallest tubes, are direct band gap semiconductors although there are differences in details. Optical study demonstrated that the absorption spectra and loss functions of BC_2N nanotubes are closely related to their diameter and charility. The optical gap observed from the

absorption spectra indicated that it can redshift or blueshift with the increasing the tube diameter, depending on the tube charility. The pronounced peaks in the loss function spectra are mainly induced by the collective excitation of π electrons below 10.0 eV and the high-frequency π+σ plasmon.

- C-doped ZnO showed showed room temperature ferromagnetism based on the combined calculation and experiment study.
- AAO template with hexagonal arrangement of nanopores was fabricated by two-step anodization. The naturally occurred self-organization process was discussed based on the electrical bridge model. Based on the model, the effect of anodizing conditions on the ordering was analyzed and the optimal anodizing conditions can be explained.
- Highly ordered carbon nanotubes were produced by AAO template synthesis. The ordered CNTs can grow within or out-of the nanopores of AAO template depending on the growth conditions, i.e., thickness of the template, catalyst, temperatures, and diameter of the nanopore. And the graphitization of AAO-template grown CNTs depends on growth conditions. The CNTs produced from ethylene and with the presence of Co catalysts are generally better in graphitization.
- Metal nanowires were produced based on the AAO template via the electrodeposition. Single-crystal nanowires with preferred orientation and polycrystal nanowires were produced by controlling the deposition conditions. The single crystalline samples, Ni and Co, have larger coercivity, higher magnetization squareness and significant anisotropy. And the optical limiting

properties of Pt, Ni, Pd and Ag nanowires are better than those of Cu and Co nanowires.

- Si nanowires (SINWs) were produced by catalyst-free thermal evaporation. The SiNWs are highly crystalline with only little impurities such as amorphous Si and SiO_x. Photoluminescence study shows that the Si band-to-band gap increases from 1.1 eV for bulk Si to 1.56 eV for our SiNWs due to quantum confinement effect. With the observation of optical limiting at 1064 nm, nonlinear scattering is believed to make dominant contribution to the limiting performance of SiNWs.
- ZnO nano-pike structures (ZnONs) were produced by oxidative evaporation and condensation of Zn powders. The purity and crystalline structures of the ZnONs samples were related to the deposition positions. High quality crystalline ZnONs (ZnON-A) have the PL and Raman spectra characteristic of perfect ZnO crystals. The low quality crystalline ZnONs (ZnON-B) have oxygen vacancies as indicated by the additional peaks in PL and Raman spectra. ZnON-B gives a strong green PL emission and exhibits excellent field emission properties with high emission current density and lower turn-on field.
- Mg doped ZnO nanowires (Mg-ZnONWs) were produced by thermally oxidizing Zn and Mg powders. A strong peak at 500 nm was observed in PL and EL spectra, respectively. Raman scattering excludes oxygen deficiency as a dominant mechanism for the green emission. Mg doping may induce charged oxygen defects. The electron trapped in these centers is in a multiplet (e.g. triplet) state. The transition from it to singlet ground state is forbidden, resulting in high efficient phosphorescence. This may be a strategic procedure in energy band engineering for long-lived charge separation.

11.2 Recommendations For Further Research

Further research work on nanostructures can proceed on two fronts, i.e. theoretical and experimental.

On the theoretical front, theoretical calculation on semiconductor nanostructures should be carried out to understand the quantum confinement effect and investigate their application to nanodevices.

On the experimental front, it may be possible to extend existing AAO-template method to synthesis of highly-ordered semiconductor nanowires. The integration of nanodevices based on AAO template could be done by combining metallic and semiconductor nanowires together.